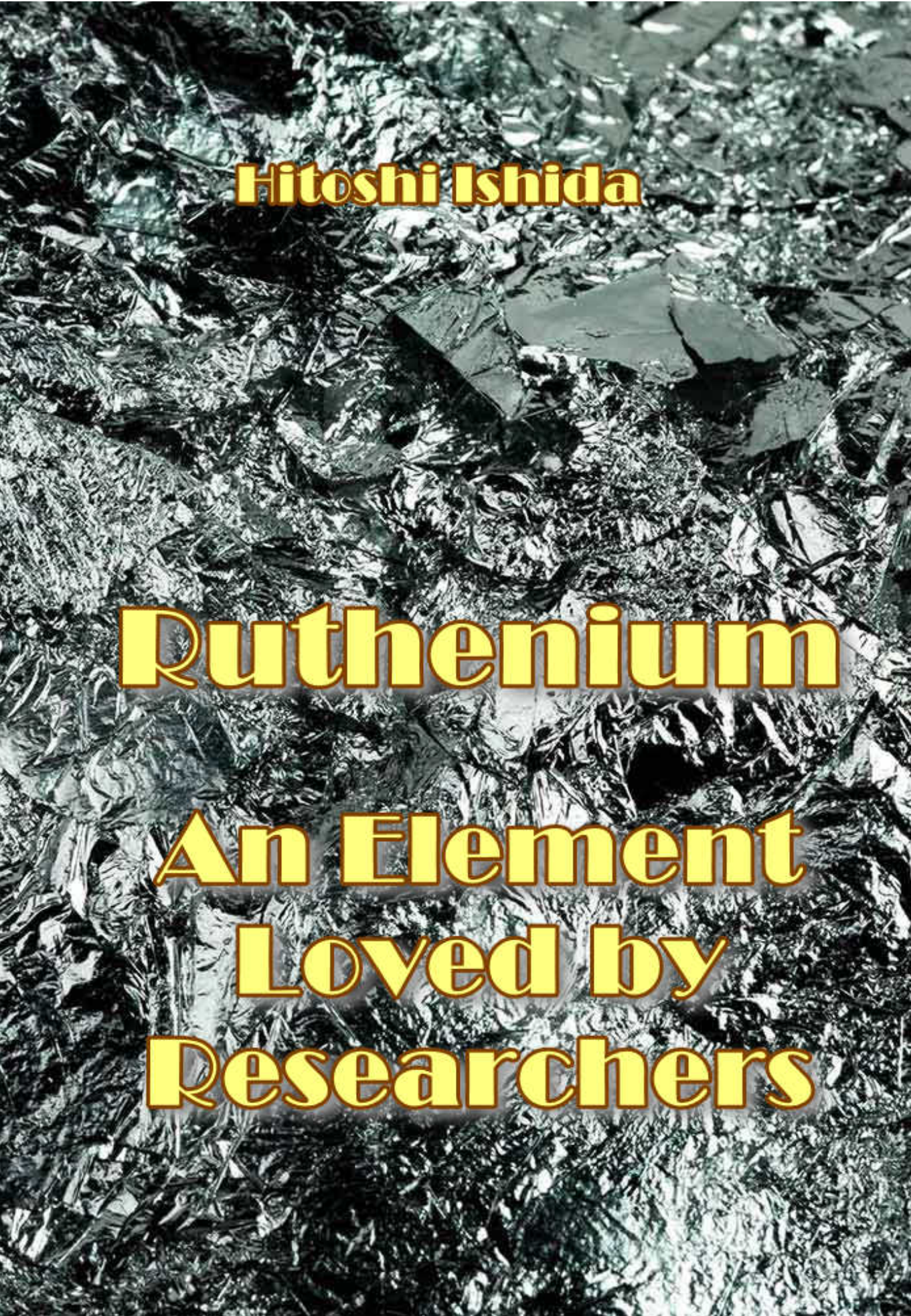
Hitoshi Ishida
Ruthenium
An Element Loved by Researchers

Detection of Bio-Relevant Metal Ions by Luminescent Ru(II)-Polypyridyl Based Sensors

Pramod Kumar and Sushil Kumar

Abstract

Biorelevant metal ions such as Cu^{2+} and Fe^{2+}/Fe^{3+} participate in various biological events which include electron transfer reactions, delivery and uptake of oxygen, DNA and RNA syntheses, and enzymatic catalysis to maintain fundamental physiological processes in living organisms. So far, several analytical techniques have been investigated for their precise detection; however, luminescence-based sensing is often superior due to its high sensitivity, selectivity, fast and easy operation and convenient cellular imaging. Owing to their immense photophysical and photochemical properties stemming from large Stokes shift, absorption in visible region, good photostability and long excited state lifetimes, Ru(II)-polypyridyl-based complexes have gained increasing interest as luminophores. Over past few decades, several Ru(II)-polypyridyl based chemosensors have rapidly been developed for detection of different biorelevant and other metal ions. The main object of this book chapter is to cover a majority of Ru(II)-polypyridyl based chemosensors showing a selective and sensitive detection of bio-relevant Cu^{2+} and Fe^{2+}/Fe^{3+} ions. The photophysical properties of Ru(II) complexes, detection of metal ions, sensing mechanism and applications of these sensors are discussed at a length.

Keywords: Ru(II)-polypyridyl, phosphorescence, sensing, biorelevant, metal ions

1. Introduction

The aim of this chapter is to familiarize readers about the luminescent sensing applications of Ru(II)-polypyridyl fragment based chemical systems for the detection of bio-relevant metal ions. Biorelevant metal ions such as Cu^{2+} and Fe^{2+}/Fe^{3+} participate in various biological events which include electron transfer reactions, delivery and uptake of oxygen, DNA and RNA syntheses and enzymatic catalysis [1, 2]. Ru(II)-polypyridyl complexes have been considered as ideal phosphorescent chemosensors due to their distinguished photochemical and photophysical properties such as absorption in visible region, emission in long wavelength red and near-infrared regions, long lifetimes of excited state, redox- and photo-stability [3]. The UV–visible spectrum of this system displays several interesting features such as ligand centered ($\pi \rightarrow \pi^*$) transitions at high energy (185–285 nm), two weak signals between 322–344 nm, and most intense peak near λ_{max} 450 nm which is attributed to the MLCT (metal to ligand charge transfer) transition [4, 5]. The Ru(II)-polypyridyl centre worked as excited state redox active agent in electron transfer

processes, and showed very good emission properties [4, 5]. Ru(II)-polypyridyl complexes are classical luminophores showing excitation at 450–470 nm and wide emission bands centred at 600–620 nm. In general, three bidentate (bipyridine/phenanthroline) or two tridentate (terpyridine) ligands have been employed to prepare Ru(II)-polypyridyl chemosensors which exhibit outstanding optical and electrochemical properties. The focus of this chapter is to illustrate the chemical versatility of such chelating systems and their utilization in the detection of different analytes. Over the past few decades, the investigation into the salient properties of ruthenium (II)-polypyridyl complexes has turned out to be a major research area which stems especially from their appealing photochemical and photophysical properties [6, 7]. The next few sections have collected selected examples where an appropriate category of receptors based on Ru(II)-polypyridyl fragment has been selected for showcasing a particular theme.

2. Ru(II)-polypyridyl linked terpyridine chelate based sensors

Terpyridine (terpy) and its derivatives are the most frequently employed N-heterocyclic chelating agents which exhibit an exceptional binding ability for various metal ions. The typical cation binding area of terpy unit contains three nearly coplanar N atoms and its complexes have widely been used as signaling units at molecular and supramolecular levels.

In 2013, Wang and group developed [8] a Ru(II)-polypyridyl based luminescent sensor **1** containing a terminal terpyridine (terpy) moiety for Fe^{2+} ions recognition (**Figure 1**). The fluorescence emission studies of probe **1** were investigated in acetonitrile: HEPES buffer solution (1/71, v/v) of pH 7.2. Luminescence based titration of Fe^{2+} (0.5 equiv) with sensor **1** in acetonitrile solution clearly displayed a visible color change (light yellow to red-purple) with concomitant changes in emission and absorption spectra of probe **1**. The emission of probe **1** was quenched at 608 nm upon successive addition of Fe^{2+} ions in aqueous CH_3CN solution. Probe **1** has exhibited excellent selectivity towards Fe^{2+} ions with a detection limit of 4.58 x 10^{-8} M and also served as a good colorimetric sensor for Fe^{2+} ion among other metal ions. A 2: 1 binding stoichiometry of Fe^{2+} with complex **1** has been found in accordance with the coordination of terminal terpy units with Fe^{2+} ion and formation of **1**-Fe^{2+} was confirmed by spectroscopic methods (**Figure 1**).

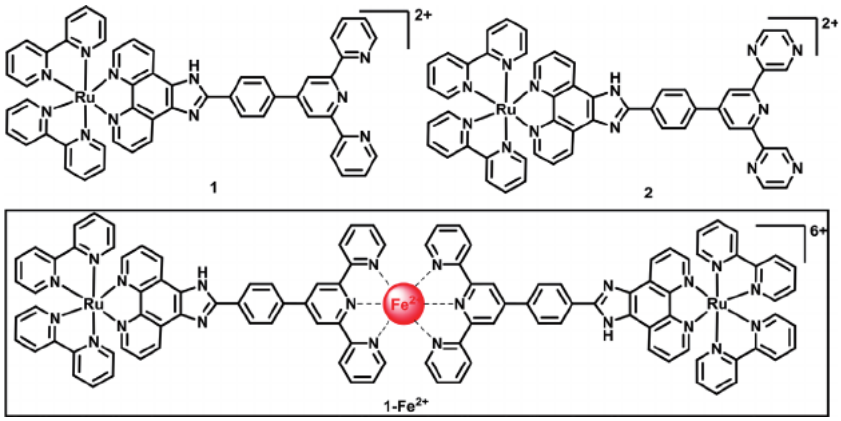

Figure 1.
Chemical drawing of probes **1–2** *and proposed binding of* **1**-Fe^{2+}.

The same group reported [9] another Ru(II)-polypyridyl based probe **2** bearing a dipyrazinylpyridine moiety in 2015 which exhibited a sensitive a selective detection for Cu^{2+} ion in presence of other metal ions (**Figure 1**). The UV–visible and emission spectral changes clearly revealed the coordination of Cu^{2+} ion with the neutral N donors of dipyrazinyl-pyridine moiety of sensor **2**. A significant quenching (upto 97%) in the luminescence intensity of probe **2** at 607 nm has been observed when 2.0 equiv. of Cu(II) ions were added to a CH_3CN/HEPES buffer solution of probe **2**. The detection limit and association constant have been calculated as 2.73×10^{-6} M and 1.88×10^{4} M^{-1} respectively, with a 1:1 binding stoichiometric ratio for complex **2**-Cu^{2+}. The luminescence of probe **2** was almost regenerated when a solution of complex **2**-Cu^{2+} was treated with excess EDTA. Probe **2** could be used for Cu^{2+} detection by probe in a wide range of pH upto 3.0–7.0 as the luminescence of **2** was independent of pH in this range.

3. Ru(II)-polypyridyl linked DPA chelate based sensors

Because of the strong coordinating affinity of N donor atoms of DPA (bis-(pyridin-2-ylmethyl)amine) unit with Zn^{2+} and Cu^{2+} ion, DPA tethered luminophores are gaining increasing interest in this research area. In year 2011, Zhang et al. constructed [10] a luminescent probe **3** having a free terminal dipicolylamine or DPA unit to detect Cu^{2+} ions (**Figure 2**). The emission signal of probe **3** at 612 nm was drastically quenched upon introducing 1.0 equiv. Cu^{2+} into an aqueous solution of probe **3** (10 mM HEPES buffer solution; pH 7.2). Job's plot data analyses displayed the formation of complex **3**-Cu^{2+} with 1:1 stoichiometric ratio (**Figure 2**). Furthermore, non-luminescent complex **3**-Cu^{2+} became emissive in the presence of sulfide ions. In the presence of S^{2-} ions, Cu(II) ion is effectively removed from **3**-Cu^{2+} to form a stable CuS species which ultimately led to a turn-on fluorescence response.

Xianghong et al. reported a Ru(II)-based probe **4** containing two DPA units as receptors for Cu^{2+} ions (**Figure 2**) [11]. The absorption and emission spectral changes observed after Cu^{2+} addition with **4** clearly indicated the coordination of Cu^{2+} with DPA moieties of complex **4**. The luminescence intensity of probe **4** at 630 nm was quenched upto a significant extent when Cu^{2+} was successively added in ethanol solution of probe **4**. Job's plot analyses revealed the formation of **4**-Cu^{2+} with 1: 2 ratio which has also been corroborated with mass spectral data. Probe **4** exhibited a selective detection of Cu(II) over other cations with a binding constant

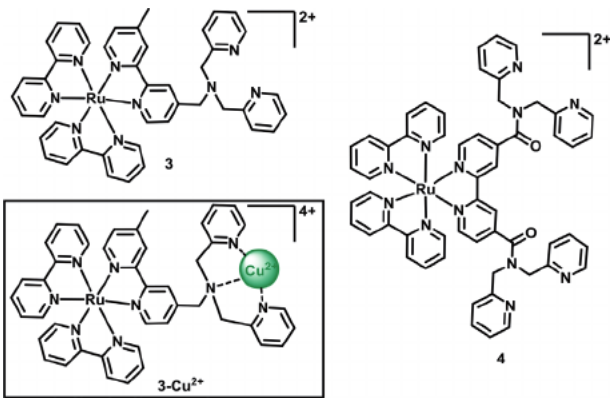

Figure 2.
Chemical drawing of probes **3–4** *with proposed binding of* **3**-Cu^{2+}.

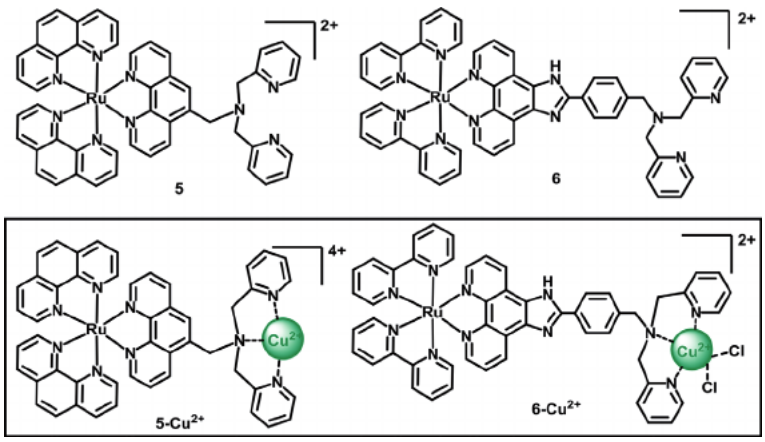

Figure 3.
Chemical drawing of probes 5–6 with their proposed binding to Cu^{2+} ions.

value of $5.89 \times 10^4\,M^{-1}$. The selective recognition of Cu(II) has been attributed to the high thermodynamic affinity of this metal ion towards N and O coordinating sites.

Liu et al. designed [12] a DPA tethered Ru(II) luminophore (**5**) which serves as an excellent luminescent probe for Cu^{2+} ion detection in pure water (**Figure 3**). The luminescence emission of probe **5** has been selectively quenched in the presence of Cu^{2+} among various other cations. An appreciable water solubility and usage in wide pH range make probe **5** a potential candidate for practical applications. The LOD value of **5** for Cu^{2+} has been calculated as 1.55×10^{-7} M. The DPA chelate of probe **5** coordinated to the copper centre through N_3 atoms and form a non-luminescent **5**-Cu^{2+} complex.

Recently, an imidazo-phenanthroline linked Ru(II) complex **6** with DPA as terminal binding site has been reported by Arora et al. (**Figure 3**) [13]. Probe **6** serves as selective and phosphorescent sensor for recognition of Cu^{2+} metal ion in aqueous medium. The addition of Cu^{2+} to probe **6** leads to coordination, as evidenced from the adequate quenching in emission signal of probe **6** at 615 nm. Probe **6** also acted as a colorimetric sensor towards Cu**2+** ions in aqueous solution as the red-orange color of **6** was turned to light yellow (visible to naked eyes) upon adding Cu^{2+} ions to it. The Job's plot data, LOD (1.89 M) and association constant ($1.14 \times 10^5\,M^{-1}$) values exhibited a 1: 1 complex formation of Cu^{2+} with probe **6**. Copper(II) selectivity of **6** is barely affected in the presence of other metal ions and biological targets such as amino acids and glucose. The emission of probe **6** was recovered when a sodium salt of EDTA was added to the non-luminescent complex **6**-Cu^{2+}.

4. Ru(II)-polypyridyl linked macrocyclic chelate based sensors

Macrocycles are particulary attractive classes of compound in different research areas because of their relative ease of functionalization and the availability of a central cavity with different conformations and sizes. Depending on the size of their macrocyclic crown, these compounds exhibit strong binding to various alkali and/or transition metal ions. A number of macrocyclic compounds have found applications and uses in sensing and other fields.

Paul et al. developed [14] a luminescent probe **7** containing a macrocyclic receptor for detection of Cu^{2+} ion in acetonitrile solution (**Figure 4**). Probe **7** displayed a typical UV–visible spectrum with absorption maxima at 453 nm (attributed to

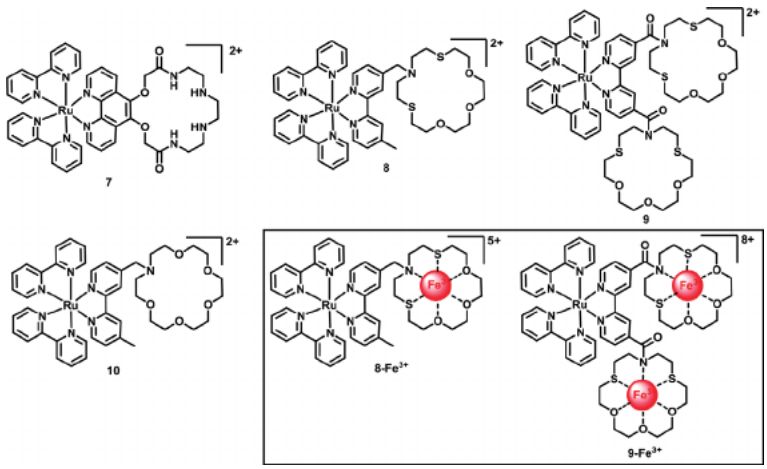

Figure 4.
Chemical drawing of probes 7–10 with their proposed binding to Fe^{3+} ion.

MLCT). Upon excitation at 460 nm, probe **7** exhibited an emission response at 603 nm. Successive addition of Cu^{2+} to CH_3CN solution of **7** resulted in a significant quenching of emission intensity. A strong affinity of coordinating sites (N and O donor atoms) available in receptor unit towards Cu^{2+} ion is favorable for appreciable binding.

Two novel Ru(II)-based fluorescent probes **8** and **9** having terminal NS_2O_3 macrocyclic rings as metal ion receptor were reported by Boricha et al. in 2012 (**Figure 4**) [15]. Probes **8** and **9** exhibited the characteristic absorption bands near 454 nm due to a MLCT transition and an emission signal in the range of 602–632 nm in acetonitrile solution. Addition of Cu^{2+} to probe **8** leads to the binding as evidenced by 87% luminescence quenching in emission intensity. On the other hand, addition of Fe^{3+} yielded a quenching in emission signal of probe **8** upto 96%. Probes **8** and **9** also displayed strong interactions with soft metal ions such as Pb^{2+} and Hg^{2+} ions. The presence of S atoms in the macrocyclic rings facilitated the affinity of these sensors towards soft acids. Probes **8** and **9** showed highest selectivity with Fe^{3+} ion and form hexa-coordinated complexes **8**-Fe^{3+} and **9**-Fe^{3+}.

For comparison, another structurally similar probe **10** containing a macrocyclic ring with NO_5 donors has also been developed (**Figure 4**) [15]. Interestingly, probe **10** served as a highly selective sensor for the detection of only Cu^{2+} ions over other metal ions, and a binding constant of 9.51 x 10^2 M^{-1} has been reported in this case. Replacement of soft donor S atoms with hard donor N atoms in the macrocycilc ring resulted with the selectivity enhancement of probes.

Due to their strong binding affinity towards metal ions and appreciable water solubility, cyclen (1, 4, 7, 10-tetraazacyclododecane) based derivatives have gained huge attraction in the research areas of chemistry and biology. The metal ion binding with cyclen unit induces a perturbation in electronic structure which results in the change of photophysical properties of luminophores.

A cyclen tethered luminescent probe **11** has been designed and synthesized by Li and group [16] for Cu^{2+} ion detection in pure water (**Figure 5**). Probe **11** exhibited classical UV–visible and emission spectra with absorption maxima at 450 nm and emission maxima at 604 nm. Upon addition of 1.0 equiv. of Cu^{2+} ions, the emission intensity was quenched to significant amount. Interaction between probe **11** and Cu^{2+} were believed to entail 1: 1 complex formation which is consistent with the availability of only one receptor per luminescent probe. Probe **11** was found suitable for Cu^{2+} detection in pH range of 5–11, and the binding constant value was

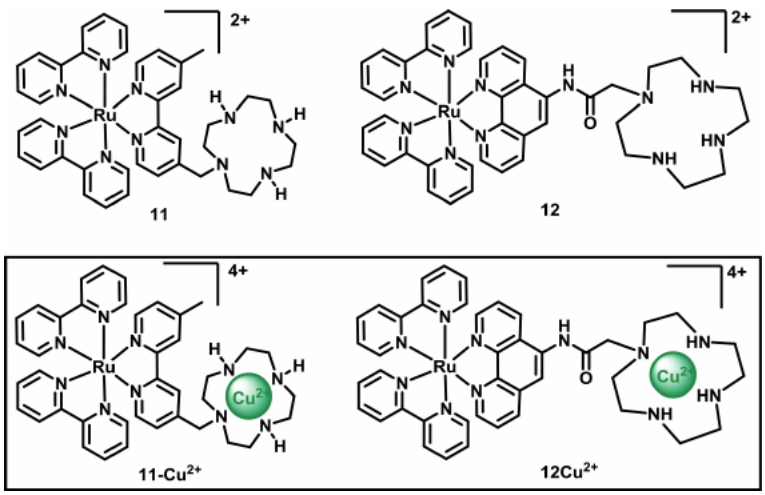

Figure 5.
Chemical drawing of probes 11–12 and their proposed binding to Cu^{2+} ion.

calculated as 2.36×10^4 M^{-1}. The strong Cu binding of **11** has been attributed to high thermodynamic stability and huge formation constant value of ensemble **11**-$Cu2^{+}$. Moreover, probe **11** displayed a off–on–off emissive response with an alternative addition of Cu^{2+} and S^{2-} ions in water.

Ye et al. developed another cyclen unit based fluorescent probe **12** to prepare a complex **12**-Cu^{2+} (**Figure 5**) [17]. Non-luminescent complex **12**-Cu^{2+} was used to selectively detect sulfide ions under physiological conditions. Upon excited with 450 nm light, probe **12** showed a luminescence response at 605 nm. The red-orange luminescence of probe **12** was significantly quenched with the addition of 10 μM Cu^{2+} ions in HEPES buffer solution. The interaction between **12** and Cu^{2+} are believed to involve 1:1 complex formation as evidenced by Job's plot and mass spectral analyses. The luminescence intensity of **12** has been almost completely recovered by treating H_2S with the non-emissive complex **12**-Cu^{2+}.

5. Ru(II)-polypyridyl linked imidazole chelate based sensors

Luminescent Ru(II)-polypyridyl complexes linked with 2-hydroxyphenylimidazo unit are gaining increasing interest in the monitoring and detection of copper ions owing to the strong binding affinity and straight coordination of 2-hydroxyphenylimidazo unit. Zhang et al. constructed [18] a luminescent probe **13** containing 2-hydroxyphenylimidazo moiety which acts as highly selective sensor for Cu^{2+} ion recognition in aqueous media (**Figure 6**). Upon exciting at 467 nm light under physiological conditions, probe **13** displayed an emission spectrum with emission maxima at 585 nm. Probe **13** provides two donor (N, O) sites to link with Cu^{2+} ion to form complex **13**-Cu^{2+} in 1:1 binding stoichiometry.

Later, Zheng's group introduced [19] another 2-hydroxyphenylimidazo based luminescent probe **14** for highly selective and effective detection of Cu^{2+} ions in CH_3CN-HEPES buffer solution of pH 7.2 (**Figure 6**). To confirm the Cu^{2+}binding with terminal 2-hydroxyphenylimidazo of **14**, the absorption and emission spectral changes have been observed. Introduction of Cu^{2+} leads to coordinate with receptor, as evidenced by the quenching in the emission intensity of probe **14**. A strong interaction of 2-hydroxyphenylimidazo moiety with Cu(II) (**14**-Cu^{2+}) is validated with a binding constant value of 1.09×10^5 M^{-1}.

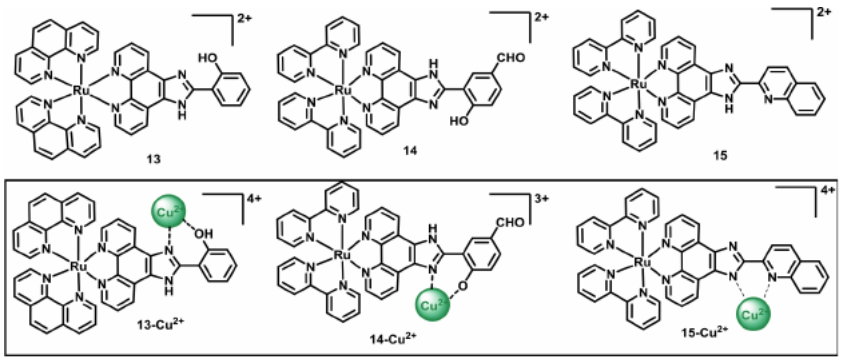

Figure 6.
Chemical drawing of probes 13–15 and their proposed binding to Cu^{2+} ion.

Recently, a novel quinoline-tethered Ru(II)-based luminescent probe **15** has been developed by Kumar et al. (**Figure 6**) [20]. Probe **15** displayed an absorption maxima at 470 nm and emission intensity at 604 nm. Addition of Cu^{2+} in the solution of probe **15** leads to the binding as evidenced by the measurement of UV–visible and emission spectral changes. A bathochromic shift in absorption wavelength at 470 nm and appearance of new band between 620 nm to 720 nm (Cu based *d-d* transition) indicated the coordination of Cu^{2+} with probe **15**. A large decrease in emission intensity at 604 nm has also been only in the presence of Cu(II), over other cations. The LoD and binding constant values are calculated as 5.07 x 10^{-8} M and 5.00 x 10^{5} M^{-1}. Interaction of probe **15** with Cu^{2+} is believed to entail 1:1 formation of complex **15**-Cu^{2+}.

In a very recent report, Song and group reported [21] a luminescent probe **16** containing a terminal pyrozole fragment connected with Ru(II) luminophore *via* imidazole linker (**Figure 7**). Probe **16** proved to be fast and highly selective fluorescent chemosensor for Cu^{2+} ions in aqueous buffer solution (pH 7.4). The emission intensity of probe **16** at 621 nm (λ_{ex} 460 nm) was adequately quenched upon introducing paramagnetic Cu^{2+} ion with a detection limit of 8.33 x 10^{-8} M. Depending on the pH of probe's solution, a protonation-deprotonation process of N atoms of imidazole fragment has also been experienced. Job's plot analyses demonstrated the formation of complex **16**-Cu^{2+} with a 1:1 binding ratio. The formation of **16**-Cu^{2+} was also confirmed by broadening in resonances and disappearance of NH signals in ^{1}H NMR spectrum of **16** on adding Cu^{2+} ions. The red luminescence of probe **16** was regenerated with addition of an excess of EDTA to complex **16**-Cu^{2+}.

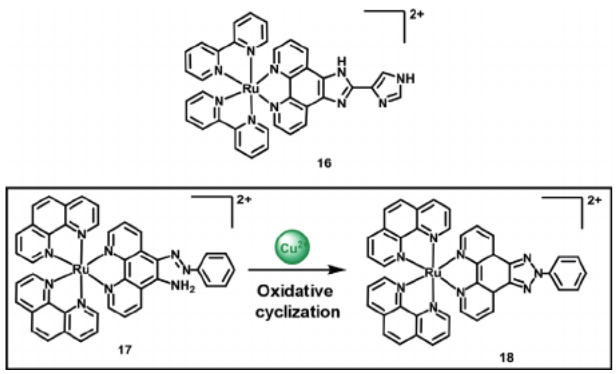

Figure 7.
Chemical drawing of probes **16–17** *and oxidative cyclization of* **17** *to* **18** *by Cu^{2+} ion.*

In 2015, Zhang et al. described [22] the synthesis of *o*-(phenylazo)aniline based non-luminescent probe **17** for sensing of Cu^{2+} ions with a emissive switch-on response (**Figure 7**). Addition of Cu^{2+} to probe **17** caused the oxidative cyclization of probe **17** to produce a highly luminescent complex **18** containing a benzotriazole fragment. Probe **17** was found completely soluble in water and exhibited an appreciable photostability in presence of light. The cyclization of *o*-(phenylazo) aniline moiety could easily be performed by introducing only 1 equiv. of Cu(II). Addition of 1 equiv. of Cu resulted with the large increase in luminescence intensity of **18**. The Cu sensing by probe **17** is unique as Cu^{2+} is only participating in cyclization reaction but does not coordinate with the receptor. Probe **17** was found highly selective for Cu^{2+} in the presence of various cations, with a detection limit of 4.42×10^{-9} M. Probe **17** has also been employed to detect Cu^{2+} in live-pea aphids with a switch-on emissive signal.

In 2013, Chao and co-workers reported [23] a dinuclear Ru(II)-based luminescent probe **19** for sensitive and selective detection of Cu^{2+} ions (**Figure 8**). Upon addition of Cu^{2+} ions (2.0 equiv.) into probe solution, the emission intensity at 600 nm was significantly quenched (96%). A naked eye color change could also be observed under UV light exposure. Binding of Cu with **19** is reported to involve 1:1 complex formation as evidenced by ESI-MS, NMR and EPR measurements, and the detection limit is computed to be 3.33×10^{-8} M. The luminescence of **19**-Cu^{2+} was recovered with an excess addition of EDTA to the mixture of Cu^{2+} and probe **19**. The selectivity studies clearly demonstrated no interference of other cations in sensing of probe **19** towards Cu^{2+} ions.

Cheng et al. developed [24] two dinuclear ruthenium complexes **20** and **21** for the luminescence based recognition of Cu^{2+} ions (**Figure 8**). Investigation of luminescence properties of these probes indicated higher emission response for probe **20** at 609 nm compared to probe **21**. Probe **20** detected Cu^{2+} selectively over other cations, and the luminescence of this probe was almost completely quenched in presence of Cu(II) ion. Nitrogen atoms from imidazole fragments and oxygen atom of furan participated in coordination to form complex **20**-Cu^{2+} with 1:1 ratio of binding. It is noteworthy that probe **21** displayed an increase in luminescence in various metal ion with no metal ion selectivity. The enhancement in emission intensity of probe **21** is attributed to the disturbance of photoinduced electron transfer process as the lone pair on S donor site becomes unavailable after metal ion coordination.

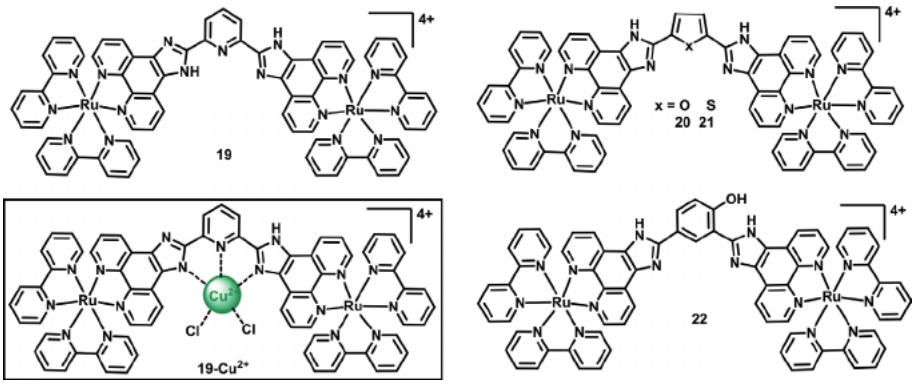

Figure 8.
Chemical drawing of probes **19–22** *and proposed binding of* **19** *to* Cu^{2+} *ion.*

Zheng et al. developed [19] a 2-hydroxyphenylimidazo based luminescent probe **22** for Cu(II) ion recognition in aqueous buffer solution (pH 7.2; HEPES) containing 1% acetonitrile (**Figure 8**). To validate the binding of Cu2+ with probe **22**, the absorption and emission spectral changes were investigated. Binding of Cu^{2+} with 2-hydroxyphenylimidazo fragment leads to a significant quenching in emission intensity of probe **22**. This probe showed a ON–OFF–ON emissive response with an alternative addition of Cu^{2+} and CN^- ions. The detection limit and the association constant for Cu ion sensing by **22** were calculated as 3.77×10^{-7} M and 4.31×10^4 M^{-1} respectively.

6. Ru(II)-polypyridyl linked triazole chelate based sensors

In recent years, 1,2,3-triazole based synthetic receptors have been considered to be an excellent motif for recognition of different analytes [25]. As N-atom containing Lewis bases, the triazole-based derivatives display strong metal ion binding properties and have been employed in different areas of research.

Triazole Ramachandran et al. constructed [26] a luminescent probe **23** containing a benzothiazole unit connected to $Ru^{II}(bpy)_3$ luminophore through a triazole linker (**Figure 9**). The probe was found highly selective towards Cu^{2+} ion detection and the red-orange emission of **23** at 630 nm was quenched upto 80% with addition of Cu^{2+} in HEPES buffer solution of pH 7.4. A 1:1 ratio of Cu binding with **23** has been confirmed with the help of Job's plot and ESI-mass spectral analyses. As evidenced by selectivity studies, other cations hardly affect the sensing ability of probe **23** towards Cu^{2+} ion. The binding constant and limit of detection values were in order of 5.11 x 10^4 M^{-1} and 7.00 x 10^{-7} M respectively.

The same group reported a dinuclear $Ru^{II}(bpy)_3$ based luminescent probe **24** which contain a *p*-tert-butylcalix[4]arene fragment as receptor for Cu^{2+} ions (**Figure 9**) [27]. As indicated by phosphorescence based titration experiments, probe **24** was found effective and selective Cu^{2+} ion sensor with a *turn-off* emission signal at 637 nm. Binding of Cu^{2+} was evidenced by the large decrease in luminescence intensity of probe **24**. The strong interaction of calixarene based receptor with Cu^{2+} is believed to involve 1:1 formation of **24**-Cu^{2+} with a binding constant value of order 2.31 x 10^4 M^{-1}. The red-orange luminescence of **24** was revived when S^{2-} ions were added to complex **24**-Cu^{2+}. Due to a very low cytotoxicity of probes **23** and **24**, cell imaging experiments have also been performed using these probes in human lung cancer A549 and MCF-7 cell lines.

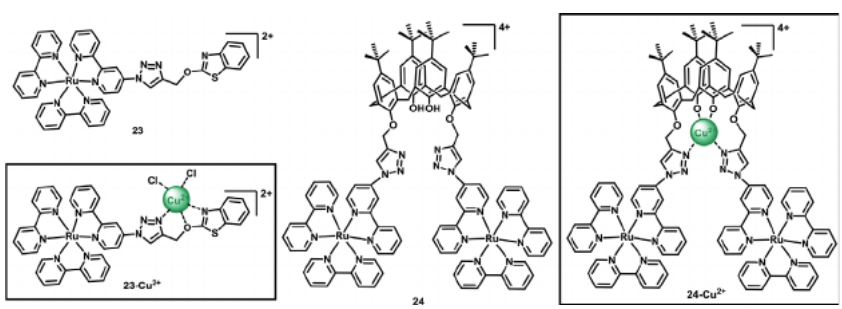

Figure 9.
Chemical drawing of probes **23–24** *and their proposed binding to* Cu^{2+} *ions.*

7. Ru(II)-polypyridyl linked carboxamide chelate based sensors

The coordination behavior of carboxamide group with different transition metal ions has extensively been investigated and well documented in the literature. The rapid growth in the development of carboxamide based organic and inorganic synthetic receptors is due to the realization of their important roles in chemistry, catalysis, medicine and the biology. In the present section, we have highlighted few luminescent sensors containing carboxamide group in the framework of metal ion receptors.

A series of luminescent Ru(II)-polypyridyl based sensors **25–27** have been designed for efficient sensing of Cu^{2+} ions. Sensors **25–27** show a MLCT absorption band at 450 nm and emission band at 620 nm after excitation this MLCT band. (**Figure 10**) [28]. Two equivalents of Cu^{2+} ion was enough to quench the emission of **25–27** completely. To selectivity of **25** towards Cu^{2+} ion in presence of other metal ions was studied in different pH and found the best selectivity and quenching at pH 5 only.

Another carboxamide linked Ru(II)-polypyridyl based sensor **28**, was developed [29] by Gopidas and co-workers showed unique chemical oxidation properties and Turn-ON emission with Cu^{2+} ion in CH_3CN (**Figure 10**). The emission intensity at 620 nm of **28** quenched by unique and fast electron transfer from the phenothiazine moiety to the Ru^{2+} core. Interestingly, the luminescence intensity of **28** enhanced by Cu^{2+} ion due to the oxidation of phenothiazine moiety Cu^{2+} ion. In presence of Cu^{2+} ion, phenothiazine is unable for emission quenching of Ru^{2+} centre.

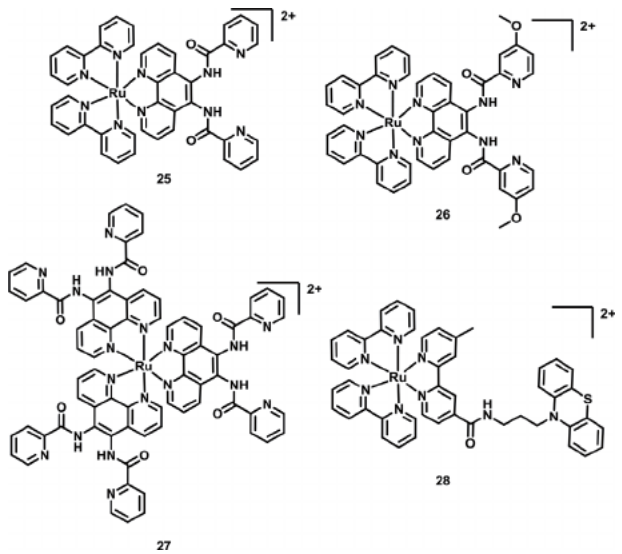

Figure 10.
Chemical drawing of probes **25–28**.

8. Ru(II)-polypyridyl linked imine chelate based sensors

Imine base ligands (Schiff bases) play important role in coordination chemistry due to their easy synthesis, high stability and insensitive properties towards air and moisture. Moreover, the electronic and steric features of these imine based ligands could easily be tuned by varying appropriate condensing partners.

These ligands bind through imine-N atom and display adequate structural flexibility and strong binding ability for various cations. Over the past decades, imine based derivatives are gaining increasing interest in the research area of electrochemical and optical sensing. In the present section, we have discussed luminescent Ru(II)-polypyridyl sensors containing an imine group in the metal ion binding site.

Kumar et al. described [30] a luminescent probe **29** containing a terminal thiophene unit linked with Ru(II)-polypyridyl based luminophore *via* imine bond (**Figure 11**). The water soluble probe having imine-N and thiphene-S coordinating sites detected Fe^{3+} ions through turn-off luminescence response at 615 nm, over other metal ions. However, a minor change in intensity has also been observed in the presence Cu^{2+} and Ag^{+} ions. A 1: 1 stoichiometry of complex **29**-Fe^{3+} was validated by Job's plot data and mass spectroscopic studies. The detection limit (LoD) and the binding constant for Fe^{3+} ion were computed as 0.11 ppm and $1.57 \times 10^3\ M^{-1}$ respectively. Moreover, the red-orange luminescence of probe 29 was restored with the addition of EDTA to a buffer solution of complex **29**-Fe^{3+}. For practical applications on real samples, probe **29** has been investigated for paper strips, polystyrene films and live cell imaging experiments.

Zhang et al. reported [31] the formation of luminescent probe **30** which displays a switch-off emission response in presence of Cu^{2+} ions in aqueous medium (**Figure 11**). Probe **30** detects Cu^{2+} selectively over various other metal ions, except a marginal quenching observed in case of Zn^{2+} ions. Binding of Cu^{2+} with **30** was evidenced by a red shift observed in absorption wavelength and a significant decrease in emission intensity. The luminescence of probe **30** was revived by treatment of non-luminescent complex **30**-Cu^{2+} with L-histidine. A limit of detection of order 3.50×10^{-10} M and an association constant value of $4.44 \times 10^3\ M^{-1}$ were measured. The effect of pH on sensing ability of probe 30 has been established in this report. The resultant data from pH studies revealed that the most significant quenching occurs in mild basic conditions. The deprotonation of phenolic-OH in basic medium increases its coordinating ability to form non-luminescent complex **30**-Cu^{2+}. Applications of probe **30** were investigated for imaging Cu^{2+} ions in live cells and real water samples.

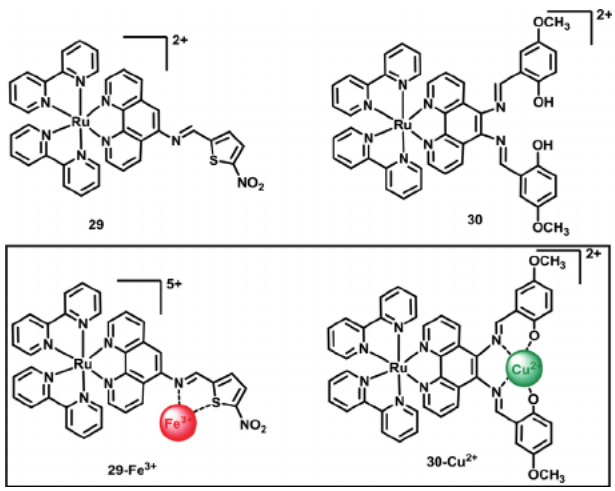

Figure 11.
Chemical drawing of probes **29**–**30** *and proposed binding of complexes* **29**-Fe^{3+}/**30**-Cu^{2+}.

9. Conclusions

The present chapter covers a majority of luminescent Ru(II)-polypyridyl based chemosensors for the selective recognition of biorelevant metal ions such as Cu^{2+} and Fe^{2+}/Fe^{3+} ions. The sensing behavior of different chemosensors varying from mono- to di-nuclear Ru(II)-polypyridyl complexes has been considered and discussed at a length. The applications encompass many fields including environmental, biological, analytical and medicinal domains. This field of luminescence sensing is quite prosperous and still emerging. Taking advantage of already known ligands topology exploiting their selective binding properties towards a particular metal ion, several chemosensors are developed. The design, detection, mechanisms and applications for different sensors presented in this chapter create huge opportunities for the development of future chemosensors.

Acknowledgements

PK thanks Mahamana Malviya College Khekra to provide infrastructure. SK acknowledges Department of Science and Technology (DST), New Delhi for finan-cial support in the form of Inspire Faculty Award [DST/INSPIRE/04/2015/002971].

References

[1] Carter KP, Young AM, Palmer AE Palmer. Fluorescent Sensors for Measuring Metal Ions in Living Systems. Chem. Rev. 2014;114:4564-4601. DOI: 10.1021/cr400546e

[2] Bertini I, Gray HB, Stiefel EI, Valentine JS. Biological Inorganic Chemistry. 1st ed. University Science Books: Sausalito CA; 2007. DOI: 10.1021/ed084p1432

[3] Meyer TJ. Photochemistry of metal coordination complexes: metal to ligand charge transfer excited states. Pure Appl Chem. 1986;58:1193-1206. DOI: 10.1351/pac198658091193

[4] Sauvage J-P, Collin JP, Chambron, JC, Guillerez S, Coudret C, Balzani V, Barigelletti F, De Cola F, Flamigni L. Ruthenium(II) and Osmium(II) Bis(terpyridine) Complexes in Covalently-Linked Multicomponent Systems: Synthesis, Electrochemical Behavior, Absorption Spectra, and Photochemical and Photophysical Properties. Chem Rev. 1994;94:993-1019. DOI: 10.1021/cr00028a006

[5] Balzani V, Juris A, Venturi M, Campagna S, Serroni S. Luminescent and Redox-Active Polynuclear Transition Metal Complexes. Chem Rev. 1996;96:759-834. DOI: 10.1021/cr941154y

[6] Daniel C. Photochemistry and photophysics of transition metal complexes: Quantum chemistry. Coord Chem Rev. 2015;282-283:19-32. DOI: 10.1016/j.ccr.2014.05.023

[7] Fantacci S, De Angelis F. A computational approach to the electronic and optical properties of Ru(II) and Ir(III) polypyridyl complexes: Applications to DSC, OLED and NLO. Coord Chem Rev. 2011;255:2704-2726. DOI: 10.1016/j.ccr.2011.03.008

[8] Zheng Z-B, Duan Z-M, Ma Y-Y, Wang K-Z., Highly Sensitive and Selective Difunctional Ruthenium(II) Complex-Based Chemosensor for Dihydrogen Phosphate Anion and Ferrous Cation. Inorg Chem. 2013;52:2306-2316. DOI:10.1021/ic301555r.

[9] Zheng, Z-B, Kang S-Y, Zhao Y, Zhang N, Yi X, Wang K-Z. pH and copper ion luminescence on/off sensing by a dipyrazinylpyridine-appended ruthenium complex. Sens Actuators B. 2015;221:614-624. DOI: 10.1016/j.snb.2015.06.124

[10] Zhang R, Yu X, Yin Y, Ye Z, Wang G, Yuan J. Development of a heterobimetallic Ru(II)–Cu(II) complex for highly selective and sensitive luminescence sensing of sulfide anions. Anal Chimica Acta. 2011;691:83-88. DOI:10.1016/j.aca.2011.02.051

[11] Xianghong L, Yuanbing C, Jiahe M, Kangle L, Aiqing Z, BingguangZ. A New Luminescent Ruthenium(II) Polypyridine-derived Dipicolylamine Complex as a Sensor for Cu^{2+} Ions. Chinese J. Chem. 2011;29:1947-1950.

[12] Liu X-W, Xiao Y, Zhang S-B. Lu J-L. A selective luminescent sensor for the detection of copper (II) ions based on a ruthenium complex containing DPA moiety. Inorg Chem Commun. 2017;84;56-58. DOI: 10.1016/j.inoche.2017.07.021

[13] Arora A, Kaushal J, Kumar A, Kumar P, Kumar S. Ruthenium(II)-Polypyridyl-Based Sensor Bearing a DPA Unit for Selective Detection of Cu(II) Ion in Aqueous Medium. Chem Select. 2019;4:6140-6147. DOI: 10.1002/slct.201900682

[14] Patra S, Boricha VP, Sreenidhi KR, Suresh E, Paul P. Luminescent metalloreceptors with pendant macrocyclic ionophore: Synthesis,

characterization, electrochemistry and ion-binding study. Inorg Chim Acta. 2010;363:1639-1648. 10.1016/j.ica.2010.01.003

[15] Boricha VP, Patra S, Parihar S, Chouhan YS, Paul P. Luminescent metalloreceptors with pendant macrocyclic ionophores with NS2O3 donor sites: Synthesis, characterization and ion-binding property. Polyhedron. 2012;43:104-113. DOI: 10.1016/j.poly.2012.06.024

[16] Li M, Liang Q, Zheng M, Fang C, Peng S. Zhao M. An efficient ruthenium tris(bipyridine)-based luminescent chemosensor for recognition of Cu(II) and sulfide anion in water. Dalton Trans. 2013;42:13509-13515. DOI: 10.1039/c3dt51047f

[17] Ye Y, An X, Song B, Zhang W, Dai Z, Yuan J. A novel dinuclear ruthenium(II)-copper(II) complex-based luminescence probe for hydrogen sulphide. Dalton Trans. 2014;43:13055-13061. DOI: 10.1039/c0xx00000x

[18] Zhang Y, Liu Z, Zhang Y, Xu Y, Li H, Wang C, Lu A, Sun S. A reversible and selective luminescent probe for Cu2+ detection based on a ruthenium(II) complex in aqueous solution. Sens Actuators B. 2015;211:449-455. DOI: 10.1016/j.snb.2015.01.116

[19] Zheng Z-B, Huang Q-Y, Han Y-F, Zuo J, Ma Y-N. Ruthenium(II) complex-based chemosensors for highly sensitive andselective sequential recognition of copper ion and cyanide. Sens Actuators B. 2017;253:203-212. DOI: 10.1016/j.snb.2017.06.145

[20] Kumar P, Kumar S. Copper ion luminescence on/off sensing by a quinoline-appended ruthenium(II)-polypyridyl complex in aqueous media. J Mol Struct. 2020; 1202:127242-127248. DOI: 10.1016/j.molstruc.2019.127242

[21] Li M, Sheth S, Xu Y, Song Q. Ru(II)-bipyridine complex as a highly sensitive luminescent probe for Cu2+ detection and cell imaging. Microchem J. 2020;156: 104848.-104855. DOI: 10.1016/j.microc.2020.104848

[22] Zhang R, Yu X, Yin Y, Ye Z, Wang G, Yuan J. Development of a heterobimetallic Ru(II)–Cu(II) complex for highly selective and sensitive luminescence sensing of sulfide anions. Anal Chim Acta. 2011;69:83-88. DOI: 10.1016/j.aca.2011.02.051

[23] P. Zhang, L. Pei, Y. Chen, W. Xu, Q. Lin, J. Wang, J. Wu, Y. Shen, L. Ji, and H. Chao, *Chem. Eur. J.,* 2013, **19**, 15494.

[24] Cheng F, He C, Ren M, Wang F, Yang Y. Two dinuclear Ru(II) polypyridyl complexes with different photophysical and cation recognition properties. Spectrochim Acta A Mol Biomol Spectrosc. 2015;136:845-851. DOI: 10.1016/j.saa.2014.09.103

[25] González M C, Otón F, Espinosa A, Tárraga A, Molina P. Tris(triazole) tripodal receptors as selective probes for citrate anion recognition and multichannel transition and heavy metal cation sensing. Org Biomol Chem 2015;13:1429-1438. DOI: 10.1039/c4ob02135e.

[26] Ramachandran M, Anandan S. Triazole appending ruthenium (II) polypyridine complex for selective sensing of phosphate anions through C-H---anion interaction and copper (II) ions via cancer cells. New J Chem. 2020;44:6186-6196. DOI: 10.1039/D0NJ00273A.

[27] Ramachandran M, Anandan S, Ashokkumar M. A luminescent on–off probe based calix[4]arene linked through triazole with ruthenium(II) polypyridine complexes to sense copper(II) and sulfide ions. New J Chem. 2019;43:9832-9842. DOI: 10.1039/c9nj01632e

[28] Comba P, Kramer R, Mokhir A, Naing K, Schatz E. Synthesis of New

Phenanthroline-Based Heteroditopic Ligands – Highly Efficient and Selective Fluorescence Sensors for Copper(II) Ions. Eur J Inorg Chem. 2006;4442-4448. DOI: 10.1002/ejic.200600469

[29] Ajayakumar G, Sreenath K, Gopidas KR. Phenothiazine attached $Ru(bpy)_3^{2+}$ derivative as highly selective "turn-ON" luminescence chemodosimeter for Cu^{2+}. Dalton Trans. 2009;1180-1186. DOI:10.1039/b813765j

[30] Kumar S, Arora A, Kaushal J, Oswal P, Kumar A, Kumar P. Developing a simple and water soluble thiophene-functionalized Ru(II)-polypyridyl complex for ferric ion detection. Inorg Chem Commun. 2019;107:107500-107506. DOI: 10.1016/j.inoche.2019.107500

[31] Zhang ST, Li P, Liao C, Luo T, Kou X, XiaoD. A highly sensitive luminescent probe based on Ru(II)-bipyridine complex for Cu2+, l-histidine detection and cellular imaging. Spectrochim Acta Part A Mol Biomol Spectrosc. 2018;201:161-169. DOI: 10.1016/j.saa.2018.05.001

Ruthenium-Tris-Bipyridine Derivatives as a Divine Complex for Electrochemiluminescence Based Biosensor Applications

Chikkili Venkateswara Raju, Mathavan Sornambigai and Shanmugam Senthil Kumar

Abstract

In electrochemiluminescence (ECL) studies, Tris (bipyridine)ruthenium(II) chloride ($Ru(bpy)_3^{2+}$) and its derivatives have been used as primary luminophores since 1972. The flexible solubility in both aqueous and non-aqueous medium and the remarkable intrinsic properties like chemical, optical and desirable electrochemical behavior drives the researcher to use $Ru(bpy)_3^{2+}$ and its derivatives as highly active ECL probes in modern analytical science. Novel surface modification of $Ru(bpy)_3^{2+}$ based ECL platforms are highly useful in the selective and sensitive detection of biomolecules, DNA analysis, immunoassays detection, and imaging of the biologically important molecules in cells and tissue of living organisms. This chapter discusses and highlights the most significant works in $Ru(bpy)_3^{2+}$ based ECL properties of reaction mechanisms and their applications.

Keywords: electrochemiluminescence, $Ru(bpy)_3^{2+}$, biosensor, annihilation mechanism, co-reactant mechanism

1. Introduction

The Electrochemiluminescence (ECL) is a process where the emission of light occurs by an excited luminophore molecule generated by reactive intermediates at the interface of the electrode and electrolyte [1]. It involves in three different kinds of processes. The first process is an electrical step, where the reactive intermediates of luminophores are generated at the electrode-electrolyte interface during the scanning of potential or applying a constant potential. In the second step, an energetic electron transfer occurs between the reactive intermediate which leads to the formation of an excited luminophore. Then the third step is a luminescence process, where the excited luminophore emits light during relaxation to the ground state. The first ECL reaction was observed by David M. Hercules in 1964, which deals with the ECL of Rubrene molecule in a non-aqueous medium [2].

1.1 ECL principle

In general, the ECL principle involves the conversion of electrical energy into radiative energy through a chemical reaction [1]. The energy required to produce an exciting luminophore molecule by the electrochemical method is referred to as a change of enthalpy which is denoted as ΔH [3]. The enthalpy change of a particular ECL reaction can be calculated by using the following equation.

$$-\Delta H\left(\text{in } eV\right) = \mathrm{E_0}^{oxi} - \mathrm{E_0}^{red} - 0.16\,eV \tag{1}$$

-ΔH refers enthalpy change, and E_0^{oxi} is oxidation potential, E_0^{red} is the reduction potential of the luminophore or co-reactant molecules. The numerical value of 0.16 eV is entropy factor (TΔS).

The energy required to generate first singlet excited state is determined by following equation.

$$\mathrm{E_s}\ \left(\text{in } eV\right) = 1239.8/\lambda\left(nm\right) \tag{2}$$

If, -ΔH≤Es, then the ECL system is referred as energy deficiency system; for energy sufficient system, -ΔH≥ Es.

1.2 Reaction mechanisms

Normally, ECL reactions follow only two kinds of reaction mechanisms named as annihilation mechanism and co-reactant mechanism. The reaction mechanism of any ECL system depends on the reaction conditions such as the selection of luminophore, potential sweep direction, and nature of electrolyte.

1.2.1 Annihilation mechanism

In the annihilation mechanism, only luminophore molecule alone will participate in the emission of light. The luminophore get oxidizes at anode during the positive potential sweep direction (anode direction) to generate cationic intermediate or cationic radical intermediate. At the same time, the anionic radical intermediate of luminophore molecule was generated at the cathode during the potential sweep towards cathode direction. Then an energetic electron transfer occurs between highly energetic anionic and cationic reactive radicals, leads to produce one excited and one ground state luminophore molecule. The excited luminophore molecule comes to the ground state by emitting energy in the form of photons. For example, the emission of light by $Ru(bpy)_3^{2+}$ molecule in acetonitrile with tetrabutylammonium tetrafluoroborate ($TBABF_4$) as an electrolyte is the best example of annihilation mechanism [4]. The reaction mechanism is given below.

$$Ru\left(bpy\right)_3^{2+} \rightarrow Ru\left(bpy\right)_3^{3+} + e^{-}\ \left(\text{oxidation } at \text{ anode}\right)\ \mathrm{E_0} = 1.2\ \mathrm{V}\ vs\ SCE \tag{3}$$

$$Ru\left(bpy\right)_3^{2+} + e^{-} \rightarrow Ru\left(bpy\right)_3^{1+}\ \left(\text{reduction } at \text{ cathode}\right)\quad \mathrm{E_0} = -1.4\ \mathrm{V}\ vs\ SCE \tag{4}$$

$$Ru\left(bpy\right)_3^{1+} + Ru\left(bpy\right)_3^{3+} \rightarrow Ru\left(bpy\right)_3^{2+} + Ru\left(bpy\right)_3^{2+*}\ \left(\text{excitation}\right) \tag{5}$$

DOI: http://dx.doi.org/10.5772/ITexLi.96819

$$Ru(bpy)_3^{2+*} \rightarrow Ru(bpy)_3^{2+} + h\nu\,(\text{emission}) \tag{6}$$

For the sake of better understanding the above mechanism is shown in **Figure 1**. The annihilation mechanism occurs only in organic electrolytes and it requires a wider potential window in order to obtain the ECL. Because of the gas evolution reactions (oxygen and hydrogen evolution), the annihilation mechanism is not taking place in an aqueous medium.

1.2.2 Co-reactant mechanism

The drawbacks of the annihilation mechanism are overcome by adding an additional reagent called as a co-reactant along with the luminophore, and the mechanism is called a co-reactant mechanism. In this type of mechanism two reagents were taken into the account, one is luminophore and the other is a co-reactant molecule. Further, the narrow potential window is sufficient to gain the ECL and it is applicable in both organic and aqueous electrolytic medium. Based on the potential sweep direction the co-reactant mechanism is further classified into two types which are discussed below.

1.2.2.1 Oxidative-reduction mechanism

The potential window is fixed to only the anodic region. The co-reactant get oxides first at the anode to form oxidizing radical intermediate which has the high

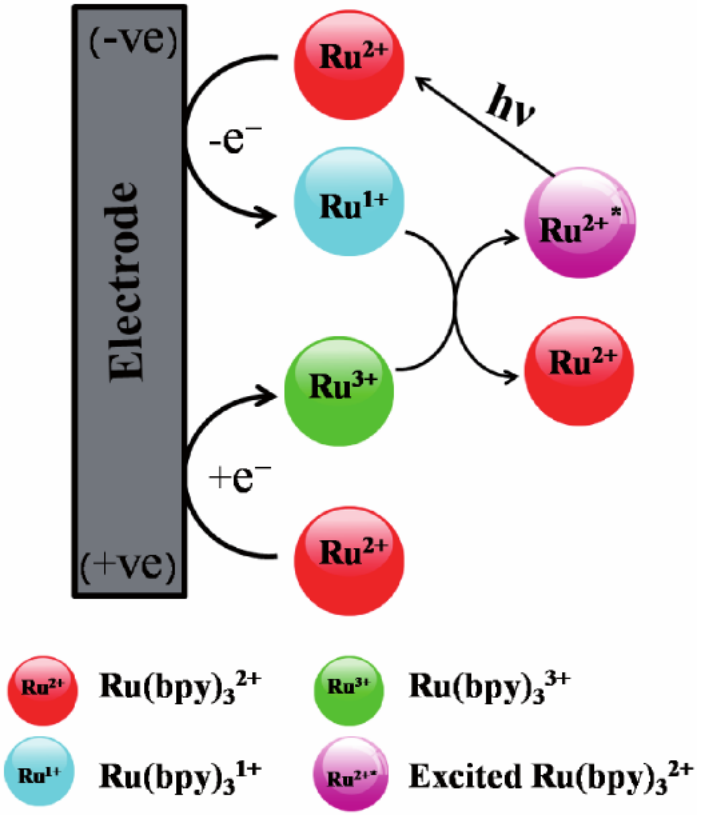

Figure 1.
The schematic representation of annihilation mechanism of $Ru(bpy)_3^{2+}$ molecule in acetonitrile.

reducing ability, then luminophore oxidizes to produce cationic reactive intermediate. After that, the co-reactant intermediate reduces the luminophore intermediate to generate an excited luminophore which emits light during energetic electron transfer reaction. The ECL of $Ru(bpy)_3^{2+}$ and tri-n-propyl amine (TPrA) system is the best example of an oxidative-reduction mechanism [5]. The reaction mechanism of $Ru(bpy)_3^{2+}$/TPrA system is given below.

$$Ru(bpy)_3^{2+} \rightarrow Ru(bpy)_3^{3+} + e^- \tag{7}$$

$$TPrA \rightarrow TPrA^{\bullet +} + e^- \tag{8}$$

$$TPrA^{\bullet +} \rightarrow TPrA^{\bullet} + H^+ \tag{9}$$

$$Ru(bpy)_3^{3+} + TPrA^{\bullet} \rightarrow Ru(bpy)_3^{2+*} + pr_2N^+CH=CH-CH_2 \tag{10}$$

$$Ru(bpy)_3^{2+*} \rightarrow Ru(bpy)_3^{2+} + \hbar \tag{11}$$

Here, $Ru(bpy)_3^{2+}$ is luminophore and TPrA acts as co-reactant. The schematic illustration for above reaction mechanism is also shown as **Figure 2**.

1.2.2.2 Reductive-oxidation mechanism

In this mechanism, the ECL is obtained by sweeping the potential exclusively to the cathode direction. The cathodic co-reactant gets reduced during cathodic potential scan where it produced high oxidizing ability of radical intermediate and then

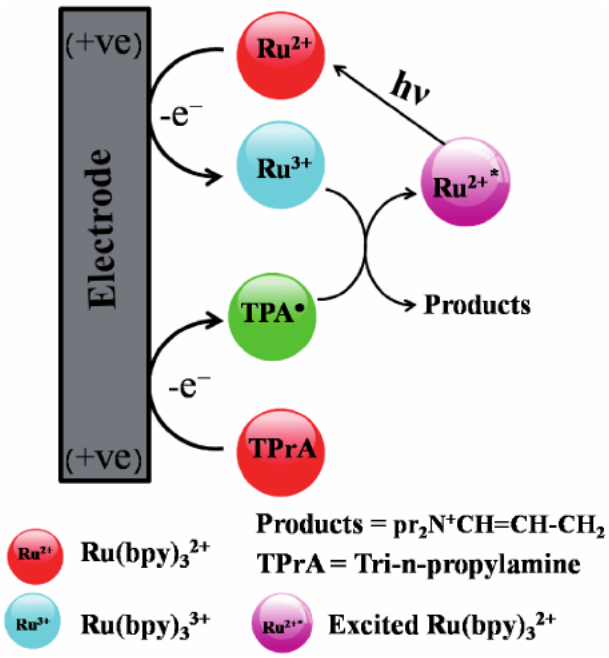

Figure 2.
The schematic illustration of oxidative-reduction mechanism of $Ru(bpy)_3^{2+}$ molecule and TPrA.

the followed by luminophores reduces to produce the anionic reactive intermediates. After that, the reduced radical intermediate of co-reactant oxidizes the anionic intermediate of the luminophore to form an excited luminophore which finally emits light. One of the classical examples for the reductive-oxidation mechanism is the ECL of $Ru(bpy)_3^{2+}$/per-sulphate ($S_2O_8^{2-}$) [6]. The reaction mechanism of this system is shown below.

$$S_2O_8^{2-} + e^- \rightarrow SO_4^{\bullet-} + SO_4^{2-} \tag{12}$$

$$Ru(bpy)_3^{2+} + e^- \rightarrow Ru(bpy)_3^{1+} \tag{13}$$

$$Ru(bpy)_3^{1+} + SO_4^{\bullet-} \rightarrow Ru(bpy)_3^{2+*} + SO_4^{2-} \tag{14}$$

$$Ru(bpy)_3^{2+*} \rightarrow Ru(bpy)_3^{2+} + h\nu \tag{15}$$

Here, $Ru(bpy)_3^{2+}$ is luminophore and $S_2O_8^{2-}$ acts as co-reactant. The above mechanism is also given as schematic diagram which is indicated as **Figure 3**.

1.3 Role of $Ru(bpy)_3^{2+}$ and its derivatives as a luminophores in ECL

The first ECL experiment with $Ru(bpy)_3^{2+}$ as a luminophore was performed by A.J. Bard *et al.* in 1972 [4]. This discovery brought brightness to the ECL and

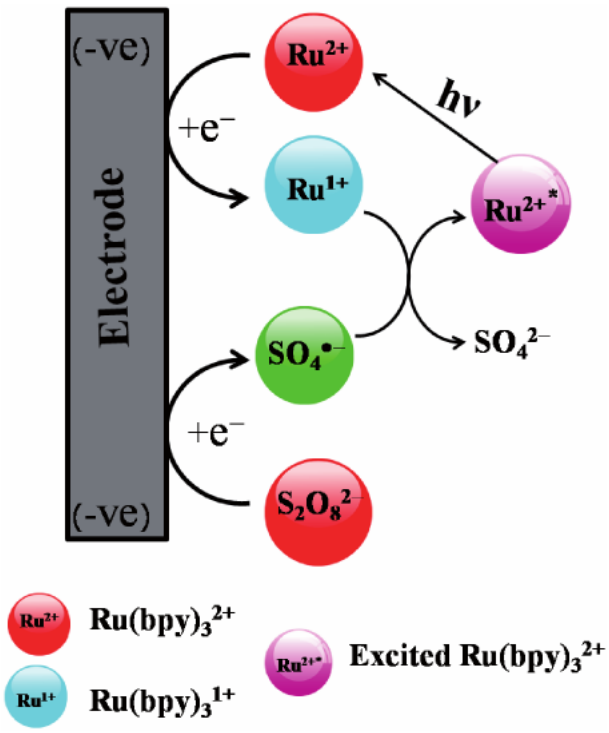

Figure 3.
The scheme of reductive-oxidation mechanism of $Ru(bpy)_3^{2+}$ molecule and persulfate.

created an endless platform for researchers to study the various kinds of ECL reactions. However, the ECL of $Ru(bpy)_3^{2+}$ was limited to organic electrolytes because the ECL follows annihilation mechanism which requires wide range potential window. To overcome this problem the ECL reaction within the narrow potential window was performed by taking additional reagent along with $Ru(bpy)_3^{2+}$ molecule. The first luminophore-co-reactant ECL reaction was carried out in 1981 by A.J. Bard group [7], oxalate was used as a first co-reactant to study the ECL reaction of $Ru(bpy)_3^{2+}$ molecule. Later on, various types of co-reactants were discovered like tri-n-propyl amine (TPrA), triethylamine (TEA), diethylamine (DEA), NADH, ascorbic acid, 2-(dibutyl amino) ethanol (DBAE), per-sulphates, hydrogen peroxide and glutathione etc [8]. $Ru(bpy)_3^{2+}$/co-reactant based ECL system plays a key role in a variety of analytical and clinical diagnostic applications. Recently *in-situ* generated co-reactants such as sulphate anion radicals and hydroxyl radicals also used as a new class of co-reactants to study the ECL of $Ru(bpy)_3^{2+}$ molecule in the aqueous system by using boron-doped diamond electrode (BDD) [9]. The superior ECL luminophore activity of $Ru(bpy)_3^{2+}$ molecule over the other luminophores is due to the high luminescent properties, elevated solubility in both organic and aqueous medium at room temperature, the reversible redox properties at the relevant potential region and high ECL quantum efficiency [10]. In general, $Ru(bpy)_3^{2+}$ has d^6 electronic configuration with octahedral structure, the emission of light is due to the metal to ligand charge transfer (MLCT) transition. The emission wavelength of $Ru(bpy)_3^{2+}$ lies between 600 to 650 nm.

In addition, the derivatives of $Ru(bpy)_3^{2+}$ were also shown their own contribution to ECL as luminophores. The linkage of aliphatic acids or aldehydes to the $Ru(bpy)_3^{2+}$ molecule gives different kind of luminophores called as acrylates. The ECL emission wavelength of $Ru(bpy)_3^{2+}$ was tuned by linking the different aliphatic compounds in acrylates (640 nm to 700 nm). And also, the $Ru(bpy)_3^{2+}$ conjugated with Schiff bases shown self-enhanced ECL signal with more intense light than $Ru(bpy)_3^{2+}$ molecule [11]. The enhanced ECL signal intensity is due to the resonance structure of imino radicals and presence of phenolic hydroxyl groups. Further, $Ru(bpy)_3^{2+}$ and its derivatives like $Ru(bpy)_3^{2+}$ dendrimers, and polypyridyl Ru-complexes used as a luminophore to study the bipolar ECL, microfluidic based ECL, wireless ECL [12, 13]. Apart from this, immobilization of $Ru(bpy)_3^{2+}$ molecule on polymer-coated electrodes shown new trend and remarkable ECL behaviour and created a solid-state platform for various kinds of analytical applications. In this context, $Ru(bpy)_3^{2+}$ incorporated on Nafion coated graphite electrode shows unusual ECL behaviour than solution-phase ECL system [14]. In similar way, $Ru(bpy)_3^{2+}$ on Nafion coated glassy carbon electrode (GCE) shown three ECL signals in co-reactant free oxygen saturated phosphate buffer solution (PBS).

Because of the excellent ECL behaviour exhibition by $Ru(bpy)_3^{2+}$ molecule, researchers tuned intrinsic properties of the $Ru(bpy)_3^{2+}$ molecule by introducing different functional groups into the parent $Ru(bpy)_3^{2+}$ and have been used in different analytical applications. In particular, $Ru(bpy)_3^{2+}$ utilized as an ECL probe in the detection of immunoassays [15], for example, the methylcytosine which belongs to a class of immunoassay detected by using ECL sensing method [13]. The DNA detection by ECL method has carried out by using $Ru(bpy)_3^{2+}$ molecule as ECL active material [16]. The double-standard DNA was detected by label-free ECL method using $Ru(phen)_3^{2+}$ as an ECL luminophore [17]. Apart from this, the ECL of $Ru(bpy)_3^{2+}$ also used in metal ions detection, bio-imaging, aptamer detection and other intracellular studies [13]. The schematic diagram is shown (**Figure 4**) the overall $Ru(bpy)_3^{2+}$ based ECL applications.

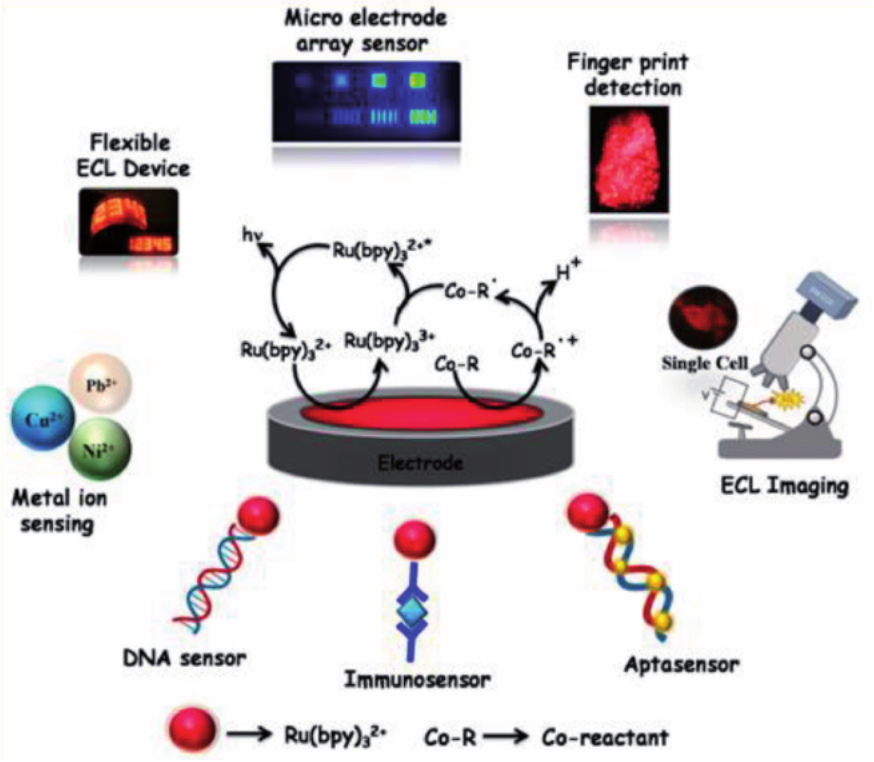

Figure 4.
Schematic illustration of ECL based applications using $Ru(bpy)_3^{2+}$ as a active probe.

2. Specific examples of $Ru(bpy)_3^{2+}$ and its derivatives for ECL studies

The ECL properties of various categories of Ru-based luminophores such as $Ru(bpy)_3^{2+}$, Nano materials doped with $Ru(bpy)_3^{2+}$ molecule, and $Ru(bpy)_3^{2+}$ immobilized on Nafion coated electrode are discussed below.

2.1 ECL of $Ru(bpy)_3^{2+}$ complex

The ECL of luminophore/co-reactant system follows only co-reactant mechanism either oxidative-reduction or reductive-oxidation mechanism. The initial discovery of $Ru(bpy)_3^{2+}$ as luminophore shown an avenue in ECL and created a way to study the various ECL reactions. The ECL of $Ru(bpy)_3^{2+}$ along with co-reactant is playing a vital role in broadening the ECL studies. Interestingly the ECL of $Ru(bpy)_3^{2+}$/TPrA system follows both co-reactant and annihilation mechanism. In the case of the co-reactant mechanism TPrA gets oxidized to form $TPA^{\bullet}$ and $Ru(bpy)_3^{2+}$ produces $Ru(bpy)_3^{3+}$ upon oxidation. The $TPA^{\bullet}$ reduces the $Ru(bpy)_3^{3+}$ to excited $Ru(bpy)_3^{2+}$ molecule which emits light (**Figure 5A**). But in the annihilation mechanism, $Ru(bpy)_3^{2+}$ electrochemically oxidizes to $Ru(bpy)_3^{3+}$ and the $TPA^{\bullet}$ directly reacts with $Ru(bpy)_3^{2+}$ to produces $Ru(bpy)_3^{1+}$, then electron transfers from $Ru(bpy)_3^{1+}$ to $Ru(bpy)_3^{3+}$ and generates excited $Ru(bpy)_3^{2+}$ molecule which emits light (**Figure 5B**).

In the reductive-oxidation mechanism, the ECL of $Ru(bpy)_3^{2+}$ occurs along with $S_2O_8^{2-}$, hydrogen peroxide (H_2O_2), and glutathione as co-reactants. The ECL of $Ru(bpy)_3^{2+}$ with glutathione is quite interesting because when the reduced

glutathione (GSH) used as a co-reactant the ECL is ROS dependent. Initially, GSH reacts with reactive oxygen species (ROS) which are produced during the oxygen reduction reaction to forms $GS^{\bullet}$, then $Ru(bpy)_3^{2+}$ reduces to $Ru(bpy)_3^{1+}$ by electrochemically and electron transfers from $Ru(bpy)_3^{1+}$ to $GS^{\bullet}$ leads to the generation of excited $Ru(bpy)_3^{2+}$ which emits light (**Figure 6A**). But in the case

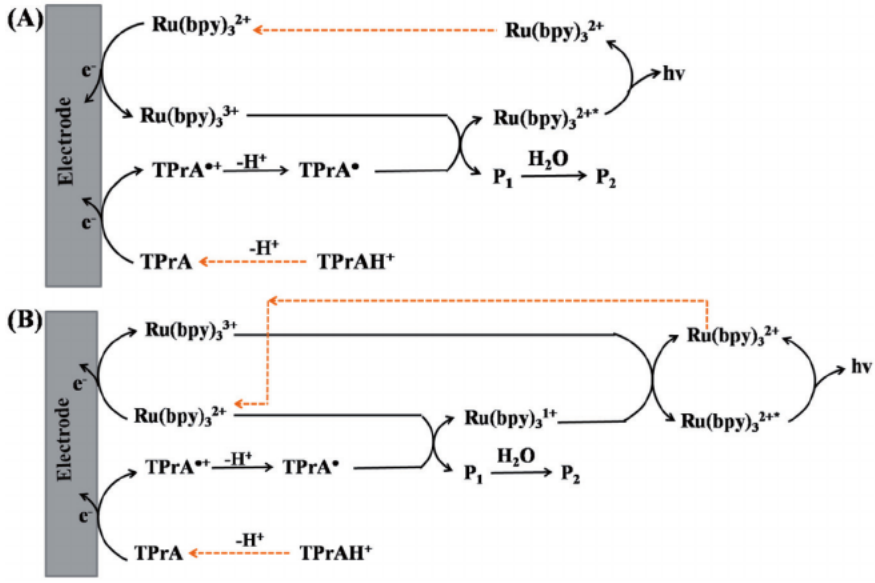

Figure 5.
ECL reaction mechanism of $Ru(bpy)_3^{2+}$/TPrA system (A, B). Copyright © 2002, American Chemical Society.

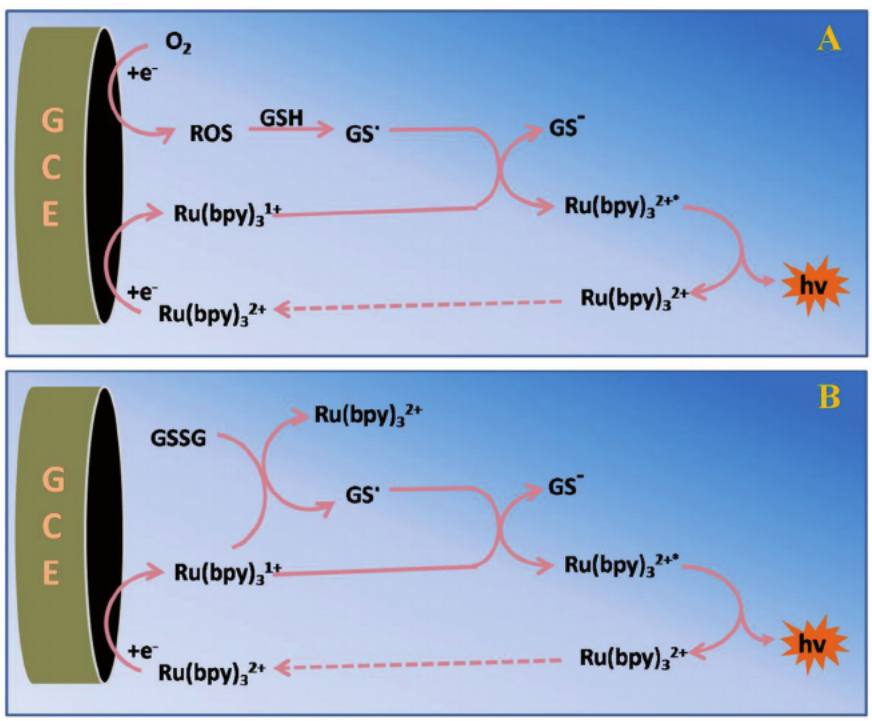

Figure 6.
ECL reaction mechanism of $Ru(bpy)_3^{2+}$/GSH (A) and $Ru(bpy)_3^{2+}$/GSSSG system (B).

of oxidized glutathione (GSSG), ECL is ROS independent, where the $GS^{\bullet}$ forms directly by reacting with $Ru(bpy)_3^{1+}$ after that excited $Ru(bpy)_3^{2+}$ obtained by reacting with $Ru(bpy)_3^{1+}$ and then light emission occurs (**Figure 6B**). However, the *in-situ* generated co-reactants were also utilized in order to study the ECL reaction by taking the $Ru(bpy)_3^{2+}$ as a luminophore [9]. Hence, $Ru(bpy)_3^{2+}$ is acting as a model and benchmark luminophore over the others. However, in order to improve further ECL light emission intensity, researchers were developed $Ru(bpy)_3^{2+}$ derivatives by doping with nano-materials, the results are discussed below.

2.2 ECL of $Ru(bpy)_3^{2+}$-doped with nanomaterials

Doping of nanomaterials with $Ru(bpy)_3^{2+}$ leads to the newer generation of ECL luminophores. The nanoparticles with the functional groups like thiols, amines, and silicates easily covalently bind with $Ru(bpy)_3^{2+}$ and its derivatives to gives highly luminescent luminophores. The $Ru(bpy)_3^{2+}$-doped nanomaterials have several advantages over conventional ECL luminophores. At first, a huge number of luminophore molecules could be encapsulated in a single target molecule site secondly the self-quenching properties of luminophores will be minimized and also the external quenchers like oxygen and water molecules are screened [18]. In this sequence, $Ru(bpy)_3^{2+}$ molecule were covalently linked with doped silica nanoparticles ($Ru(bpy)_3^{2+}$-DSNPs) showed bright ECL signal in 0.1 M acetonitrile with Tetrabutylammonium hexafluorophosphate ($MeCN/TBAPF_6$) potential scan from -1.6 V to +1.5 V [18]. This ECL signal is obtained by annihilation route in the absence of a co-reactant. Further, interesting ECL results were shown by making

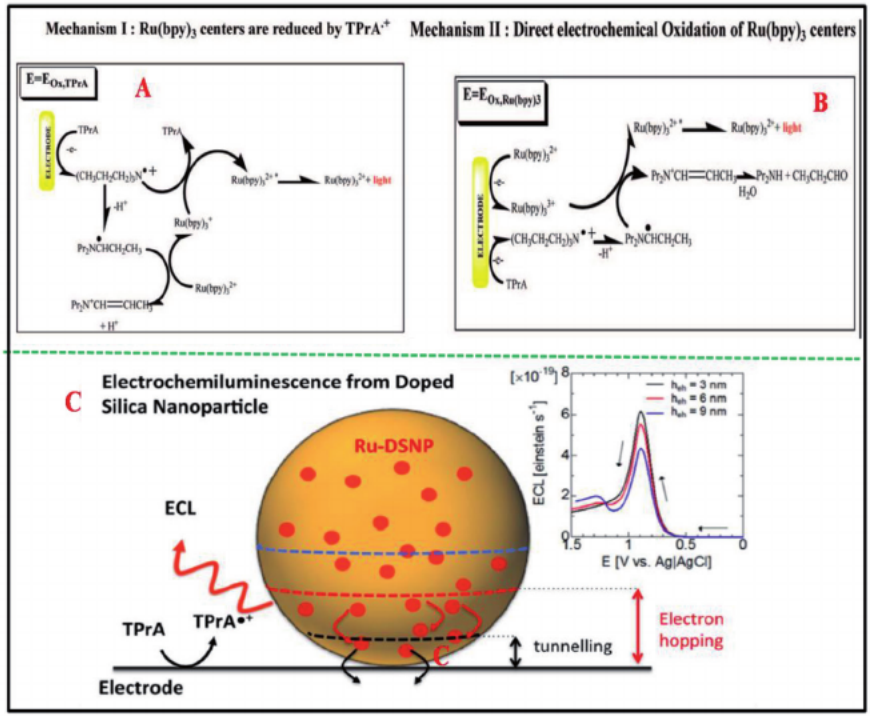

Figure 7.
(A, B) ECL reaction mechanism of DSNP/TPrA system. Copyright © 2009, American Chemical Society. The schematic representation of ECL generation in Ru-DSNP/TPrA system (C) Copyright © 2015, American Chemical Society.

a self-assembled monolayer (DSNPs-SH SAM) on a gold electrode surface in the presence of TPrA [18].

There are two ECL signals were obtained at 0.91 V and 1.23 V during the potential scan from 0 to 1.6 V in 0.1 M phosphate buffer solution (PBS). For the first cycle, the ECL at 0.91 V is much intense than the second peak (at 1.23 V) [18]. In general, the TPrA oxidation on a gold electrode is prevents in PBS because of Au-oxide formation, but DSNPs-SH SAM formation on gold surface creates hydrophobic nature and suppresses the Au-oxide formation. The hydrophobic formation allows the direct oxidation of TPrA and generates more number of $TPA^{\bullet}$ which directly reduces the $Ru(bpy)_3^{2+}$ (in DSNPs) to form $Ru(bpy)_3^{1+}$. Then $Ru(bpy)_3^{1+}$ oxidized by reacting with $TPrA^{\bullet+}$ to generates excited $Ru(bpy)_3^{2+}$ molecule which emits light at 0.91 V (**Figure 7A**). The second peak at 1.23 V is due to electrochemical oxidation of both TPrA and $Ru(bpy)_3^{2+}$ molecule (see **Figure 7B**). On the second cycle onwards the first ECL (at 0.91 V) was disappeared whereas the peak at 1.23 V remains as such because the DSNPs-SH SAM detaches from the electrode surface. This again leads to further Au-oxide growth on Au surface and suppresses the TPrA oxidation, obviously decreases ECL intensity at 0.91 V. Similarly, Ru-DSNP/TPrA exhibits ECL in PBS, the emission is due to the electron hopping between the electrode and $Ru(bpy)_3^{2+}$ as well as between two adjacent $Ru(bpy)_3^{2+}$ presents on DSNP as shown in **Figure 7C**. Another attempt has been carried out by covenant linkage of nitrogen-doped carbon nanodots (NCNDs) with the $Ru(bpy)_3^{2+}$ molecule. The NCNDs acting as co-reactant which is electrochemically oxidized at electrode to produce reactive radicals which have the capability to form excited $Ru(bpy)_3^{2+}$ molecule in generating the ECL [19]. This kind of doping of nanomaterials with the $Ru(bpy)_3^{2+}$offers in enhancing the ECL intensity of $Ru(bpy)_3^{2+}$ and leads to create a new platform for various analytical applications.

2.3 ECL of $Ru(bpy)_3^{2+}$ immobilized on Nafion coated electrodes

The immobilization of $Ru(bpy)_3^{2+}$ into the Nafion coated electrode surface either by chemical or electrochemical methods develops a highly stable and intense solid-state ECL platform. The solid-state ECL has several advantages over solution-phase ECL system. The minute amount of luminophore is sufficient to study the ECL reaction, the luminophore molecule could be regenerated on the electrode surface and also the solubility problem could be overcome. The Nafion is a cation exchange polymer with chemically inert and high thermal stability. It is used for immobilization of positively charged species like $Ru(bpy)_3^{2+}$ molecules. The first reports on immobilization of $Ru(bpy)_3^{2+}$ into the Nafion coated electrodes by Rubinstein and Bard have been extended to lot of studies on ECL reactions [20]. The ECL intensity of $Ru(bpy)_3^{2+}$ controlled by varying the Nafion concentration, thickness of the Nafion coating on the electrode surface and amount of loading of luminophore. For example, the bright ECL observed for $Ru(bpy)_3^{2+}$ immobilized on Nafion Langmuir-Schaefer coated GCE in the presence of TPrA, the highest intense ECL signal obtained for 20 layers coated electrode [21]. In a similar way, $Ru(bpy)_3^{2+}$ immobilized on Nafion coated GCE electrode exhibited three ECL signals in oxygen saturated PBS [22]. The highest ECL intensity was observed when the 6.58 μm thickness of Nafion is coated on the electrode surface. In addition, the modified GCE surfaces also utilized to immobilize the $Ru(bpy)_3^{2+}$ and studied the ECL reactions in order to explore a different kinds of applications [23].

However, the immobilization of $Ru(bpy)_3^{2+}$ on Nafion coated noble metal surfaces like gold electrode shown superior ECL behaviour over the carbon based-electrodes. For instance, $Ru(bpy)_3^{2+}$/Nafion/gold electrode shown unique and

unusual ECL properties [24]. The ECL obtained at very less cathode potentials without co-reactant in the potential region of 0 to 1.2 V in PBS. The ECL spectrum reveals that the observed ECL is because of the formation of excited $Ru(bpy)_3^{2+}$ by electrochemical reaction. Similar way, the ECL of $Ru(bpy)_3^{2+}$ which is presents on Nafion coated nanoporous gold electrode (NPG) is abnormal than the conventional system [25]. In this system $Ru(bpy)_3^{2+}$ molecules is immobilized electrochemically in the acidic electrolyte, as prepared $Ru(bpy)_3^{2+}$/Nafion/NPG composite used to study the ECL in PBS. There is a bright ECL signal obtained at less cathode potential (at 0.1 V *vs* Ag/AgCl) during the potential sweep from 0 to 1.6 V to -1 V. The *in-situ* generated hydroxyl anions (OH^-) from the NPG surface during the reduction playing a key role to gets the ECL at very less potentials. As shown in **Figure 8**, the NPG get oxidized during the potential scan from 0 to 1.6 V to form a gold-hydroxide layer (Au-OH_3). At the same time, the $Ru(bpy)_3^{2+}$ which is immobilized on the electrode surface ($Ru(bpy)_3^{2+}$/Nafion/NPG) also undergoes oxidation to forms $Ru(bpy)_3^{3+}$ intermediate. During the reduction, the Au-OH_3 converts into Au^0 and liberates OH^- ions. The presence of Nafion does not allow diffusion of OH^- ions from electrode surface to bulk electrolyte solution. It results in generation of $OH^\bullet$ by reacting with $Ru(bpy)_3^{3+}$. Then an energetic electron transfer arises from $OH^\bullet$ to $Ru(bpy)_3^{3+}$ leads to the generation of excited $Ru(bpy)_3^{2+}$ molecule which emits light as indicated in **Figure 8**. This type of solid-state ECL which is obtained at very less potentials has several advantages and also has scope in various analytical application points of view. The recent trend in ECL is involving in the development of solid-state ECL for point-of-care applications. The immobilization of luminophores on polymer-coated electrodes helps in creating a solid-state platform in improving the ECL signal intensity as well as could be useful in different analytical applications.

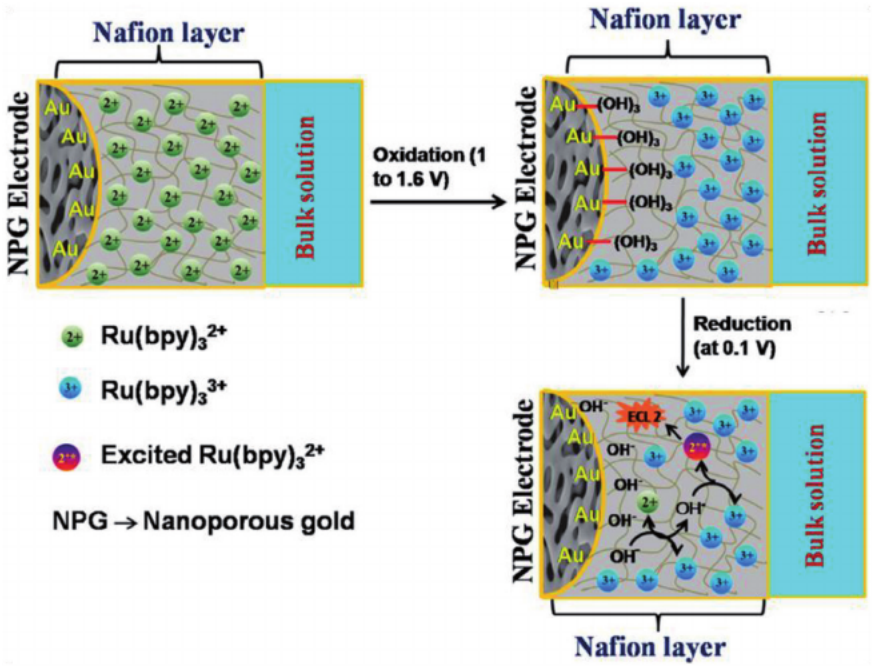

Figure 8.
The schematic representation of solid-sate ECL mechanism involving in $Ru(bpy)_3^{2+}$/Nafion/NPG composite in 0.1 M PBS (pH 7.4).

3. ECL applications

The ECL technique has several distinct advantages over many other detection systems, such as ECL provides excellent sensitivity with a detection limit at very low concentrations (subpicomolar) because of no background signal and an extremely wide dynamic range of orders of magnitude. Also, it allows the coupling of multiple labels to oligonucleotides or peptides without affecting immune reactivity. Finally, the simple instrumentation, the highly sensitive and rapid measurement, high-throughput analysis, made ECL a powerful detecting tool in the ultrasensitive detection of biomarkers. Therefore, it is of more interest among researchers to improve sensitivity and extend the applications of ECL immunoassays, DNA sensing, Bio-imaging, and point-of-care applications. Most of the ECL analysis studies utilize $Ru(bpy)_3^{2+}$ and its derivatives as ECL probe. The role of $Ru(bpy)_3^{2+}$ as an ECL label in different kind of sensing applications are discussed in a detailed way as follows.

3.1 Immunoassays sensing

One of the most important analytical applications of ECL is the use of commercial bioassay based on the $Ru(bpy)_3^{2+}$/TPrA systems. In which the derivatives of $Ru(bpy)_3^{2+}$ are used as ECL-active labels and TPrA as an efficient co-reactant. In the area of clinical diagnosis, multi-component detection is highly adapted than single-component detection. A sandwich-type ECL immunoassay array was used for the detection of multiple protein detection by incorporating the antibody coated single-walled carbon-nanotube (SWCNT) forest micro wells surrounded by the hydrophobic polymer [26]. These carboxylated SWNTs offers a more conductive surface area for the attachment of capture antibodies for Prostate-Specific Antigen (PSA) and interleukin-6 (IL-6) at the bottom of different micro-wells by amidization. The ECL signals were measured with the CCD camera, and the limit of detection for the PSA and IL-6 was observed to be 1 pg mL^{-1} and 0.25 pg mL^{-1}, which is better than the commercially available bead-based protein measurement systems. As shown in **Figure 9**, the ECL enzyme-linked immunosorbent assay was developed and used to determine the methyl-cytosine in DNA [27]. The anti-methyl cytosine antibody conjugated with acetylcholinosterase, in which the acetylcholinosterase converted acetylthiocholine (substrate) to thiocholine (product). This thiocholine

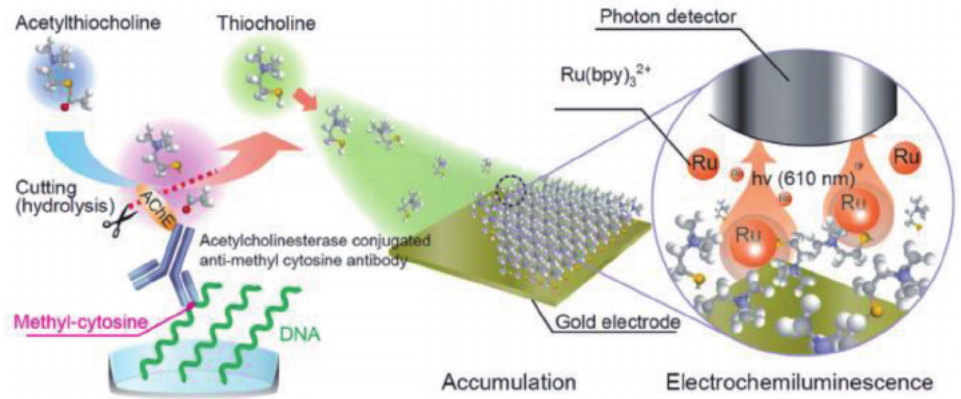

Figure 9.
Scheme for the principle of ECL determination of methyl-cytosine. Copyright © 2012, American Chemical Society.

is a bifunctional molecule that exhibits both the effect of ECL acceleration and surface accumulation *via* gold-thiol binding. Due to the accumulation and acceleration effect on ECL, the quantitative measurement of methyl-cytosine was found to have higher sensitivity with the linear range from 1 pmol to 100 pmol, which is sufficient to achieve the real DNA measurements. In order to increase the ECL emission intensity of the $Ru(bpy)_3^{2+}$-derivatives based ECL system, a novel and the self-enhanced ECL luminophore of the Ru(II) complex was developed by using the poly(ethylenimine) as a co-reactant, and also to form a coil-like nanocomposite with $[Ru(bpy)_2(5\text{-}NH_2\text{-}1,10\text{-}phen)^{2+}]$ [28]. By adopting the self-enhanced ECL luminophore in the sandwich-type ECL immunoassay, ultrasensitive detection of apurinic/apyrimidinic endonuclease-1 was demonstrated for the first time with the improved detection sensitivity from pg mL^{-1} to fg mL^{-1}.

The ultrasensitive detection of human C-reactive protein (CPR) was demonstrated by the addition of multiple $Ru(bpy)_3^{2+}$ to a single antibody with the encapsulation of a hydrophobic compound in the polystyrene microbeads [29]. With the sandwich-type immunoassay, a high sensitive CPR detection has been achieved with the detection limit as low as 0.01 μg mL^{-1}. The obtained LOD was found to be lower than the presently available high-sensitive CPR assay systems. Based on the previous work, a similar idea of holding multiple labels was developed by the preparation of sub-micrometer-sized liposomes containing $Ru(bpy)_3^{2+}$ as the ECL-active labels for CPR immunoassay. The addition of 0.1 M TPrA in the electrolytic solution (0.1 M PBS) containing 0.1 M NaCl and 1% Triton X-100, the release of the ECL label $Ru(bpy)_3^{2+}$ from the liposome can be realized. The above described approach allows the bioassay to be carried out in the aqueous solutions, which is compatible with the currently available commercial ECL instrumentation. Later, this work has been extended to the application in detecting hemagglutinin, which plays a significant role in the influenza virus infection.

3.2 DNA sensors

DNA detection is of great importance in the areas of clinical testing, forensics analyses, gene expression analysis, and biological warfare agent detections. ECL has been used as a powerful analytical tool in the DNA probe assays. Similar to the ECL immunoassays, DNA probe assays is also based on the $Ru(bpy)_3^{2+}$/TPrA ECL Systems. Generally, ECL DNA probe assays can be classified into two types: (1) Label-free, and (2) Label ECL detection [13, 30]. In the year of 1991, Blackburn *et al.* first reported the use of ECL of $Ru(bpy)_3^{2+}$ in developing the immunoassay and DNA probe assay for clinical diagnostics [31]. The general principle for the detection of DNA using the ECL label is outlined in **Figure 10A**. In this strategy, the ssDNA is immobilized on the electrode surface, and followed by attachment of the complementary target strand ssDNA tagged with the ECL label hybridizes with the immobilized ssDNA. Then the electrode assembly is placed in an electrolyte solution containing the co-reactant and allowed for the measurement of ECL [32]. Later, Xu *et al.* developed the ECL biosensor for the detection of DNA, based on the adsorption reaction on the film modified electrode surface. In this work, firstly tagged ssDNA was immobilized on the electrode surface coated with an organized aluminium phosphate film. By immersing the film in the DNA solution, the amount of immobilized DNA-$Ru(bpy)_3^{2+}$ was determined by the ECL emission resulting from the electrochemical oxidation of $Ru(bpy)_3^{2+}$ and TPrA in the solution [33]. An ultrasensitive ECL method has been developed for the detection of DNA hybridization by using polystyrene microspheres/beads, as the carriers of a huge numbers of hydrophobic ECL-active labels $Ru(bpy)_3[B(C_6F_5)_4]$ as shown in **Figure 10B**. The label-free ECL DNA detection was achieved based on the catalytic oxidation of

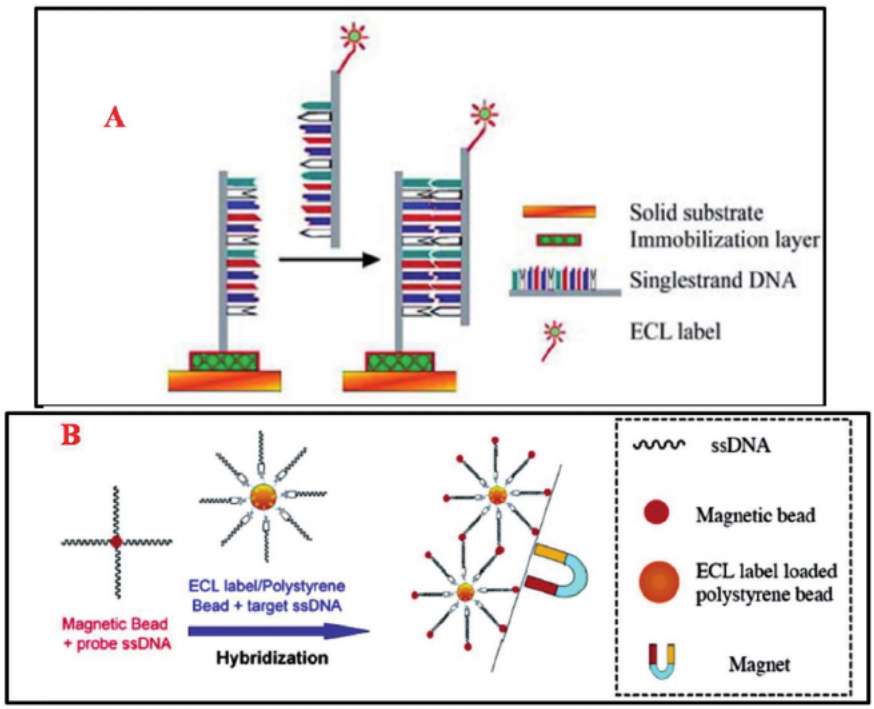

Figure 10.
Schematic diagram of solid-state ECL detection of DNA hybridization (A) Copyright © 2003, American Chemical Society. Schematic diagram of DNA hybridization on a polystyrene bead as the ECL label carrier and a magnetic bead for the separation of analyte-contained ECL label/polystyrene beads (B) Copyright © 2004, American Chemical Society.

guanine and adenine base using a glassy carbon electrode modified CNT/Nafion/ $Ru(bpy)_3^{2+}$ has been reported [34]. The ECL signals for the dsDNA and their denatured counterparts could be detected with a very lower concentration of 30.4 nM and a single-base mismatch gene p53 gene sequence segment was detected with the concentration of 0.4 nM.

3.3 Bio-imaging

An important breakthrough in the analytical application of the ECL technique is the combination of this transduction technique with microscopy. The combination of ECL along with a microscope leads to marvelous investigation in imaging of cell and tissue of living beings, nanomaterial imaging, and imaging of single-particle collisions [35]. The ECL imaging setup consists of (i) bright-field microscopy, (ii) a potentiostat, and (iii) the charge-coupled device (CCD) for recording the image [36]. The ECL emission signal is directly proportional to the concentration of the luminophore and the co-reactant; hence, the ECL technique enables the sensitive detection and quantification of both luminophore and the co-reactant. This widens the application of the ECL technique in detecting various biomolecules, such as proteins, enzymatic substrates, and nucleic acids.

In the most of Bio-imaging analysis, the $Ru(bpy)_3^{2+}$ molecule utilized as the ECL luminophore due to high quantum efficiency. For example, Valenti *et al.* used $Ru(bpy)_3^{2+}$ as ECL label in imaging the single Chinese Hamster Ovary (CHO) cell [37]. Initially, the cells are cultured on a glassy carbon electrode and incubated with biotin X which is capable of reacting with amino groups of the protein. Then the

$Ru(bpy)_3^{2+}$ molecule is labeled with streptavidin (SA@Ru). The biotin group reacts with SA@Ru and attaches the cell membrane throughout the ECL measurements as shown in **Figure 11a**. Further similar strategy used to imaging the MCF10A cell, in this case, CNT electrode used to incubate the cells and $Ru(bpy)_3^{2+}$ labeled with monolocal antibody (Ab@Ru) serves as ECL probe as shown in **Figure 11b**. The ECL imaging has performed in the PBS (pH 7.4) containing TPrA at anodic applied potential of 1.35 V. **Figure 11c** and **d** displays the PL image and ECL image of CHO cells on GC electrode. PL image shows a spatial distribution of SA@Ru labels with an entire cell appearance (**Figure 11c**). But in the case of the ECL image, the cell border glows with red color whereas cell nucleus is dark (**Figure 11d**). This is because ECL labels (SA@Ru) specifically located on the target cell. Thus the ECL is more specific to image single cell over the PL. Similar kind of results was observed in the case of MCF10A cell, the PL shows the emission of the light entire the cell (**Figure 11e**) whereas ECL image emits light only at a specified cell membrane (**Figure 11f**). Apart from this, the microelectrode arrays also used in single cell imaging by adopting ECL strategy [38].

3.4 Aptamer-based sensors

Aptamers are peptide or oligonucleotide molecules and also a functional DNA or RNA structures. Aptamers can specifically bind with small molecules as well as peptides and proteins. Aptamers exhibit remarkable advantages over conventional molecular recognition systems like antigen-antibody interactions because of their easier synthesis protocols, simple labeling, and high stability [30]. The combination ECL tool along with aptamer showed attractive results in biosensor applications and several aptamer-based ECL biosensors have been developing to detect small

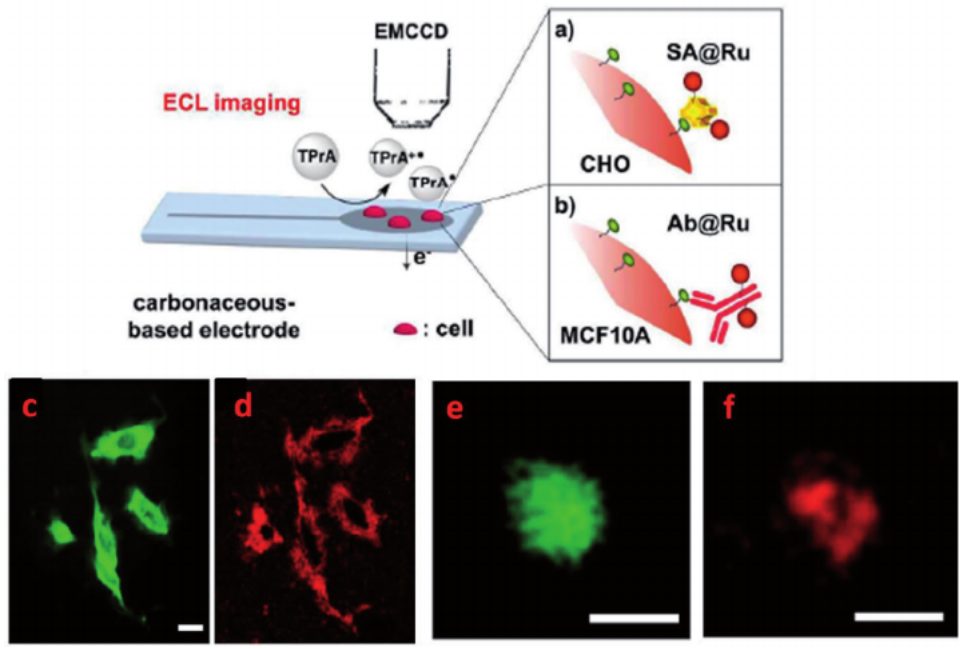

Figure 11.
The schematic illustration of principle involving in ECL imaging (a, b) PL and ECL images of SA@Ru attached CHO cells (c, d) and PL, ECL images of Ab@Ru attached MCF10A cells (e, f) Copyright © 2017, American Chemical Society.

molecules. In most of the aptamer-based ECL sensors, the $Ru(bpy)_3^{2+}$ molecule and its derivatives using as ECL label along with TPrA as co-reactant, due to unique and high quantum efficiency. For example, thrombin was detected by $Ru(bpy)_3^{2+}$ molecule as ECL probe, in this the captured aptamers with AuNPs labels were immobilized on thiolated ITO electrode via Au-S linkage and then catches the target aptamer [39]. After that, the $Ru(bpy)_3^{2+}$ molecule label was tagged with aptamer and studied the ECL experiments in TPrA containing PBS. This ECL strategy allows the detection of thrombin at a very low level with 10 nM of LOD. In addition to this, thrombin is detected by using tris(1, 10-phenanthroline) ruthenium ion ($Ru(phen)_3^{2+}$) intercalated into double standard DNA (dsDNA) as ECL sensing probe along with antithrombinthiolated aptamer [40].

The modification of gold electrode for ECL sensor is shown in **Figure 12**. Initially, the gold electrode soaked in a solution containing 2-mercaptoethanol in order to block the electrode exposing surface, then antithrombin aptamer adsorbed on the electrode surface as shown in **Figure 12A**. After that ds-DNA is placed between the aptamer and ss-DNA to intercalate the luminophore molecule (**Figure 12B**). To intercalate the $Ru(phen)_3^{2+}$ into the ds-DNA, the modified electrode is dipped in the ds-DNA solution. ECL experiments performed in PBS (pH 7.5) containing TPrA, a sharp ECL signal observed at 1.1 V which is due to the energetic electron transfer between reactive intermediates of $Ru(phen)_3^{2+}$ and TPrA. The ECL intensity decreases during the addition of 5 pM of thrombin into the electrolytic solution [40]. The decrease in the ECL signal is due to the detachment of $Ru(phen)_3^{2+}$ molecule from ds-DNA and occupation by thrombin as indicated in **Figure 12D**. This ECL methodology provides to sense the thrombin in the range of 0.05 to 50 pM with the detection limit of 0.02 pM.

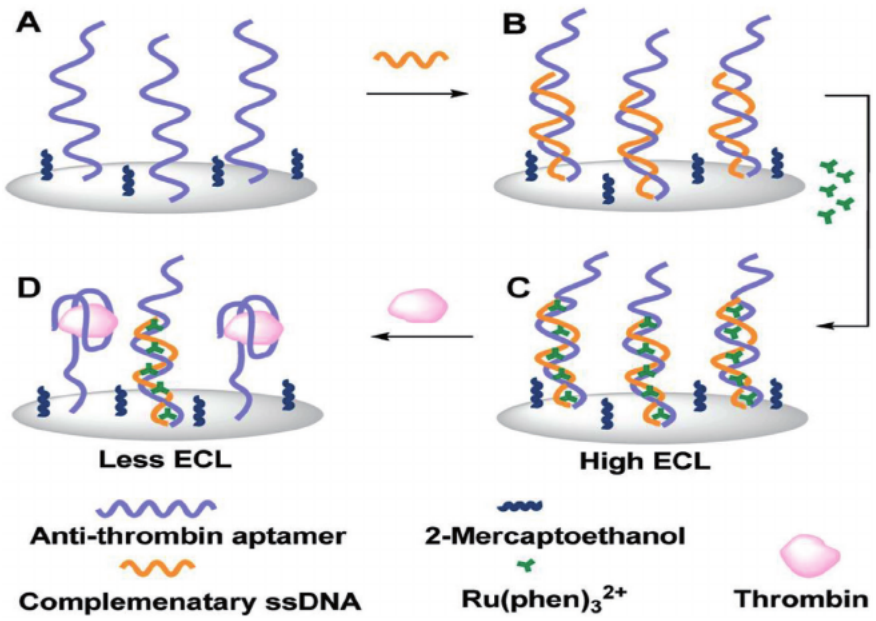

Figure 12.
Schematic representation of the principle involving in thrombin detection by aptamer-based ECL sensor. (A) The adsorption of thiolatedantithrombin aptamer on and the 2-mercaptoethanol block to the electrode. (B) The formation of the ds-DNA between aptamer and its complementary ss-DNA. (C) The intercalation of $Ru(phen)_3^{2+}$ into the ds-DNA sequence. (D) Dissociation of ds-DNA and release of $Ru(phen)_3^{2+}$ due to the interaction between thrombin and its aptamer, resulting in the decreased ECL emission which was used to quantify thrombin. Copyright © 2009, American Chemical Society.

3.5 Metal ion detection

Heavy metal ions such as Hg, Pb, Sn and, Cd are highly toxic and undegradable, causes serious health issues to humans [41]. The heavy metal ions migrate into the soil from industrial wastage, pesticides, fertilizers, spilling of petrochemicals. As migrated metal ions contaminants food and food security has become a worldwide worry. For the past few decades, the ECL has been using as one of the leading analytical technique in detecting such metal pollutants in food as well as soil. In this context, bipolar ECL (BP-ECL) has employed in detecting the Cu^{2+} and Cd^{2+} ions [42]. This method offers high sensitivity, low cost and provides both qualitative and quantitative information. The mixed luminophores of $Ru(bpy)_3^{2+}$ molecule along with $Ir(ppy_3)$ acting as ECL sensing probe. The multicoloured ECL emission is obtained at 540 nm (green) 610 nm (orange) at the driving potential of 5.5 V in the presence of both luminophores along with TPrA. The BP-ECL method offers the determination of Cd^{2+} ion in the range of 1 μM to 75 μM with the limit of detection of 0.094 μM (10 ppm) and also the Cu^{2+} ion detected within the dynamic range of 0.1 μM to 1/75 μM with 0.008 μM of LOD. In addition to this, $Ru(bpy)_3^{2+}$ linked with crown ethers used as an ECL probe to determine the Pb (II) ion [43], and also the solid-state ECL has been employed by using $Ru(bpy)_3^{2+}$ as an ECL probe to detect the Pb (II) ion in trace level [44]. The Pb(II) ion detected in the linear range of $1x10^{-6}$ μM to $1x10^{2}$ μM by ECL turn-off method. Another class of heavy metal Hg (II) ion detected by the employing cathodic ECL of $Ru(bpy)_3^{2+}$/NHS system [45]. This system includes the zero background signal, wide dynamic detection range and highly sensitive and selective to detect Hg (II) in physiological pH. The ECL intensity gradually increases upon each addition of Hg (II) ion into the solution in the linear range of 0.001 μM to 20 μM. This cathodic ECL method shows the limit of detection of 0.1 nM towards Hg (II) detection without interfering with other metal ions.

3.6 Point-of-care applications

Now a day's ECL becomes one of the dynamic, highly sensitive, and well established tools in point-of-care applications. ECL strategy has been used in the fabrication of point-of-care testing devices (POCT) like ECL detectors,

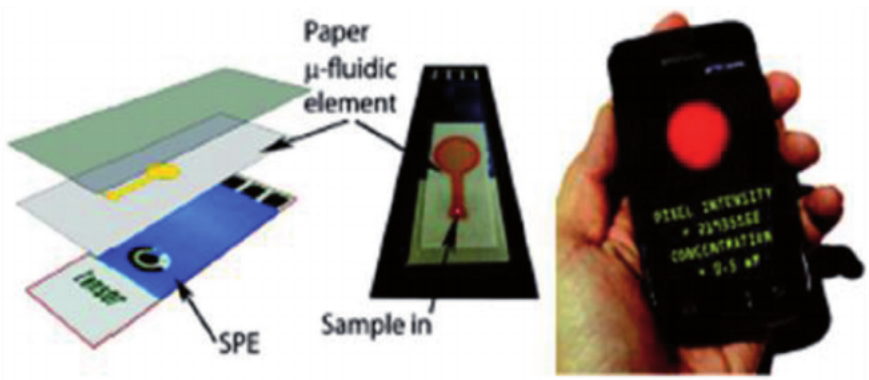

Figure 13.
Schematic diagram of a paper-based microfluidic ECL sensor. Using inkjet-printed paper fluidic substrates and screen-printed electrodes, this ECL sensor can be read with mobile phone cameras. Copyright © 2011, American Chemical Society.

bipolar ECL devices, wireless ECL, and microfluidic chips. These POCT devices are designed by using luminophores as sensing probes, the $Ru(bpy)_3^{2+}$ is a benchmark material among the various luminophores due to high quantum efficiency. The portable devices with lower prices could be useful for hospital/nonhospital purposes. The paper-based ECL sensors are one of the best cheapest ECL devices to detect biological molecules at trace level [46]. This type of ECL sensor has advantages that possess high sensitivity, selectivity, and rapid detection. The paper-based microfluidic devices made by patterning the papers into hydrophilic channels separated by hydrophobic barriers which allow the uniform distribution of samples into the regions. The photoresist materials like wax, polydimethylsiloxane, alkylketene dimer, polystyrene, poly(o-nitrobenzyl methacrylate), fluorochemicals, methylsilsesquioxane, and toner used as hydrophobic barriers [47]. Yan *et al.* developed a paper-based ECL 3D device. The device made with two different kinds of patterned cellulose papers called paper-A and paper-B. These two papers were converted into screen printed working paper electrode (SPWPE) by using carbon paste, the Ag/AgCl used as a reference electrode. As fabricated SPWPE used for point-of-care applications. The $Ru(bpy)_3^{2+}$ used as an ECL sensing probe along with TPrA as a co-reactant. The ECL signal intensity enhanced by 10-fold in the presence of CEA antibody [46]. Apart from this, microfluidic-based ECL sensor shown much attention in point-of-care applications due to flexibility, cheaper cost, portability, and porosity. **Figure 13** represents the schematic illustration of paper-based the microfluidic ECL sensor device. The inkjet printing is used to prepare microfluidic substrate, then it is combined with screen-printed electrodes which produce portable, disposable and photo-detectorless ECL sensor device. Initially, the printed paper based microfluidic filled with 13 μl of 10 mM $Ru(bpy)_3^{2+}$ solution and allowed to dry. After drying the paper microfluidic substrate is further laminated on Zensor screen-printed electrode (SPE) with 80 μm thickness. The small slit is made during the lamination to introduce the sample. The $Ru(bpy)_3^{2+}$ serves as ECL sensor probe and the mobile phone used to detect the ECL signal. The conventional photodetector used to detect the DBAE and NAD in the range of 0.9 μM and 72 μM respectively. In addition to this, the wireless ECL and bipolar ECL sensors also used as in fabricating the point-of- care testing devices for hospital/nonhospital purposes.

4. Conclusions and future perspective

The $Ru(bpy)_3^{2+}$ and its derivatives play a crucial role in the development of ECL based sensor devices. Due to its chemical stability, confined electrochemical behaviour, and high ECL quantum efficiency, $Ru(bpy)_3^{2+}$ complex acts as one of the best model luminophores. The variety of ECL experiments were studied by using different forms of $Ru(bpy)_3^{2+}$ like Ru-chelates, doped nanoparticles-$Ru(bpy)_3^{2+}$ and polymer-$Ru(bpy)_3^{2+}$ complex and used as an ECL label in detecting the immunoassays, DNA detection, aptamer sensing, bio-imaging, and metal ion sensing. The dynamic and progressive ECL of $Ru(bpy)_3^{2+}$ also offers to use it as a sensing probe in point-of-care testing devices such as portable ECL sensor devices, wireless ECL kits, paper-based microfluidic ECL devices, and bipolar ECL devices. Moreover, these kinds of ECL-based sensor kit will extent to the development of sensing of food adulterants to detect the toxic, hazardous and harmful compounds in food. In near future, the fabrication of $Ru(bpy)_3^{2+}$ based ECL sensor kits will be useful in various clinical diagnostic applications, pharmaceutical, and other point-of-care applications.

Acknowledgements

C.V. Raju thanks the CSIR for the award of Senior Research Fellowship (SRF), M. S. thanks to DST for providing inspire fellowship and S.S.K. thanks Department of Science and Technology (EMR/2017/004 4 49) for their financial support.

References

[1] M.M. Richter: Electro chemiluminescence (ECL).Chem.Rev. 2004;104:3003-3036. DOI:10.1021/cr020373d

[2] D.M. Hercules: Chemiluminescence Resulting from Electrochemically Generated Species. Science. 1964;145:808-809. DOI:10.1126/science.145.3634.808

[3] H. Tachikawa, A.J. Bard: Electrogenerated chemluminescence. Effect of solvent and magnetic field on ECL of rubrene systems. Chem. Phys. Lett. 1974;26:246-251. DOI:10.1016/0009-2614(74)85407-2

[4] N.E. Tokel, A.J. Bard: Electrogenerated chemiluminescence. IX. Electrochemistry and emission from systems containing tris(2,2'-bipyridine) ruthenium(II) dichloride. J. Am. Chem. Soc. 1972;94:2862-2863. DOI:10.1021/ja00763a056

[5] W. Miao, J.-P. Choi, A.J. Bard: Electrogenerated Chemiluminescence 69: The Tris(2,2'-bipyridine) ruthenium(II), ($Ru(bpy)_3^{2+}$)/ Tri- n -propylamine (TPrA) System. A New Route Involving $TPrA^{\bullet+}$ Cation Radicals.J. Am. Chem. Soc. 2002;124:14478-14485. DOI:10.1021/ja027532v

[6] H.S. White, A.J. Bard: Electrogenerated chemiluminescence. 41. Electrogenerated chemilum inescence and chemiluminescence of the $Ru(2,2^1\text{-bpy})_3^{2+}$-$S_2O_8^{2-}$ system in acetonitrile-water solutions.J. Am. Chem. Soc. 1982;104:6891-6895. DOI:10.1021/ja00389a001

[7] I. Rubinstein, A.J. Bard: Electrogenerated Chemiluminescence. 37. Aqueous Ecl Systems Based on Ru(2,2'-bipyridine)$_3^{2+}$ and Oxalate or Organic Acids Israel. J. Am. Chem. Soc. 1981;103:512-516.DOI.10.1021/ja00393a006

[8] Y. Yuan, S. Han, L. Hu, S. Parveen, G. Xu: Coreactants of tris(2,2′-bipyridyl) ruthenium(II) Electrogenerated Chemiluminescence.Electrochim. Acta. 2012;82:484-492. DOI:10.1016/j.electacta.2012.03.156

[9] Irkham, A. Fiorani, G. Valenti, N. Kamoshida, F. Paolucci, Y. Einaga: Electrogenerated Chemiluminescence by in Situ Production of Coreactant Hydrogen Peroxide in Carbonate Aqueous Solution at a Boron-Doped Diamond Electrode. J. Am. Chem. Soc. 2020;142:1518-1525. DOI:10.1021/jacs.9b11842

[10] P. McCord, A.J. Bard: Electrogeneratedchemiluminescence. Part 54.Electrogenerated chemiluminescence of ruthenium(II) 4,4'-diphenyl-2,2'-bipyridine and ruthenium(II) 4,7-diphenyl-1,10-phenanthroline systems in aqueous and acetonitrile solutions. J. Electroanal. Chem. 1991;318:91-99. DOI:10.1016/0022-0728(91)85296-2

[11] P. Li, Z. Jin, M. Zhao, Y. Xu, Y. Guo, D. Xiao: Self-enhanced electrogenerated chemiluminescence of ruthenium(II) complexes conjugated with Schiff bases. Dalton Trans. 2015;44:2208-2216. DOI:10.1039/C4DT03310H

[12] S.E.K. Kirschbaum, A.J. Baeumner: A review of electrochemiluminescence (ECL) in and for microfluidic analytical devices. Anal Bioanal Chem. 2015;407:3911-3926. DOI:10.1007/s00216-015-8557-x

[13] Z. Liu, W. Qi, G. Xu: Recent advances in electrochemiluminescence. Chem. Soc. Rev. 2015;44:3117-3142. DOI:10.1039/c5cs00086f

[14] H. Cui, X.-Y. Zhao, X.-Q. Lin: Cathodic electrochemiluminescence of $Ru(bpy)_3^{2+}$/Nafion coated on graphite oxide electrode in purely aqueous

solution. Luminescence. 2003;18:199-202. DOI:10.1002/bio.724

[15] X. Chen, Y. Liu, Q. Ma: Recent advances in quantum dot-based electrochemiluminescence sensors.J. Mater. Chem. C. 2018;6:942-959. DOI:10.1039/C7TC05474B

[16] H. Wei, E. Wang: Electro chemiluminescence of tris(2,2′-bipyridyl)ruthenium and its applications in bioanalysis: A review. Luminescence. 2011;26:77-85. DOI:10.1002/bio.1279

[17] Y. Chen, J. Xu, J. Su, Y. Xiang, R. Yuan, Y. Chai: In Situ Hybridization Chain Reaction Ampli fi cation for Universal and Highly Sensitive Electrochemiluminescent Detection of DNA. *Anal. Chem.* 2012;84:7750-7755. DOI:10.1021/ac3012285

[18] S. Zanarini, E. Rampazzo, L. Della Ciana, M. Marcaccio, E. Marzocchi, M. Montalti, F. Paolucci, L. Prodi: $Ru(bpy)_3^{2+}$ Covalently Doped Silica Nanoparticles as Multicenter Tunable Structures for Electrochemiluminescence Amplification. J. Am. Chem. Soc. 2009;131:2260-2267. DOI:10.1021/ja8077158

[19] S. Carrara, F. Arcudi, M. Prato, L. De Cola: Amine-Rich Nitrogen-Doped Carbon Nanodots as a Platform for Self-Enhancing Electrochemiluminescence. Angew. Chem. Int. Ed. 2017;56:4757-4761. DOI:10.1002/anie.201611879

[20] I. Rubinstein, A.J. Bard: Polymer films on electrodes. 5. Electrochemistry and chemiluminescence at Nafion-coated electrodes. J. Am. Chem. Soc. 1981; 103:5007-5013. DOI:10.1021/ja00407a006

[21] P. Bertoncello, L. Dennany, R.J. Forster, P.R. Unwin: Nafion−Tris(2-2'-bipyridyl)ruthenium(II) Ultrathin Langmuir−Schaefer Films: Redox Catalysis and Electrochemiluminescent Properties.*Anal. Chem*. 2007;79:7549-7553. DOI:10.1021/ac070811m

[22] L. Zheng, Y. Chi, Q. Shu, Y. Dong, L. Zhang, G. Chen: Electrochemiluminescent Reaction between $Ru(bpy)_3^{2+}$ and Oxygen in Nafion Film.J. Phys. Chem. C. 2009;113:20316-20321. DOI:10.1021/jp902239j

[23] Z. Guo, S. Dong: Electrogenerated chemiluminescence determination of dopamine and epinephrine in the presence of ascorbic acid at carbon nanotube/nafion-$Ru(bpy)_3^{2+}$ composite film modified glassy carbon electrode. Electroanalysis. 2005;17:607-612. DOI:10.1002/elan.200403129

[24] B. Qi, X.-B. Yin, Y. Du, X. Yang: Unique electrochemiluminescence behavior of $Ru(bpy)_3^{2+}$ in a gold/Nafion/$Ru(bpy)_3^{2+}$ composite.Mater. Lett. 2008;62:458-461. DOI:10.1016/j.matlet.2007.05.065

[25] C. Venkateswara, M. Sornambigai, S. Senthil: Unraveling the reaction mechanism of co-reactant free in-situ cathodic solid state ECL of $Ru(bpy)_3^{2+}$ molecule immobilized on Nafion coated nanoporous gold electrode.Electrochim. Acta. 2020;358:136920. DOI:10.1016/j.electacta.2020.136920

[26] N.P. Sardesai, J.C. Barron, J.F. Rusling: Carbon nanotube microwell array for sensitive electrochemiluminescent detection of cancer biomarker proteins.*Anal. Chem*. 2011;83:6698-6703. DOI:10.1021/ac201292q

[27] R. Kurita, K. Arai, K. Nakamoto, D. Kato, O. Niwa: Determination of DNA methylation using electrochemiluminescence with surface accumulable coreactant.*Anal. Chem*. 2012;84:1799-1803. DOI:10.1021/ac202692f

[28] M. Zhao, X.D.Y.Q. Chai, J. Han, G.F. Gui, R. Yuan, Y. Zhuo: A reagentless electrochemiluminescent immunosensor for apurinic/apyrimidinic endonuclease 1 detection based on the new $Ru(bpy)_3^{2+}$/bi-arginine system. Anal. Chim. Acta. 2014;846:36-43. DOI:10.1016/j.aca.2014.07.017

[29] W. Miao, A.J. Bard:Electrogenerated Chemiluminescence. C-Reactive Protein Determination at High Amplification with $[Ru(bpy)_3]^{2+}$-Containing Microspheres. Anal. Chem.2004;76:7109-7113. DOI:10.1021/ac048782s

[30] L. Hu, G. Xu: Applications and trends in electrochemiluminescence. Chem. Soc. Rev. 2010;39:3275-3304. DOI:10.1039/b923679c

[31] F. Zhang, H. Chen, P.G. He, Y.Z. Fang: Research on DNA electrochemiluminescence biosensing. Chinese Journal of Analytical Chemistry. 2013;41:1-9. DOI:10.1016/S1872-2040(13)60618-0

[32] R. Pyati, M.M. Richter: ECL—Electrochemical luminescence, Annu. Rep. Prog. Chem., Sect. C: Phys. Chem. 2007;103:12-78. DOI:10.1039/B605635K

[33] W. Miao, A.J. Bard: DNA Hybridization Detection at High Amplification with $[Ru(bpy)_3]^{2+}$-Containing Microspheres. Anal. Chem.2004;76:5379-5386. DOI:10.1021/ac0495236

[34] X.H. Xu, A.J. Bard: Immobilization and Hybridization of DNA on an Aluminum(III) Alkanebisphosphonate Thin Film with Electrogenerated Chemiluminescent Detection.J. Am. Chem. Soc. 1995;117:2627-2631. DOI:10.1021/ja00114a027

[35] A. Zanut, A. Fiorani, S. Rebeccani, S. Kesarkar, G. Valenti:Electrochemil uminescence as emerging microscopy techniques. Anal Bioanal Chem. 2019;411:4375-4382. DOI:10.1007/s00216-019-01761-x

[36] J. Zhang, S. Arbault, N. Sojic, D. Jiang: Electrochemiluminescence Imaging for Bioanalysis. Annu Rev Anal Chem.2019;12:275-295. DOI:10.1146/annurev-anchem-061318-115226

[37] G. Valenti, S. Scarabino, B. Goudeau, A. Lesch, M. Jovic, M. Sentic, S. Rapino, S. Arbault, F. Paolucci, N. Sojic: Single Cell Electrochemiluminescence Imaging:From the Proof-of-Concept to Disposable Device-Based Analysis.J. Am. Chem. Soc. 2017;139:16830-16837 (2017). DOI:10.1021/jacs.7b09260

[38] M. Sentic, F. Virgilio, A. Zanut, D. Manojlovic, S. Arbault, M. Tormen, N. Sojic, P. Ugo: Microscopic imaging and tuning of electrogenerated chemiluminescence with boron-doped diamond nanoelectrode arrays. Anal Bioanal Chem.2016;408:7085-7094. DOI:10.1007/s00216-016-9504-1

[39] L. Fang, Z. Lü, H. Wei, E. Wang: A electrochemiluminescence aptasensor for detection of thrombin incorporating the capture aptamer labeled with gold nanoparticles immobilized onto the thio-silanized ITO electrode. Anal. Chim. Acta. 2008;628:80-86. DOI:10.1016/j.aca.2008.08.041

[40] X. Yin, Y. Xin, Y. Zhao: Label-Free Electrochemiluminescent Aptasensor with Attomolar Mass Detection Limits Based on a $Ru(phen)_3^{2+}$-Double-Strand DNA Composite Film Electrode. Anal. Chem. 2009;81:9299-9305. DOI:10.1021/ac901609g

[41] R.A. Wuana, F.E. Okieimen: Heavy Metals in Contaminated Soils: A Review of Sources , Chemistry , Risks and Best Available Strategies for Remediation. International Scholarly Research Network. 2011; DOI:10.5402/2011/402647

[42] S. Carrara, C.F. Hogan: Multi-colour bipolar electrochemiluminescence for heavy metal ion detection. Chem. Commun. 2019;55:1024-1027. DOI:10.1039/c8cc08472f

[43] B.D. Muegge, M.M. Richter: Electrochemiluminescent Detection of Metal Cations Using a Ruthenium (II) Bipyridyl Complex Containing a Crown Ether Moiety. Anal. Chem. 2002;74:547-550.DOI:10.1021/ac010872z

[44] X. Shan, T. Pan, Y. Pan, W. Wang, X. Chen, X. Shan: Highly Sensitive and Selective Detection of Pb(II) by NH2-SiO2/Ru $(bpy)_3^{2+}$-UiO66 based Solid-state ECL.Electroanalysis. 2020;32:462-469. DOI:10.1002/elan.201900424

[45] Y.J. Muhammad Saqib, Shahida Bashir b, Shimeles Addisu Kitte, Haijuan Li: High-efficiency cathodic electrochemiluminescence of tris(2,2′- bipyridine)ruthenium(II)/N-hydroxy compounds system and its use for sensitive "turn-on" detection of mercury (II) and methyl blue. Chem. Commun. 2020;56:1827-1830. DOI:10.1039/C9CC09973E

[46] J. Yan, L. Ge, X. Song, M. Yan, S. Ge, J. Yu: Paper-Based Electrochemiluminescent 3D Immunodevice for Lab-on-Paper, Specific, and Sensitive Point-of-Care Testing. Chem. Eur. J.2012;18:4938-4945. DOI:10.1002/chem.201102855

[47] S.C. Somasekhar R. Chinnadayyala, Jinsoo Park, Hien Thi Ngoc Le, Mallesh Santhosh, Abhijit N. Kadam: Recent Advances in Microfluidic Paper-based Electrochemiluminescence Analytical Devices for Point-of-care Testing Applications. Biosens. Bioelectron. 2019;126:68-81. DOI:10.1016/j.bios.2018.10.038

Surface-Confined Ruthenium Complexes Bearing Benzimidazole Derivatives: Toward Functional Devices

Masa-aki Haga

Abstract

Substitutionally inert ruthenium complexes bearing benzimidazole derivatives have unique electrochemical and photochemical properties. In particular, proton coupled electron transfer (PCET) in ruthenium–benzimidazole complexes leads to rich redox chemistry, which allows e.g. the tuning of redox potentials or switching by deprotonation. Using the background knowledge from acquired from their solution-state chemistry, Ru complexes immobilized on electrode surfaces have been developed and these offer new research directions toward functional molecular devices. The integration of surface-immobilized redox-active Ru complexes with multilayer assemblies via the layer-by-layer (LbL) metal coordination method on ITO electrodes provides new types of functionality. To control the molecular orientation of the complexes on the ITO surface, free-standing tetrapodal phosphonic acid anchor groups were incorporated into tridentate 2,6-bis(benzimidazole-2-yl) pyridine or benzene ligands. The use of the LbL layer growth method also enables "coordination programming" to fabricate multilayered films, as a variety of Ru complexes with different redox potentials and pK_a values are available for incorporation into homo- and heterolayer films. Based on this strategy, many functional devices, such as scalable redox capacitors for energy storage, photo-responsive memory devices, proton rocking-chair-type redox capacitors, and protonic memristor devices have been successfully fabricated. Further applications of anchored Ru complexes in photoredox catalysis and dye-sensitized solar cells may be possible. Therefore, surface-confined Ru complexes exhibit great potential to contribute to the development of advanced functional molecular devices.

Keywords: Ru benzimidazole complex, surface immobilization, layer-by-layer assembly, molecular devices, redox chemistry, proton-coupled electron transfer (PCET), heterolayer, multilayer film, memory, phosphonic acid, redox capacitor, protonic memristor

1. Introduction

Ruthenium is a precious metal that belongs to the platinum-group elements [1]. As ruthenium can adopt various oxidation numbers, its coordination complexes adopt a wide variety of oxidation states from -II to VIII [2]. When nitrogen-based donor ligands are coordinated to a central ruthenium atom, the resulting ruthenium

complexes generally prefer the +II and + III oxidation states, but occasionally also adopt the +IV and + V states. Arguably the most studied Ru complexes with nitrogen-based donor ligands are those that contain the hexaammineruthenium dication, $[Ru(NH_3)_6]^{2+}$, and the tris(2,2′-bipyridine)ruthenium(II) dication, $[Ru(bpy)_3]^{2+}$ (bpy = 2,2′-bipyridine) [3–6]. $[Ru(bpy)_3]^{2+}$ was first reported by Burstall [7] and is easily obtained from the reaction of $RuCl_3 \cdot nH_2O$ with an excess amount of bpy in aqueous ethanol. $[Ru(bpy)_3]^{2+}$ exhibits a stable low-spin t_{2g}^6 electronic configuration as well as a reversible one-electron oxidation at +1.29 V (vs SCE) and successive one-electron reductions at −1.33 V, −1.52 V, −1.76 V, and − 2.4 V vs. SCE; the oxidation is a Ru(II/III) metal-center-based process, while the reductions occur on the bpy ligands. $[Ru(bpy)_3]^{2+}$ exhibits a metal-to-ligand charge transfer (MLCT) band at 452 nm and bright luminescence at 612 nm (lifetime: 600 ns) under MLCT excitation. This luminescence arises from the triplet MLCT photoexcited state, which allows this complex to serve as a photosensitizer for a wide scope of photoenergy conversion processes and as a photocatalyst for organic transformations [8]. Therefore, it is hardly surprising that during the past five decades, numerous studies on photoactive $[Ru(bpy)_3]^{2+}$ complexes have been reported [3]. The tuning of their physical properties, such as their absorption/emission maxima or redox potential, via ligand modification has been achieved by introducing substituents on bpy or by replacing the bpy ligand with other *N*-heteroaromatic ligands. This tuning has led to a wide range of functional materials based on $[Ru(bpy)_3]^{2+}$.

For example, replacing one of the bpy ligands in $[Ru(bpy)_3]^{2+}$ with an *N*-heteroaromatic ligand comprising a benzimidazole and a pyridine group shifts the Ru(II/III) oxidation potential in negative direction because benzimidazole is a stronger σ-donor and weaker π-acceptor than pyridine [9]. Furthermore, the coordinated benzimidazole N–H imino group acts as a Brønsted acid, and the corresponding deprotonated benzimidazolate site can coordinate to another metal ion (**Figure 1**) [10]. Protonated or *N*-alkyl benzimidazolium ions can act as precursors for *N*-heterocyclic carbene (NHC) metal complexes [11, 12]. The representative pyridine-containing ligands 2,2′-bipyridine (bpy) and 2,2′,2″-terpyridine (tpy) form chelate complexes with bidentate and tridentate coordination modes. When one or two pyridine groups are replaced with benzimidazole, the resulting bidentate- and tridentate-coordinating ligands are known as 2-(2-pyridyl)benzimidazole and 2,6-bis(benzimidazol-2-yl)pyridine, respectively (**Figure 2**) [13, 14].

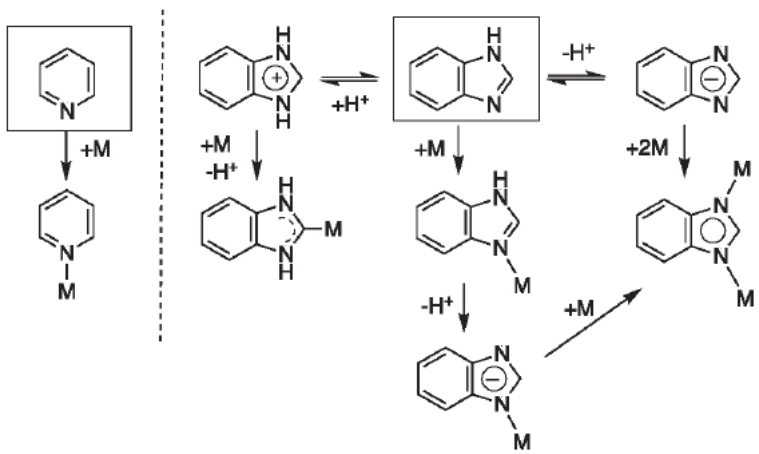

Figure 1.
Coordination modes of pyridine and benzimidazole as ligands.

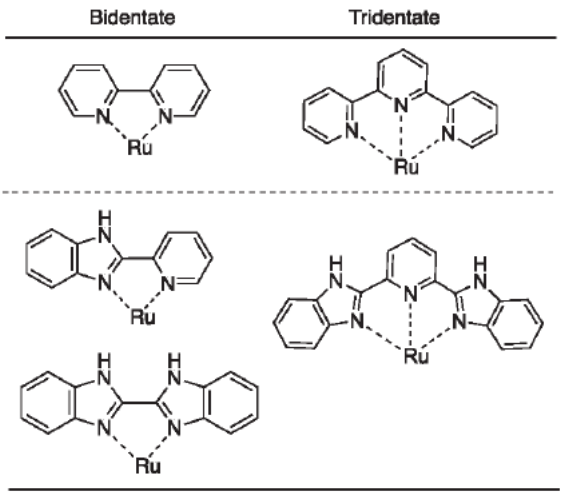

Figure 2.
Chemical structures of bidentate and tridentate ligands that contain pyridine and benzimidazole group(s).

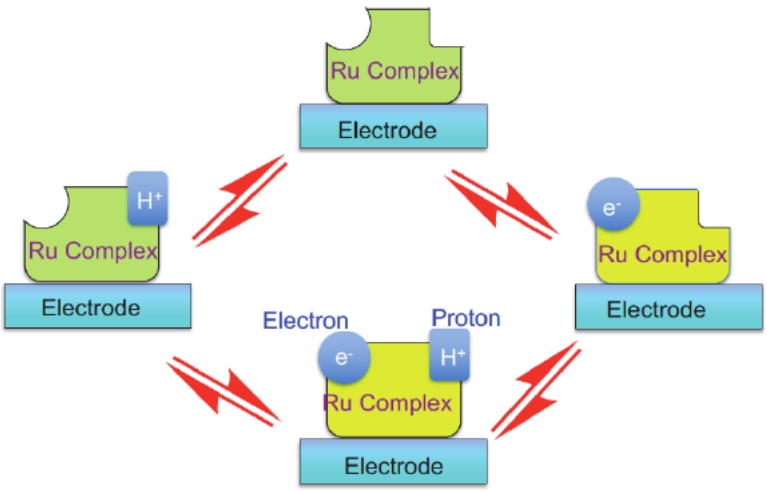

Figure 3.
Schematic illustration of molecular devices based on electron/proton-responsive Ru complexes confined to a surface.

This chapter focuses on the molecular design of ruthenium complexes with *N*-heteroaromatic ligands, particularly benzimidazole derivatives. In Ru–benzimidazole complexes in aqueous solution, the solution pH strongly affects the Ru(II/III) oxidation potential, which is derived from the proton-coupled electron transfer (PCET) reaction in solution [15]. The proton-responsiveness of Ru–benzimidazole complexes has been exploited to obtain switching functionality in multinuclear Ru complexes [16, 17]. In addition, ligand modification via *N*-alkylation of the benzimidazole N–H imino group has been used to achieve the anchoring of redox-active Ru complexes [18, 19]. and the layer-by-layer (LbL) assembly of Ru complexes on indium-tin oxide (ITO) surfaces toward molecular electronic devices [20–22]. **Figure 3** presents a schematic illustration of our conceptual approach for molecular devices based on surface-confined Ru complexes with electron/proton-responsiveness.

2. Molecular design of functional Ru complexes with benzimidazole ligands

2.1 Bridging ligands that contain benzimidazole groups

Benzimidazole ligands can be synthesized by the Phillips condensation reaction between an organic carboxylic acid or nitrile and *o*-phenylenediamine [23]. **Figure 4** shows the structures of benzimidazole ligands bridging two Ru centers that have been used by our group [17, 24–26] and others [27, 28] for the preparation of dinuclear Ru complexes. Depending on the chemical structure of the linker moiety, significant electronic coupling between the two ruthenium ions is posible. In addition, the oxidation processes of the Ru centers in aqueous solution involve PCET reactions, resulting in switching of the metal–metal interaction via the change in electron density on the conjugated linker ligand.

2.2 Introducing anchor groups in benzimidazole ligands

Surface modification plays an important role in controlling the electron-transfer events and chemical reactivity in photocatalysis, as well as the charge-transport process in heterojunctions. Recently, several reviews of the applications of surface modification toward dye-sensitized solar cells and electrochemical catalysts for hydrogen/oxygen-evolution reactions have been published [21, 29–34], showing the importance of such interdisciplinary research. In the area of solar-energy conversion, Grätzel-type dye-sensitized solar cells composed of mesoporous TiO_2 on fluorine-doped SnO_2 (FTO) with immobilized Ru complexes that contain 2,2′-bipyridyl-4,4′-dicarboxylate and other bpy-derived ligands have been developed [35]. Interestingly,

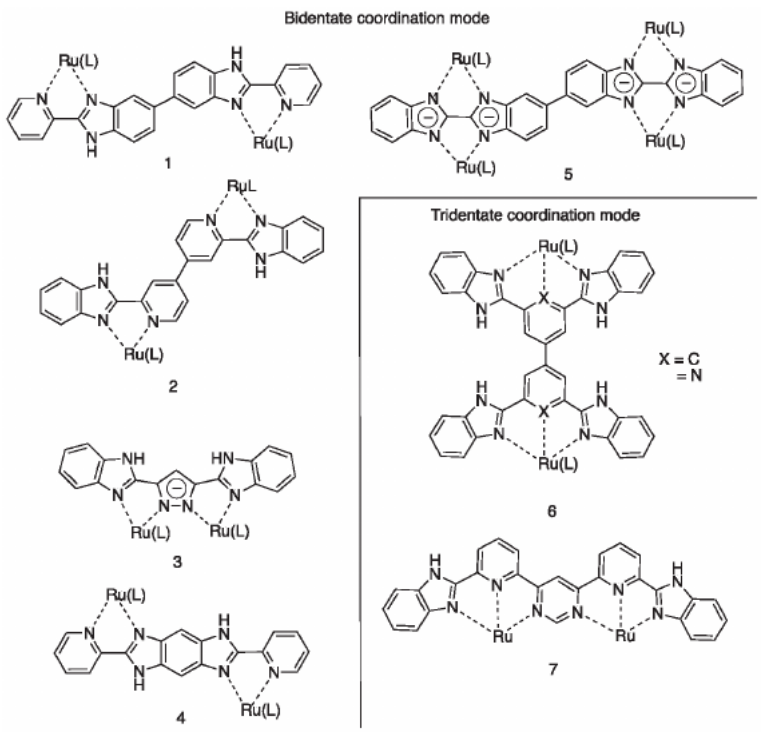

Figure 4.
Chemical structures of benzimidazole-containing ligands that bridge two Ru centers in bis-bidentate or bis-tridentate coordination modes.

the electron-injection efficiency from the photoexcited-state Ru complex to TiO_2 was found to strongly dependent on the anchoring group [34, 36, 37].

Given that the adsorption strength of a Ru complex on a surface depends on the combination of the anchoring group and the surface material, judicious selection of both is necessary for effective surface functionalization. Recently, indium-tin oxide (ITO)-coated glass or polymer substrates have been employed in a wide variety of electronic display devices such as organic light-emitting diodes (OLEDs) [38]. Transparent ITO electrodes are also employed as cell windows for spectroelectrochemistry. Therefore, ITO is a suitable substrate for monitoring both the electrochemical and spectrochemical changes in redox-active Ru complexes immobilized on its surface. The phosphonic acid group, which is known to immobilize on ITO electrodes, has been employed to anchor the Ru complexes [39]. Furthermore, organic phosphonic acids are known to bind zirconium(IV) ions to form a solid two-dimensional layer structure, [40]. which demonstrates their suitability for use in a layer-by-layer growth method based on redox-active metal complexes. Therefore, we developed several new tridentate benzimidazole ligands with phosphonic acid or phosphonate ester anchor groups (**Figure 5**). Alkylation of the imino N–H groups of the benzimidazole moieties using bromoalkyl-diethylphosphonate derivatives furnished chelating benzimidazolyl ligands with ethyl-protected phosphonates, which were used for the synthesis of Ru complexes [41]. After the ethyl-protected phosphonate Ru complexes had been purified, the diethyl phosphonate groups were deprotected to provide the corresponding Ru complexes with phosphonic acid groups. In particular, the tridentate ligand **XP** (**Figure 5**) contains several methylene groups on its side-arms; these methylene moieties are sterically hindered, thus fixing the conformation of the phosphonic acid anchor groups upon surface immobilization.

2.3 Molecular design of redox-active Ru complexes with anchor groups

Ru complexes are substitutionally inert, and the octahedral coordination geometry around the Ru ion is maintained throughout the Ru(II/III) redox reaction. Therefore, they can be immobilized on a surface to design redox-active molecular devices. When three bidentate ligands are coordinated to an octahedral Ru complex, the formation of Δ and Λ optical isomers is possible, but in the case of Ru complexes surrounded by two tridentate ligands with C_{2v} symmetry, no optical isomers do not exist. Hence, surface-confined Ru complexes that contain tridentate ligands with C_{2v} symmetry such as 2,6-bis(benzimidazolyl)pyridine with phosphonic acid anchors are often selected for surface immobilization [21, 42]. Furthermore, the molecular orientation of Ru complexes self-assembled on a surface is crucial to the construction of further

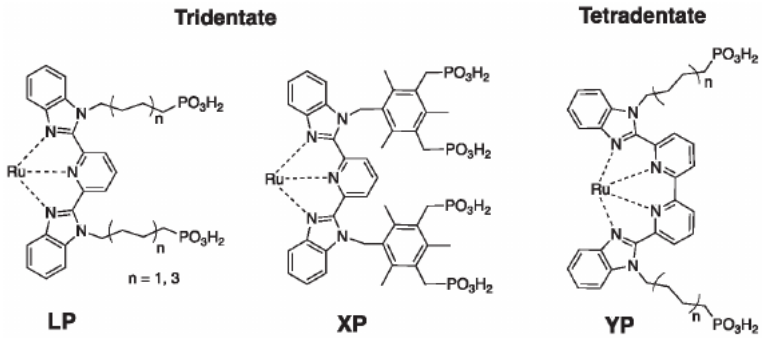

Figure 5.
Chemical structures of benzimidazole-containing ligands with phosphonic acid anchor groups and their abbreviations.

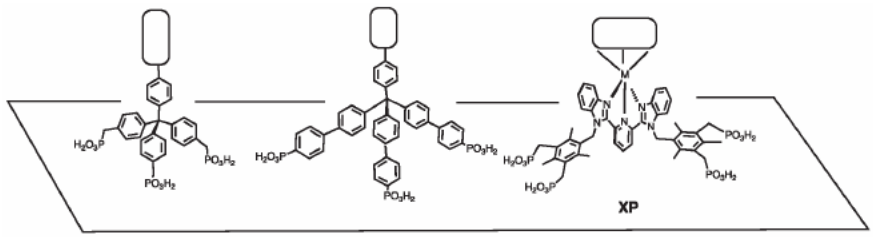

Figure 6.
Chemical structures of free-standing multipodal phosphonic acid anchor groups on a surface [43–45].

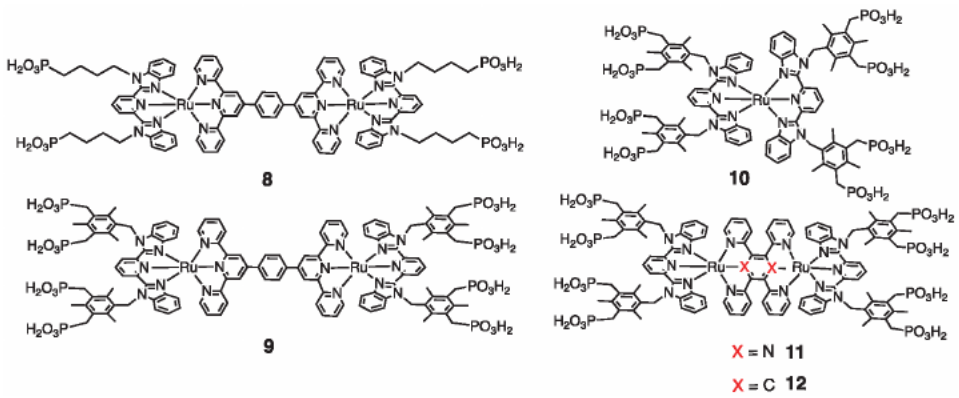

Figure 7.
Chemical structures of rod-shaped dinuclear Ru complexes that bear free-standing multipodal anchor groups at both ends.

layered structures. To maintain the vertical orientation of the Ru complexes on a surface, free-standing multipodal anchor groups with phosphonic acid have been developed over the last two decades. Several examples are shown in **Figure 6** [21, 43–46]. together with our multipodal tridentate benzimidazole ligand with phosphonate anchors, **XP. Figure 7** shows a new series of rod-shaped Ru complexes with 2,6-bis (benzimidazolyl)pyridine moieties and bi- or tetrapodal phosphonic acid groups at both ends that have been reported by our group. Mononuclear Ru complex **10** exhibits a spherical-shaped structure around the central Ru ion, while the other dinuclear Ru complexes **8, 9, 11,** and **12** exhibit a rod-like structure with a Ru–Ru axis [21, 43]. When the dinuclear Ru complexes are immobilized on a surface, the Ru–Ru axis can be oriented vertically or horizontally relative to the surface plane. In AFM measurements, the obtained molecular heights of the dinuclear Ru complexes **9**, **10**, and **11** immobilized on an ITO surface were consistent with the predicted heights for the vertical orientation of the dinuclear Ru complexes at the ITO surface. Ru complexes **8–12** can be dissolved in aqueous solution by adjusting the solution pH, given that the phosphonic acid groups at both ends of these act as polybasic acids.

3. Characterization and functionality of surface-immobilized redox-active Ru complexes

3.1 Surface modification by Ru complexes bearing phosphonic acid anchors

When Ru complexes bearing phosphonic acid anchors are immobilized on an ITO or mica surface by immersion of the substrate into a solution of the Ru

complex, the surface coverage of the Ru complex is dependent on the immersion time and the concentration of the complex in the solution. The temporal evolution of the surface coverage can be analyzed using the kinetic Langmuir equation (Eq. (1)), and curve fitting with a rate constant parameter, k.

$$\Gamma_t = \Gamma_s(1 - exp\,(-kC^*t)) \tag{1}$$

Here, $\Gamma(t)$, k, C, and t refer to the surface coverage, rate constant, concentration of the Ru complex, and time, respectively [33, 46]. A typical kinetic plot for a Ru–**XP** complex with an acridine group at the top is shown in **Figure 8**. This surface-immobilized Ru–**XP** complex is able to capture double-stranded DNA from solution [46].

Another chemical approach to evaluate the surface coverage is using the thermodynamic Langmuir isotherm based upon the concentration dependence of the adsorption of the Ru complex.

$$\Gamma_i/(\Gamma_s - \Gamma_i) = exp\,(\Delta G_{ads}^{o}/RT)C_B \tag{2}$$

Here, Γ_i, Γ_s, C_B, and ΔG_{ads} refer to the surface adsorption at a given concentration, the adsorption at saturation, the concentration of the bulk solution, and the free energy of adsorption, respectively. The adsorption of a Ru complex on a mica and ITO surface can be fitted with the typical Langmuir isotherm model. The free energy of adsorption for Ru complex **9** was found to be −33.4 kJ/mol.

In recent years, several binding modes for the absorption of phosphonic acid groups on metal oxides have been proposed based on intensive studies using polarization modulation infrared reflection adsorption spectroscopy (PM-IRRAS), X-ray photoelectron spectroscopy (XPS), and density functional theory (DFT) calculations in recent years, and the bidentate or tridentate binding modes are considered to be most probable (**Figure 9**) [30, 32, 34, 44, 47]. The optimum solution pH value for the adsorption of Ru complexes **8–12** depends on the complex*; i.e.*, pH = 6 is optimal for complexes **8–11,** while pH = 4 is better for complex **12.**

Atomic force microscopy (AFM) measurements have been used to provide clear surface images depicting the adsorption of these Ru complexes, particularly the surface morphology (*e.g.* height and surface coverage). **Figure 10** shows AFM images of Ru complex **9** on a flattened ITO surface. The samples were prepared using two different immersion conditions, *i.e.*, a dilute solution of the Ru complex with a short immersion time (1 μM; 10 min) and a higher concentration solution with a longer immersion time (25 μM; 3 h). As shown on the left in **Figure 10**, for the dilute

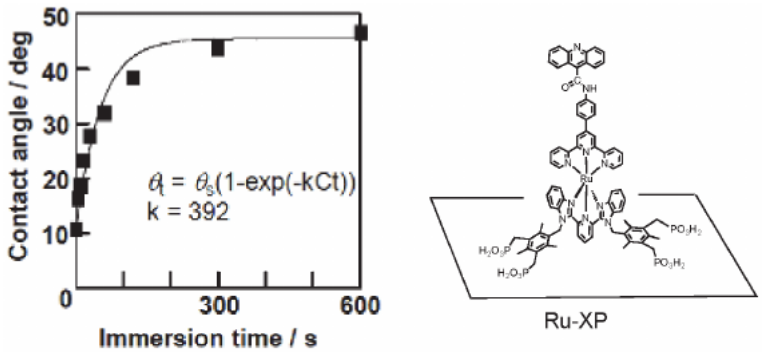

Figure 8.
*Chemisorption kinetics of the Ru–**XP** complex determined by the temporal evolution of the surface coverage of the Ru–**XP** complex (right) on a mica surface. (left) Plot of contact angle versus immersion time [46].*

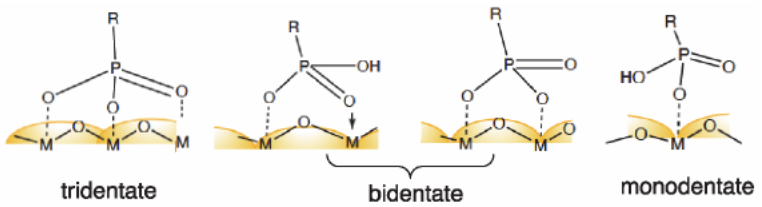

Figure 9.
Proposed surface binding modes of phosphonic acid groups on a metal oxide (MO_x) surface (M = metal) [30].

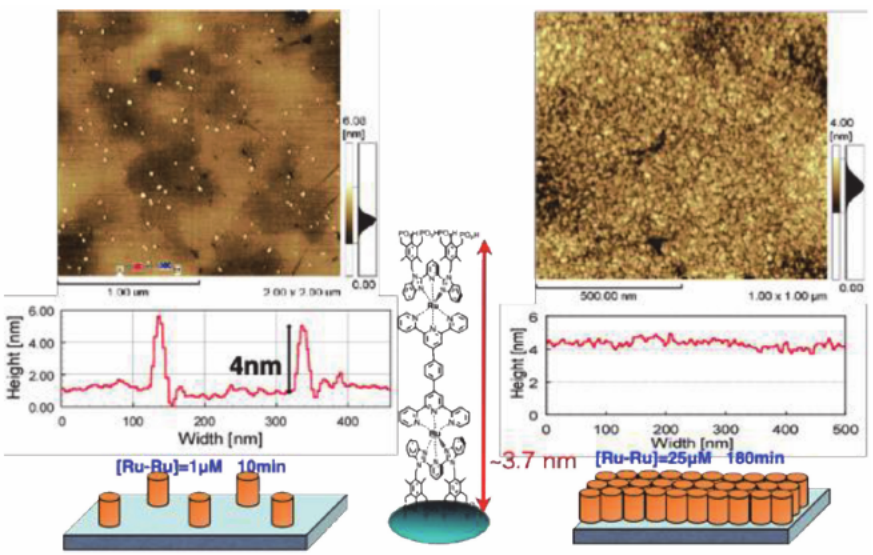

Figure 10.
*AFM images of dinuclear Ru complex **9** immobilized on a flat ITO surface using either a 1 μM solution of complex **9** with an immersion time of 10 min (left) or a 25 mM solution for 3 h (right). Plots show cross-sectional height profiles. In the schematic drawings of the surface images, **9** is shown as a cylinders.*

condition, scattered dots were observed on the surface. The average height of the dots was approximately 4 μm, which is consistent with the height that was predicted for vertically oriented complex **9** using a molecular model. The AFM image on the right in **Figure 10** shows that the surface was fully covered with spherical domains with a diameter of ~20–50 μm when the concentrated conditions were used.

One advantage of ITO electrodes is that they enable the use of UV–vis spectroscopy to monitor the surface immobilization process. Ru(II) complexes bearing *N*-heteroaromatic ligands exhibit a relatively strong metal-to-ligand charge transfer (MLCT) band in the visible wavelength region. In particular, the temporal changes during the immobilization or multilayering processes of such complexes on modified ITO substrates are easily monitored via the absorbance changes in the UV–vis spectra. Furthermore, electrochemical methods such as cyclic voltammetry (CV) can be used to determine the surface coverage of redox-active Ru complexes immobilized on an ITO electrode [48].

3.2 PCET reaction of Ru-benzimidazole complexes in solution and on ITO electrodes

Ru complexes with benzimidazole derivative ligands act as Brønsted acids and exhibit proton-coupled electron transfer (PCET) reactions in aqueous solution [49, 50].

For example, $[Ru(mbibzim)(bibzimH_2)]^{2+}$ (**13**) (mbibzim = 2,6-bis(1-methylbenzimidazol-2-yl)pyridine and $bibzimH_2$ = 2,6-bis(benzimidazole-2-yl)pyridine) behaves as a dibasic acid, as shown in **Figure 11**. The Ru(II/III) oxidation potential of **13**, which results from a PCET reaction, strongly depends on the pH-value ($2 < pH < 9$) in a Britton–Robinson buffer/CH_3CN(1:1 v/v) solution [14, 49, 50]. The PCET reaction of **13** can be described by the square scheme in **Figure 12**, in which complex **13** is abbreviated as Ru–LH_2. This reaction involves both electron transfer and proton-transfer equilibria. In the half-wave potential/pH plot of **13**, the so-called Pourbaix diagram, the half-wave potential is gradually shifted in the negative potential direction with increasing solution pH (**Figure 13**). Based on this diagram, the pK_a values of **13** were determined to be 6.31 and 7.94 for the Ru(II) oxidation state, and < 2 and 3.60 for the Ru(III) oxidation state. When the central pyridine group in the $bibzimH_2$ ligand is replaced with a cyclometallated phenylene group, the resulting Ru complex **14** shows a lower Ru(II/III) oxidation potential than complex **13**; the pK_a values of **14** also increase compared to those of **13**, *i.e.*, to 10.91 and > 12 for the Ru(II) oxidation state and to 6.46 and 9.15 for the Ru(III) oxidation state [51].

In biological systems, protons play a very important role in reactions and energy storage. Proton gradients are the driving force for the synthesis of ATP in biological membranes. Applications of proton gradients in energy storage in materials chemistry have shown that PCET chemical systems can be used for energy storage in redox batteries and capacitors. Ru complexes **13** and **14**, which show PCET with different potentials and pK_a values in unbuffered aqueous solutions, have been used to construct two half-cells separated by a Nafion membrane [51]. The Pourbaix diagrams of complexes **13** and **14** are shown in **Figure 14**; the initial oxidation states of **13** and **14** were Ru(II) and Ru(III), respectively. Upon charging, the oxidation of **13** from the Ru(II) to the Ru(III) state releases the proton(s), while the reduction of **14** from Ru(III) to Ru(II) at the other half-cell captures the proton(s). As a result,

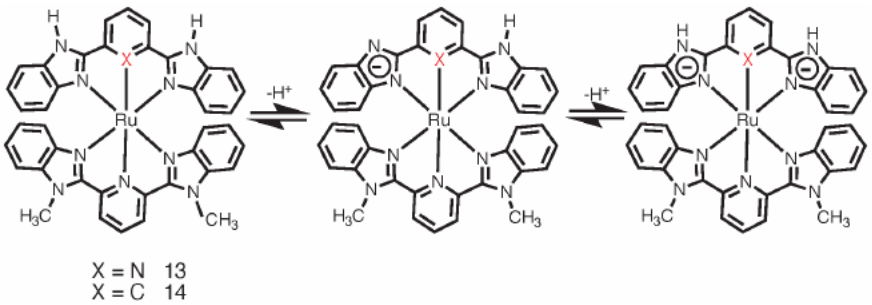

Figure 11.
*Stepwise proton-transfer equilibria of Ru(II)(LMe)(LH_2) complexes (**13**: X = N; **14**: X = C) that act as Brønsted dibasic acids. The total charge of the Ru complex is omitted.*

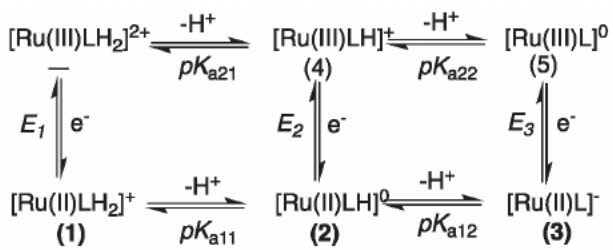

Figure 12.
*Square scheme of the electron–proton equilibria of Ru complexes **13** or **14** as dibasic acids. Numbers in parentheses indicate the Ru species present in the Pourbaix diagram in **Figure 13**.*

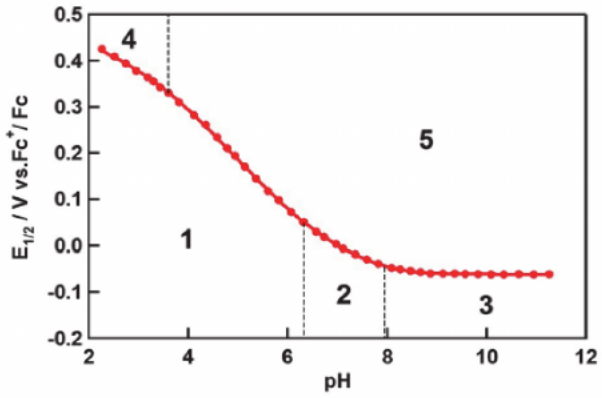

Figure 13.
*Pourbaix diagram of Ru complex **13** in CH_3CN/BR buffer (1/1 v/v) [51].*

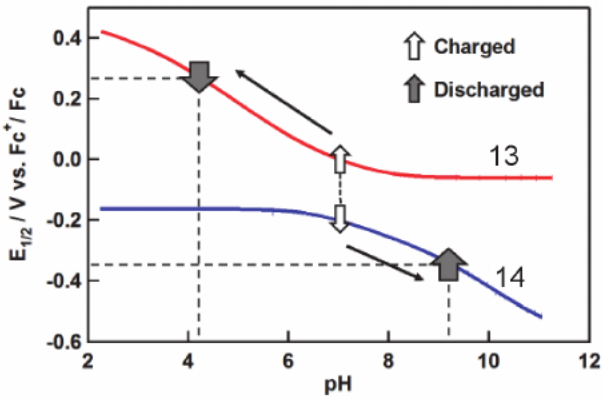

Figure 14.
*Pourbaix diagram for a solution redox battery based on a pair of Ru complexes, **13** and **14**, which both exhibit PCET reactions in CH_3CN/BR buffer (1/1 v/v).*

the electrical energy was stored as a pH gradient between the half-cells. The concept of using a PCET system in this way had been implemented with organic quinone derivatives, [52] but its scope was extended to redox-flow batteries by using a pH-tunable Fe(III) azamacrocyclic complex as both the catholyte and anolyte based on the multiple protonated forms of the Fe complex [53].

The PCET chemistry of Ru complexes that contain benzimidazole derivatives in solution can be extended to surface-bound systems by attaching surface-anchoring groups to the Ru complexes as described in the previous section.

Dinuclear Ru complexes **15**, **16,** and **17** (**Figure 15**) have N–H sites that can be deprotonated on the bridging ligand and the phosphonic acid anchoring groups at both ends. When **15** and **16** are assembled on an ITO electrode, the surface-immobilized redox-active Ru(II) complexes exhibit a well-defined CV response with a typical shape derived from adsorbed chemical species [20]. **Figure 16** shows the CV responses that originate from the Ru(II/III) oxidation process of immobilized complex **15** at different pH values; these responses arise from a well-defined two-electron oxidation wave corresponding to the Ru(II)–Ru(II)/Ru(III)–Ru(III) PCET process in **15** [24]. Upon changing the pH of the aqueous solution was changed, Ru complexes **8**–**17** immobilize stably via the phosphonic acid groups on the ITO electrode at pH = 1.0–9.0, but at pH >9.5, the Ru complexes easily detached from the ITO surface.

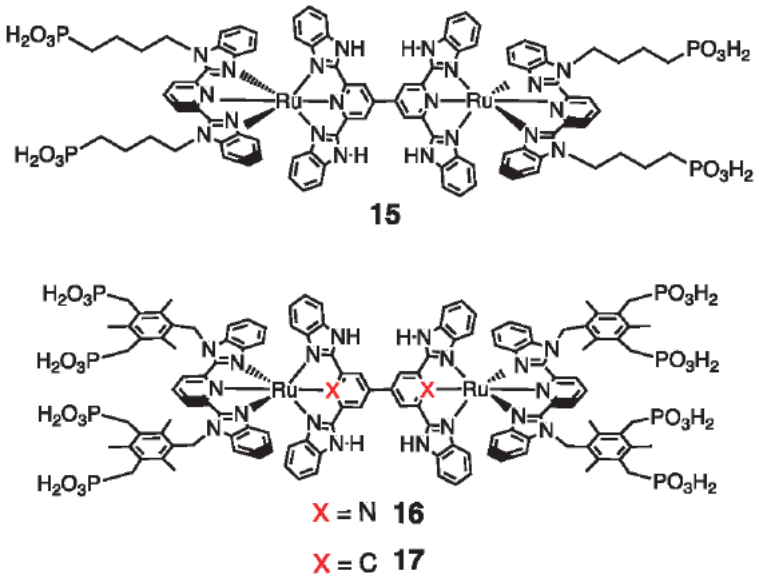

Figure 15.
Chemical structures of dinuclear Ru complexes bearing both a benzimidazole bridging ligand from which protons can dissociate and free-standing multipodal phosphonic acid anchor groups at both ends [24].

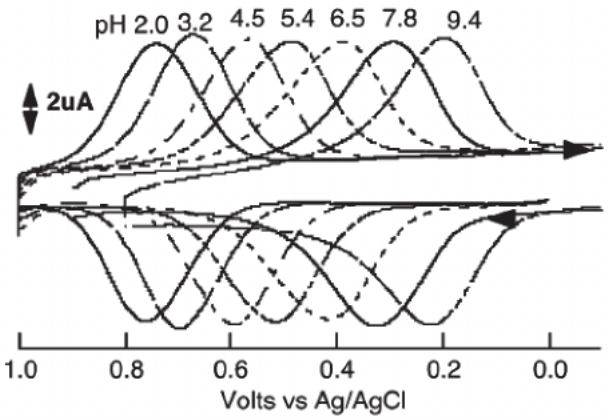

Figure 16.
Cyclic voltammograms of Ru complex **15** *immobilized on an ITO electrode at different pH values in CH_3CN-BR buffer (1/1 v/v) [24].*

The anodic peak current, i_{pa}, is expressed as shown in Eq. (3), where n, ν, A, and Γ represent the number of electrons, scan rate, electrode area, and surface coverage, respectively. Therefore, the anodic peak current for complex **15** is linearly proportional to the scan rate ν, indicating that the Ru complex is a surface-bound species. The total area of the anodic wave is related to the surface coverage of the Ru complex, which was determined to be 0.80×10^{-10} mol cm^{-2}.

$$i_{pa} = \frac{n^2F^2\nu}{4RT}A\Gamma \tag{3}$$

Given that the spectral change due to the redox reactions of a monolayer film of **15** on the ITO electrode can be observed by UV–vis spectroscopy, even surface-assembled monolayer films of Ru complexes on an ITO electrode can be detected.

Upon the oxidation of **15** under an applied potential of +0.8 V vs. Ag–AgCl at pH = 6.5, the differential absorption spectrum demonstrates strong bleaching of the MLCT band at 550 nm and π-π^* transitions of the ligands at 364 nm, along with absorbance increases at 400 and $\sim$ 750 nm, which are characteristic spectral features of Ru(III)–L complexes [24].

3.3 Fabrication of multilayer films based on Ru complexes by layer-by-layer (LbL) growth

Surface modification using a molecular monolayer film alone enables only a single set of functionalities to be incorporated, and the measurable physical quantities, such as optical absorption or current value, are very low due to the low molecular density on the surface. On the other hand, multi-layer modification has the advantages of allowing various molecular units to be deposited at the surface, achieving greater increases in physical quantities such as optical density and charge stored, and enables the integration of various functionalities at the interface [31]. Thus, the integration of functional metal complexes on an electrode holds great promise for applications in *e.g.* molecular-based devices for photochemical energy production/transduction, photocatalysis, and information storage, among other applications [54]. To achieve this integration, the LbL assembly method, in which multilayer structures are constructed via molecular interactions between two layers on a solid surface, is an appropriate technique [39]. LbL assembly using electrostatic interactions, [55]. hydrogen bonding, and coordination metal–ligand bonds has been reported [21, 56]. Among these, structures based on metal-coordination assembly are robust toward environmental changes, such as variations in pH or ionic strength, in aqueous solution.

The formation of well-ordered zirconium(IV) bisphosphonate multilayer films is a well-known method for LbL assemblies on a solid surface that has been developed by Mallouk and others [40]. This method is based on the reconstitution of a two-dimensional layered compound, $Zr(HPO_3)_2$, on a gold surface via self-assembly of molecular units with metal ions. Starting from self-assembled 4-mercaptobutylphosphonic acid on the gold surface as a primer layer, alternate immersion of the modified gold substrate into a zirconium(IV) oxychloride solution and a bisphosphonic acid solution leads to multilayer films composed of a two-dimensional zirconium–phosphonate framework structure via LbL growth [40].

Similarly, the rod-shaped Ru complexes **8**–**16** with polyphosphonic acid groups at both ends were immobilized by self-assembly on an ITO electrode. The polyphosphonic acids at one side of the complexes were attached to the ITO surface, while the other side of the polyphosphonic acid groups remained free to interact with metal ions in solution. Multilayer films of the Ru complexes could thus be obtained by successive alternate immersion in a zirconium(IV) ion and a Ru complex solution (**Figure 17**) [57]. The immobilized Ru film on the ITO substrate was monitored via UV–vis spectroscopy, CV, and the AFM-surface-scratching method throughout each stage of the LbL growth. The use of these monitoring techniques during LbL growth is shown in **Figure 18** with the combination of Ru complex **11** and zirconium as an example.

In each physical measurement, the physical quantities, such as absorbance, amount of charge, and the height of the scratch increased linearly with increasing number of layers. Two types of growth models have been proposed for LbL growth from the surface-primer points via metal coordination on a solid surface (**Figure 19**) [59]. The first model involves dendritic divergent growth, which would result in an exponential increase in the physical quantities, while the second model involves linear growth of a layered structure. In the case of Ru complex **11**,

DOI: http://dx.doi.org/10.5772/ITexLi.97071

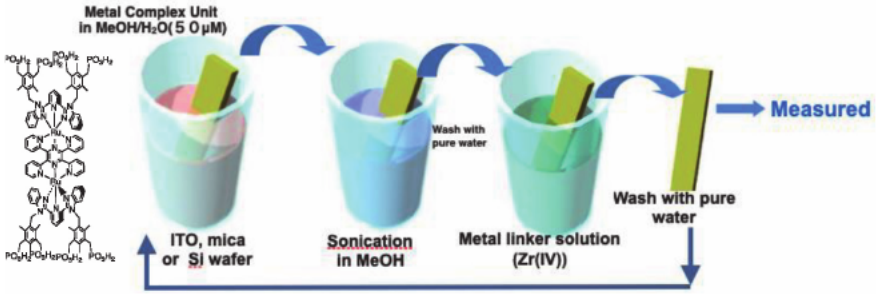

Figure 17.
Illustration of the layer-by-layer (LbL) assembly by successive immersion of a solid substrate such as ITO, mica, or a Si wafer into (i) a solution of a given Ru complex with phosphonate anchors, and (ii) a solution of Zr(IV) ions. After washing, this immersion process was conducted repeated several times.

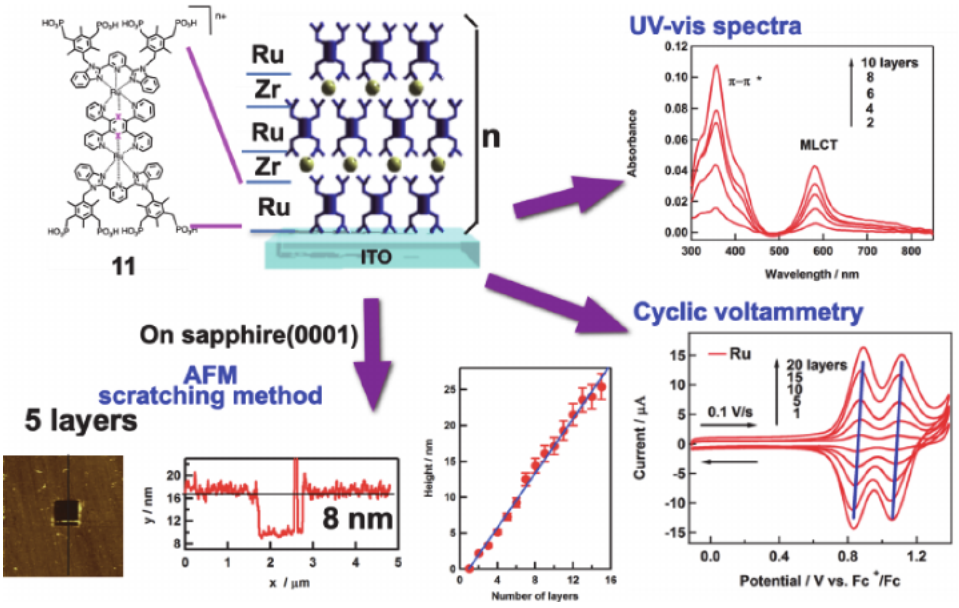

Figure 18.
Illustration of the LbL multilayer film of ***11*** *and monitoring of its LbL growth using UV–vis spectroscopy, CV, and the AFM-scratching method, together with a plot of the height of the scratch vs. the number of layers.*

the linear increase in the physical quantities such as absorbance indicates the formation of well-ordered two-dimensional multilayer films on the solid surfaces.

The use of the LbL method on a solid surface makes it possible to accumulate various molecular units with different chemical functionalities by adjusting the number of layers and metals in the multilayer films. Furthermore, the sequential order of the various complex units can be varied; the units can be arranged in order of descending or ascending potential or pK_a to produce hetero-multilayer films. Such gradients in the layers play an important role in energy transduction. Therefore, "coordination programming" at the surface is possible via judicious choice of molecular units [60]. For example, when two different complexes A and B are assembled into a four-layered film on a solid substrate and a primer layer A is fixed as the first immobilized layer, seven combinations can be obtained by varying the order of the successive layers (substrate|ABAB, |AAAB, etc.). As a result, various films with different potential gradients can be created, and their rectification of electron transfer can be evaluated. Finally, in the fabrication of heterolayers using

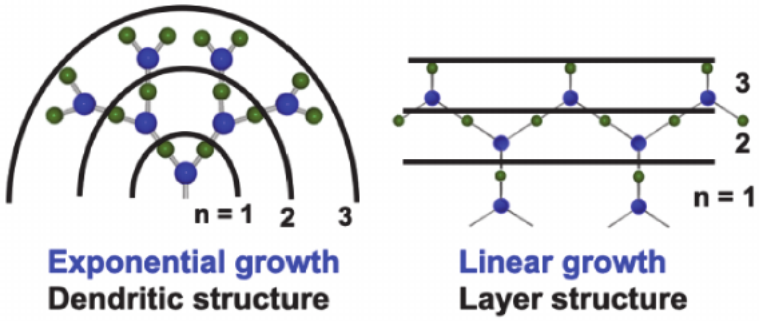

Figure 19.
Illustration of two-layer-growth models: Dendritic divergent growth (left) and linear growth (right) [58].

metal-coordination via the LbL method by immersion in solutions of each component, it is important to ensure that each layer is segregated and that the components are not mixed with others within the layer. In particular, care should be taken using metal ions with substitutionally labile properties, such as Ni(II) and Co(II) ions.

3.4 Functionality of LbL-multilayer films based on Ru complexes

3.4.1 Electron-transfer rate in homo-multilayer Ru complex films on ITO electrodes

Measuring electron-transfer events in multilayer LbL films composed of redox-active Ru complexes on an ITO electrode is fundamental to determine whether electrons can be transmitted through the multiple layers of Ru complexes as the number of layers is increased.

CV measurements of homo-multilayer films of **11** (X = N) to evaluate their electron-transfer rate showed two one-electron oxidation waves. With increasing number of layers, the peak current during CV increased almost linearly. The peak-potential separation between the anodic and cathodic waves was unchanged at a scan rate of 0.1 $V \cdot s^{-1}$, but at 1 $V \cdot s^{-1}$, the separation increased with an increasing number of layers. Using Laviron's procedure, [61] the heterogeneous electron-transfer rate between the Ru complexes in the layers and the ITO electrode was determined for different numbers of layers. The electron-transfer rates gradually decreased with increasing number of layers, and a small attenuation coefficient was obtained from the slope of the plots of $\ln(k_{app})$ as a function of the thickness of films (L). The dependence of the electron-transfer rate, k_{app}, on the distance is expressed by the following equation:

$$k_{app} = k^0 \, exp\,\{-\beta L\} \tag{4}$$

In addition, potential-step chronoamperometry (PSCA) measurements furnished a relatively small value for the apparent electron-transfer rate, k_{app} (β = 0.014 $Å^{-1}$) [62].

Multi-layer films of ruthenium complex **9** were grown on an ITO substrate using hydrogen-bonding interactions. In these films, free-standing ruthenium complexes of **9** adsorbed on an ITO electrode via its tetrapod phosphonic acid anchors interacts with complexes of **9** that are dissolved in the solution via multiple hydrogen bonds between the free phosphonic acid groups at its surface and those of the complex **9** in solution at pH = 6. Surprisingly, the film thickness of the resulting multiply hydrogen-bonded system was controlled by the immersion time and the solution

pH. The current–voltage (*I–V*) characteristics of the multilayered Ru film grown on ITO were measured with a sandwich-type two-terminal devices using the conductive polymer PEDOT:PSS as the top electrode. Based on the observed current, the value of the coefficient for the attenuation with increasing film thickness was relatively small (β = 0.012–0.021Å^{-1}) [43]. This small β value for the multilayer Ru complex film system indicates that long-range electron transport can be expected to be possible even though the system exhibits low conductivity. To clarify the reason for the long-range electron transport in the Ru multilayer film despite its low conductivity, first-principles calculations using Green's non-equilibrium function technique and theoretical analysis of the experimental results were performed. The results indicated that the metal centers covered with the π electrons of the ligands become "stepping stone" sites that provide a resonant tunneling mechanism [43]. Small β values were also reported for terpyridine-metal-complex nanowires produced by the sequential metal-coordination method [63].

3.4.2 Redox-active LbL multilayer films in redox capacitors

As portable electronic devices continue to proliferate, cost-effective cheap energy storage devices that are small, flexible, and low cost and provide high performance during the charging and discharging cycle are in high demand. Molecular-based supercapacitors are promising candidates in terms of these requirements. Redox-active Ru complexes are suitable for the fabrication of energy storage devices, since multilayer molecular Ru assemblies obtained via the LbL method can be scaled by increasing the number of layers, which leads to enhancement of the electrical capacitance in such films [57].

The charge–discharge properties of a sixty-five-layer film of Ru complex **11**, ITO|(Ru complex **11**)$_{65}$, were examined under galvanostatic experimental conditions by applying various constant current densities from 10 to 100 μA·cm^{-2}. The galvanostatic charge and discharge curves show two small plateaus at 0.12 V and 0.37 V vs. Pt, which correspond to two reversible Ru(II)/Ru(III) redox processes (**Figure 20**). A maximum capacitance of 92.2 F·g^{-1} was found at an applied current density of 10 μA·cm^{-2}, but the capacitance decreased to 63.3 F·g^{-1} at the highest

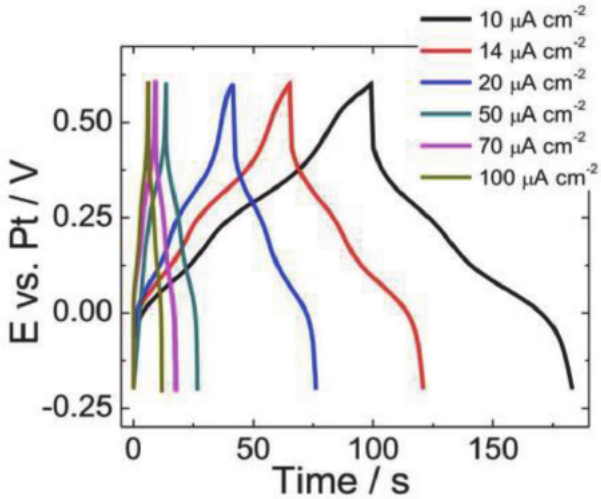

Figure 20.
Galvanostatic charge–discharge curves of ITO|(Ru complex ***11****)$_{65}$ in CH_3CN/0.1 M $HClO_4$ at different current densities [57].*

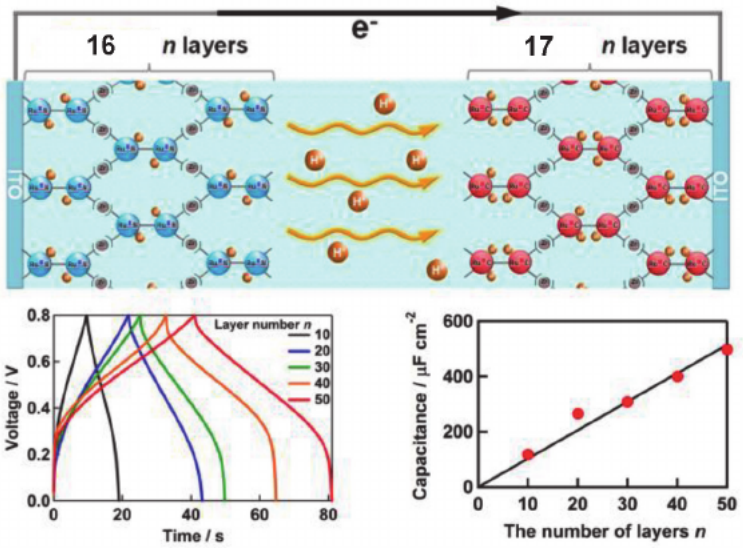

Figure 21.
*Schematic illustration of two half-cells composed of multilayer ITO|(**16**)$_n$ and ITO|(**17**)$_n$ (top), galvanostatic charge–discharge curves for **16** and **17** with different layer numbers,* n *(bottom left), and a plot of the capacitance as a function of* n *(bottom right) [20].*

current density of 100 μA·cm^{-2} (**Figure 20**). Stability tests of the Ru multilayer films (>1000 galvanostatic charge–discharge cycles) showed a capacitance retention of 72% [57].

3.4.3 PCET reactions in Ru-multilayer films for energy storage devices

PCET reactions can be used in energy-storage devices such as redox-flow batteries or two half-cells in unbuffered aqueous solution as described in Section **4.2.** The frameworks of dinuclear Ru complexes **16** and **17** are basically formed by chemical modification of the mononuclear Ru complexes **13** and **14** via the C–C coupling of two **13** or **14** units. Thus, the PCET behaviors of complexes **16** and **17** were almost the same as those of **13** and **14,** except that the number of electrons involved in the PCET reaction was doubled to result in a two-electron process due to the C–C coupling of two molecular units of **13** and **14** and the surface immobilization on an electrode. The Ru complexes **16** and **17** were immobilized by the LbL method on an ITO electrode and applied in a redox capacitor device, in which an aqueous solution was sandwiched between two electrodes composed of multilayer films of **16** and **17** to evaluate the cell performance (**Figure 21**) [20]. Under galvanostatic conditions at a constant current density of 10 μA·cm^{-2}, stable charge–discharge behavior occurred, as shown in **Figure 21**.

During the charging process, the multilayer **16** acted as the anode and the following oxidation reaction proceeded, resulting in the release of protons:

$$\mathrm{Ru(II)_2L_NH_2} \rightarrow \mathrm{Ru(III)_2L_N} + 2e^- + 2H^+. \quad (5)$$

At the same time, the multilayer electrode of **17** acted as a cathode, and the following reduction took place, resulting in the capture of protons:

$$\mathrm{Ru(III)_2L_CH_3} + 2e^- + H^+ \rightarrow \mathrm{Ru(II)_2L_cH_4}. \quad (6)$$

where **16** and **17** are represented as $Ru_2L_NH_n$ and $Ru_2L_CH_n$, and L_NH_n and L_CH_n indicate the bridging ligand bearing the indicated number of protons on the benzimidazole groups. In other words, the capacitance increased with an increasing number of layers [20].

On the other hand, when all four imino N–H protons on the benzimidazole moieties were protected by N–Me groups, the capacitance decreased by 77% compared to that of the original PCET-type capacitor. This result strongly suggests that the proton movement plays a more important role than the anion movement in the charge storage. Furthermore, the proton movement accompanying the redox reaction in the Ru multilayer films on the ITO electrode was confirmed using a pH-indicator probe in aqueous solution. In this type of LbL films composed of Ru complexes that exhibit PCET-type redox reactions, the capacitance increases almost linearly with the number of layers (**Figure 21**) [20].

To obtain proton rocking-chair-type redox capacitors that use protons as the charge carriers, the quinone/hydroquinone couple is often used [52, 64–67]. However, at neutral pH, the electron–proton transfer rate of the quinone/hydroquinone couple is slower than that of the Ru(II/III) couple. The use of the LbL method to fabricate multilayered structures of redox-active Ru complexes that exhibit PCET is advantageous, as the storage capacity can be enhanced by increasing the number of redox-active modular units on demand.

3.5 Sequentially assembled heterolayer films of Ru complexes

One advantage of the LbL assembly method using metal coordination at the interface is that a combinatorial approach can be employed to construct sequentially ordered hetero-multilayer films(*cf.* Section **4.3)**.

Monolayer films of the Ru complexes **11** and **12** on ITO showed two well-defined CV waves at +0.83 and + 1.04 V and at −0.37 and + 0.09 V vs. Fc+/Fc, which were assigned to Ru(II)–Ru(II)/Ru(II)–Ru(III) and Ru(II)–Ru(III)/Ru(III)–Ru(III) processes, respectively. Due to the large differences between the potentials of **11** and **12**, heterolayer films made from combinations of **11** and **12** exhibited interesting electronic/photonic behaviors such as electron-transfer blocking, rectification, and vectorial photoelectron transfer. **Figure 22** shows the CV responses of the heterolayer films ITO|$(\mathbf{11})_n/(\mathbf{12})_n$ (n = 1, 2, where n stands for the number of layers) and ITO|$(\mathbf{12})_n/(\mathbf{11})_n$ (n = 1,3) and the alternating heterolayer films ITO|$(\mathbf{11/12})_4$ and ITO|$(\mathbf{12/11})_4$ in CH_3CN (0.1 M $HClO_4$) [22, 62]. The ITO|$(\mathbf{11})_1/(\mathbf{12})_1$ bilayer hetero-film exhibited four waves (**Figure 22a**), which correspond to the redox processes from both the inner **11** and outer **12** layers; the Ru(II)–Ru(III)/Ru(III)–Ru(III) process of **11** and the Ru(III)–Ru(III)/Ru(III)–Ru(IV) process of **12** overlap at +1.11 V. However, the peak separation of the outer layer of **12** increased at higher scan rates, while the peak separation for the waves from the inner layer of **11** remained unaffected. This result indicated a slower ET rate from the outer layer of **12** due to the higher spatial separation relative to the inner **11** film [22].

Conversely, for the ITO||$(\mathbf{11})_2|(\mathbf{12})_2$ hetero-film, in the first scan over the potential range of −0.5 V to +0.7 V vs. Fc+/Fc, only oxidative waves from **11** at +0.83 and + 1.04 V vs. Fc+/Fc were present; no waves from the outer **12** layer were observed (see blue line in **Figure 22a**). However, when the potential was scanned in the negative direction to −0.5 V, a large cathodic wave appeared at approximately −0.5 V vs. Fc^+/Fc, and subsequently, a new anodic pre-peak at approximately +0.64 V (marked as x) was observed in the potential scan in the positive direction. The new pre-peak x was assigned as a catalytic oxidation wave derived from the ET of the outer **12** layers through ET mediation; that is, direct ET from the outer **12** layer to the electrode was blocked by the bilayer of **11**, and an avalanche ET from

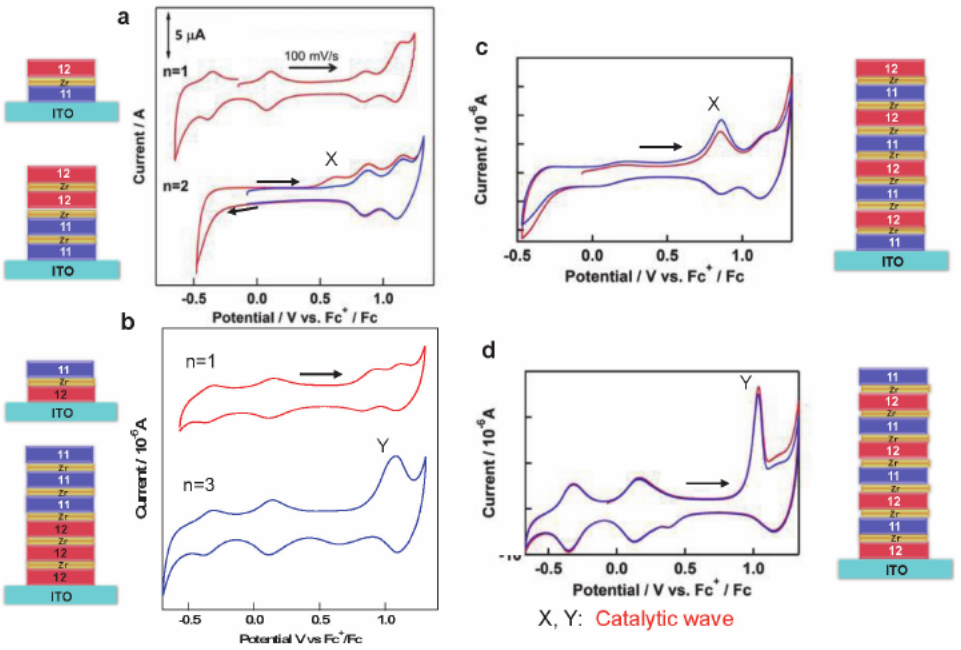

Figure 22.
Cyclic voltammograms of heterolayer films of Ru complexes **11** *and* **12** *with varying sequences: (a) ITO|(***11***)$_n$/(***12***)$_n$ (n = 1, 2, where n stands for the number of layers), (b) ITO|(***12***)$_n$/(***11***)$_n$ (n = 1, 3), (c) alternating ITO|(***11/12***)$_4$ and (d) ITO|(***12/11***)$_4$ in CH_3CN (0.1 M $HClO_4$) [22, 62].*

the outer **12** layers to the inner holes in **11** occurred through the potential gradient once a hole was generated in the inner **11** layers at the onset of the first **11** oxidation wave (**Figure 23**). Consequently, the large cathodic peak at −0.5 V was assigned to the catalytic reduction wave of the **12** film mediated by the reduction process of the inner **11** film. Furthermore, the sequence of the **11** and **12** layers on the ITO electrode leads to characteristic CV responses depending on the sequence and the number of layers, as shown in **Figure 22** [62].

Silicon-based *pn* heterojunctions play an important role in various types of electronic devices, such as diodes, transistors, solar cells and light-emitting diodes (LEDs). The potential difference at the *pn* junction causes blockage of charge transport, resulting in a rectification effect. Under photoirradiation, current flows through the external circuit, which acts as a silicon-based solar cell. Similarly, the photo-response of Ru-complex heterolayer films has been examined [22]. Photoirradiation of the ITO|(**11**)$_4$/(**12**)$_4$ hetero-multilayer film in CH_3CN (0.1 M $HClO_4$) at the open circuit potential of +0.45 V produced a *cathodic photocurrent.* The action spectrum of this film is nearly identical to the UV–vis absorption

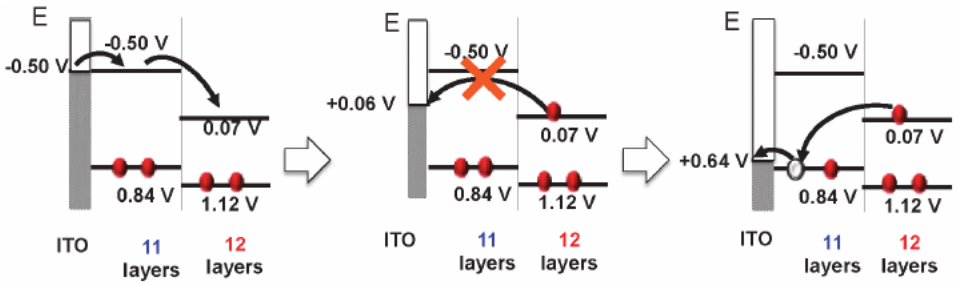

Figure 23.
*Rectified ET mechanism for the CV response of the ITO‖(**11**)$_2$|(**12**)$_2$ hetero-film shown in* ***Figure 22a*** *[22].*

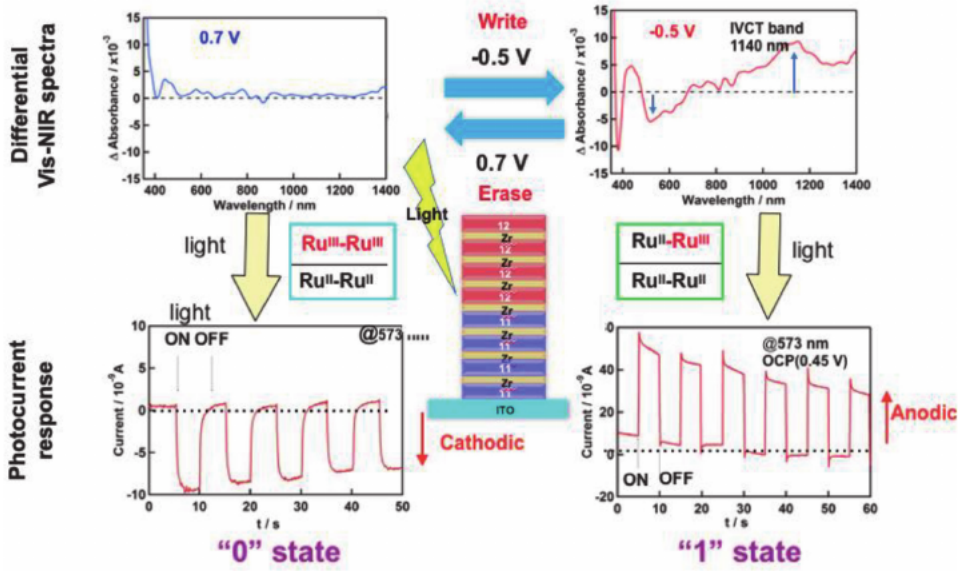

Figure 24.
*Switching between the "0" and "1" states by applying potentials of −0.5 V and + 0.7 V in the ITO|(**11**)$_4$/(**12**)$_4$ hetero-film (top), and the corresponding photocurrent responses (bottom) [22].*

spectrum of **11**, which indicates the inner **11** layers are the main contributor to the photoexcitation, although little photo-response was observed for homo-Ru–complex multilayer films such as ITO|(**11**)$_n$ or ITO|(**12**)$_n$. Interestingly, the direction of the photocurrent on the ITO|(**11**)$_4$/(**12**)$_4$ heterolayer film switched from *cathodic* to *anodic* after the application of a potential pulse at −0.5 V. This photo-response change arose from the generation of a charge trapping state after the application of the pulse; the outer layers of **12** were reduced by the potential, and this reduced state was maintained as a charge-trapping state until holes were generated on the inner **11** layers by electrochemical oxidation or photoexcitation. This charge trapping state was recognized from the differential Vis–NIR spectra, in which a new inter-valence charge-transfer (IVCT) band at 1140 nm appeared for the mixed-valence state of **12** (**Figure 24**). Thus, the heterolayer film ITO|(**11**)$_4$/(**12**)$_4$ represents a typical example of a photo-responsive memory device; the writing process is achieved by applying a potential of either −0.5 or + 0.7 V, and the readout process is achieved by measuring the direction of the photocurrent [22]. Accordingly, the judicious selection of both redox potentials and the sequential ordering of the Ru modular units on the ITO surface makes it possible to design functional electronic devices such as molecular diodes and memory devices.

4. Molecular-device applications using Ru complexes on ITO

The idea of molecular devices is based on a next-generation paradigm to overcome the limitations associated with Moore's law, which states that the number of transistors per silicon chip doubles every year, and the use of individual molecules as active electronic components. The first single molecular device was the theoretical proposal of a molecular diode by Aviram and Ratner; [68] subsequently, the concept of molecular electronic devices was further developed by Carter [69]. Various molecules have demonstrated basic electronic functionality as switches, as diodes for rectification, and as optical devices, storage devices, and sensing devices

for future information technologies [54, 70]. The recent experimental development of single-molecular conductance measurements using metal–molecule–metal junctions [71] has opened a new avenue for the realization of molecular electronic devices through the judicious selection of molecules [70, 72–76]. Ru complexes are substitutionally inert in both the Ru(II) and Ru(III) oxidation states, and also exhibit fast self-exchange ET rates due to the small reorganization energy of the Ru (II/III) couple. Therefore, the use of a mixed-valence Ru(II)–Ru(III) complex as a perturbing motif branching from a conducting molecular wire has been proposed by Carter. Here, two molecular devices based on Ru complexes are discussed; the first is a Ru-complex molecular junction that exhibits rectification switching in response to humidity, and the other is a two-terminal memristor device based on the PCET reactions of Ru complexes.

4.1 Rectification switching in Ru complex molecular junctions in response to external humidity

Conductive-probe atomic force microscopy (C-AFM) was employed to measure the *I–V* characteristics of self-assembled monolayers of Ru complexes on an ITO electrode. An ITO-coated Pt probe was used as the C-AFM tip in order to employ the same material for the top and bottom electrode, and the *I–V* curves were measured via the two-terminal method [77].

Under dry (low humidity) conditions, the *I–V* plots of both mononuclear **10** and dinuclear complex **11** became symmetric in the positive and negative potential range, indicating that the molecules at the junction behaved as a molecular wire or resistor (**Figure 25**). However, under the wet (high humidity) conditions, the *I–V* curves became asymmetric and showed diode-like behavior *only* for dinuclear Ru complex **11**, while they remained symmetric for **10**. The rectification ratio *R* (= $|I(-V)|/|I(V)|$ was found to have a high value of ~1000, where $|I(V)|$ represents the absolute value of the forward or reverse current density at a certain voltage. When the measurement conditions were changed from wet to dry, the *I–V* plots for **11** became symmetric again. This rectification switching via humidity change occurred repeatedly for **11** (**Figure 26**); conversely, such switching was not observed for **10** [77].

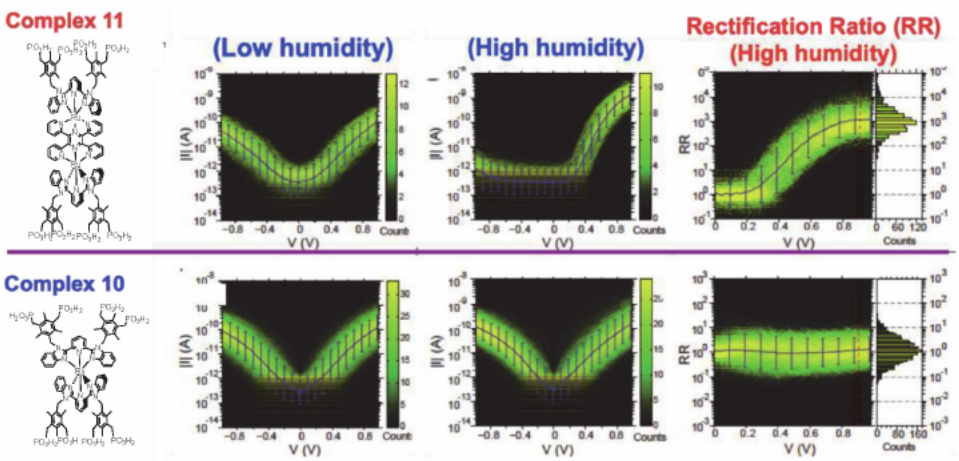

Figure 25.
Structures of Ru complexes **10** *(top) and* **11** *(bottom), log |I|–V curves of the* **10** *and* **11** *molecular junctions under low humidity (5%) and high humidity (60%) conditions, and 2D histograms of the rectification ratio (R) at high humidity [77].*

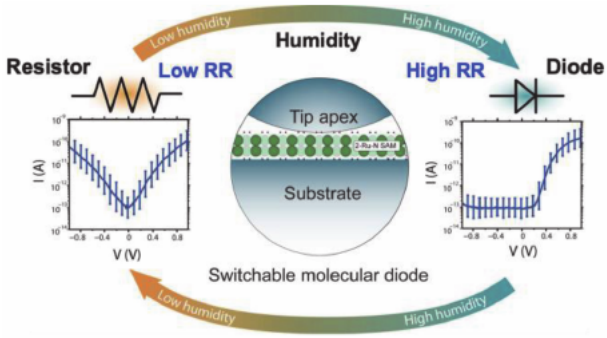

Figure 26.
Conceptual illustration of a humidity-switchable molecular diode [78].

Several factors need to be considered to explain this behavior. The tip-radius affected the asymmetry of the *I–V* curves, whereby a small tip (50 nm radius) leading to a larger rectification ratio *R* on account that water molecules were more strongly attracted to the smaller tip. However, this effect could not fully explain the absence of asymmetry for **10**. Based on combined theoretical and experimental results, water molecules and counter-ion displacement have an important influence on two localized molecular orbitals in **11**, and under an applied voltage bias, a large asymmetry was induced externally via water molecules screening the counter-ions. Thus, via these rectifying properties, the self-assembled Ru complex **11** molecular junctions act as nanoscale sensors with ON/OFF switching in response to external humidity [77].

4.2 Protonic memristor devices based on Ru complexes with PCET

Recently, memristors have attracted substantial attention as the fourth passive element after resistors, capacitors, and inductors. The memristor was predicted by Chua in 1971 as a new electronic circuit element linking charge and magnetic flux, [79] and the first example of such a device was demonstrated experimentally in 2008. This first memristor device consisted of TiO_{2-x} sandwiched between two Pt metal terminals, in which the oxygen defects led to filament formation, and the defects acted as mobile charged dopants and drifted in the applied electric field [80]. As a result, the device exhibited a periodic pinched hysteresis loop in its *I–V* curves. Since then, not only metal oxides, but also many other materials such as organic polymers and metal chalcogenide films, have been sandwiched between the two terminals to fabricate devices with a non-linear hysteretic *I–V* loop [81, 82]. In the two-terminal devices, non-linear changes in the current occur during the voltage sweep, and the associated resistance changes. This type of electric element is generally referred to as a memristor. In recent years, the memristor has become relevant in the context of the action of synapses in the neuromorphic systems of the brain. In biological synapses, ion/molecule migration is used for signal transduction. Inspired by the ion migration in the synapse system, we developed a system in which a proton serves as the charge carrier at the interface between Ru complexes with PCET properties and a proton-conducting polymer such as poly(4-vinylpyridine) (P4VP). In Section 4.4.3, a charge-storage system was constructed from two electrodes modified with films of the Ru complexes **16** and **17**, which show PCET properties in unbuffered 0.1 M $NaClO_4$ solution, and the resulting two-terminal cells showed a stable charging–discharging process via a proton rocking-chair-type mechanism. The unbuffered aqueous solution was replaced with

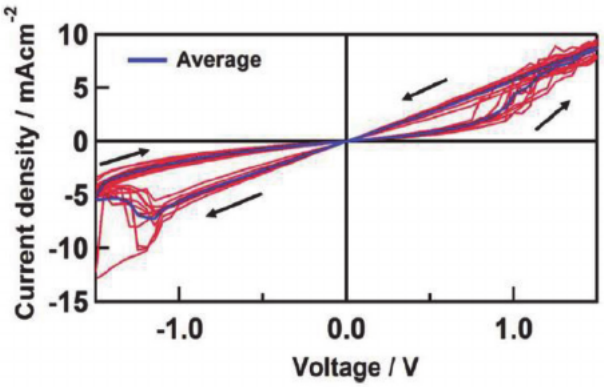

Figure 27.
I–V *plots of the two-terminal device ITO|(**16**)$_3$/P4VP/(**17**)$_3$|ITO, showing ten scans on the same device. The blue line indicates the average of the ten scans [83].*

proton-conducting P4VP (pK_a ~ 4.0–5.2), and the resulting two-terminal heterolayer device, ITO|(**16**)$_3$/P4VP/(**17**)$_3$|ITO, was tested. **Figure 27** shows the typical *I–V* characteristics of the two-terminal device, which produced "8" shaped and non-linear *I–V* loop curves [83].

To elucidate the coupling of the proton-transfer ability of P4VP and the PCET reactions of Ru complexes **16** and **17** at the hetero-interface, CV measurements were performed in 0.1 M $NaClO_4$ aqueous solution (**Figure 28**). A large negative potential shift was observed for the Ru(II/III) peak of the ITO|(**16**)$_3$/P4VP film compared to that of ITO|(**16**)$_3$ without P4VP. This negative potential shift arises from the hydrogen-bonding interactions between the N–H benzimidazolyl groups in **16** and the pyridine groups in P4VP, based on a previous study of the hydrogen-bonding interactions between the N–H imino groups in Ru–benzimidazole-derivative complexes and *N*-heteroaromatics such as pyridine [84]. In this study, the magnitude of the shift was strongly correlated to the pK_a values of both components (i.e., the complex and the heteroaromatic component) [84]. On the other hand, only a small potential shift was observed between the peak of the ITO|(**17**)$_3$/P4VP film and that of ITO|(**17**)$_3$ without P4VP. The difference between these two systems was attributed to the pK_a difference between the Ru complexes in the Ru(II) and Ru(III) oxidation states.

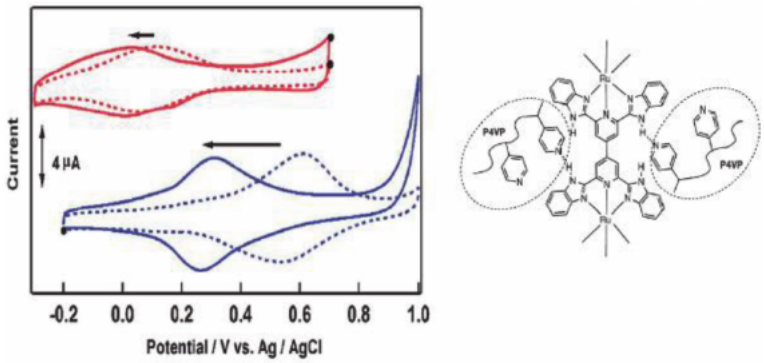

Figure 28.
*Cyclic voltammograms of ITO|(**16**)$_3$/P4VP (blue solid lines) and ITO|(**17**)$_3$/P4VP films (red solid lines), together with those of ITO|(**16**)$_3$ (blue dotted lines) and ITO|(**17**)$_3$ films (red dotted lines), in 0.1 M $NaClO_4$ aqueous solution, as well as a schematic illustration of the hydrogen-bonding interactions between the Ru complex **16** and the P4VP polymer [83].*

In the initial stage, the **16** site of the two terminal device ITO|(**16**)$_3$/P4VP/(**17**)$_3$|ITO is in the Ru(II) oxidation state with pK_a values in the range of 4.1–8.8, while the **17** site on the other side is in the Ru(III) state with pK$_a$ values in the range of 5.2–9.8. The pK_a value of the intervening P4VP polymer is 4.0–5.2. Thus, the proton gradient across the interfaces is small, and it is equilibrated through hydrogen bonding between the P4VP and both **16** and **17** (**Figure 29**). When a bias potential of +1.5 V is applied to the two-terminal ITO|(**16**)$_3$/P4VP/(**17**)$_3$|ITO device, redox processes occur on the immobilized Ru complexes, namely, the oxidation of **16** from the Ru (II) state to Ru(III) takes place at the positive-potential side of the terminal, accompanied by the reduction of **17** from the Ru(III) state to Ru(II) at the other terminal. The resulting redox reactions induce large changes in the pK_a of **16** and **17** relative to those of their initial Ru(II) or Ru(III) states, resulting in a large proton gradient across the immobilized Ru complex/P4VP interfaces (**Figure 11**). Specifically, the pK_a of **16** drops to <3.8, which means that protons are easily released upon the oxidation of **16**, while on the **17** side, the pK_a increases to >8.4. Given the pK_a value of the intervening P4VP is 4.0–5.2, the (**16**)/P4VP proton transfer equilibrium is shifted toward the protonation of the P4VP side, while at the (**17**)/P4VP side, the equilibrium shifts toward the protonation of the film of **17** upon reduction of the Ru center. The proton conductivity through the protonated P4VP layer is improved by the resulting large pK_a gradient, resulting in enhanced conduction until the opposite redox reactions take place at both terminals. When the bias potential was scanned in the negative direction toward −1.5 V, the pK_a gradient returned to the initial state, and the current decreased in the absence of a driving force for electron or proton transport between **16**/P4VP and P4VP/**17**.

Therefore, the large pK$_a$ difference in the Ru complexes **16** and **17** induced by the PCET redox reactions at the two terminals cause a proton gradient across the intervening proton-conducting P4VP, leading to high proton conductivity under an applied voltage. The change in the proton gradient due to the PCET redox reaction in the two-terminal device can be applied to use the proton-conducting switching devices as protonic memristors [83].

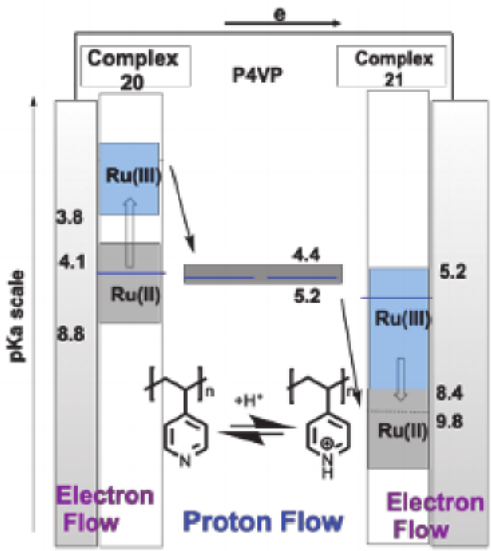

Figure 29.
*Schematic illustration of the proton-conduction switching in the two-terminal device ITO|(**16**)$_3$/P4VP/(**17**)$_3$|ITO and the pK_a gradient under the applied positive bias potential. The numbers refer to the pK_a values of the Ru(II) and Ru(III) complexes [83].*

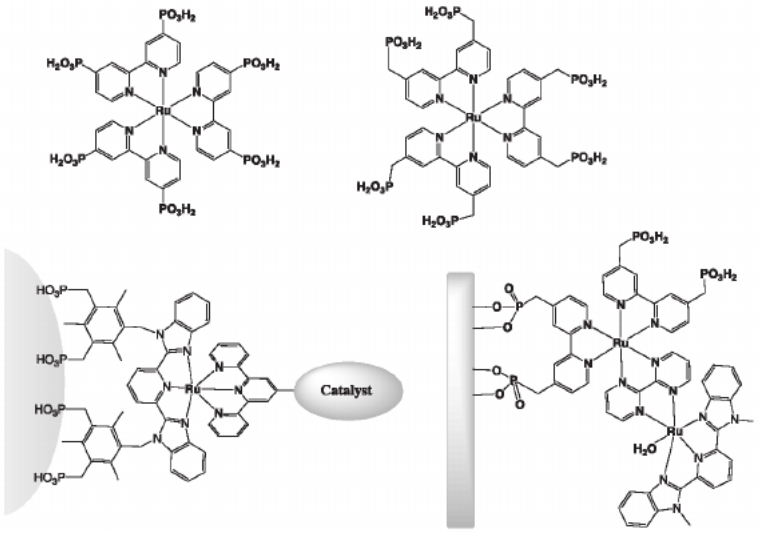

Figure 30.
Chemical structures of $Ru(bpy)_3$ derivatives that contain phosphonic acid anchors and surface-confined Ru catalyst and chromophore–catalyst assemblies [85, 86].

5. Miscellaneous devices based on Ru–benzimidazole complexes for solar-energy transduction

Further important applications for ruthenium complexes include photoredox catalysts and dye-sensitized solar cells. In particular, $Ru(bpy)_3$ or $Ru(tpy)_2$ derivatives have been used as photosensitizer dyes on mesoporous TiO_2 surfaces in Grätzel-type solar cells. Over the past two decades, many Ru complexes with phosphonate anchors have been reported, [33] and many Ru dyes derived from $Ru(bpy)_3$ derivatives that contain phosphonate anchors (**Figure 30**). Additionally, Ru-2,6-bis(benzimidazole-2-yl)pyridine complexes have been employed as photoredox catalysts [85, 86]. The Ru–benzimidazole bond is known to be more stable than the Ru–pyridine bond in the photoexcited state, rendering such Ru-benzimidazole complexes promising candidates for photoelectrochemical redox catalysts.

6. Conclusion

Substitutionally inert ruthenium complexes bearing benzimidazole derivatives have unique electrochemical and photochemical properties. In particular, proton-coupled electron-transfer in ruthenium–benzimidazole complexes endows them with rich redox chemistry and makes them useful as a modular unit for redox mediators or reactive sites for switching by external stimuli. In this chapter, the role of PCET reactions on Ru–benzimidazole complexes in energy-storage applications and the tuning of metal–metal interactions in aqueous solution was emphasized first. Based on this knowledge acquired from solution chemistry, the chemistry of Ru complexes confined on an electrode surface via their self-assembling from solution for the fabrication of the surface functional molecular devices on electrodes was discussed. Indium-tin oxide (ITO) is often chosen as the electrode due to its transparency and wide use as a substrate in electronics. To immobilize the redox-active Ru complexes on an ITO electrode, tetrapod phosphonic acid anchor groups

are often incorporated into tridentate 2,6-bis(benzimidazole-2-yl)pyridine or benzene ligands, which enables the construction of free-standing self-assembled monolayer structures on an ITO electrode. Starting from this monolayer as a primer layer, multilayer films can be constructed by the LbL layer growth method. The resulting multilayers using redox-active Ru complexes as a modular unit exhibited long-range electron transport even in films with over 60 layers (~100 nm thick) through the "stepping-stone" mechanism. Furthermore, a combinatorial approach to LbL layer growth can be used to obtain bespoke functional heterolayer films via material design. Using this strategy, blocking of electron transfer or rectification can be made to occur in such Ru complex heterolayer films, which results in charge trapping; the trapped electrons can subsequently be released via photo-irradiation, which leads to the new concept of photo-responsive memory devices. The CV response of multilayer films of Ru complexes with PCET depends strongly on the pH value. By judicious selection of the redox potentials and pK_a values of the two Ru complexes with PCET properties, two-electrode cells based on the Ru complex multilayer films that acted as proton rocking-chair-type redox capacitors can be obtained. Furthermore, by sandwiching a proton-conducting polymer between two Ru multilayer terminals, new type of protonic memristor device can be fabricated.

Therefore, surface-confined Ru complexes exhibit highly promising potential for the development of new functional molecular-based devices.

Acknowledgements

The author gratefully acknowledges financial support from MEXT via Grants-in-Aid for Scientific Research, No. 21108003 (Coordination Programming) and JP17H05383 (Coordination Asymmetry) as well as from the Institute of Science and Engineering at Chuo University. The author would also like to thank Dr. Katsuaki Kobayashi, Prof. Katsuhiko Kanaizuka, Dr. Hiroaki Ozawa, as well as all of his past students and coauthors in my papers for their great help and their contributions.

Dedication

This chapter is dedicated to my good friend Prof. Wolfgang Kaim on the occasion of his 70th birthday, and to my late wife, Masako Haga, who has supported my research activities for many years.

References

[1] Higgins S. Regarding ruthenium. Nat Chem. 2010;2:1100-1100.

[2] Seddon EA, Seddon KR. The Chemistry of Ruthenium. Amsterdam, The Netherlands: Elsevier; 1984.

[3] Holder AA, Lilge L, Browne WR, Lawrence MAW, Bullock JL, editors. Ruthenium Complexes: Photochemical and Biomedical Applications. Weinheim, Germany: Wiley-VCH; 2018.

[4] Juris A, Balzani V, Barigelletti F, Campagna S, Belser P, von Zelewsky A. Ru(II) Polypyridine Complexes: Photophysics, Photochemistry, Electrochemistry, and Chemiluminescence. Coord. Chem. Rev. 1988, 84:85-277.

[5] Campagna S, Puntoriero F, Nastasi F, Bergamini G, Balzani V. Photochemistry and Photophysics of Coordination Compounds:Ruthenium. Top. Curr. Chem.2007; 280: 117 – 214.

[6] Ceroni P, Bergamini G, Balzani, V. Old Molecules, New Concept:[Ru $(bpy)_3]^{2+}$ as a Molecular Encoder-Decoder. Angew. Chem. Int. Ed. 2009; 48(45):8516-8518.

[7] Burstall FH. Optical Activity dependent on Co-ordinated Bivalent Ruthenium. 34. Optical activity dependent on co-ordinated bivalent ruthenium. J Chem Soc. 1936:173 - 175.

[8] Kalyanasundaram K. Photochemistry of polypyridine and porphyrin complexes. London, San Diego: Academic Press; 1992.

[9] Haga M, Tanaka T. Synthesis and properties of mixed-ligand ruthenium (ii)complexes containing 2-(2-pyridyl) benzimidazole and related ligands. Chem Lett. 1979;8(7):863-864.

[10] Haga M. Synthesis and protonation-deprotonation reactions of ruthenium (ii) complexes containing 2,2'-bibenzimidazole and related ligands. Inorg Chim Acta. 1983;75:29 - 35.

[11] Liu Q, Zhao X, Hu Z, Zhao Z, Wang H. Synthesis and structural studies of N-heterocyclic carbene Ag(I) and Hg(II) complexes and recognition of dihydrogen phosphate anion. Sci Rep. 2017;7(1):7534. DOI: 10.1038/s41598-017-07961-8.

[12] Roland S, Ling X, Pileni MP. N-Heterocyclic carbene ligands for Au nanocrystal stabilization and three-dimensional self-assembly. Langmuir. 2016;32(31):7683-7696. DOI: 10.1021/acs.langmuir.6b01458.

[13] Haga M. Synthesis and properties of tris(2,2'-bibenzimidazole)ruthenium (II) dication, $[Ru(BiBzImH_2)_3]^{2+}$. Inorg Chim Acta. 1983;77:L39-L41.

[14] Xiaoming X, Haga M, Matsumura-Inoue T, Ru Y, Addison AW. Synthesis and proton transfer linked redox tuning of ruthenium(II) complexes with tridentate 2,6-bis(benzimidazol-2'-yl) pyridine ligands. J Chem Soc Dalton Trans. 1993:2477-2484.

[15] Bond AM, Haga M. Spectrophotometric and voltammetric characterization of complexes of bis-(2,2'-bipyridine)(2,2'-bibenzimidazole) ruthenium and osmium in oxidation state II, III, and IV in acetonitrile-water mixtures. Inorg Chem. 1986;25:4507 - 4514.

[16] Haga M, Ano T, Kano K, Yamabe S. Proton-induced switching of metal-metal interaction in dinuclear ruthenium and osmium complexes bridged by bis-2,2'-(2-pyridyl)-bibenzimidazole'. Inorg Chem. 1991;30: 3843 - 3849.

[17] Haga M, Ali MM, Koseki S, Fujimoto K, Yoshimura A, Nozaki K, et al. Proton-induced tuning of electrochemical and photophysical properties in mononuclear and dinuclear ruthenium complexes containing 2,2'-bis(benzimidazol-2-yl)-4,4'-bipyridine: Synthesis, molecular structure, and mixed-valence state and excited-state properties. Inorg Chem. 1996;35(11):3335-3347. DOI: 10.1021/ic950083y.

[18] Haga M, Hong H, Shiozawa Y, Kawata Y, Monjushiro H, Fukuo T, et al. Synthesis and proton-coupled electron transfer reaction of self-assembled monolayers of ruthenium(II) complex containing tridentate 2,6-bis (benzimidazol-2-yl)-pyridine on gold surface. Inorg Chem. 2000;39:4566 - 4573.

[19] Kohmoto M, Ozawa H, Yang L, Hagio T, Matsunaga M, Haga M. Controlling the adsorption of ruthenium complexes on carbon surfaces through noncovalent bonding with pyrene anchors: An electrochemical study. Langmuir. 2016;32(17):4141-4152. DOI: 10.1021/acs.langmuir.6b00405.

[20] Yoshikawa K, Motoyama D, Hiruma Y, Ozawa H, Nagano S, Haga M. Proton-rocking-chair-type redox capacitors based on indium tin oxide electrodes with multilayer films containing Ru complexes. ACS Appl Mater Interfaces. 2018;10(32):26990-27000. DOI: 10.1021/acsami.8b05907.

[21] Haga M, Kobayashi K, Terada K. Fabrication and functions of surface nanomaterials based on multilayered or nanoarrayed assembly of metal complexes. Coord Chem Rev. 2007;251: 2688-2701.

[22] Nagashima T, Ozawa H, Suzuki T, Nakabayashi T, Kanaizuka K, Haga M. Photoresponsive molecular memory films composed of sequentially assembled heterolayers containing ruthenium complexes. Chem – Eur J. 2016;22:1658– 1667.

[23] Haga M. Benzimidazole Ligands. In: McCleverty JA, Meyer TJ, editors. Comprehensive Coordination Chemistry II, Vol. 1. Elsevier Pergamon Press; Oxford, UK; San Diego, CA, USA, 2003. p. 125-134.

[24] Haga M, Takasugi T, Tomie A, Ishizuya M, Yamada T, Hossain MD, et al. Molecular design of a proton-induced molecular switch based on rod-shaped Ru dinuclear complexes with bis-tridentate 2,6-bis(benzimidazol-2-yl) pyridine derivatives. Dalton Trans. 2003 (10):2069-2079. DOI: 10.1039/b300130j.

[25] Haga M, Ano T, Ishizaki T, Kano K, Nozaki K, Ohno T. Synthesis and proton-coupled redox properties of mononuclear or asymmetric dinuclear complexes of ruthenium, rhodium, and/or osmium containing 2,2'-bis-(2-pyridyl)-bibenzimidazole. J Chem Soc Dalton Trans. 1994:263 - 272.

[26] Ohno T, Nozaki K, Haga M. Metal-to-ligand charge transfer excited state of a biruthenium(II) compound bridged by 2,6-(2-pyridyl)benzodiimidazole. Inorg Chem. 1992;31:4256 - 4261.

[27] Yin J, Elsenbaumer RL. Efficient synthesis and characterization of novel bibenzimidazole oligomers and polymers as potential conjugated chelating ligands. J Org Chem. 2005;70: 9436 - 9446.

[28] Yin J, Elsenbaumer RL. Syntheses of homochiral multinuclear Ru complexes based on oligomeric bibenzimidazoles. Inorg Chem. 2007;46:6891- 6901.

[29] Galoppini E. Linkers for anchoring sensitizers to semiconductor nanoparticles. Coord Chem Rev. 2004; 248(13-14):1283-1297. DOI: 10.1016/j.ccr.2004.03.016.

[30] Pujari SP, Scheres L, Marcelis ATM, Zuilhof H. Covalent surface modification of oxide surfaces. Angew Chem Int Ed. 2014;53(25):6322-6356. DOI: 10.1002/anie.201306709.

[31] Cao Jr. R, Díaz-García AM, Cao R. Coordination compounds built on metal surfaces. Coord Chem Rev. 2009;253(9-10):1262-1275. DOI: 10.1016/j.ccr.2008.08.010.

[32] Queffélec C, Petit M, Janvier P, Knight DA, Bujoli B. Surface modification using phosphonic acids and esters. Chem Rev. 2012;112(7):3777-3807. DOI: 10.1021/cr2004212.

[33] Paniagua SA, Giordano AJ, Smith OL, Barlow S, Li H, Armstrong NR, et al. Phosphonic acids for interfacial engineering of transparent conductive oxides. Chem Rev. 2016;116(12):7117-7158. DOI: 10.1021/acs.chemrev.6b00061.

[34] Materna KL, Crabtree RH, Brudvig GW. Anchoring groups for photocatalytic water oxidation on metal oxide surfaces. Chem Soc Rev. 2017;46(20):6099-6110. DOI: 10.1039/c7cs00314e.

[35] Grätzel G. Mesoscopic solar cells for electricity and hydrogen production from sunlight. Chem Lett. 2005;34:8-13.

[36] Bae E, Choi W, Park J, Shin HS, Kim SB, Lee JS. Effects of surface anchoring groups (carboxylate vs phosphonate) in ruthenium-complex-sensitized TiO_2 on visible light reactivity in aqueous suspensions. J Phys Chem B. 2004;108:14093-14101.

[37] Zhang L, Cole JM. Anchoring groups for dye-sensitized solar cells. ACS Appl Mater Interfaces. 2015;7(6):3427-3455. DOI: 10.1021/am507334m.

[38] Sakamoto K, Kuwae H, Kobayashi N, Nobori A, Shoji S, Mizuno J. Highly flexible transparent electrodes based on mesh-patterned rigid indium tin oxide. Sci Rep. 2018;8(1):2825. DOI: 10.1038/s41598-018-20978-x.

[39] Dalle KE, Warnan J, Leung JJ, Reuillard B, Karmel IS, Reisner E. Electro- and solar-driven fuel synthesis with first row transition metal complexes. Chem Rev. 2019;119(4):2752-2875. DOI: 10.1021/acs.chemrev.8b00392.

[40] Mallouk TE, Kim H-N, Ollivier PJ, Keller SW, editors. Ultrathin Films Based on Layered Materials. Oxford, UK: Pergamon; 1996.

[41] Sevrain CM, Berchel M, Couthon H, Jaffrès PA. Phosphonic acid: preparation and applications. Beilstein J Org Chem. 2017;13:2186-2213. DOI: 10.3762/bjoc.13.219.

[42] Haga M, Yutaka T. Inorganic supramolecular architectures at surfaces. In: Pombeiro AJL, Amatore C, editors. Trends in Molecular Electrochemistry: Marcel Dekker; 2004. p. 311-336.

[43] Terada K, Nakamura H, Kanaizuka K, Haga M, Asai Y, Ishida T. Long-range electron transport of ruthenium-centered multilayer films via a stepping-stone mechanism. ACS Nano. 2012;6(3):1988-1999. DOI: 10.1021/nn300126m.

[44] Loewe RS, Ambroise A, Muthukumaran K, Padmaja K, Lysenko AB, Mathur G, et al. Porphyrins bearing mono or tripodal benzylphosphonic acid tethers for attachment to oxide surfaces. J Org Chem. 2004;69:1453-1460.

[45] Long B, Nikitin K, Fitzmaurice D. Self-assembly of a tripodal pseudorotaxane on the surface of a titanium dioxide nanoparticle. J Am Chem Soc. 2003;125:5152- 5160.

[46] Kobayashi K, Tonegawa N, Fujii S, Hikida J, Nozoye H, Tsutsui K, et al. Fabrication of DNA nanowires by

orthogonal self-assembly and DNA intercalation on a Au patterned Si/SiO_2 surface. Langmuir. 2008;24:13203-13211.

[47] Gliboff M, Sang L, Knesting KM, Schalnat MC, Mudalige A, Ratcliff EL, et al. Orientation of phenylphosphonic acid self-assembled monolayers on a transparent conductive oxide: A combined NEXAFS, PM-IRRAS, and DFT study. Langmuir 2013;29:2166-2174.

[48] Yang L, Ozawa H, Koumoto M, Yoshikawa K, Matsunaga M, Haga M. "Janus-type" ruthenium complex bearing both phosphonic acids and pyrene groups for functionalization of ITO and HOPG surfaces. Chem Lett. 2015;44(2):160-162. DOI: 10.1246/cl.140979.

[49] Kojima T. Development of functionality of metal complexes based on proton-coupled electron transfer. Dalton Trans. 2020;49(22):7284-7293. DOI: 10.1039/d0dt00898b.

[50] Huynh MHV, Meyer, TJ. Proton-Coupled Electron Transfer. Chem. Rev. 2007;107(11);5004-5064. DOI: 10.1021/cr0500030.

[51] Motoyama D, Yoshikawa K, Ozawa H, Tadokoro M, Haga M. Energy-storage applications for a pH gradient between two benzimidazole-ligated ruthenium complexes that engage in proton-coupled electron-transfer reactions in solution. Inorg Chem. 2017;56(11):6419-6428. DOI: 10.1021/acs.inorgchem.7b00518.

[52] Emanuelsson R, Sterby M, Strømme M, Sjödin M. An all-organic proton battery. J Am Chem Soc. 2017;139(13):4828-4834. DOI: 10.1021/jacs.7b00159.

[53] Tsitovich PB, Kosswattaarachchi AM, Crawley MR, Tittiris TY, Cook TR, Morrow JR. An Fe^{III} azamacrocyclic complex as a pH-Tunable catholyte and anolyte for redox-flow battery applications. Chem – Eur J. 2017;23(61):15327 - 15331.

[54] Liu D, Miao Q. Recent progress in interface engineering of organic thin film transistors with self-assembled monolayers. Mater Chem Front. 2018;2(1):11-21. DOI: 10.1039/c7qm00279c.

[55] Decher G. Layered nanoarchitectures via directed assembly of anionic and cationic molecules. In: Comprehensive Supramolecular Chemistry. Volume 9: Templating, Self-assembly, and Self-organization. Atwood JL, Davies JED, Macnicol D, Vogtle F, editors: Elsevier Science Ltd.; 1996. p. 507-528.

[56] Ariga K, Ji Q, Hill JP, Bando Y, Aono M. Forming nanomaterials as layered functional structures toward materials nanoarchitectonics. NPG Asia Mater. 2012;4(5):e17. DOI: 10.1038/am.2012.30.

[57] Kaliginedi V, Ozawa H, Kuzume A, Maharajan S, Pobelov IV, Kwon NH, et al. Layer-by-layer grown scalable redox-active ruthenium-based molecular multilayer thin films for electrochemical applications and beyond. Nanoscale. 2015;7(42):17685-17692. DOI: 10.1039/c5nr04087f.

[58] Choudhury J, Kaminker R, Motiei L, de Ruiter G, Morozov M, Lupo F, et al. Linear vs exponential formation of molecular-based assemblies. J Am Chem Soc. 2010;132:9295-9297.

[59] Shinomiya T, Ozawa H, Mutoh Y, Haga M. A redox-active porous coordination network film based on a Ru complex as a building block on an ITO electrode. Dalton Trans. 2013;42(45):16166-16175. DOI: 10.1039/c3dt51484f.

[60] Nishihara H. Coordination programming: A new concept for the creation of multifunctional molecular

systems. Chem Lett. 2014;43(4):388-395. DOI: 10.1246/cl.140010.

[61] Laviron E. General expression of the linear potential sweep voltammogram in the case of diffusionless electrochemical systems. J Electroanal Chem. Interfacial Electrochem. 1979;101:19-28.

[62] Nagashima T, Suzuki T, Ozawa H, Nakabayashi T, Oyama M, Ishida T, et al. Electrochemical behavior of sequentially assembled homo and heterolayer molecular films based on dinuclear ruthenium complexes. Electrochim Acta. 2016;204:235-244.

[63] Karipidou Z, Branchi B, Sarpasan M, Knorr N, Rodin V, Friederich P, et al. Ultrarobust thin-film devices from self-assembled metal-terpyridine oligomers. Adv Mater. 2016;28(18):3473-3480. DOI: 10.1002/adma.201504847.

[64] Er S, Suh C, Marshak MP, Aspuru-Guzik A. Computational design of molecules for an all-quinone redox flow battery. Chem Sci. 2015;6(2):885-893. DOI: 10.1039/c4sc03030c.

[65] Tomai T, Mitani S, Komatsu D, Kawaguchi Y, Honma I. Metal-free aqueous redox capacitor via proton rocking-chair system in an organic-based couple. Sci Rep. 2014;4:3591. DOI: 10.1038/srep03591.

[66] Ji Y, Goulet MA, Pollack DA, Kwabi DG, Jin S, Porcellinis D, et al. A phosphonate-functionalized quinone redox flow battery at near-neutral pH with record capacity retention rate. Adv. Energy Mater. 2019;9(12) DOI: 10.1002/aenm.201900039.

[67] Wedege K, Dražević E, Konya D, Bentien A. Organic redox species in aqueous flow batteries: Redox potentials, chemical stability and solubility. Sci Rep. 2016;6:39101. DOI: 10.1038/srep39101.

[68] Aviram A, Ratner MA. Molecular rectifiers. Chem Phys Lett. 1974;29:277 - 283.

[69] Carter FL. The molecular device computer:point of departure for larger scale cellular automata. Physica D. 1984; 10:175-194.

[70] Jeong H, Kim D, Xiang D, Lee T. High-yield functional molecular electronic devices. ACS Nano. 2017;11 (7):6511-6548. DOI: 10.1021/acsnano.7b02967.

[71] Xu B, Tao NJ. Measurement of single-molecule resistance by repeated formation of molecular junctions. Science. 2003;301:1221-1223.

[72] Schwarz F, Kastlunger G, Lissel F, Riel H, Venkatesan K, Berke H, et al. High-conductive organometallic molecular wires with delocalized electron systems strongly coupled to metal electrodes. Nano Lett. 2014;14 (10):5932-5940. DOI: 10.1021/nl5029045.

[73] Aradhya SV, Venkataraman L. Single-molecule junctions beyond electronic transport. Nat Nanotechnol. 2013;8(6):399-410 DOI: 10.1038/nnano.2013.91.

[74] Meng F, Hervault Y-M, Shao Q, Hu B, Norel L, Rigaut S, et al. Orthogonally modulated molecular transport junctions for resettable electronic logic gates. Nat. Commun. 2014;5:3023.

[75] Milan DC, Vezzoli A, Planje IJ, Low PJ. Metal bis(acetylide) complex molecular wires: concepts and design strategies. Dalton Trans. 2018;47:14125 - 14138.

[76] Tanaka Y, Kato Y, Tada T, Fujii S, Kiguchi M, Akita M. “Doping” of polyyne with an organometallic fragment leads to highly conductive metallapolyyne molecular wire. J Amer Chem Soc. 2018;140:10080 - 10084.

[77] Atesci H, Kaliginedi V, Celis Gil JA, Ozawa H, Thijssen JM, Broekmann P, et al. Humidity-controlled rectification switching in ruthenium-complex molecular junctions. Nat Nanotechnol. 2018;13(2):117-121. DOI: 10.1038/s41565-017-0016-8.

[78] https://mom.dcb.unibe.ch/mom_pages/mom_2018-02.html.

[79] Chua L. Memristor-The missing circuit element. IEEE Trans Circuit Theory. 1971;18:507-519.

[80] Strukov DB, Snider GS, Stewart DR, Williams RS. The missing memristor found. Nature 2008;453(7191):80-83. DOI: 10.1038/nature06932.

[81] Bessonov AA, Kirikova MN, Petukhov DI, Allen M, Ryhanen T, Bailey MJA. Layered memristive and memcapacitive switches for printable electronics. Nat Mater. 2015;14(2):199-204. DOI: 10.1038/nmat4135.

[82] Chua L. Five non-volatile memristor enigmas solved. Appl. Phys. A. 2018; 124(8):563. DOI: 10.1007/s00339-018-1971-0.

[83] Hiruma Y, Yoshikawa K, Haga M. Bio-inspired protonic memristor devices based on metal complexes with proton-coupled electron transfer. Faraday Discuss. 2019;213:99-113. DOI: 10.1039/c8fd00098k.

[84] Haga M, Tsunemitsu A. The outer-sphere interactions in ruthenium and osmium complexes I. Spectrophotometric and voltammetric studies on the hydrogen bonding interactions of bis(2,2'-bipyridine)(2-(2'-pyridyl)benzimidazole)ruthenium (II) cation and its derivatives with aromatic nitrogen heterocycles. Inorg Chim Acta. 1989;164:137-142.

[85] Tamaki Y, Ishitani O. Supramolecular photocatalysts constructed with a photosensitizer unit with two tridentate ligands for CO_2 reduction. Faraday Discuss. 2017;198: 319-335. DOI: 10.1039/c6fd00220j.

[86] Ashford DL, Gish MK, Vannucci AK, Brennaman MK, Templeton JL, Papanikolas JM, et al. Molecular chromophore–catalyst assemblies for solar fuel applications. Chem Rev. 2015; 115(23):13006-13049. DOI: 10.1021/acs.chemrev.5b00229.

Mechanisms of Photoisomerization and Water Oxidation Catalysis of Ruthenium(II) Aquo Complexes

Yuta Tsubonouchi, Eman A. Mohamed, Zaki N. Zahran and Masayuki Yagi

Abstract

Polypyridyl ruthenium(II) complexes have been widely researched as promising functional molecules. We have found unique photoisomerization reactions of polypyridyl ruthenium(II) aquo complexes. Recently we have attempted to provide insight into the mechanism of the photoisomerization of the complexes and distinguish between the *distal*−/*proximal*-isomers in their physicochemical properties and functions. Moreover, polypyridyl ruthenium(II) aquo complexes have been intensively studied as active water oxidation catalysts (WOCs) which are indispensable for artificial photosynthesis. The catalytic aspect and mechanism of water oxidation by the *distal*-/*proximal*-isomers of polypyridyl ruthenium(II) aquo complexes have been investigated to provide the guided thought to develop more efficient molecular catalysts for water oxidation. The recent progress on the photoisomerization and water oxidation of polypyridyl ruthenium(II) aquo complexes in our group are reviewed to understand the properties and functions of ruthenium complexes.

Keywords: Ruthenium aquo complexes, Photoisomerization, Water oxidation catalysis, Artificial photosynthesis

1. Introduction

Polypyridyl ruthenium(II) complexes have been widely researched as promising functional molecules due to appealing photochemical [1–3] and photophysical [4–6] properties as well as redox properties [7, 8], which enable them to exhibit a number of functions such as electrochromism [9, 10], proton-coupled electron transfer [11–13] and photocatalysis [14, 15]. As a result, the polypyridyl ruthenium(II) complexes have been applied to a large variety of devices including sensors [16], photovoltaic cells [17], displays [18] and artificial photosynthesis [19, 20].

We presented irreversible and stoichiometric photoisomerization of *distal*-$[Ru(tpy)(pynp)OH_2]^{2+}$ (*d*-**1**) (tpy = 2,2′;6′,2″-terpyridine, pynp = 2-(2-pyridyl)-1,8-naphthyridine) to *proximal*-$[Ru(tpy)(pynp)OH_2]^{2+}$ (*p*-**1**) as shown in **Figure 1** [21–23], which had not been characterized previously for polypyridyl ruthenium

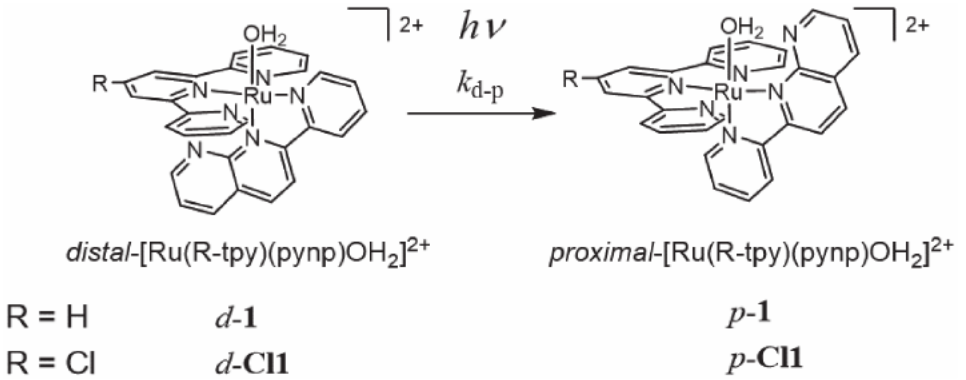

Figure 1.
Photoisomerization of distal-*[Ru(Rtpy)(pynp)OH$_2$]$^{2+}$ to* proximal-*isomers.*

(II) aquo complexes although various photochemical reactions of the ruthenium(II) complexes have been reported [24–33]. We have attempted to provide insight into the mechanism of the photoisomerization of polypyridyl ruthenium(II) aquo complexes and distinguish between the *distal*−/*proximal*-isomers in their physicochemical properties and functions [21–23, 34–36]. We have also developed new synthetic strategy to form dinuclear ruthenium(II) complexes utilizing the photoisomerization [37, 38]. Moreover, polypyridyl ruthenium(II) aquo complexes have been intensively studied as active WOCs [21, 22, 34, 35, 37, 39, 40] which are indispensable for artificial photosynthesis. The catalytic aspect and mechanism of water oxidation by the *distal*-/*proximal*-isomers of polypyridyl ruthenium(II) aquo complexes have been investigated to provide the guided thought to develop more efficient molecular catalysts for water oxidation. In this chapter, we review the recent progress on the photoisomerization and water oxidation of polypyridyl ruthenium(II) aquo complexes in our group.

2. Photoisomerization of polypyridyl ruthenium(II) aquo complexes

With respect to the photoisomerization of polypyridyl Ru(II) aquo complexes, the photoisomerization of *cis*-$[Ru(bpy)_2(OH_2)_2]^{2+}$ (bpy = 2,2′-bipyridine) to its trans form in aqueous media was first reported by Meyer [24]. The mechanism of the photoisomerization reaction was later investigated by Planas et al. [41]. In this case, the *trans* form was present as a photostationary state and slowly went back to the original *cis* form. To the best of our knowledge, the *cis*-$[Ru(bpy)_2(OH_2)_2]^{2+}$ had been the only one polypyridyl Ru(II) aquo complex that exhibits photoisomerization behavior before we presented the photoisomerization of *d*-**1** to *p*-**1** [21]. Furthermore, we reported the reversible photoisomerization equilibrium between *distal- and proximal*-$[Ru(tpy)(pyqu)OH_2]^{2+}$ (*d*-**2** and *p*-**2**) isomers with a ligand of 2-(2-pyridyl)quinoline (pyqu) instead of pynp, in contrast to the irreversible photoisomerization of *d*-**1** to *p*-**1**. The aspect and mechanism of the irreversible photoisomerization of *d*-**1** are first described, followed by those of the reversible one of *d*−/*p*-**2** in this section.

2.1 Irreversible photoisomerization of *distal*-[Ru(Xtpy)(pynp)OH$_2$]$^{2+}$ to the *proximal*-isomer

Photoisomerization behavior of *d*-**1** was investigated by ^{1}H-NMR and UV–Vis spectroscopy. Upon irradiation of visible light to a D_2O solution of *d*-**1**, the NMR

peak at 9.6 ppm due to *d*-**1** decreased with the irradiation time and disappeared completely after 25 min under the experimental conditions (**Figure 2A**) [21]. The new peak at 8.9 ppm assigned to *p*-**1** increased with the concomitant decrease of *d*-**1**. **Figure 2B** displays the concentration profile of *d*-**1** and *p*-**1**, which indicates that irreversible and stoichiometric photoisomerization from *d*-**1** to *p*-**1** proceeds in water by visible light irradiation (**Figure 1**). By contrast, no isomerization of *d*-**1** in water was found to occur under thermal treatment. The photoisomerization rate showed a first-order dependence on *d*-**1** concentration, and the kinetic analysis provided the observed rate constant ($(k_{d\text{-}p})_{obs}/s^{-1}$) of photoisomerization (*distal* to *proximal*) to be 4.1 x 10^{-3} s^{-1} under the conditions employed ($\lambda > 420$ nm, 180 mW cm^{-2}). The $(k_{d\text{-}p})_{obs}$ values increased linearly with respect to the light intensity below 255 mW cm^{-2}, indicating that the photoexcited state participated in photoisomerization under the employed conditions. Arrhenius plots of the photoisomerization gave a straight line in a range of 10 ~ 35°C, providing 41.7 kJ mol^{-1} of activation energy (E_a) for the photoisomerization (**Table 1**). Interestingly, the $(k_{d\text{-}p})_{obs}$ value decreased drastically at pD > 7 (pD = −log [D^+]), while it was unchanged over pD 1-7. The UV–Vis spectrophotometric pH titration of *d*-**1** gave pK_a of 9.7 attributed to the deprotonation of an aquo ligand to form the hydroxo complex, *distal*-[Ru(tpy)(pynp)OH]$^+$. The trend of $(k_{d\text{-}p})_{obs}$ change depending on pH corresponds to the fraction of *d*-**1** (aquo form) dissolved in the solution versus pH, suggesting that the hydroxo form of *d*-**1** is inert for the photoisomerization [21, 22].

The internal quantum yield (Φ) for photoisomerization, which is defined as the ratio of the number of the photoisomerized complexes to the number of incident photons of a given energy, was estimated from the UV–vis spectral change in the experiment under monochromatic light irradiation (520 nm, 26.4 mW cm^{-2}). The Φ values were calculated according to the following equation:

$$\Phi = \frac{hcN_A k_{pi} n_{int}}{p\lambda A(1\text{-}T)} \quad (1)$$

where h, c, N_A, k_{pi}, n_{int}, p, λ, A and T are Plank's constant, the speed of light, Avogadro's number, the rate constant for photoisomerization, initial amount of the complex, photon flux, wavelength, the irradiated area and the transmittance,

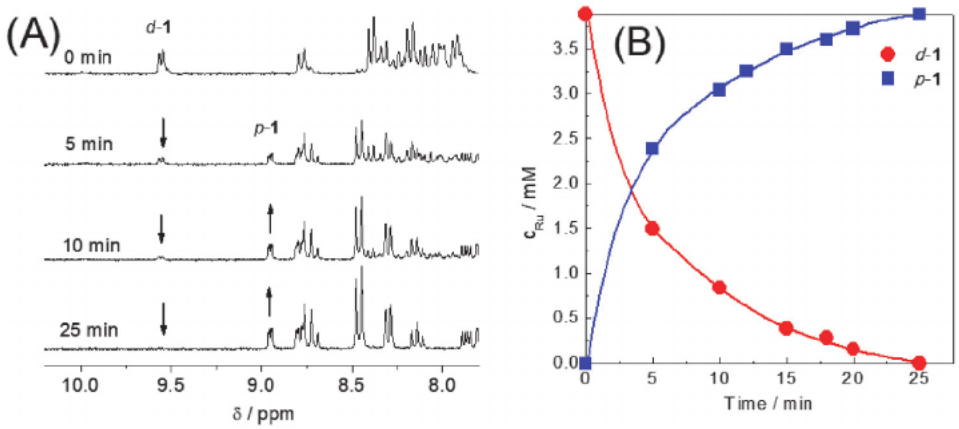

Figure 2.
(A) Time course of ^1H NMR spectral changes during the photoisomerization of d-**1** *in D_2O with 180 mW cm^{-2} visible light irradiation ($\lambda > 420$ nm). (B) Kinetic profiles of* d-**1** *(red circle) and of* p-**1** *(blue square). (Reproduced with permission of American Chemical Society from ref. [21]).*

Complexes	λ_{max} / nm (ε / M^{-1} cm^{-1})	pK_a	c_{Ru} / mM	Photoisomerization parameters				Ref.
				$(k_{d\text{-}p})_{obs}$ / s^{-1b}	$(k_{p\text{-}d})_{obs}$ / s^{-1b}	Φ / % (λ = 520 nm)	E_a / kJ mol^{-1}	
d-**1**	527 (9,300)	9.7	0.088	n.m.	—	1.5	n.m.	[21]
			3.9	4.1×10^{-3}	—	0.31	41.7	[34]
p-**1**	524 (9,300)	10.7	3.9	—	n.r	—	—	[21]
d-**Cl1**	524 (8,600)	9.3	0.088	n.m.	—	2.1	n.m.	[35]
			3.9	4.9×10^{-3}	—	n.m.	n.m.	
p-**Cl1**	518 (8,900)	10.9	3.9	—	n.r	—	—	[35]
d-**2**	501 (8,300)	9.4	3.9	1.2×10^{-2}	—	1.1	23.3	[34]
p-**2**	502 (8,700)	10.5	3.9	—	4.3×10^{-3}	0.34	30.6	[34]
d-**3**	614 (5,700)	n.m.	2.0	n.m.	—	0.05	n.m.	[37]
p-**3**	612 (6,200)	n.m.	—	n.m.	n.m.	n.m.	n.m.	[37]

[a] c_{Ru} is concentrations of ruthenium complexes. The marks of "n.m." and "n.r." mean "not measured" and "no reaction", respectively.
[b] The filtered halogen lamp was used for visible light irradiation (λ > 420 nm, 180 mW cm^{-2}).

Table 1.
Summary of the observed rate constants and internal quantum yields of photoisomerization of d–/p-**1**, d–/p-**Cl1**, d–/p-**2** *and* d–/p-**3** *isomers at 25°C.*[a]

respectively. The Φ values for photoisomerization from *d*-**1** to *p*-**1** are 1.5 and 0.31% at 0.088 and 3.9 mM, respectively, as shown in **Table 1**.

In order to investigate influence of chloro substituent on photoisomerization of *d*-**1**, *distal*- and *proximal*-$[Ru(Cl\text{-}tpy)(pynp)OH_2]^{2+}$ (*d*-**Cl1** and *p*-**Cl1**; Cl-tpy = 4′-chloro-2,2′;6′,2″-terpyridine) complexes were prepared. When an aqueous solution of *d*-**Cl1** was irradiated with visible light (λ > 420 nm, 180 $mWcm^{-2}$), the stoichiometric photoisomerization of *d*-**Cl1** to *p*-**Cl1** was observed as it is for *d*-**1** (**Figure 1**). The rate constant for photoisomerization of *d*-**Cl1** was estimated to be $(k_{d\text{-}p})_{obs}$ = 4.9×10^{-3} s^{-1} [35], which is higher than that ($(k_{d\text{-}p})_{obs}$ = 4.1×10^{-3} s^{-1}) [22, 34] observed for *d*-**1** under the same conditions (**Table 1**). Additionally, the Φ value of *d*-**Cl1** (2.1%) is higher than that (Φ =1.5%) of *d*-**1**.

Several groups reported that some polypyridyl complexes undergo photosubstitution reactions *via* the triplet metal centered (^{3}MC) state from the ^{3}MLCT excited state [25–27]. According to the reports, a possible mechanism for the photoisomerization of *d*-**1** and *p*-**1** isomers was speculated as follows. The ^{3}MLCT excited state of *d*-**1** is generated by absorption of visible light. The photodissociation of the aquo ligand from the exited *d*-**1** proceeds through the thermal accessible ^{3}MC state, leading to the formation of the penta-coordinated $[Ru(tpy)(pynp)]^{2+}$ intermediate. The *p*-**1** isomer is formed by re-coordination of a water molecule to the penta-coordinated intermediate from the opposite direction of a tpy plane. The temperature-dependent transient absorption spectroscopic measurements of *d*-**1** suggest existence of the thermally activated process from the ^{3}MLCT state with an E_a of 49 kJ mol^{-1} [22], which is close to those from the ^{3}MLCT state to the ^{3}MC state reported for various polypyridyl Ru complexes [42–45]. The agreement of the E_a value (49 kJ mol^{-1}) with that (41.7 kJ mol^{-1}) calculated from the Arrhenius plot for the photoisomerization (**Table 1**) also supports the possibility that a main activation process of the photoisomerization reaction is the thermal transition from the ^{3}MLCT state to the ^{3}MC state. However, Density functional

theory (DFT) calculations suggested a different activation process, where the *distal*-penta-coordinated intermediate changes the conformation to *proximal*-penta-coordinated intermediate for *p*-**1** while maintaining the otherwise octahedral structure of *d*-**1** [22].

To obtain deeper mechanistic insights into the irreversible photoisomerization, the ^{3}MLCT excited states of the *d*-**1** and *p*-**1** were characterized by the time-resolved infrared spectroscopy (TR-IR) [36]. The decay of the photoexcited ^{3}MLCT states for both isomers were investigated by the TR-IR analysis, and the lifetimes of the excited state for the *d*-**1** and *p*-**1** were determined to be 9.7 ns and 6.4 ps, respectively. In general, the decay of the ^{3}MLCT excited states of Ru polypyridyl complexes occurs on nanosecond timescale or above, because the transition from a triplet excited state to a singlet ground state is forbidden by spin selection rules. The very short excited lifetime (6.4 ps) for *p*-**1** imply that a non-radiative process from the ^{3}MLCT state was accelerated, so that *p*-**1** is inert for photoisomerization to *d*-**1**.

The large difference in lifetimes of the ^{3}MLCT state between *d*-**1** and *p*-**1** was interpreted by geometry optimization calculations using DFT of both *d*-**1** and *p*-**1** isomers in the singlet ground (S_0) and ^{3}MLCT (T_1) states. While both the structures of *d*-**1** and *p*-**1** isomers in the S_0 states (indicated by lighter color atoms in **Figure 3**) show no considerable distortion, the aquo ligand was restricted by a hydrogen bond (1.48 Å) between its H atom and an N atom on the pynp ligand for *p*-**1**. The transition from S_0 state to T_1 state of *d*-**1** results in a significant change in the dihedral angle of the pynp plane to the tpy plane from 180° to 161°, together with bending at the bond between the naphthyridine and pyridine rings. The distortion for *d*-**1** is likely to originate from the steric hindrance between the extended π*-orbital of the pynp ligand and the π-orbital of the tpy ligand owing to the charge localization on the pynp ligand in the T_1 state. In the case of *p*-**1**, on the other hand, no considerable distortion was observed in the transition (**Figure 3**), but the Ru-O (1.98 Å) and hydrogen bonds (1.06 Å) between the pynp and the water ligands were shorter compared with the Ru-O (2.12 Å) and hydrogen bonds (1.48 Å) in the S_0 state. The shortened hydrogen bond is attributed to the charge localization on the pynp ligand in the T_1 state.

Figure 4 shows the DFT-calculated energy diagram of *d*-**1** and *p*-**1** in the S_0, T_1 and putative ^{3}MC states. *p*-**1** in the S_0 state is more stable than *d*-**1** by 65 kJ mol^{-1} because of hydrogen bond interaction between the pynp and the aquo ligand. The energy difference between the S_0 and T_1 states for *d*-**1** is 176 kJ mol^{-1}, which is remarkably higher than that (101 kJ mol^{-1}) for *p*-**1**. The higher energy difference for *d*-**1** is mainly due to the significant distortion of the pynp ligand on the transition from the S_0 to T_1 states (**Figure 3**). As a result, the energy of *d*-**1** in the T_1 state is higher than that of *p*-**1** in the T_1 state by 140 kJ mol^{-1}. Considering the similar ligand field for both isomers, the energy difference in the ^{3}MC state between *d*-**1** and *p*-**1** is assumed to be not as much as that (140 kJ mol^{-1}) in T_1 states. For *p*-**1**, the ^{3}MC state is presumed to be located at much higher energies than that in the T_1 state. This suggests the possibility of the different decay mechanism of *p*-**1** in the T_1 state from the case of *d*-**1** (usual lifetime of 9.7 ns), exhibiting the non-radiative decay through the thermally populated ^{3}MC state. The possible mechanism is direct relaxation of the T_1 to S_0 states according to the energy-gap law: the decay rate decreases exponentially with increasing the energy gap between excited and ground states [46–48]. Considering almost the same geometries of *p*-**1** between the S_0 and T_1 states, the law can be applied as the weak coupling limit. The lower energy band gap of 101 kJ mol^{-1} between the S_0 and T_1 states for *p*-**1** could explain the short lifetime, at least qualitatively, based on the energy gap law. The direct relaxation mechanism is consistent with the non-thermal decay process suggested by the very quick decay (unusual lifetime of 6.4 ps) for *p*-**1** in the T_1 state. The direct relaxation

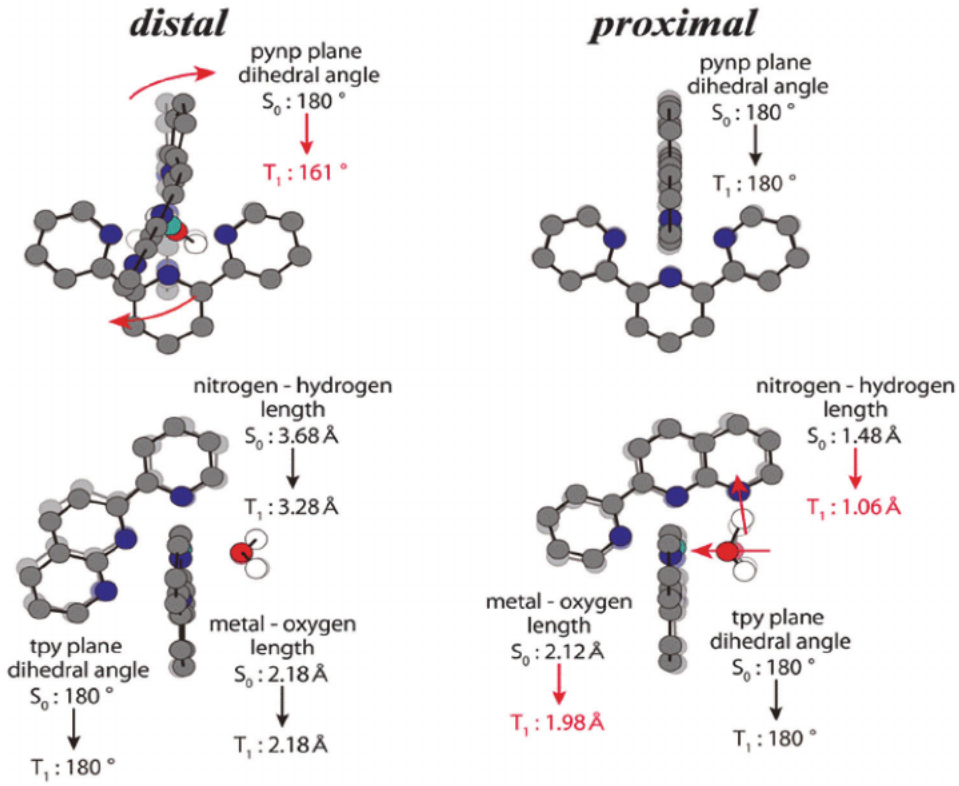

Figure 3.
Overlay of optimized structures of d-**1** *and* p-**1** *in the S_0 (lighter color) and T_1 (deeper color) states. The top and bottom structures are illustrated from the horizontal directions of the pynp and tpy planes, respectively. The colored labels of atoms are as follows: Green, Ru; gray, carbon; red, oxygen; blue, nitrogen; white, hydrogen. (reprinted with permission from ref. [36] copyright 2015 Elsevier).*

process from the T_1 states to the S_0 state (not *via* the ^{3}MC state) could explain the inert photoisomerization of *p*-**1**.

2.2 Reversible photoisomerization between *distal*- and *proximal*-[Ru(tpy)(pyqu)OH_2]$^{2+}$ isomers

The photoisomerization between *d*-**2** and *p*-**2** was examined to reveal the influence of structures of bidentate ligands on the photoisomerization of *d*-**1** (**Figure 5**) [34]. On irradiation of visible light to a D_2O solution of *p*-**2**, the 8.9 ppm peak characteristic of *p*-**2** in the ^{1}H NMR spectrum (**Figure 6A**) decreased with increasing the 9.5 ppm peak assigned to the *d*-**2** isomer. The ^{1}H NMR spectral change reached saturation in 5 min, while the 8.9 ppm peak did not completely disappear. This result suggests that the photoisomerization of *p*-**2** to *d*-**2** reaches a photostationary state (**Figure 5**). This shows that irreversible photoisomerization alters to reversible one by the replacement of the pynp ligand to pyqu in mononuclear Ru aquo complexes [21, 22]. From the integrated peak areas at 8.9 and 9.5 ppm, the equilibrated concentration ratio of *p*-**2**:*d*-**2** was calculated to be 76:24 (**Figure 6B**). The kinetic profiles of the photoisomerization of *p*-**2** to *d*-**2** were well fitted with a reversible reaction model, giving the observed rate constants of the forward reaction (*proximal* to *distal*, $(k_{p\text{-}d})_{obs}/s^{-1}$) of $4.3 \pm 0.1 \times 10^{-3}\ s^{-1}$ and the back reaction (*distal* to *proximal*, $(k_{d\text{-}p})_{obs}/s^{-1}$) of $1.2 \pm 0.03 \times 10^{-2}\ s^{-1}$ under the conditions employed ($\lambda > 420$ nm, 180 mW cm^{-2}), respectively (**Table 1**) [34]. The observed equilibrium constant were given to K_{obs} ($= (k_{p\text{-}d})_{obs}/(k_{d\text{-}p})_{obs}$) = 0.34 ± 0.01 under

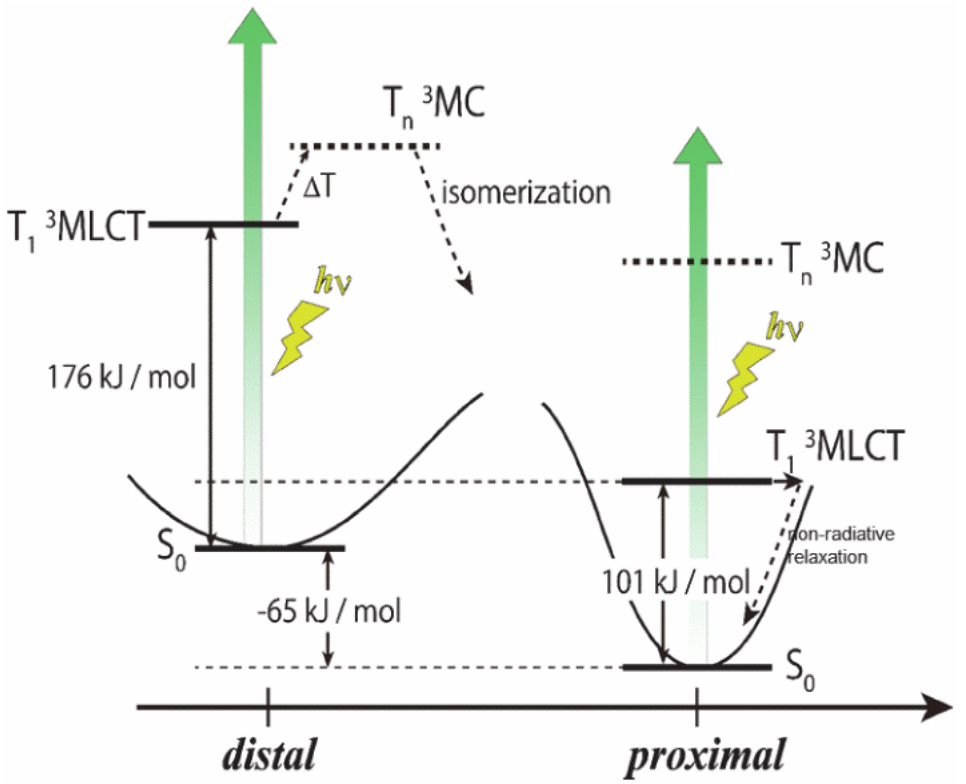

Figure 4.
DFT-calculated energy diagram of d-**1** *and* p-**1** *in the S_o and T_1 states. The speculated energy levels of T_n ^{3}MC states were described. (see text) (reprinted with permission from ref. [36] copyright 2015 Elsevier).*

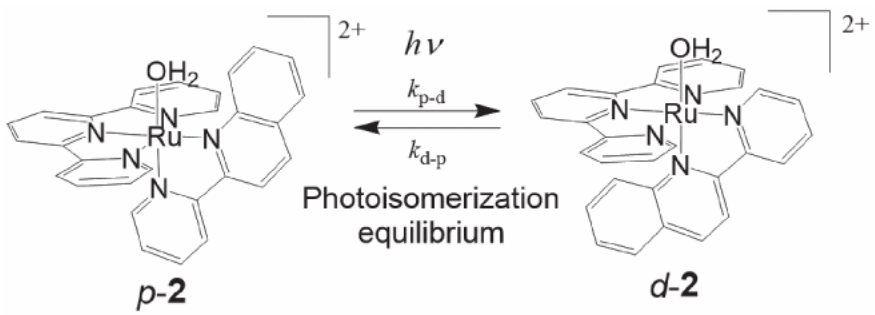

Figure 5.
Photoisomerization equilibrium between proximal- *and* distal-*[Ru(tpy)(pyqu)OH$_2$]$^{2+}$* (p-**2** *and* d-**2**) *isomers.*

the employed conditions. Both $(k_{p\text{-}d})_{obs}$ and $(k_{d\text{-}p})_{obs}$ increased linearly with respect to light intensity up to 180 mW cm^{-2}, suggesting that the photoexcited states of *p*-**2** and *d*-**2** isomers are also involved in the forward and back reactions, respectively [34]. As shown in **Figure 7**, $(k_{p\text{-}d})_{obs}$ and $(k_{d\text{-}p})_{obs}$ decreased from pD = 8 to 12, and the photoisomerization did not take place at all above pD =12 [34]. This result implies that both hydroxo isomers, *proximal*- and *distal*-[Ru(tpy)(pyqu)OD]$^+$ are inert for the forward and back photoisomerization reactions, respectively, as observed in the case of *distal*-[Ru(tpy)(pynp)OH]$^+$ [21, 22]. The pD-dependent $(k_{p\text{-}d})_{obs}$ and $(k_{d\text{-}p})_{obs}$ analysis demonstrated inflection points at pD = 10.5 and 9.8 for the

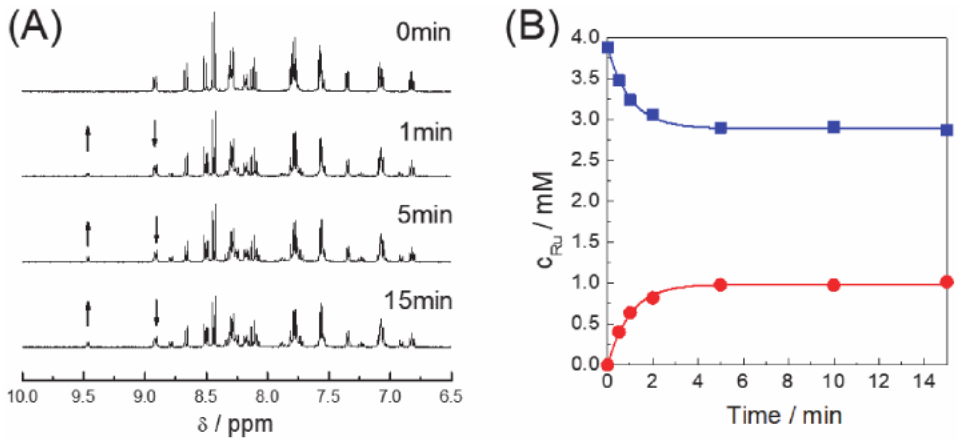

Figure 6.
(A) Time course of ^{1}H NMR spectral changes during the photoisomerization of p-**2** *(3.9 mM, pD = 8.4) with 180 mW/cm^2 visiblelight irradiation (λ > 420 nm) in D_2O. (B) Kinetic profiles of* p-**2** *(blue square) and* d-**2** *(red circles). (reproduced from ref. [34] with permission of John Wiley & Sons, Inc.).*

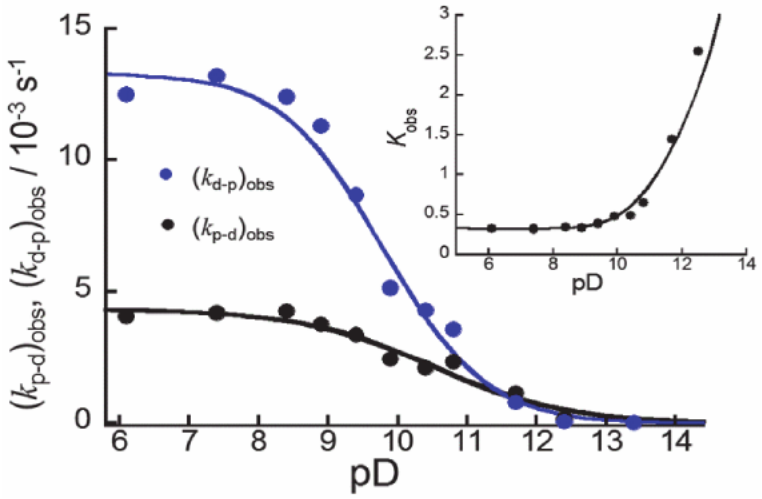

Figure 7.
Plots of observed rate constants ($(k_{p-d})_{obs}$ and $(k_{d-p})_{obs}$) vs. pD for the photoisomerization reactions shown in ***Figure 5****. Visible light (λ > 420 nm, 180 mW/cm^2) was irradiated to the* p-**2** *(3.9 mM) in D_2O at 25°C. Inset shows diagram of observed equilibrium constants K_{obs} vs. pD. (reproduced from ref. [34] with permission of John Wiley & Sons, Inc.).*

forward and back reactions, respectively. These values are close to the pK_a of *p*-**2** (pK_a = 10.5) and *d*-**2** (pK_a = 9.4) (**Table 1**). The difference in pK_a values (1.1) between *p*-**2** and *d*-**2** results in the markedly pD-dependent K_{obs} values (inset of **Figure 7**). K_{obs} increased above pH = 9, and reached its maximum value (K_{obs} = 2.5) at pH = 12. This trend is consistent with the observation that the yield of *d*-**2** generated in the photoisomerization raised from 26–65% on increasing from pH 5.7 to 12.

The thermal dependent kinetics for $(k_{p-d})_{obs}$ and $(k_{d-p})_{obs}$ in a temperature range of 25 to 70°C gives E_a = 30.6 ± 2.9 and 23.3 ± 2.1 kJ mol^{-1} for the forward and back reactions, respectively. The higher E_a of the forward reaction ($(k_{p-d})_{obs}$) compared to the back one ($(k_{d-p})_{obs}$) is attributable to the unfavorable loss of the hydrogen bond (C-H···O) between the H atom bonded to 8-C of the quinoline moiety of the pyqu ligand and the O atom of the aquo ligand upon water

dissociation for photoisomerization. The van't Hoff plots for K_{obs} gave $\Delta H = 7.7 \pm 2.7$ kJ mol^{-1}, that is close to enthalpy for the hydrogen bond (5.4 kJ mol^{-1}) of C-H···O in the benzene-water complex [49].

The Φ values for the forward and back photoisomerization reactions were estimated to be 0.34% and 1.1% from the experiments using monochromatic light (520 nm, 26.4 mW cm^{-2}) (**Table 1**). The higher Φ (1.1%) of *d*-**2** compared to that (0.34%) of *p*-**2** could be attributed to the enthalpy of hydrogen bond (C-H···O) of *p*-**2** (decreased Φ for *p*-**2**) and the steric repulsion between the H atom bonded to 8-C of the quinoline moiety of pyqu and the tpy plane for *d*-**2** (increased Φ for *d*-**2**). The Φ value of 1.1% for photoisomerization from *d*-**2** to *p*-**2** is 3.5 times higher than that (0.31%) for the photoisomerization from *d*-**1** to *p*-**1** under the same concentration [34]. This could also be ascribed to the dominant steric repulsion between the tpy ligand and the H atom bonded to 8-C of the quinoline ring of pyqu for *d*-**2**, compared to the repulsion between the tpy ligand and the uncoordinated nitrogen of the naphthyridine ring of pynp for *d*-**1**.

2.3 New synthetic strategy for dinuclear ruthenium(II) complexes utilizing the photoisomerization

The photoisomerization of Ru(II) aqua complexes was applied to the strategic synthesis of dinuclear Ru complexes that are difficult to be synthesized by conventional thermal reactions so far. Herein, we succeeded to newly synthesize several dinuclear Ru(II) complexes, *proximal*, *proximal*-[Ru_2(tpy)$_2$LXY]$^{3+}$ (L = 5-phenyl-2,8-di(2-pyridyl)-1,9,10- anthyridine, X and Y = other coordination sites; denoted as *p*,*p*-**Ru_2XY**) utilizing the photoisomerization of a mononuclear Ru aquo complex [37]. The tetradentate backbone ligand L was used to form a *proximal*, *proximal* - dinuclear Ru(II) structure (**Figure 8**). The reaction of [Ru(tpy)Cl$_3$] with L gave *distal*-[Ru(tpy)LCl]$^+$ (*d*-**3Cl**) selectively in ethanol in a 59% isolated yield. This selective formation of *d*-**3Cl** was possibly caused by the steric hindrance of L with a chloro ligand. *d*-**3Cl** was then converted to *distal*-[Ru(tpy)LOH$_2$]$^{2+}$ (*d*-**3**) by chloro subtraction with a silver salt in water in a 90% isolated yield. The thermal reaction of *d*-**3** with a second ruthenium center [Ru(tpy)Cl$_3$] for dimerization failed to give

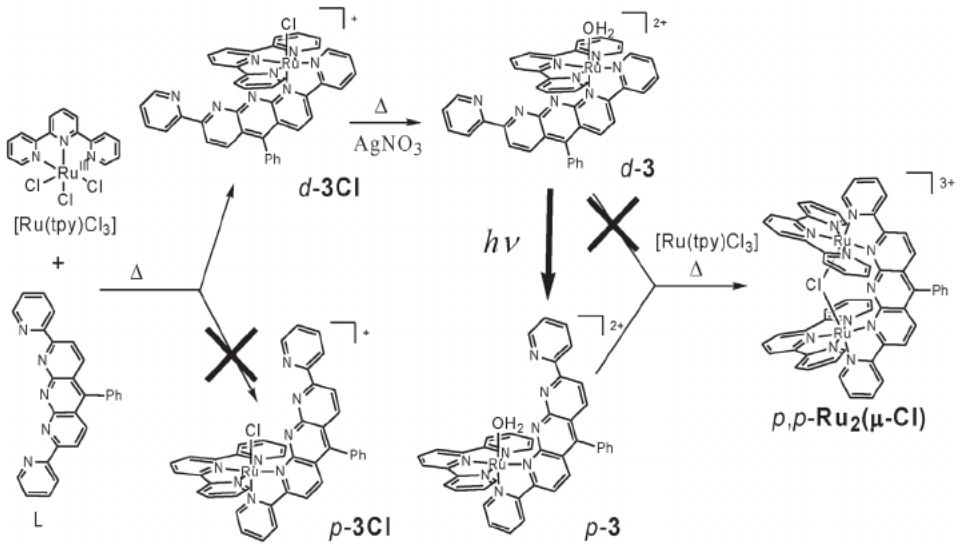

Figure 8.
Synthetic scheme of a μ-Cl bridged dinuclear ruthenium complex, p,p-***Ru_2 (μ-Cl)*** *using photoisomerization of* d-*3. (reproduced from ref. [37] with permission of American Chemical Society).*

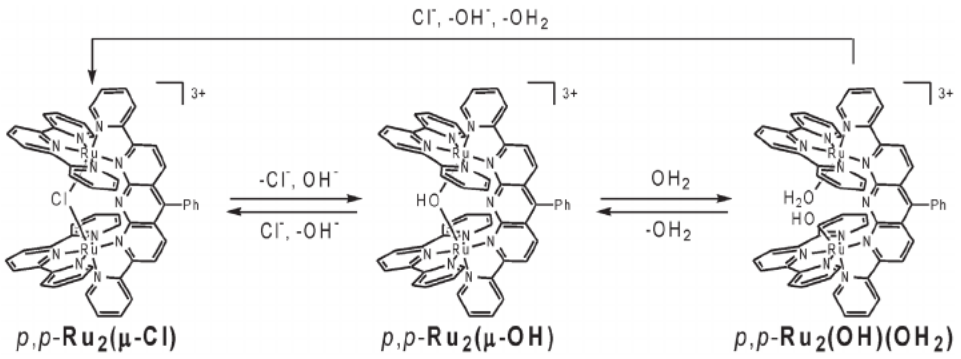

Figure 9.
Reversible bridging-ligand substitution reactions among p,p-***Ru₂(μ-Cl),*** p,p-***Ru₂(μ-OH)*** p,p-***Ru₂(OH)(OH₂).***

the *proximal*, *proximal*-dinuclear Ru(II) complex owing to the steric hindrance located between the tpy ligand on the *d*-**3** and the one on [Ru(tpy)Cl_3]. However, if the photoisomerization of *d*-**3** to *proximal*-[Ru(tpy)LOH_2]$^{2+}$ (*p*-**3**) is utilized (**Figure 8**), the steric constraint of *d*-**3** for formation of the *proximal*,*proximal*-dinuclear Ru(II) species could be avoided. The photoisomerization of *d*-**3** stoichiometrically progressed to form *p*-**3** in water/ethanol mixture under visible light irradiation ($\lambda > 420$ nm). The subsequent thermal reaction of *p*-**3** with [Ru(tpy)Cl_3] in water/ethanol mixture successfully generated *proximal*,*proximal*-[Ru_2(tpy)$_2$L(μ-Cl)]$^{3+}$ (*p*,*p*-**Ru_2(μ-Cl)** in a 67% isolated yield that was unambiguously characterized by X-ray diffraction [37]. The *p*,*p*-**Ru_2(μ-Cl)** was converted to the *proximal*,*proximal*-[Ru_2(tpy)$_2$L(μ-OH)]$^{3+}$ (*p*,*p*-**Ru_2(μ-OH)**) in neutral or slightly basic aqueous medium via substitution of the μ-Cl bridge with an OH^- ion as shown in **Figure 9** [37, 38]. The *p*,*p*-**Ru_2(μ-OH)** was then converted to *proximal*,*proximal*-[Ru_2(tpy)$_2$L(OH)(OH_2)]$^{3+}$ (*p*,*p*-**Ru_2(OH)(OH_2)**) via insertion of a water molecule to the central core to reach equilibrium between *p*,*p*-**Ru_2(μ-OH)** (~10%) and *p*,*p*-**Ru_2(OH)(OH_2)**.

3. Water oxidation catalysis by ruthenium(II) aquo complexes

The mononuclear ruthenium polypyridyl aquo complexes are promising WOCs to understand water oxidation chemistry and provide the guided thought for efficient WOCs because of their simple structures, high catalytic activities, ease of chemical modification, and informative knowledge including catalytic mechanisms [13, 21–23, 34, 35, 40, 50–52]. Controlling the electron density on the metal center as an active site by alternating the substituent groups on their ligands is a common approach to reveal the mechanism and influencing factors for water oxidation catalysis.

The molecular WOCs take part in the process of the four electrons and four protons removal from two water molecules, either consecutively or concerted, to form the O-O bond. Understanding the mechanism of the O-O bond formation is vital in improvement of molecular WOCs. Two main classes of proposed reaction mechanisms at metal centers are shown in **Figure 10**; water nucleophilic attack (*WNA*) on metal-oxo centers (M = O) and interaction of two M-O centers (*I2M*) [53–56]. In the *WNA* mechanism (**Figure 10a**), an electrophilic high-valent metal-oxo (M^{n+} = O) species is formed via multiple consecutive oxidation steps. A nucleophilic attack of a water molecule on the M^{n+} = O species occurs, that leads to formation of a hydroperoxide ($M^{(n-2)+}$-OOH) species. Further oxidation and

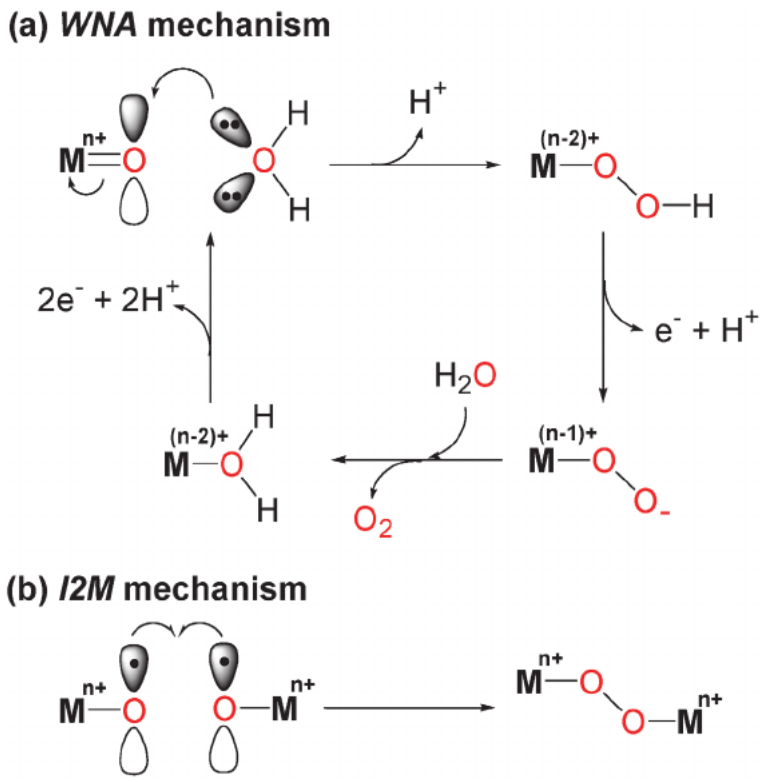

Figure 10.
Schematic representation of the two mechanistic pathways for O-O bond formation. (reproduced with permission from ref. [20]. Copyright 2019 Wiley).

deprotonation steps generate a $M^{(n-1)+}$-OO^{-} intermediate, which releases O_2 and converts to $M^{(n-2)+}$-OH_2 with incorporation of OH_2. A lot of mononuclear complexes have been proposed to undergo the *WNA* mechanism for water oxidation [21–23, 34, 35, 40, 51, 52, 57, 58]. In the *I2M* mechanism (**Figure 10b**), the coupling of either two M^{n+}-O oxyl radicals or coupling of one M^{n+}-O oxyl radical with another M^{n+}-O unit of a non-radical character affords a peroxo M^{n+}-O-O-M^{n+} intermediate, which releases O_2 and returns to 2 $M^{(n-2)+}$-OH_2 with incorporation of OH_2. It involves intramolecular [37, 59, 60] and intermolecular [61, 62] pathways.

In this section, we introduce our recent progress on chemical and electrochemical water oxidation catalyses by mono- and dinuclear ruthenium(II) aquo complexes in homogeneous systems. Firstly, substitution effects on the catalytic activity and mechanism of mononuclear ruthenium(II) aquo complexes for chemical water oxidation are described in Section 3-1. Secondly, the difference in the catalytic properties between *distal*−/*proximal*-isomers is explicated in Section 3-2. Finally, the electrocatalytic activities of a series of dinuclear ruthenium(II) complexes are discussed in Section 3-3.

3.1 Substitution effect on the catalytic activities of mononuclear ruthenium complexes for water oxidation

To investigate the catalytic aspects of $[Ru(Rtpy)(bpy)(H_2O)]^{2+}$ (Rtpy = 2,2′:6′,2″-terpyridine derivatives) complexes (**4R**) having a variety of 4′-substituent groups on Rtpy ligand (**Figure 11**), chemical water oxidation experiments were performed in a homogeneous aqueous solution using a Ce^{IV} as a

sacrificial oxidant [39, 40]. For **4EtO** (R = EtO), O_2 was significantly evolved from the catalytic solution, and the amount (n_{O2}/μmol) of O_2 evolved increased linearly until 100 min and then saturated to 35 μmol at 4 h, which is 5 times higher than that for **4H** (**Figure 12**) [39]. The initial O_2 evolution rates (v_{O2}/mol s^{-1}) were calculated from the initial slopes. The v_{O2} for **4EtO** increased with the Ce^{IV} concentration (c_{Ce}/M) and reached a saturation at c_{Ce} = 1.0 M (**Figure 13**), indicating that O_2 evolution is zero order with respect to Ce^{IV} under the large excess Ce^{IV} conditions. This behavior was well-analyzed by Michaelis–Menten-like kinetics to give the maximum catalytic rate (v_{max}) of 1.5 (±0.08) x 10^{-1} mol s^{-1} (**4EtO** mol)$^{-1}$ and the constant (K_m = 1.2 (±0.06) mmol) in terms of the Ce^{IV} concentration for the half value of v_{max}. The oxidation reaction from Ru^{IV}=O to Ru^{V}=O by Ce^{IV} could involve the redox equilibrium prior to oxygen evolution because the redox potential (1.45 V vs. SCE) of Ru^{IV}=O/Ru^{V}=O for **4EtO** is close to standard potential (E° = 1.47 V vs. SCE (1.71 V vs. NHE) [63]) of $Ce^{III/IV}$. The redox equilibrium presumably leads to saturation of the v_{O2} with increase of the Ce^{IV} concentration (**Figure 13**). The v_{O2} increased linearly with the **4EtO** concentration (c_{Ru}/M) under the large excess Ce^{IV} conditions (c_{Ce} = 0.1 M, c_{Ru} = ∼ 0.2 mM, 5.0 ml water) (**Figure 14**), showing that the O_2 evolution is a first order process with respect to **4EtO**. This result is consistent with the case of earlier-reported mononuculear Ru(II) aquo complexes [50, 51].

The mechanism of water oxidation by **4R** is shown in **Figure 15** based on the WNA mechanism [50, 51, 56]. **4R** (abbreviated to Ru^{II}-OH_2 as the oxidation state) is oxidized by Ce^{IV} to Ru^{III}-OH_2 by a 1-electron process, and subsequently oxidized to Ru^{IV}=O by two-proton/one-electron process at pH = 1.0 [39, 40]. Ru^{IV}=O is further oxidized to Ru^{V}=O, involving the above-mentioned redox equilibrium (step I, **Figure 15**). Ru^{V}=O undergoes water nucleophilic attack (step II, **Figure 15**) to

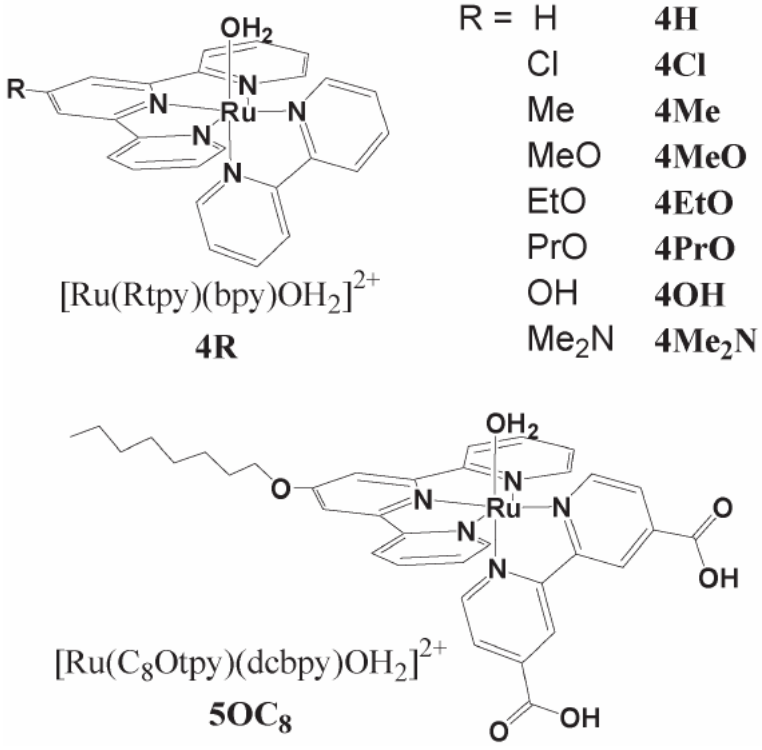

Figure 11.
Chemical structures of mononuclear ruthenium(II) aquo complexes.

DOI: http://dx.doi.org/10.5772/ITexLi.99730

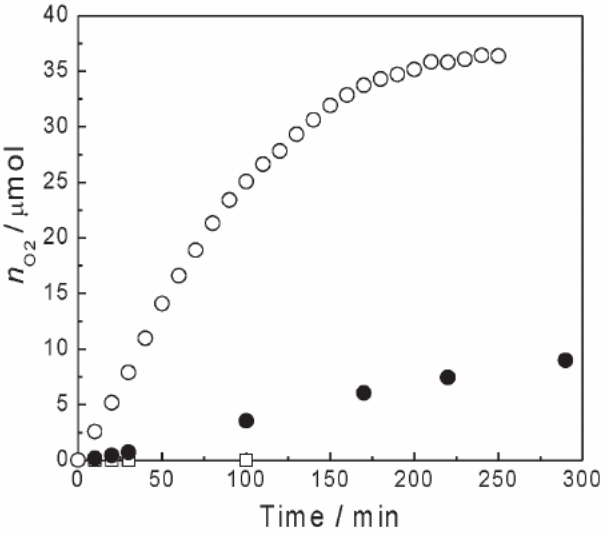

Figure 12.
*Time courses of the amount (n_{O2}/Mol) of O_2 evolved in chemical water oxidation experiments in an aqueous solution at 25°C using a Ce^{IV} oxidant. c_{Ce} = 0.1 M (0.5 mmol); complexes, 20 μM (0.1 μmol); pH = 1.0; liquid volume, 5.0 ml. (○) **4EtO**, (●) **4H** and (□) without complex. (reproduced with permission from ref. [39]. Copyright 2011 the Royal Society of Chemistry).*

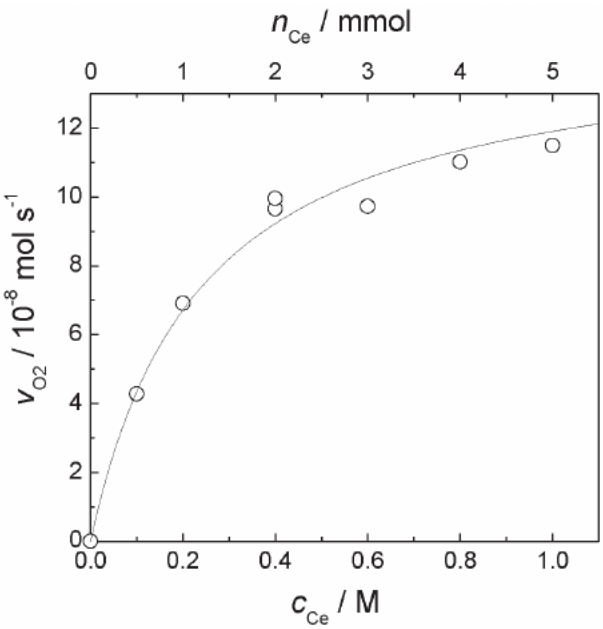

Figure 13.
*Plots of v_{O2} versus the Ce^{IV} concentration (c_{Ce}/M) in chemical water oxidation experiments using 0.2 mM **4EtO** (5.0 ml water) at 25°C. the solid line is the simulated curve based on a Michaelis–Menten-like kinetic equation. (reproduced with permission from ref. [39]. Copyright 2011 the Royal Society of Chemistry).*

form an O-O bond in the Ru^{III}-OOH intermediate. Finally, O_2 is produced via further oxidation to Ru^{IV}-OO^-, with Ru^{II}-OH_2 regenerated by incorporation of water.

The v_{O2} showed a first-order dependence on the complex amount for all the **4R** derivatives (**Figure 14**) [40], suggesting that O_2 is produced by a unimolecular

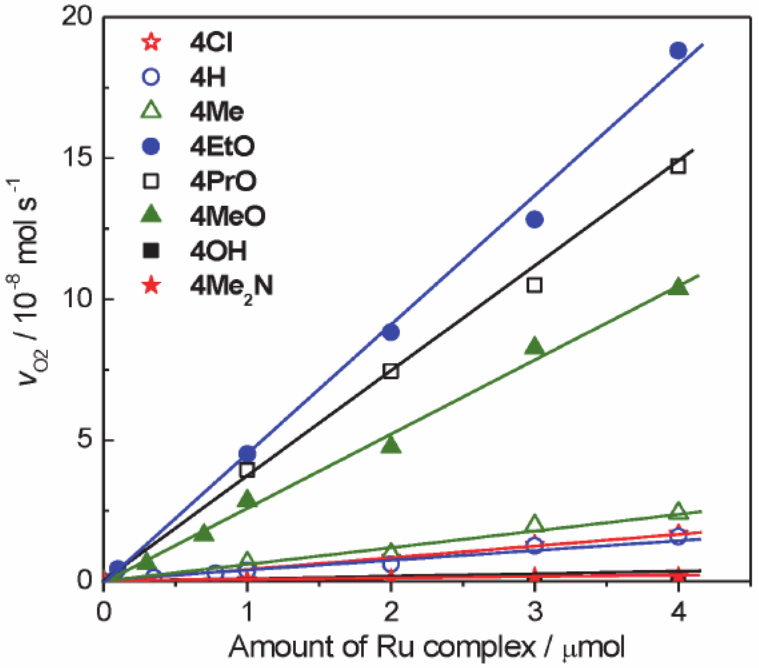

Figure 14.
*Plots of initial O_2 evolution rate (v_{O2}/Mol s^{-1}) versus the amount of **4R** complexes. c_{Ce}= 0.1 M, 5.0 ml water, pH = 1.0. (reproduced with permission from ref. [40]. Copyright 2019 American Chemical Society).*

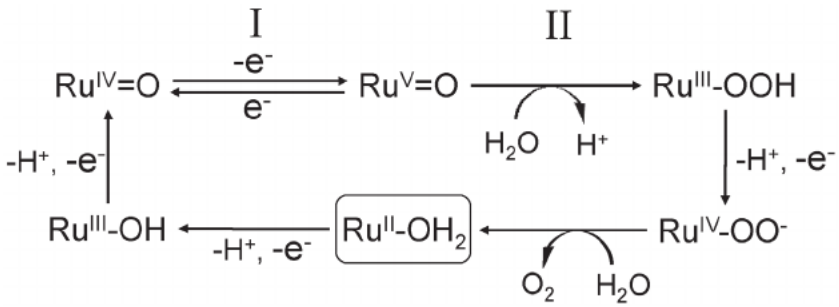

Figure 15.
*Mechanism of water oxidation by **4R** complexes at pH = 1.0. (reprinted with permission from ref. [40]. Copyright 2019 American Chemical Society).*

reaction of **4R**. Turnover frequencies (k_{O2}/s^{-1}) were calculated from the slopes of the linear relationships. The k_{O2} values were largely affected by the Rtpy ligands, being variable from 0.05 to 44 x 10^{-2} s^{-1} (as the highest k_{O2} for **4EtO**) by a factor of 880 (**Table 2**). The k_{O2} values were plotted with respect to Hammett constant σ_p of the 4′-substituents of Rtpy ligands in **Figure 16A**. However, the Me_2N group is protonated to give Me_2NH^+ under the catalytic conditions (pH = 1.0), and the σ_p value of Me_2NH^+ was assumed as σ_p = 0.71 of the midpoint between σ_p = 0.60 for protonated amino group and σ_p = 0.82 for protonated trimethylamino group [64]. The k_{O2} values were almost constant (3.4 ~ 6.1 x 10^{-2} s^{-1}) in a range of σ_p = −0.17 (R = Me) ~ 0.23 (R = Cl), although the k_{O2} value (5 x 10^{-4} s^{-1}) of **4Me$_2$N** is lower than these values. The k_{O2} value increased sharply at σ_p = −0.24 (R = EtO) to 4.4 x10^{-1} s^{-1} as the maximum, and thereafter decreased with the σ_p decrease to −0.37 (R = OH). This result demonstrates that very critical Hammett constant

Complexes	Abbreviation	$k_{O2}/10^{-3}$ s^{-1}	Ref
$[Ru(tpy)(bpy)OH_2]^{2+}$	**4H**	34	[39]
$[Ru(Cltpy)(bpy)OH_2]^{2+}$	**4Cl**	43	[40]
$[Ru(Metpy)(bpy)OH_2]^{2+}$	**4Me**	61	[40]
$[Ru(MeOtpy)(bpy)OH_2]^{2+}$	**4MeO**	240	[40]
$[Ru(EtOtpy)(bpy)OH_2]^{2+}$	**4EtO**	440	[40]
$[Ru(PrOtpy)(bpy)OH_2]^{2+}$	**4PrO**	331	[40]
$[Ru(OHtpy)(bpy)OH_2]^{2+}$	**4OH**	0.9	[40]
$[Ru(Me_2Ntpy)(bpy)OH_2]^{2+}$	**4Me$_2$N**	0.5	[40]
distal-$[Ru(tpy)(pynp)OH_2]^{2+}$	*d*-**1**	3.8	[21]
proximal-$[Ru(tpy)(pynp)OH_2]^{2+}$	*p*-**1**	0.48	[21]
distal-$[Ru(Cltpy)(pynp)OH_2]^{2+}$	*d*-**1Cl**	6.3	[35]
proximal-$[Ru(Cltpy)(pynp)OH_2]^{2+}$	*p*-**1Cl**	0.39	[35]
distal-$[Ru(tpy)(pyqu)OH_2]^{2+}$	*d*-**2**	1.0	[34]
proximal-$[Ru(tpy)(pyqu)OH_2]^{2+}$	*p*-**2**	1.7	[34]

Table 2.
Summary of k_{O2} *by mononuclear Ru(II) aquo complexes.*

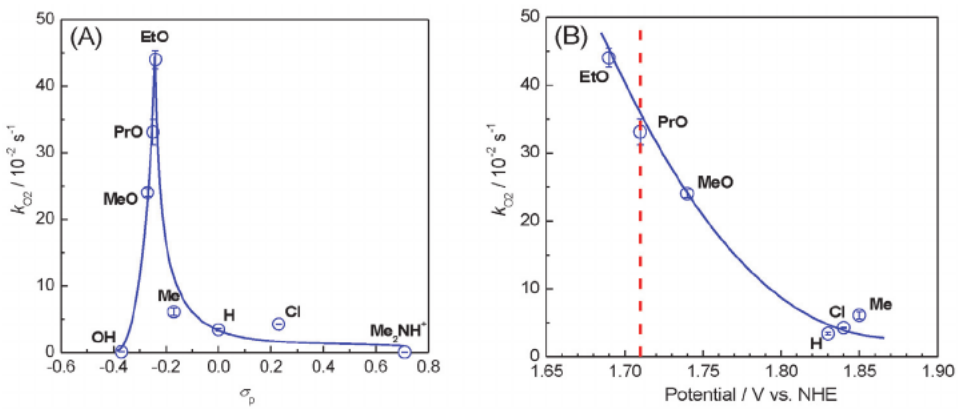

Figure 16.
Plots of the turnover frequency (k_{O2}/s^{-1}) versus *Hammett constant* (σ_p) *of 4′-substituent groups (A) and* versus *the redox potentials of a* Ru^{IV}=O/Ru^{V}=O *pair (B). The* Me_2N *group is protonated to a* Me_2NH^+ *group under the experimental conditions for water oxidation (pH = 1.0), and the* σ_p *value of* Me_2NH^+ *was assumed as* $\sigma_p = 0.71$ *of the midpoint between* $\sigma_p = 0.60$ *for protonated amino group and* $\sigma_p = 0.82$ *for protonated trimethylamino group [64]. The redox potentials were estimated from* E_{ap} *values, where* E_{ap} *is an anodic peak potential corresponding to the* Ru^{IV}=O/Ru^{V}=O *couple in a cyclic voltammogram for each of* ***4R*** *complexes. The red dashed line indicates the standard redox potential of* $Ce^{III/IV}$ *[63]. (Reproduced with permission from ref. [40]. Copyright 2019 American Chemical Society).*

($\sigma_p = -0.27 \sim -0.24$) exists for the high k_{O2} values. The very low k_{O2} values for **4OH** and **4Me$_2$N** arise from the difficulty of Ru^{V}=O formation. Most likely, **4OH** and **4Me$_2$N** are considered to decompose through their ligand oxidation during water oxidation catalysis, as reported recently [65, 66].

The k_{O2} values were plotted with respect to redox potentials of Ru^{IV}=O/Ru^{V}=O in **Figure 16B**. The k_{O2} values increased with the decrease of the redox potentials in an order of **4H**, **4Cl**, **4Me** < **4MeO** < **4PrO** < **4EtO**. This indicates that the potential for formation of Ru^{V}=O species is essential in the water oxidation catalysis under the employed conditions. This k_{O2} profile can be explained by the increased

fraction of Ru^{V}=O in the equilibrium. In this case, the oxidation rate (step I in **Figure 15**) from Ru^{IV}=O to Ru^{V}=O by Ce^{IV} could be comparable with the rate of the nucleophilic attack of water on Ru^{V}=O (step II in **Figure 15**) to be involved in a rate-determining step. The O-O bond formation process *via* water nucleophilic attack could be no longer a rate-determining step singularly. One might deservedly expect that the k_{O2} values of **4H**, **4Cl**, and **4Me** with the higher redox potentials of Ru^{IV}=O/Ru^{V}=O are higher than those of **4MeO**, **4PrO** and **4EtO** with the lower redox potentials since water nucleophilic attack on Ru^{V}=O (step II, **Figure 15**) is assumed to accelerate because of the higher electrophilicity of the oxo of Ru^{V}=O for the formers. By contrast, the k_{O2} values of **4H**, **4Cl**, and **4Me** were indeed lower than those of **4MeO**, **4PrO** and **4EtO**, which could be explained by the slow oxidation rate (step I in **Figure 15**) from Ru^{IV}=O to Ru^{V}=O involved in a rate-determining step.

3.2 Comparison in catalytic activities between *distal* and *proximal* isomers of mononuclear ruthenium complexes

To explore the catalytic aspects of a series of *distal* and *proximal* isomers for the mononuclear Ru(II) aquo complexes, chemical water oxidation experiments were conducted in a homogeneous aqueous solution using a Ce^{IV} oxidant [21, 22]. O_2 was significantly evolved from a mixed solution of *d*-**1** and Ce^{IV}, and n_{O2} increased linearly with time until 50 min (**Figure 17**). v_{O2} increased linearly with respect to the amount of the complex, and the slope of the linear relationship provides k_{O2} = 3.8 x 10^{-3} s^{-1} (**Figure 18**). The same chemical water oxidation experiments were carried out after visible light irradiation to the solution of *d*-**1** for 1 h to generate *p*-**1** completely (**Figure 1**). n_{O2} dramatically decreased compared with the case before light irradiation (**Figure 17**). The linear plot of v_{O2} with the catalyst

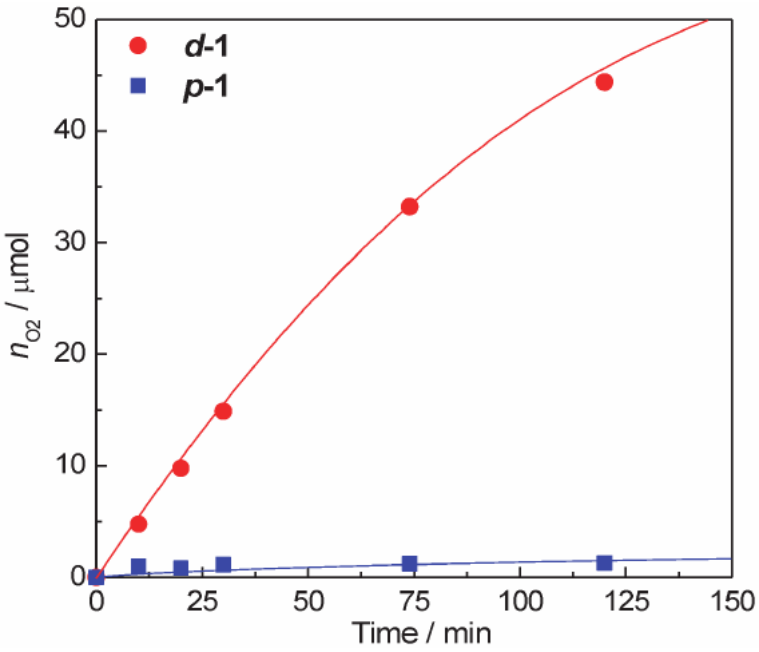

Figure 17.
*Time courses of the amount (n_{O2}/μmol) of O_2 evolved in chemical water oxidation experiments in an aqueous solution at 25 °C using a Ce^{IV} as a sacrificial oxidant. c_{Ce} = 0.1 M (0.5 mmol); Ru complex, 1.0 μmol; pH = 1.0; liquid volume, 5.0 ml. (●) d-**1**, (■) p-**1**. (Reproduced with permission from ref. [21]. Copyright 2011 American Chemical Society).*

amount provided k_{O2} = 4.8 x 10^{-4} s^{-1} for *p*-**1**, indicating that the observed k_{O2} value is decreased due to photoisomerization of *d*-**1** to *p*-**1** by nearly an order of magnitude. This result tells us that we have to pay attention to the observed catalytic activity decrease due to photoisomerization of *d*-**1** to *p*-**1** when *d*-**1** is applied to photocatalytic systems.

The chemical water oxidation catalyzed by *d*-**1Cl** and *p*-**1Cl** was investigated under the same conditions as the *d*−/*p*-**1** isomer system to understand the effect of 4′-chloro-substitusion on tpy ligand on the catalytic activity of the *distal*−/*proximal*-isomer complexes for water oxidation [35]. v_{O2} increased linearly with respect to the complex amount for *d*-**1Cl** and *p*-**1Cl**, as is the case of the *d*−/*p*-**1** isomer system (**Figure 18**). k_{O2} (6.3×10^{-3} s^{-1}) for *d*-**1Cl** was 15 times higher than that (3.9×10^{-4} s^{-1}) for *p*-**1Cl**. From a perspective of the effect of the chloro-substitution on tpy, k_{O2} for *d*-**1Cl** was also 1.6 times higher that (3.8×10^{-3} s^{-1}) for *d*-**1**, while k_{O2} for *p*-**1Cl** was 1.2 times lower than that (4.8×10^{-4} s^{-1}) for *p*-**1**. If assuming that the O-O bond formation *via* the nucleophilic attack of water on the Ru^{V}=O intermediate is the rate-determining step, k_{O2} could increase by the chloro substitution because electrophilicity of Ru^{V}=O increased, as is the case for *d*-**1Cl** relative to *d*-**1**. However, another explanation is needed for the k_{O2} decrease for *p*-**1Cl** relative to *p*-**1**. For instance, there are cases that the rate for oxidation of Ru^{IV}=O to Ru^{V}=O could be involved in a rate-determining step, or that the stabilities of the complexes are different, as pointed out in the Section 3-1.

The k_{O2} value (1.7×10^{-3} s^{-1}) of *p*-**2** was higher than that (1.0×10^{-3} s^{-1}) of *d*-**2** by a factor of 1.7 (**Table 2**) [34]. This result is in contrast to the *d*−/*p*-**1** and *d*−/*p*-**1Cl** isomer systems, in which k_{O2} of *distal*-isomers are higher than those of the *proximal*-ones by one order of magnitude. The k_{O2} value of *p*-**2** is 3.5 times higher

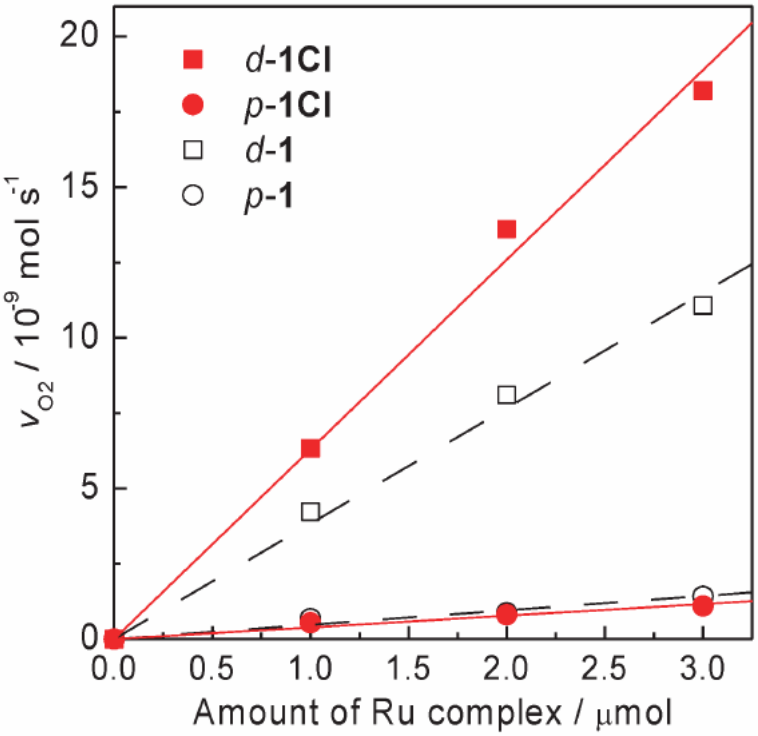

Figure 18.
Plots of initial rate (v_{O2} / mol s^{-1}) of O_2 evolved vs. the amount (μmol) of d-***1Cl*** (■), p-***1Cl*** (●), d-***1*** (□), p-***1*** (○). *Conditions:* c_{Ce} *= 0.1 M (0.5 mmol); liquid volume, 5.0 mL; pH = 1.0. (reproduced with permission from ref. [35]. Copyright 2015 Elsevier).*

than that (4.8×10^{-4} s^{-1}) of *p*-**1**, though the value of *d*-**2** is 3.8 times lower than that (3.8×10^{-3} s^{-1}) of *p*-**2** under the same conditions.

3.3 Electrocatalytic activities of a series of dinuclear ruthenium complexes for water oxidation

We investigated catalytic activities of *p*,*p*-**$Ru_2(OH)(OH_2)$** and the related mono- and dinuclear Ru(II) complexes (**Figures 8** and **9**) for electrochemical water oxidation in homogeneous solution [37]. The cyclic voltammogram (CV) of *p*,*p*-**$Ru_2(OH)(OH_2)$** displayed a higher anodic current after 1.2 V vs. SCE attributed to water oxidation (**Figure 19**). The catalytic current density increased to 3.5 mA cm^{-2} (the blank without the complex generates 0.31 mA cm^{-2}) at a potential of 1.4 V and pH 6.0, that is 4.8 and 9.2 times higher compared to those of *d*-**3** and *p*,*p*-**$Ru_2(\mu$-Cl)**. Importantly, the current density value (3.5 mA cm^{-2} at pH 6.0) obtained from *p*,*p*-**$Ru_2(OH)(OH_2)$** was much higher than that (1.4 mA cm^{-2} at pH 9.0) obtained for *p*,*p*-**$Ru_2(\mu$-OH)**, under even thermodynamically unfavorable pH conditions. These results suggest that the *proximal*,*proximal*-dinuclear Ru(II) core structure with vicinal aquo and hydroxo groups is inevitably essential for efficient electrocatalytic water oxidation. Bulk electrolysis was performed in a nearly neutral phosphate buffer solution (pH 6.0) for *p*,*p*-**$Ru_2(OH)(OH_2)$** at 1.3 V vs. SCE. A higher charge amount of 2.1 C compared to the that (0.55 C) of the blank without the complex was obtained, and a 4.2 μmol (Faradaic efficiency 76–80%) of O_2 was

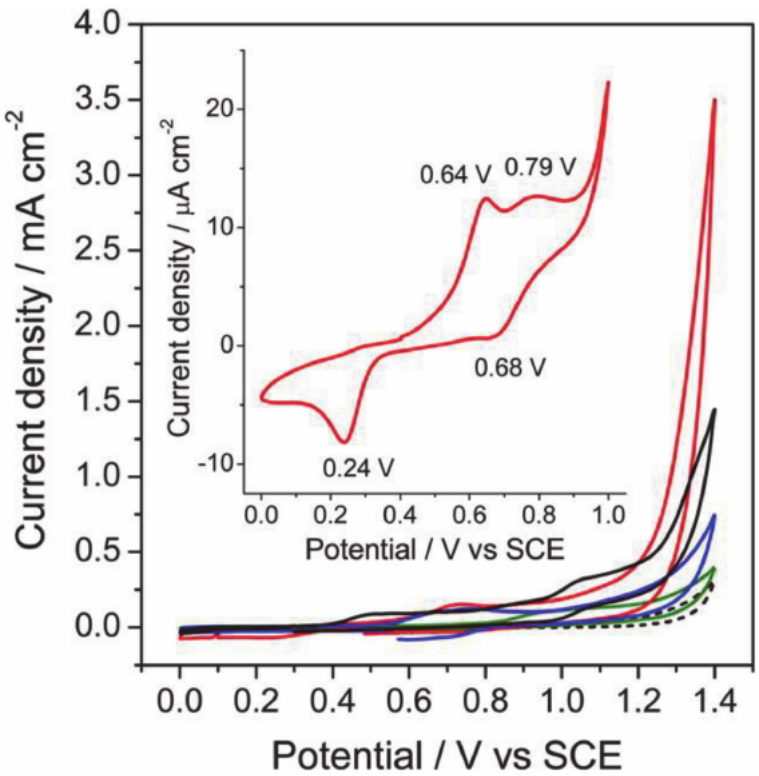

Figure 19.
CVs of 1 mM p,p-***$Ru_2(OH)(OH_2)$*** *(red),* d-*3 (blue),* p,p-***$Ru_2(\mu$-Cl)*** *(green), and blank (black dots) in a 0.1 M phosphate buffer (pH 6.0) at a scan rate of 50 mV* s^{-1}. *CV of* p,p-***$Ru_2(\mu$-OH)*** *(black) was measured at pH 9.0 because it gradually converts to* p,p-***$Ru_2(\mu$-Cl)*** *at acidic conditions. Inset shows CV of 0.5 mM* p,p-***$Ru_2(OH)(OH_2)$*** *in a 0.1 M phosphate buffer (pH 7.0) at a scan rate of 20 mV* s^{-1}. *(Reprinted with permission from ref. [37] with permission of American Chemical Society).*

produced after 1 h electrolysis. This evolved O_2 amount obtained by ***p*,*p*-Ru$_2$(OH)(OH$_2$)** corresponds to 5.3 equivalent of the total ***p*,*p*-Ru$_2$(OH)(OH$_2$)** amount (0.6 μmol) in the electrolyte solution, ensuring the catalytic water oxidation. The UV–Visible absorption spectrum of the electrolyte solution after the electrolysis displayed an intense band at 694 nm, assigned to *proximal*,*proximal*-$[Ru^{III}_2(tpy)_2L(OH)_2]^{4+}$ (abbreviated to Ru^{III}-OH:Ru^{III}-OH as a oxidation state). This observation suggests that Ru^{III}-OH:Ru^{III}-OH is involved in the catalytic cycle. For the proposed electrocatalytic cycle for water oxidation under neutral conditions, ***p*,*p*-Ru$_2$(OH)(OH$_2$)** was electrochemically oxidized by the proton-coupled electron transfer reactions *via* Ru^{III}-OH:Ru^{III}-OH and Ru^{IV}=O:Ru^{IV}–OH states most possibly to the Ru^{V}=O:Ru^{V}=O state, which could oxidize water to O_2 together with the regeneration of Ru^{III}-OH:Ru^{III}-OH.

In order to provide mechanistic insights into O–O bond formation for O_2 production, the H/D isotope effect on electrocatalytic water oxidation by ***p*,*p*-Ru$_2$(OH)(OH$_2$)** and ***d*-3** were examined in H_2O and D_2O media. A large H/D isotope effect (1.7) on electrocatalytic water oxidation by ***d*-3** was observed relative to the blank experiment (1.1). This result is consistent with the proton transfer-concerted O–O bond formation by the *WNA* mechanism. On the other hand, the isotopic effect (1.1) on the electrocatalysis by ***p*,*p*-Ru$_2$(OH)(OH$_2$)** was comparable with the blank (1.1). The lower isotope effect indicates proton-non-concerted chemical reaction process in the electrocatalytic cycle, and ***p*,*p*-Ru$_2$(OH)(OH$_2$)** is likely to produce O_2 *via* the *I2M* mechanism.

4. Conclusions

Recent progress on the aspects and mechanistic insights of photoisomerization of Ru(II) aquo complexes in our group was reviewed to unveil the photoisomerization reactions and its mechanism comprehensively. The controls of properties and functions of mononuclear Ru(II) aquo complexes by the photoisomerization were exemplified in terms of their water oxidation catalyses. An example of application of the photoisomerization is demonstrated; the employment of the photoisomerization enabled to synthesize the dinuclear Ru(II) complexes that have been difficult to be synthesized by conventional thermochemical processes. The synthesized dinuclear complexes also serve as efficient catalysts for water oxidation. New design and development of variety types of Ru complexes are desired to explore unique reactions, functions and application based on the photoisomerization for future molecular systems such as artificial photosynthetic devices.

References

[1] Thompson DW, Ito A, Meyer TJ. [Ru(bpy)$_3$]$^{2+*}$ and other remarkable metal-to-ligand charge transfer (MLCT) excited states. Pure Appl Chem 2013;85:1257–1305. https://doi.org/10.1351/PAC-CON-13-03-04.

[2] Kinoshita T, Dy JT, Uchida S, Kubo T, Segawa H. Wideband dye-sensitized solar cells employing a phosphine-coordinated ruthenium sensitizer. Nat Photonics 2013;7:535–539. https://doi.org/10.1038/nphoton.2013.136.

[3] Caspar J V., Meyer TJ. Photochemistry of tris(2,2′-bipyridine) ruthenium(2+) ion (Ru(bpy)$_3^{2+}$). Solvent effects. J Am Chem Soc 1983;105:5583–5590. https://doi.org/10.1021/ja00355a009.

[4] Hammarström L, Johansson O. Expanded bite angles in tridentate ligands. Improving the photophysical properties in bistridentate Ru^{II} polypyridine complexes. Coord Chem Rev 2010;254:2546–2559. https://doi.org/10.1016/j.ccr.2010.01.006.

[5] Winkler JR, Netzel TL, Creutz C, Sutin N. Direct Observation of Metal-to-Ligand Charge-Transfer (MLCT) Excited States of Pentaammineruthenium(II) Complexes. J Am Chem Soc 1987;109:2381–2392. https://doi.org/10.1021/ja00242a023.

[6] Abrahamsson M, Jäger M, Kumar RJ, Österman T, Persson P, Becker H-C, et al. Bistridentate Ruthenium (II)polypyridyl-Type Complexes with Microsecond ^{3}MLCT State Lifetimes: Sensitizers for Rod-Like Molecular Arrays. J Am Chem Soc 2008;130:15533–15542. https://doi.org/10.1021/ja804890k.

[7] Rillema DP, Allen G, Meyer TJ, Conrad D. Redox properties of ruthenium(II) tris chelate complexes containing the ligands 2,2′-bipyrazine, 2,2′-bipyridine, and 2,2′-bipyrimidine. Inorg Chem 1983;22:1617–1622. https://doi.org/10.1021/ic00153a012.

[8] Juris A, Balzani V, Barigelletti F, Campagna S, Belser P, von Zelewsky A. Ru(II) polypyridine complexes: photophysics, photochemistry, eletrochemistry, and chemiluminescence. Coord Chem Rev 1988;84:85–277. https://doi.org/10.1016/0010-8545(88)80032-8.

[9] Moon HC, Lodge TP, Frisbie CD. Solution-processable electrochemiluminescent ion gels for flexible, low-voltage, emissive displays on plastic. J Am Chem Soc 2014;136:3705–3712. https://doi.org/10.1021/ja5002899.

[10] Banasz R, Wałęsa-Chorab M. Polymeric complexes of transition metal ions as electrochromic materials: Synthesis and properties. Coord Chem Rev 2019;389:1–18. https://doi.org/10.1016/j.ccr.2019.03.009.

[11] Weinberg DR, Gagliardi CJ, Hull JF, Murphy CF, Kent CA, Westlake BC, et al. Proton-Coupled Electron Transfer. Chem Rev 2012;112:4016–4093. https://doi.org/10.1021/cr200177j.

[12] Pannwitz A, Wenger OS. Proton coupled electron transfer from the excited state of a ruthenium(ii) pyridylimidazole complex. Phys Chem Chem Phys 2016;18:11374–11382. https://doi.org/10.1039/c6cp00437g.

[13] Okamura M, Yoshida M, Kuga R, Sakai K, Kondo M, Masaoka S. A mononuclear ruthenium complex showing multiple proton-coupled electron transfer toward multi-electron transfer reactions. Dalton Trans 2012;41:13081–13089. https://doi.org/10.1039/c2dt30773a.

[14] Nicewicz DA, MacMillan DWC. Merging photoredox catalysis with organocatalysis: The direct asymmetric alkylation of aldehydes. Science (80-) 2008;322:77–80. https://doi.org/10.1126/science.1161976.

[15] Troian-Gautier L, Turlington MD, Wehlin SAM, Maurer AB, Brady MD, Swords WB, et al. Halide Photoredox Chemistry. Chem Rev 2019;119:4628–4683. https://doi.org/10.1021/acs.chemrev.8b00732.

[16] Poynton FE, Bright SA, Blasco S, Williams DC, Kelly JM, Gunnlaugsson T. The development of ruthenium(II) polypyridyl complexes and conjugates for: In vitro cellular and in vivo applications. Chem Soc Rev 2017;46:7706–7756. https://doi.org/10.1039/c7cs00680b.

[17] O'Regan B, Grätzel M. A low-cost, high-efficiency solar cell based on dye-sensitized colloidal TiO_2 films. Nature 1991;353:737–740. https://doi.org/10.1038/353737a0.

[18] Buda M, Kalyuzhny G, Bard AJ. Thin-Film Solid-State Electroluminescent Devices Based On Tris(2,2′-bipyridine) ruthenium(II) Complexes. J Am Chem Soc 2002;124:6090–6098. https://doi.org/10.1021/ja017834h.

[19] Concepcion JJ, House RL, Papanikolas JM, Meyer TJ. Chemical approaches to artificial photosynthesis. Proc Natl Acad Sci 2012;109:15560–15564. https://doi.org/10.1073/pnas.1212254109.

[20] Zahran ZN, Tsubonouchi Y, Mohamed EA, Yagi M. Recent Advances in the Development of Molecular Catalyst-Based Anodes for Water Oxidation toward Artificial Photosynthesis. ChemSusChem 2019;12:1775–1793. https://doi.org/10.1002/cssc.201802795.

[21] Yamazaki H, Hakamata T, Komi M, Yagi M. Stoichiometric photoisomerization of mononuclear ruthenium(II) monoaquo complexes controlling redox properties and water oxidation catalysis. J Am Chem Soc 2011;133:8846–8849. https://doi.org/10.1021/ja2024228.

[22] Hirahara M, Ertem MZ, Komi M, Yamazaki H, Cramer CJ, Yagi M. Mechanisms of photoisomerization and water-oxidation catalysis of mononuclear ruthenium(II) monoaquo complexes. Inorg Chem 2013;52:6354–6364. https://doi.org/10.1021/ic400054k.

[23] Hirahara M, Yagi M. Photoisomerization of ruthenium(II) aquo complexes: mechanistic insights and application development. Dalton Trans 2017;46:3787–3799. https://doi.org/10.1039/C7DT00079K.

[24] Durham B, Wilson SR, Hodgson DJ, Meyer TJ. Cis-Trans Photoisomerization in $Ru(bpy)_2(OH_2)_2^{2+}$. Crystal Structure of trans-$[Ru(bpy)_2(OH_2)(OH)](ClO_4)_2$. J Am Chem Soc 1980;102:600–607. https://doi.org/10.1021/ja00522a026.

[25] Durham B, Walsh JL, Carter CL, Meyer TJ. Synthetic Applications of Photosubstitution Reactions of Poly (Pyridyl) Complexes of Ruthenium(II). Inorg Chem 1980;19:860–865. https://doi.org/10.1021/ic50206a014.

[26] Pinnick D V., Durham B. Photosubstitution reactions of $Ru(bpy)_2XY^{n+}$ complexes. Inorg Chem 1984;23:1440–1445. https://doi.org/10.1021/ic00178a028.

[27] Hecker CR, Fanwick PE, McMillin DR. Evidence for Dissociative Photosubstitution Reactions of $[Ru(trpy)(bpy)(NCCH_3)]^{2+}$. Crystal and Molecular Structure of $[Ru(trpy)(bpy)(py)](PF_6)_2 \bullet (CH_3)_2CO$. Inorg Chem 1991;30:659–666. https://doi.org/10.1021/ic00004a013.

[28] Howerton BS, Heidary DK, Glazer EC. Strained ruthenium

complexes are potent light-activated anticancer agents. J Am Chem Soc 2012; 134:8324–8327. https://doi.org/10.1021/ja3009677.

[29] Albani BA, Peña B, Leed NA, De Paula NABG, Pavani C, Baptista MS, et al. Marked improvement in photoinduced cell death by a new tris-heteroleptic complex with dual action: Singlet oxygen sensitization and ligand dissociation. J Am Chem Soc 2014;136: 17095–17101. https://doi.org/10.1021/ja508272h.

[30] Porter GB, Sparks RH. Photoracemization of Ru (Bipyridine)$_3^{2+}$. J Photochem 1980;13:123–131. https://doi.org/10.1016/0047-2670(80)85004-0.

[31] Rachford AA, Rack JJ. Picosecond isomerization in photochromic ruthenium - Dimethyl sulfoxide complexes. J Am Chem Soc 2006;128: 14318–14324. https://doi.org/10.1021/ja0641305.

[32] Miyazaki S, Kojima T, Fukuzumi S. Photochemical and thermal isomerization of a ruthenium(II)-alloxazine complex involving an unusual coordination mode. J Am Chem Soc 2008;130:1556–1557. https://doi.org/10.1021/ja077954a.

[33] Bonnet S, Limburg B, Meeldijk JD, Gebbink RJMK, Killian JA. Ruthenium-decorated lipid vesicles: Light-induced release of [Ru(terpy)(bpy)(OH_2)]$^{2+}$ and thermal back coordination. J Am Chem Soc 2011;133:252–261. https://doi.org/10.1021/ja105025m.

[34] Hirahara M, Hakamata T, League AB, Ertem MZ, Takahashi K, Nagai S, et al. Mechanisms and Factors Controlling Photoisomerization Equilibria, Ligand Exchange, and Water Oxidation Catalysis Capabilities of Mononuclear Ruthenium(II) Complexes. Eur J Inorg Chem 2015; 2015:3892–3903. https://doi.org/10.1002/ejic.201500642.

[35] Takahashi K, Zhang X, Hirahara M, Sato T, Saito K, Yui T, et al. Influence of chloro substituent on photoisomerization, redox reactions and water oxidation catalysis of mononuclear ruthenium complexes. J Photochem Photobiol A Chem 2015;313: 117–125. https://doi.org/10.1016/j.jphotochem.2015.05.029.

[36] Tanaka S, Takahashi K, Hirahara M, Yagi M, Onda K. Characterization of the excited states of distal- and proximal-[Ru(tpy)(pynp)OH_2]$^{2+}$ in aqueous solution using time-resolved infrared spectroscopy. J Photochem Photobiol A Chem 2015;313:87–98. https://doi.org/10.1016/j.jphotochem.2015.06.018.

[37] Hirahara M, Nagai S, Takahashi K, Saito K, Yui T, Yagi M. New Series of Dinuclear Ruthenium(II) Complexes Synthesized Using Photoisomerization for Efficient Water Oxidation Catalysis. Inorg Chem 2015;54:7627–7635. https://doi.org/10.1021/acs.inorgchem.5b01264.

[38] Hirahara M, Nagai S, Takahashi K, Watabe S, Sato T, Saito K, et al. Mechanistic Insight into Reversible Core Structural Changes of Dinuclear μ-Hydroxoruthenium(II) Complexes with a 2,8-Di-2-pyridyl-1,9,10-anthyridine Backbone Prior to Water Oxidation Catalysis. Inorg Chem 2017;56:10235–10246. https://doi.org/10.1021/acs.inorgchem.7b00978.

[39] Yagi M, Tajima S, Komi M, Yamazaki H. Highly active and tunable catalysts for O_2 evolution from water based on mononuclear ruthenium(ii) monoaquo complexes. Dalton Trans 2011;40:3802. https://doi.org/10.1039/c0dt01826k.

[40] Watabe S, Tanahashi Y, Hirahara M, Yamazaki H, Takahashi K, Mohamed EA, et al. Critical Hammett Electron-Donating Ability of Substituent Groups for Efficient Water Oxidation Catalysis by Mononuclear

Ruthenium Aquo Complexes. Inorg Chem 2019;58:12716–12723. https://doi.org/10.1021/acs.inorgchem.9b01623.

[41] Planas N, Vigara L, Cady C, Miró P, Huang P, Hammarström L, et al. Electronic Structure of Oxidized Complexes Derived from cis-$[Ru^{II}(bpy)_2(H_2O)_2]^{2+}$ and Its Photoisomerization Mechanism Inorg Chem 2011;50:11134–42. https://doi.org/10.1021/ic201686c.

[42] Allsopp SR, Cox A, Kemp TJ, Reed WJ. Inorganic photophysics in solution. Part 1.—Temperature activation of decay processes in the luminescence of tris(2,2′-bipyridine) ruthenium(II) and tris(1,10-phenanthroline)ruthenium(II) ions. J Chem Soc Faraday Trans 1 1978;74:1275–89. https://doi.org/10.1039/f19787401275.

[43] Durham B, Caspar J V, Nagle JK, Meyer TJ. Photochemistry of $Ru(bpy)_3^{2+}$. J Am Chem Soc 1982;104:4803–4810. https://doi.org/10.1021/ja00382a012.

[44] Norrby T, Börje A, Åkermark B, Hammarström L, Alsins J, Lashgari K, et al. Synthesis, Structure, and Photophysical Properties of Novel Ruthenium(II) Carboxypyridine Type Complexes. Inorg Chem 1997;36:5850–5858. https://doi.org/10.1021/ic9705812.

[45] Li C, Hoffman MZ. Electron Localization or Delocalization in the MLCT Excited States of $Ru(bpy)_3^{2+}$ and $Ru(phen)_3^{2+}$. Consequences to Their Photochemistry and Photophysics in Fluid Solution. Inorg Chem 1998;37:830–832. https://doi.org/10.1021/ic970959w.

[46] Caspar J V, Kober EM, Sullivan BP, Meyer TJ. Application of the energy gap law to the decay of charge-transfer excited states. J Am Chem Soc 1982;104:630–632. https://doi.org/10.1021/ja00366a051.

[47] Caspar J V., Meyer TJ. Application of the energy gap law to nonradiative, excited-state decay. J Phys Chem 1983;87:952–957. https://doi.org/10.1021/j100229a010.

[48] Kober EM, Caspar J V., Lumpkin RS, Meyer TJ. Application of the energy gap law to excited-state decay of osmium(II)-polypyridine complexes: Calculation of relative nonradiative decay rates from emission spectral profiles. J Phys Chem 1986;90:3722–3734. https://doi.org/10.1021/j100407a046.

[49] Li S, Cooper VR, Thonhauser T, Puzder A, Langreth DC. A Density Functional Theory Study of the Benzene−Water Complex. J Phys Chem A 2008;112:9031–9036. https://doi.org/10.1021/jp801693p.

[50] Masaoka S, Sakai K. Clear Evidence Showing the Robustness of a Highly Active Oxygen-evolving Mononuclear Ruthenium Complex with an Aqua Ligand. Chem Lett 2009;38:182–183. https://doi.org/10.1246/cl.2009.182.

[51] Concepcion JJ, Jurss JW, Templeton JL, Meyer TJ. One site is enough. Catalytic water oxidation by $[Ru(tpy)(bpm)(OH_2)]^{2+}$ and $[Ru(tpy)(bpz)(OH_2)]^{2+}$. J Am Chem Soc 2008;130:16462–16463. https://doi.org/10.1021/ja8059649.

[52] Wasylenko DJ, Ganesamoorthy C, Henderson MA, Koivisto BD, Osthoff HD, Berlinguette CP. Electronic modification of the $[Ru^{II}(tpy)(bpy)(OH_2)]^{2+}$ scaffold: Effects on catalytic water oxidation. J Am Chem Soc 2010;132:16094–16106. https://doi.org/10.1021/ja106108y.

[53] Meyer TJ, Sheridan M V., Sherman BD. Mechanisms of molecular water oxidation in solution and on oxide surfaces. Chem Soc Rev 2017;46:6148–6169. https://doi.org/10.1039/C7CS00465F.

[54] Kärkäs MD, Verho O, Johnston E V., Åkermark B. Artificial Photosynthesis: Molecular Systems for Catalytic Water Oxidation. Chem Rev 2014;114: 11863–12001. https://doi.org/10.1021/cr400572f.

[55] Garrido-Barros P, Gimbert-Suriñach C, Matheu R, Sala X, Llobet A. How to make an efficient and robust molecular catalyst for water oxidation. Chem Soc Rev 2017;46:6088–6098. https://doi.org/10.1039/c7cs00248c.

[56] Shaffer DW, Xie Y, Concepcion JJ. O–O bond formation in ruthenium-catalyzed water oxidation: single-site nucleophilic attack vs. O–O radical coupling. Chem Soc Rev 2017;46:6170–6193. https://doi.org/10.1039/C7CS00542C.

[57] Matheu R, Ertem MZ, Benet-Buchholz J, Coronado E, Batista VS, Sala X, et al. Intramolecular Proton Transfer Boosts Water Oxidation Catalyzed by a Ru Complex. J Am Chem Soc 2015;137:10786–10795. https://doi.org/10.1021/jacs.5b06541.

[58] Schulze M, Kunz V, Frischmann PD, Würthner F. A supramolecular ruthenium macrocycle with high catalytic activity for water oxidation that mechanistically mimics photosystem II. Nat Chem 2016;8:576–583. https://doi.org/10.1038/nchem.2503.

[59] Wada T, Ohtsu H, Tanaka K. Catalytic four-electron oxidation of water by intramolecular coupling of the oxo ligands of a bis(ruthenium-bipyridine) complex. Chem - A Eur J 2012;18:2374–2381. https://doi.org/10.1002/chem.201102236.

[60] Romain S, Bozoglian F, Sala X, Llobet A. Oxygen-oxygen bond formation by the Ru-Hbpp water oxidation catalyst occurssolely via an intramolecular reaction pathway. J Am Chem Soc 2009;131:2768–2769. https://doi.org/10.1021/ja808166d.

[61] Duan L, Bozoglian F, Mandal S, Stewart B, Privalov T, Llobet A, et al. A molecular ruthenium catalyst with water-oxidation activity comparable to that of photosystem II. Nat Chem 2012; 4:418–423. https://doi.org/10.1038/nchem.1301.

[62] Maji S, Vigara L, Cottone F, Bozoglian F, Benet-Buchholz J, Llobet A. Ligand geometry directs O-O bond-formation pathway in ruthenium-based water oxidation catalyst. Angew Chemie - Int Ed 2012;51:5967–5970. https://doi.org/10.1002/anie.201201356.

[63] Bard, A. J., ed., Encyclopedia of Electrochemistry of the Elements, Marcel Dekker, Inc., 1973. n.d.

[64] Hansch C, Leo A, Taft RW. A survey of Hammett substituent constants and resonance and field parameters. Chem Rev 1991;91:165–195. https://doi.org/10.1021/cr00002a004.

[65] Kagalwala HN, Tong L, Zong R, Kohler L, Ahlquist MSG, Fan T, et al. Evidence for Oxidative Decay of a Ru-Bound Ligand during Catalyzed Water Oxidation. ACS Catal 2017;7:2607–2615. https://doi.org/10.1021/acscatal.6b03278.

[66] Liu Y, Chen G, Yiu S-M, Wong C-Y, Lau T-C. Intermediates in the Oxidative Degradation of a Ruthenium-Bound 2,2′-Bipyridyl-Phenoxy Ligand during Catalytic Water Oxidation. ChemCatChem 2018;10:501–504. https://doi.org/10.1002/cctc.201701319.

Recent Advances in Ru Catalyzed Transfer Hydrogenation and Its Future Perspectives

Nidhi Tyagi, Gongutri Borah, Pitambar Patel and Danaboyina Ramaiah

Abstract

Over the past few decades, Ru catalyzed transfer hydrogenation (TH) and asymmetric transfer hydrogenation (ATH) reactions of unsaturated hydrocarbons, imine, nitro and carbonyl compounds have emerged as economic and powerful tools in organic synthesis. These reactions are most preferred processes having applications in the synthesis of fine chemicals to pharmaceuticals due to safe handling as these do not require hazardous pressurized H_2 gas. The catalytic activity and selectivity of Ru complexes were investigated with a variety of ligands based on pincer NHC, cyclophane, half-sandwich, organophosphine *etc*. These ligands coordinate to Ru center in a proper orientation with a labile group replaced by H-source (like methanol, isopropanol, formic acid, dioxane, THF), which facilitate the β-hydrogen transfer to generate metal hydride species (Ru-H) and produce desired reduced product. This chapter describes the recent advances in TH and ATH reactions with homogeneous and heterogeneous Ru catalysts having different ligand environments and mechanistic details leading to their sustainable industrial applications.

Keywords: ruthenium, transfer hydrogenation/asymmetric transfer hydrogenation, homogeneous, heterogeneous catalysts, mechanistic studies

1. Introduction

Ruthenium was first discovered in 1844 by Karl Ernst Claus and he had named it as Ruthenia (in Latin Russia) in the honor of his motherland. In fact, in 1827, Gottfried Osann had found three new metals from the Ural Mountains and one of these metals was named as Ruthenium. However, its isolation could not be reproduced and hence his claims were withdrawn on these metals. Ruthenium is a noble transition metal with attractive properties and has found uses in different fields of science and technology. From the commercial point of view, ruthenium has been used in a variety of applications such as its alloy with other heavy metals used for voltage regulators, jewelry, fountain pen nibs and electromechanical devices *etc*. Although, ruthenium metal is known ever since the early nineteen centuries, but its first complex was reported in the second half of twentieth century having application in hydrogenation and hydroformylation [1].

Currently, ruthenium complexes are being widely used in academics and industrial purposes such as photosensitizers, biomedical, semiconductor industry as well as catalysts. Some variety reactions, like Diels–Alder, eco-friendly CO_2 hydrogenation to hydrocarbon, transfer hydrogenation of unsaturated substrates, oxidation of alcohols, atom transfer radical addition (ATRA), metathesis (ring closing metathesis (RCM)/ring-opening polymerization (ROMP)) are catalyzed by inevitably the ruthenium complexes. Among these reactions, the hydrogenation is one of the most explored reaction. As quoted by Rylander, it is "*one of the most powerful weapons in the arsenal of the synthetic organic chemist*" [2]. This reaction finds immense manufacturing applications in pharmaceuticals, agrochemicals, petrochemicals, food industry, fine chemicals, fragrances as well as bulk chemicals. The process of hydrogenation (HY) or asymmetric hydrogenation (AH) is used to reduce unsaturated substrates (alkenes, alkynes, aldehydes, ketones, esters, imines, nitriles, carbon monoxide *etc*.) in presence of hydrogen gas and catalysts to give enantiomerically-enriched compounds. Alternate strategy for the hydrogenation is the transfer hydrogenation (TH) and asymmetric transfer hydrogenation (ATH) reactions, which require sacrificial hydrogen donor. These hydrogen donors include organic hydrogen source or different azeotropic mixtures with hydrogen acceptor substrates and catalysts in presence or absence of base promoters (NaOH, KOH, Et_3N, Cs_2CO_3 *etc*.) (**Figure 1**). This approach is the most preferred and widely applied due to safe handling and which do not require hazardous pressurized H_2 gas or pressure reactors.

The first ruthenium TH catalyst reported was a simple $16e^-$ $[RuCl_2(PPh_3)_3]$ complex, which effectively reduce acetophenone in presence of ^{i}PrOH through inner sphere mechanism involving the following steps; i) insertion, ii) reductive elimination, iii) oxidative addition and iv) β-elimination. It was found that small amount of a base facilitates the rate of TH reaction to approximately thousand-fold. Furthermore, the incorporation of basic nitrogen in a ligand, which coordinates directly to Ru (II) is an interesting approach, which was successfully applied by Noyori and coworkers through a half-sandwich chiral SS-**1**, for catalyzed reduction of several aromatic ketones (**2–6**) (**Figure 2**). $[Ru^{II}Cl(TsDPEN)(\eta^6$-p-cymene/mesitylene)] (now commercially available) complexes (TsDPEN = N-tosylated-1,2-diamine), in presence of formic acid-triethylamine azeotropic mixture gave good yields of reduced products with enantiomeric excess (ee) (**Figure 2**). It was also correlated that reactivity and enantioselectivity of complexes were found to depend on optimum steric and electronic properties of the arene and TsDPEN ligands. Efficiency of this robust catalyst (R,R-**1**) can be seen by the reduction of multifunctional ketone, which gave R benzylic alcohol (**5**) in *ca.* 92% ee without affecting other functional groups. This conversion was explained through, outer-sphere mechanism with a six-membered transition state (TS) by concerted hydride transfer process (TS shown in **Figure 2**). To further improve the catalytic property, Noyori and co-workers have modified SS-**1**/RR-**1** with different ligand frames [3]. The significance of these asymmetric hydrogenation studies has been renowned and hence Ryōji Noyori was awarded Nobel Prize in 2001 for his immense contributions

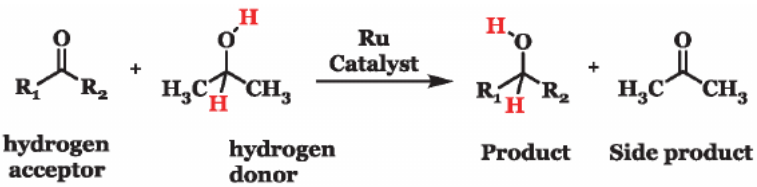

Figure 1.
Ru catalyzed transfer hydrogenation reaction in presence of hydrogen donor and acceptor.

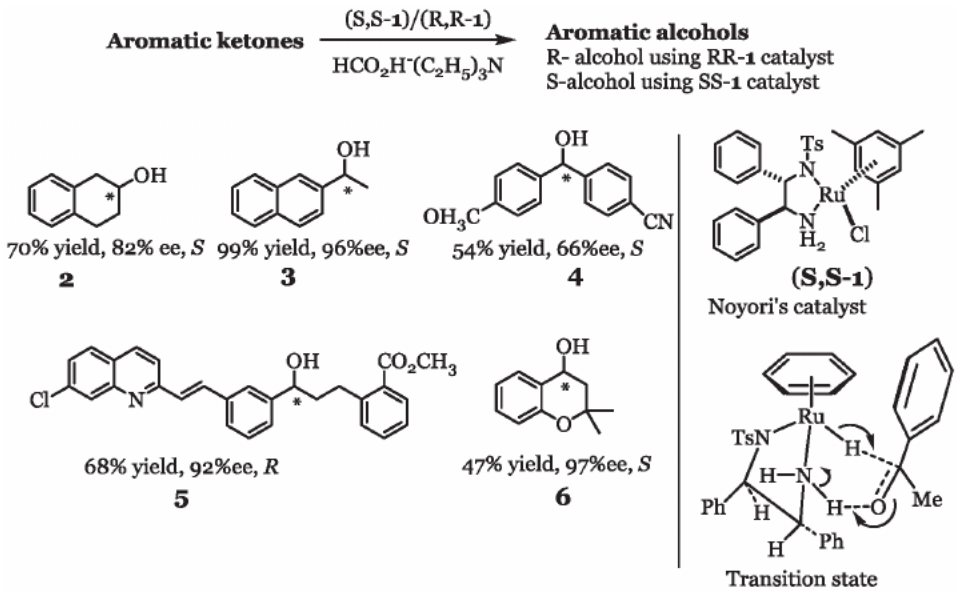

Figure 2.
Structures of selected alcohols (2–6), catalyst Ru-TsDPEN (SS-1) and proposed six membered transition state (TS).

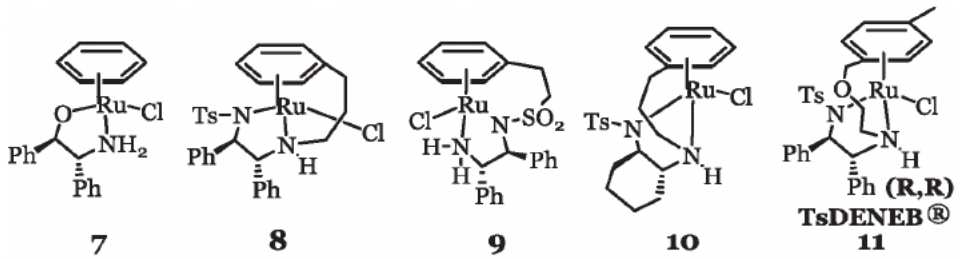

Figure 3.
Selected asymmetric transfer hydrogenation catalyzed, tethered or non-tethered Ru(II) catalysts (7–11).

in this field. Will and co-workers have further modified SS-**1**/RR-**1** by tethering of the arene ring and diamine (or amino alcohol) ligand to increase the stability of the catalyst, to restrict the rotation of the η^6-arene ring and to yield sterically controlled reduction products. Structures of few efficient catalysts **7**–**11**, are shown in **Figure 3** [4–6].

This chapter discusses recent advances of the homogeneous and heterogeneous TH and ATH reactions and primarily reduction of carbonyls, olefins, imines, nitriles, esters and heterocycles formation with a focus on modification of ligands environment. Furthermore, the mechanistic details were also discussed wherever possible with limitations as well as future perspectives in this important area.

2. Advances in ruthenium catalyzed transfer hydrogenation

Realistic relevance of the asymmetric synthesis by TH/ATH in fine chemicals, pharmaceuticals, materials and industrial use required designing and exploration of efficient catalysts. Ru with versatile oxidation states, coordination geometries offered by a variety of ligand moieties make it a good candidate for catalytic

TH/ATH. The crucial requirement for the efficient catalysts is to have a labile coordination site/anionic ligands and efficient chelation or backbone of the ligands to give high turnover numbers (TONs). In this regard, to get good selectivity and activity of the catalysts, the multi-talented ligand architectures are essential. Literature reveals that various ligands such as pincer NHC, cyclophanes, half-sandwich, organo-phosphine, pyridylideneamide, polydentate etc. [7] have been developed by different research groups to improve the selectivity of the catalysts. The following section will discuss the recent advancements in the modification of ligands architecture and their influence on catalytic efficacy.

2.1 Homogeneous transfer hydrogenation

2.1.1 Transfer hydrogenation of carbonyl compounds

The transfer hydrogenation (TH) and asymmetric transfer hydrogenation (ATH) of carbonyl substrates are the most explored and favorable due to polar nature of C=O bond. Although Noyori has set the milestone for TH using TsDEPN ligands however, researchers still used this system with various modifications to improve stability and selectivity of the catalysts. Anderson and co-workers have reported extremely active proline based 2-aza-norbornyl amino alcohol ligands (**Figure 4**) for the ATH process. The [Ru(p-cymene)(**13**)] in presence of ^{i}PrOH catalyzed TH of acetophenone with S/C = 1000 to give *ca*. 97% conversion, *ca.* 96% *ee* (TOF_{50} = 8500 h^{-1}) within 25 min. The reason for this enhanced activity in comparison with the [Ru(p-cymene)(**12**)] (*ca.* 90% conversion, *ca.* 94% *ee*, TOF_{50} = 1050 h^{-1}) was due to the incorporation of polarized C-O bond/dioxolane ring in the ligand frame. This catalyst was able to reduce various aromatic ketones having electron donating and withdrawing substituents (at various positions *e.g. ortho, meta, para)* with admirable enantioselectivity. Theoretical calculations have indicated the lowering of transition state energy (1.3 kcal mol^{-1}) in the case of [Ru(p-cymene)(**13**)] catalyst, and the increased catalytic rate was rationalized through involving the dipole interactions between dioxolane moiety and the substrate (**13a**) [8].

In search of new ligand frame-work for effective and selective TH reaction of aromatic ketones, Ramaiah and co-workers [9] have established a promising new class of air−/moisture-stable ruthenophane/ruthenium(II)-π complexes (**19–20**) and compared their TH activity (**Figure 5**), for the first time with the literature reported catalysts. The structure stiffness of the ligands allows forming the complexes (**19–20**) through π-interactions between the anthracene moiety and ruthenium cation instead of insertion or NHC coordinated complexes. These catalysts were highly selective to aromatic ketones over to aliphatic and aldehyde groups and showed efficient conversion (*ca.* 100%) of acetophenone to 1-phenylethanol in

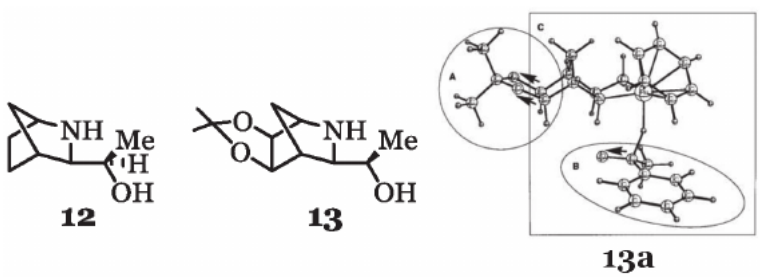

Figure 4.
*Blueprint of aza-norbornyl amino alcohol ligands (**12, 13**) and low energy TS (**13a**) determined theoretically involving remote dipole interactions (Ref. [8]).*

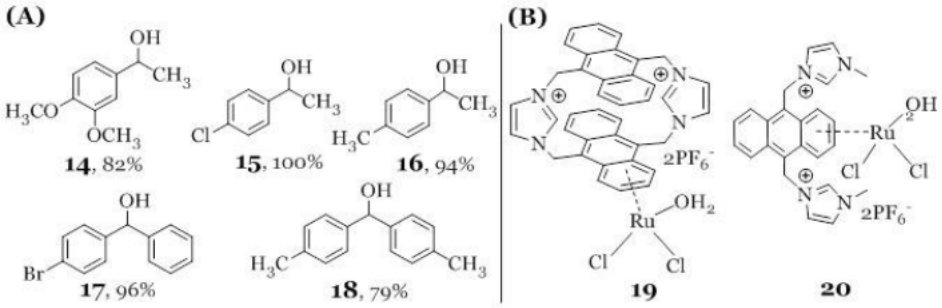

Figure 5.
*(A) Few selected reduced products (**14–18**) along with structures of (B) ruthenophane catalysts **19, 20**.*

presence of a base, ^{i}PrOH and 2 mol% catalyst loading (80 °C). A series of substrates were scrutinized which showed efficient conversion to the reduced products (selected alcohols shown in **Figure 5**). In comparison to **20**, the catalyst **19** showed a better catalytic efficiency ascribed to different binding interactions through coordinative and cation-π interactions. The presence of labile ancillary ligands also participates in enhancement of efficient TH capabilities. Additionally, these robust catalysts showed exceptionally good conversion of the ketones to the reduced products (**14–18**) in comparison with the commercially available [Ru(p-cymene)Cl_2]$_2$ and the "Hoveyda-Grubbs" catalysts, under identical catalytic conditions.

N-heterocyclic carbenes (NHC) are another significantly important class of ligands for homogeneous ruthenium catalyzed TH reactions. Recently, different versions of NHC based ligands have been designed with an aim to synthesize thermally stable and efficient catalysts. These ligands in turn can influence steric and electronic properties of metal center through strong σ-donor capability [10]. The mononuclear and binuclear ruthenium complexes (**Figure 6**, **21–25**) (cationic/neutral) having NHC ligands with "three-legged piano-stool" type geometry was reported by Ramaiah and co-workers [11]. These anthracene/arene based catalysts interestingly showed efficient and selective TH of a variety of aromatic ketones. Notably, very small amount of cationic catalysts (**21–23**) (0.5 mol%) exhibited efficient reduction of ketones (*ca.* 100%) in comparison to neutral catalysts (2 mol %) in presence of ^{i}PrOH and base (0.1 mM) within 2 h at 80 °C. Whereas [Ru(p-cymene)Cl_2]$_2$ and the second generation "Hoveyda-Grubbs" catalysts showed moderate yields of reduced products (ca. 47% and ca. 60%, respectively) under identical situations.

The cooperative binding of NHC and pyridine substituents to the ruthenium center in cationic catalysts facilitates high catalytic activity in comparison to the neutral complexes. Reduction of the substrate was supported by well-established mechanism (**Figure 7**), wherein the active catalyst **A** formed by the addition of *iso*-propoxide, upon *β*-hydride transfer intermediate and Ru-H species **B** formed. Interaction of substrate **B** to give **C**, which upon subsequent hydride transfer to the substrate form the intermediate **D**. Furthermore, the reduced product resulted by the reaction of **D** with ^{i}PrOH in presence of the base with regeneration of the active species **A**. *In-silico* studies have further confirmed that the intermediates hypothesized were energetically constructive and reaction follows a thermodynamically steady pathway [11].

An innovative class of pincer pyridylideneamides (PYAs) with strong *σ*-donating ability was disclosed by Albrecht and co-workers [12]. PYAs core was tethered with different chelating groups (cyclo-metalated aryl ring/pyridine/pyridylidene/one-more PYA/triazolylidene), which can bind to metal center either *via* π-acidic (neutral donor) or π-basic (zwitterionic pyridinium amide) donor

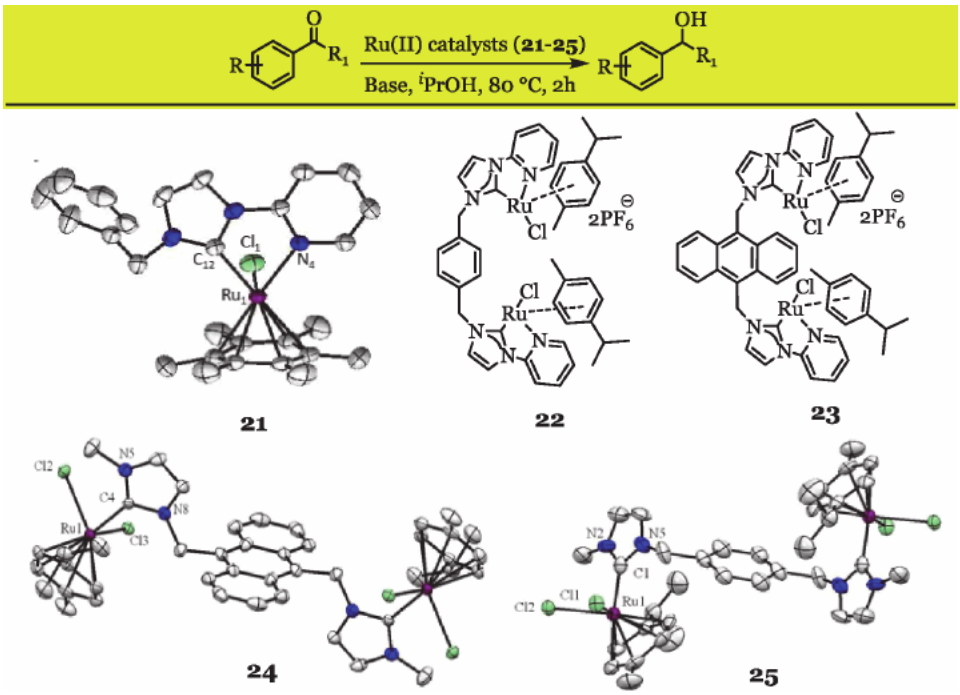

Figure 6.
Structures of NHC based cationic and anionic ruthenium catalysts **21–25** *(Ref. [11]).*

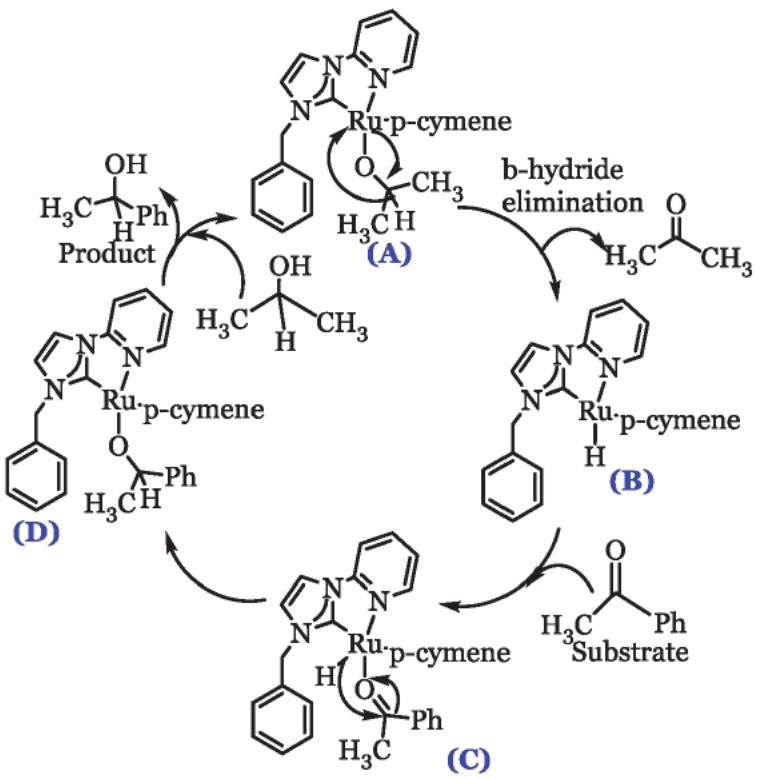

Figure 7.
*Proposed mechanism of transfer hydrogenation of ketones using cationic ruthenium catalyst (***21***).*

capability. A series of ruthenium complexes (**26**–**30**) (**Figure 8**) customized with PYA ligands were synthesized and confirmed through various techniques *e.g.* NMR, X-ray crystal structure, HR-MS and other studies. These robust Ru-PYA catalysts (1 mol%) displayed high catalytic activity (*ca.* 100% conversion) in TH of benzophenone (as model substrate) and established a relationship between chelate potency and ruthenium centered catalytic activity. The catalytic activity of the complexes (**26**–**30**) were tuned by electronic configuration of the ligands and the enhanced catalytic activity in the case of **26** correlated by NMR (with large shift difference $\Delta\delta$ = 1.03 ppm, then the other complexes) and electrochemical studies. It was concluded that the substrate reduction was followed first-order reaction rate *via* mononuclear reaction pathway [12].

Transfer hydrogenation of the mixed acetate/acetylacetonate ruthenium phosphine catalyst (**31**), [Ru(OAc)(acac)PP] (PP=PPh_3/bis(diphenylphosphino)-butane) with superior stability and activity was reported. As in the earlier cases, the addition of basic additive significantly enhanced the catalytic efficiency. The effect of NH function of these mixed ruthenium(II) phosphine complexes was demonstrated by incorporating (aminomethyl)pyridine (ampy) to [Ru(OAc)(acac)PP]. The Ampy moiety binds to the metal center upon opening/de-coordination of the acetate. The mixed catalysts (*ca.* 0.1 mol%) in absence of basic additives (ampy/en/bza) showed very low conversion (*ca.* 38–75%, TOF = 100–930 h^{-1}) at 90 °C in 8 h. Addition of 10 equivalents of ampy surpasses the catalytic conversion up to *ca.* 99% (TOF = 125,000 h^{-1}) at a very low 0.03 mol% [Ru(OAc)(acac)(ampy)(dppb)] catalyst (**31**) loading in 5 min. The pathway proposed (**Figure 9**) displayed the important role of NH function for rapid reduction of the substrate *via* outer sphere mechanism, in which the first step was the formation of a five-coordinated species **A** after dissociation of the acetate ion. The second step was the coordination of ^{i}PrOH with the six-member TS (**B**). The third step was the formation of Ru-H species (**C**), which formed the substrate coordinated TS (**D**) and finally upon transfer of hydrogen led to the regeneration of species **A** [13].

2.1.2 Transfer hydrogenation of olefins and imines

Imines and olefins are also demanding and challenging substrates for TH/ATH. Noyori's catalyst [RuCl(TsDPEN)(η^6-p-cymene)] in azeotropic mixture showed

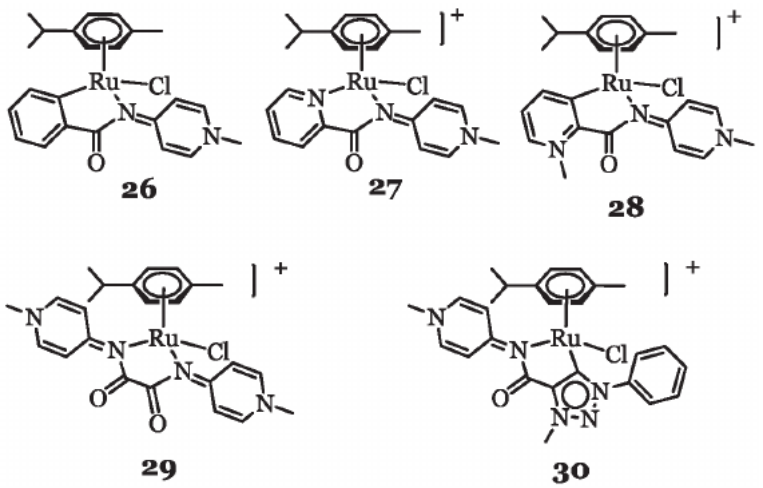

Figure 8.
*Structures of the pyridylideneamide based ruthenium catalysts (**26**–**30**) investigated.*

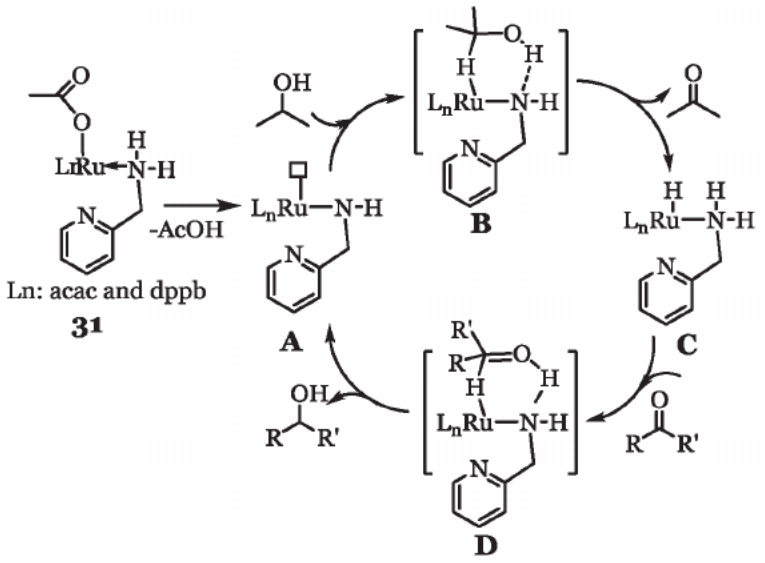

Figure 9.
*Proposed mechanism of transfer hydrogenation of the mixed ruthenium phosphine catalyst (**31**).*

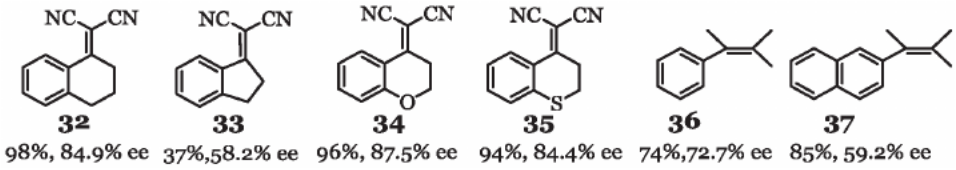

Figure 10.
*Selected examples of few activated alkenes (**32–37**) investigated.*

ATH of activated alkenes (α,α-dicyano alkenes) (**32–37, Figure 10**) in good yields with moderate enantioselectivity [14]. Various alkenes were tested and to enhance the enantioselectivity, TsDPEN and η-arene ligands with different substitutions were explored. For example, 1-naphthylsulfonyl-DPEN gave high yields and enantioselectivity (*ca.* 96% and *ca.* 81% *ee*) at 85 °C. Different optimization studies revealed that temperature as well as steric hindrances on the arene moiety was important parameters for the observed catalytic activity. **Figure 10** shows few examples of activated alkenes (**32–37**), which gave moderate to good yields and high enantioselectivity. Of these examples, the reduction of the five membered analogue, 1-indanylidenemalononitrile (**33**) gave the product (*ca.* 37%, 58.2% *ee*) along with high yields of the byproduct and negligible enantioselectivity. This was confirmed that the 1,4 addition product was formed due to high acidity of *γ*-allylic C–H in **33**. Furthermore, the chiral *β*,*β*- disubstituted acids were effortlessly achieved by hydrolyzing the chiral malononitriles with concentrated HCl [14].

Another recent ATH application of Noyori's catalyst (RR-**1**/SS-**1**) was reported by Meyer and Cossy. ATH of the strained difluorocyclopropenes and their analogues are appealing substrates because of emerging application of *gem*-difluorocyclopropanes in different drugs (Zosuquidar, phase III clinical trials, for acute myeloid leukemia). The *gem*-difluorocyclopropenyl methyl ester as the model substrate was tested for ATH in ^{i}PrOH/CH_2Cl_2 (10/1) (RT, 1 h) using the catalyst (S,S)-**1** (10 mol%), which afforded *ca.* 85% yield of **38** with a measurable *cis* diastereomer (*cis*/*trans* > 96:4) (*ca.* 94% *ee*), whereas (RR)-**1** yielded, *ca.* 83% *ent*-**38** in *ca.* 98% *ee*. Reduction, condensation and subsequent reaction of **38** with *p*-bromobenzoyl

chloride yielded *p*-bromobenzoate (*ca.* 61%). Ester substituents were selected because of their cleavability specifically, under acidic and basic conditions to give *cis*-(*ca.* 67%) and *trans*-*(ca. 81%)*-*gem*-difluorocyclopropane-carboxylic acids, respectively. The scope of ATH on few selected substrates in presence of (S,S)-**1** is represented in **Figure 11**, (**38–44**). Detailed mechanistic studies have shown that the first step showed the formation of (S,S)-**II**, (**45**) with the loss of acetone and followed by hydride transfer to yield Michael acceptor (**A**) (**Figure 12**). To decrease the steric hindrance between *gem*-difluorinated C3 and *p*-cymene moieties, two different TS-I, **46** and TS-II, **46** were proposed. To restore, (S,S)-**1** gave enols (**47** and *ent*-**47**), while the former upon tautomerization gave *cis*-difluorocyclopropane (**48**) as the major enantiomer. However, *ent*-**47** under the kinetically controlled conditions and with proton transfer from the less hindered face at C1 yielded *ent*-**48**. The synthetic applications of these difluorocyclopropane was investigated further for the formation of a variety of nitrogen heterocycles as future building blocks in medicinal chemistry [15].

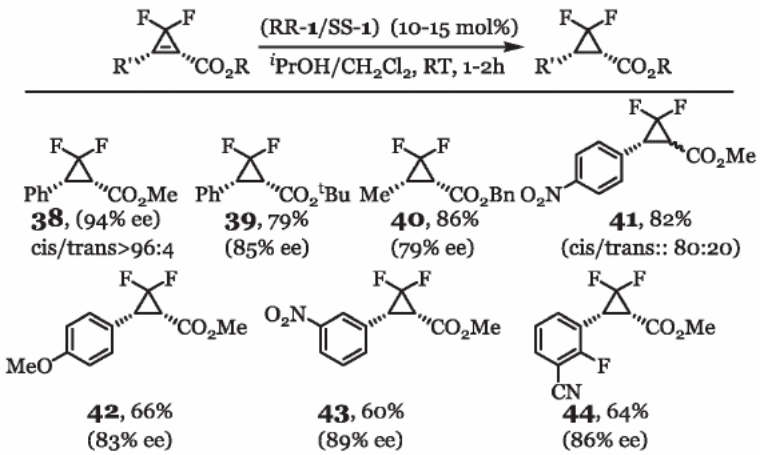

Figure 11.
Few selected enantioenriched gem-*difluorocyclopropanes (38–44) achieved.*

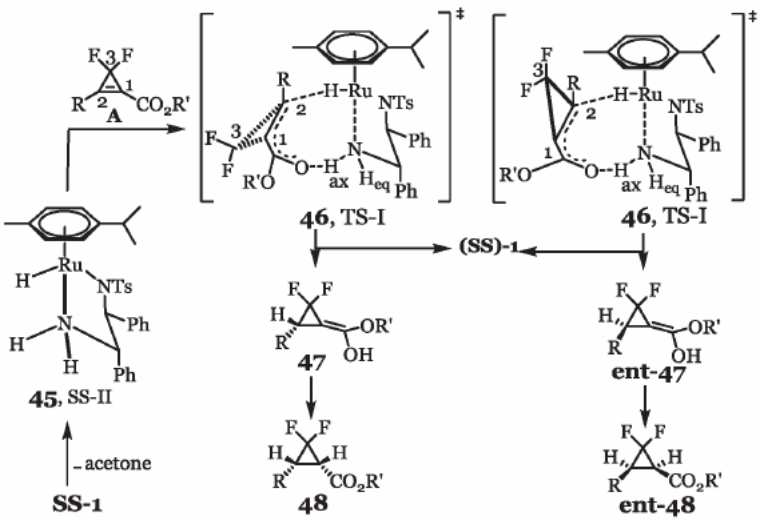

Figure 12.
Proposed mechanism for asymmetric transfer hydrogenation of gem-*difluorocyclopropanes (48, ent-48).*

In-depth study of the pyrazole/phosphine-supported ruthenium complex in TH of olefins and alkynes under semi-hydrogenation conditions resulted in unusual *E*-selectivity. The catalyst **49**/**49′** was synthesized in moderate yields by refluxing $RuCl_2(PPh_3)_2$ and pyrazole ligand in acetonitrile while its structure was analyzed through NOE experiments (**Figure 13**) and X-ray analysis, which confirmed the dimeric nature in chlorobenzene/hexane. Interestingly, upon addition of two equivalents of acetonitrile in chlorobenzene, the dimer was found to undergo dissociation to yield the active catalyst. Efficient reduction of 3,3- dimethylbutene-1 was achieved in good yields (*ca*. 90%) in presence of 1 mol% of **49**/**49′** and 2 mol% of KO^tBu in ^{i}PrOH at 80 °C. Different types of alkene substrates (mono/disubstituted/terminal/α,β-unsaturated esters/anthracene) were investigated and which could be reduced easily without any isomerization (in case of terminal hexane). The mechanism of this reduction was suggested through the involvement of conventional dihydride intermediate (**50**), which was formed by the reaction of **49**/**49′** in presence ^{i}PrOH and base (**Figure 13**). The labile solvent further replaced the substrate to give the adduct **51**, while the alkyl adduct **52** was formed by a reversible step through alkene insertion into Ru-H bond. The alcohol coordination to the vacant site of **53** followed by reductive elimination of cyclohexane and upon subsequent proton transfer shift generated **54**. The alkoxide (**54**), upon β-H shift afforded π-coordinated ketone dihydride species, (**55**), which after alkene substitution regenerated **51** to activate the catalytic cycle again [16].

Guijarro and co-workers have reported the first example of chemoselective ATH of the conjugated sulfinylimines substrates, (**56a-k**). Desulfinylation of these reduced products (**57a-k**) gave the corresponding deprotected allylic amines, which could be

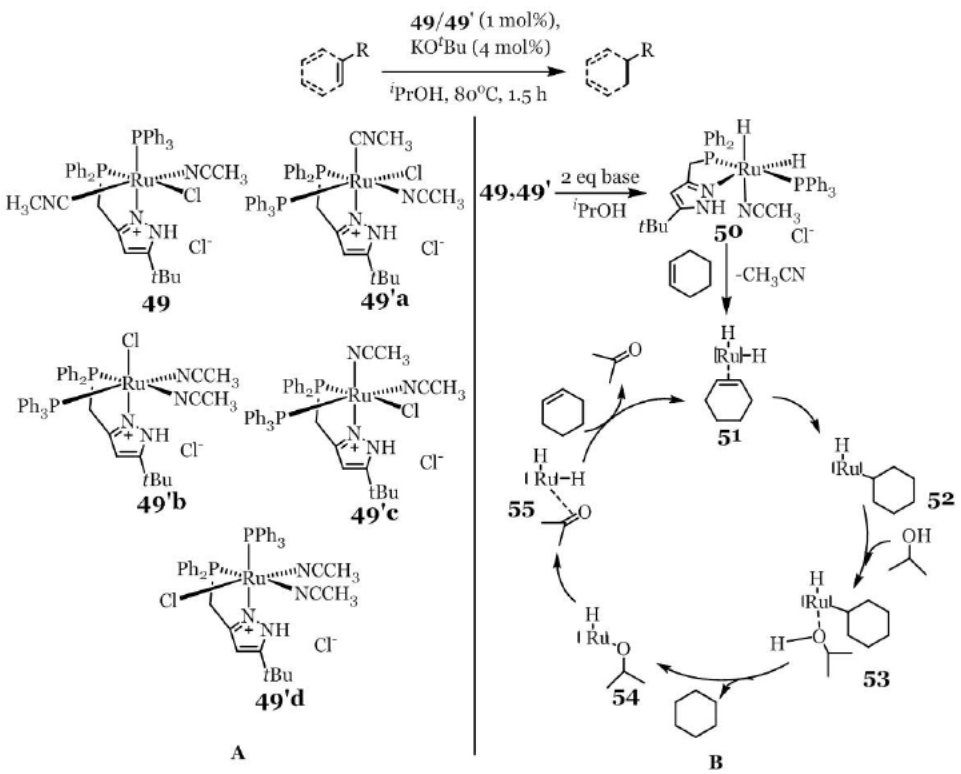

Figure 13.
*(A). Structure of the catalyst (**49**) and its structure (**49'a-49'd**). (B). Proposed mechanism for TH of cyclohexene.*

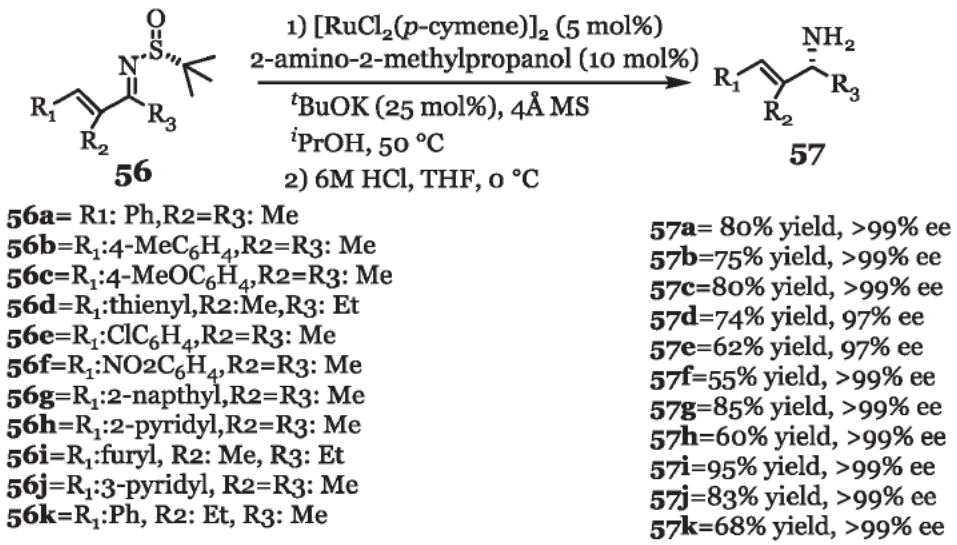

Figure 14.
Ruthenium-catalyzed asymmetric transfer hydrogenation of α,β-unsaturated imines (57a-57 k).

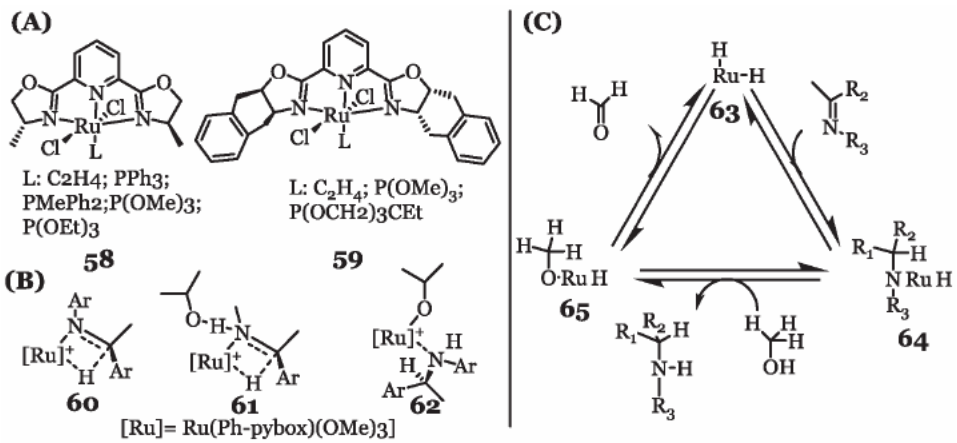

Figure 15.
(A) Catalysts [Ru(Cl)2 (R-pybox)(C2H4)] (58–59) with a monodentate phosphane and phosphite ligands. (B) Proposed intermediates 60–62 for transfer hydrogenation of imines. (C) Proposed mechanism of transfer hydrogenation of imine with dihydro Ru complex (63).

important for pharmaceutical applications. **Figure 14**, shows ATH of various *α,β*-unsaturated imines functionalized with different substituents (for *eg.* electron releasing/electron withdrawing/naphthyl/pyridyl *etc*). The substituents on C=C and C=N affect the chemoselectivity of the reduced products. In general, the substrate with R1: aromatic/heteroaromatic, R2: alkyl/aryl, R3: alkyl, functionality yielded excellent *ee* of the allylic amines. It is also interesting to note that ATH of the imines with (E)-Ph-CH=CH- fragment preferred to reduce both C=C and C=N bonds. This simple and straight forward method of reduction of the allylic imines opens up a new avenue for the synthesis of building blocks useful in designing of new drugs [17].

The *trans*-isomers of [Ru(Cl)$_2$(R-pybox)(L)] (**58–59**, **Figure 15A**) with a monodentate phosphane and phosphite ligands were developed to catalyze HY/ATH of *N*-aryl imines (in ^{i}PrOH) derived from acetophenones to yield the amine products in significantly high enantioselectivity (c*a*. 99%). It is interesting to note

that the reduction reactions were performed under hydrogen pressure behaved as TH reactions, which was confirmed by various labelling experiments as well as by the proposed intermediates (**60**–**62**, **Figure 15B**). From these analysis, it was speculated that a common hydride $[Ru(H)(Ph\text{-}pybox)(P(OMe)_3)]^+$ species was produced *in situ* under either HY or TH [18].

Azua and co-workers have recently reported the first example of microwave assisted ruthenium catalyzed TH of imines in presence of glycerol as the hydrogen donor. Reduction of *in-situ* synthesized imine using NHC ruthenium complex (1 mol %) with sulfonate N-wingtips yielded enhanced conversion of amine in glycerol (*ca.* 77%) and base under microwave conditions (200 W). This improved yield in comparison to the conventional method (*ca.* 17%) was due to the formation of a highly polar zwitterionic nature of the complex to absorb microwave irradiation efficiently. Additionally, the base free catalytic conversion showed quantitative yield of imine (*ca.* 63%) due to sulfonated wingtip as an internal base [19]. $RuH_2(PPh_3)_4$ was a well-known active TH catalyst for the reduction of imine in the absence of a base. This catalyst was efficiently catalyzed by several imine derivatives as well as cyclic imines. The proposed mechanism (**Figure 15C**) proceeds through classical hydride transfer steps from Ru-H (**63**) to imine, which was confirmed through isotope labelling experiments, wherein incorporation of deuteride to methylidene carbon was observed [20].

2.1.3 Ruthenium catalyzed synthesis of heterocycles

The functionalized heterocyclic compounds have attracted attention due to their predominant applications in pharmaceutical industries for designing of new drugs. Recently, the Food and Drug Administration (FDA) had declined to grant new chemical entity (NCE) exclusivity to enantiomers that were part of the previously approved racemic mixtures. Therefore, the purity of enantiomers is very important and can be overcome by using appropriately designed catalysts. Although the reports on synthesis of heterocycles using ruthenium catalysts are well-known but their synthesis *via* ruthenium catalyzed ATH is not much explored. Pabalo and co-workers have reported an admirable example of ruthenium catalyzed ATH for production of enantiomerically enhanced heterocycles *eg*. aziridines, pyrrolidines, piperidines and azepanes. They have employed their established approach of enantiomerically pure *N*-(*tert*-butylsulfinyl)haloimines as the substrate, and imine bond was reduced *via* ATH in presence of ^{i}PrOH, $[RuCl_2(p\text{-cymene})]_2$ catalyst and achiral 2-amino-2-methylpropan-1-ol ligand (50 °C) (**Figure 16**). The reduced haloamines in presence of a base (^{t}BuOK) yielded the *N*-protected saturated heterocycles through intramolecular nucleophilic substitution in excellent yields with diastereomeric ratio up to >99:1. The *N*-protected aziridines and pyrrolidines were synthesized by one-pot ATH-cyclization sequence (Ru:L:^{t}BuOK = 1:2:5 mol %) in high yields (*ca.* 85–90%) and diastereomeric ratios (selected examples **66**–**69** are shown in **Figure 17**). In the case of piperidines and azepanes, the process was

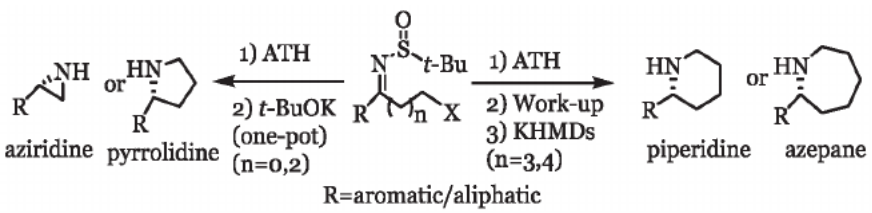

Figure 16.
Synthesis of selected N*-protected heterocycles.*

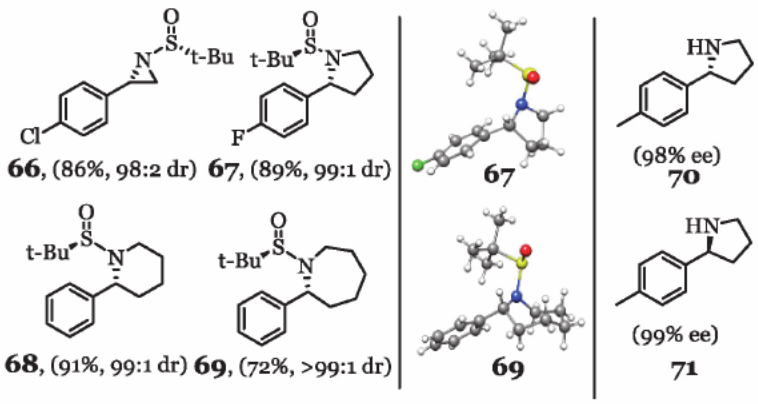

Figure 17.
*Asymmetric transfer hydrogenation examples of selected N-protected aziridine (**66**), pyrrolidine (**67**), piperidines (**68**) and azepane (**69**) and X-ray crystal structures of **67**, **69** (from ref. [21]) as well as structure of free pyrrolidines (**70**, **71**).*

modified with treatment of potassium bis(trimethylsilyl)amide (KHMDS), which gave moderate yields and diastereoselectivity (**68–69**). On the other hand, the pyrrolidine derivatives (**70–71**) were obtained by desulfinylation of N-sulfinylpyrrolidines by the reaction with HCl/MeOH. As representative examples, the single crystal of **67** and **69** were analyzed, which confirmed the stereogenic center obtained by Ru catalyzed ATH [21].

Asymmetric tetrahydroisoquinolines (THIQs) are yet another indispensable class of heterocycles with pharmacological applications due to their structural resemblance with neurotransmitters. In this context, Noyori-Ikariya catalysts (arene/Ru/TsDPEN) were found applications in ATH of electron-rich/ortho substituted 3,4-dihydroisoquinolines (DHIQs) only to give THIQs in high enantioselectivity (*ee*'s). In contrast, these catalysts were found to be ineffective with the meta/para substituted electron-poor DHIQs, which are important for the synthesis of solifenacin and TRPM8 antagonists (pharama targets). Wills and co-workers have modified the arene/Ru/TsDPEN catalysts with tethered thiophene/furan/ester groups to basic nitrogen of TsDPEN ligand. It was found that the ATH of these demanding substrates (DHIQs) showed good catalytic efficiency with the modified catalyst (1 mol %) in presence of formic acid-triethylamine (5:2) azeotrope. The furan-based catalyst (**77**) exhibited best results of ATH of DHIQs with remarkable enantioselectivity (*ee*) of *ca.* 90% and 93% for the conversion to THIQs (**72–76**) (**Figure 18**).

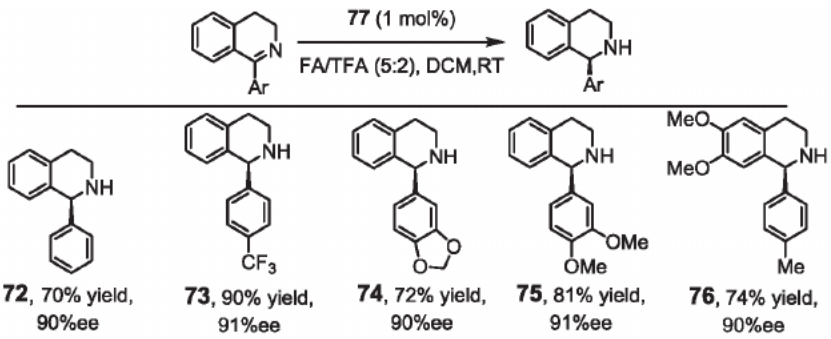

Figure 18.
Asymmetric transfer hydrogenation of few selected dihydroisoquinolines (DHIQs).

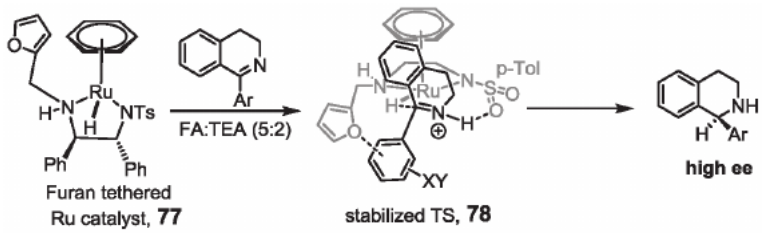

Figure 19.
Stabilization of TS state for asymmetric transfer hydrogenation of dihydroisoquinolines (DHIQs).

The proposed mechanism (**Figure 19**) of this asymmetric reduction supported the extra stabilization of TS state **78** through the interaction of furan moiety of the catalyst with the aryl moiety of substrate [22]. Recently, the pyrazole/phosphine based ruthenium catalyst (1 mol %) also showed high TH activity of a variety of *N*-heterocyclic substrates. For example, TH of isoquinoline surprisingly gave the product with reduced all-carbon rings, which are accountable to the electronic properties of the catalyst [16].

2.1.4 Selected transfer hydrogenation/asymmetric transfer hydrogenation of nitriles, esters and acetates

The nitrile-based substrates have received less attention for TH/ATH reactions, in spite of their industrial significance. In earlier studies, TH of benzonitrile catalyzed by $RuH_2(PPh_3)_4$ gave very low yields of the reduced product and showed the requirement of focused research in this area [20]. Beller and co-workers have reported NHC based $[Cp(IPr)Ru(pyr)_2][PF_6]$, catalyst (0.5 mol% catalyst, 1.5 mol% KO^{t}Bu, ^{i}PrOH), which effectively catalyzed TH of various aromatic nitriles to give the corresponding aromatic imines (*ca.* 24–99%). The function of base was to convert $[Cp(IPr)Ru(pyr)_2][PF_6]$ to $Cp(IPr)RuH_3$ which was confirmed through kinetic data as well as mechanistic steps, migratory insertion and release of the product after a metathesis with IPA [23]. Additionally, the extensive screening experiments of various ruthenium pre-catalysts in presence and absence of different ligands was performed. The best catalyst system $(\{Ru(p\text{-cymene})Cl_2\}_2$ (1 mol %)/DPPB (2 mol%) in presence of NaOH (10 mol %) and 2-butanol at 120 °C, showed the reduction of various aliphatic/aromatic/hetero aromatic nitriles to primary amines [24]. Remarkably, high TH catalytic activity of bifunctional Ru^{II}(-phenpy-OH) catalyst was reported for a variety of nitrile substrates *via* outer-sphere mechanism in the presence of excess of PPh_3. The presence of –OH in the ligand support as a supplementary for the metal hydride formation *via* direct interaction of –OH with the metal coordinated halide ion [25].

Kim and co-workers have disclosed $RuH_2(CO)(PPh_3)_3$ (10 mol%) catalyst stabilized with pyridine ligand (20 mol%), which showed selective method of imine formation from nitriles substrate under base free conditions through hemiaminal intermediate mechanism [26]. Nikonov and co-workers have revealed half-sandwich $[Cp(IPr)Ru(py)_2]PF_6$ complexes for TH of nitriles with comparatively high catalyst loading [24]. To further improve pyrazole/ phosphine-supported cationic ruthenium complex (**49**/**49′**) was reported that showed high activity in the catalytic TH of nitriles. This active catalyst (**49**/**49′**, 1 mol%) in presence of nitriles, KO^{t}Bu (5 mol %), ^{i}PrOH (80 °C, 24 h) gave moderate to excellent imine products. Further, upon treatment of imine with HCl yielded the analogous primary ammonium salts [16].

Another and less explored substrate for TH is the esters and acetates. In this context, Nikonov and co-workers have reported the first example of $[Cp(PiPr_3)Ru$

$(CH_3CN)_2]PF_6$ catalyzed reductive conversion of the electrophilic phenyl benzoates and trifluoroacetates, which gave alcohols in low yields [27]. The catalyst [Cp(IPr) $Ru(pyr)_2][PF_6]$, effectively catalyzed TH of conjugated systems such as α,β-unsaturated esters to give β-isopropoxy substituted esters (Michael addition of IPA) along with TH reduced products (ca. 45–99%) [23].

3. Heterogeneous transfer hydrogenation

With the fast advances in sustainable chemistry, the heterogeneous catalytic systems are profoundly used by industries for large scale production, economics as well as technological point of view. The advantage of heterogeneous catalytic systems over homogeneous is basically the easy handling, recycling and easy separation of the catalyst from the reaction mixture. For heterogeneous transfer hydrogenation, ruthenium catalyst can be immobilized on/in various materials such as nanoparticle, polymers, silica and carbon surfaces [28–30]. Such catalysts can be separated easily from the reaction mixture by simple filtration, centrifuge or applying magnetic force. Despite of this, the ruthenium catalyzed heterogeneous TH mostly limited to the reduction of carbonyl groups only.

3.1 Heterogeneous transfer hydrogenation of carbonyl compounds

Over last few decades, the field of heterogeneous TH of ketones by employing primary and secondary alcohols as donors in presence of heterogeneous catalysts is growing tremendously. In this context, various research groups have developed several ruthenium-based heterogeneous catalytic systems by altering the incorporation of ruthenium in/on various materials. Due to the importance and demand of catalytic ATH, significant efforts have been dedicated for the development of immobilized forms of the Noyori–Ikariya and other well-established catalysts. In this context, several polystyrene (PS) supported ruthenium complexes (**79**–**82**, **Figure 20**) were prepared initially and their catalytic properties were studied by several groups.

Marcos and co-workers have synthesized Noyori catalyst **79** immobilized on a chlorosulfonylated PS. They used the catalyst in asymmetric transfer hydrogenation of ketones and formic acid as hydrogen source and triethylamine as base at 40 °C [31]. When 0.67 mol% of the catalyst was used, the reduction of acetophenone

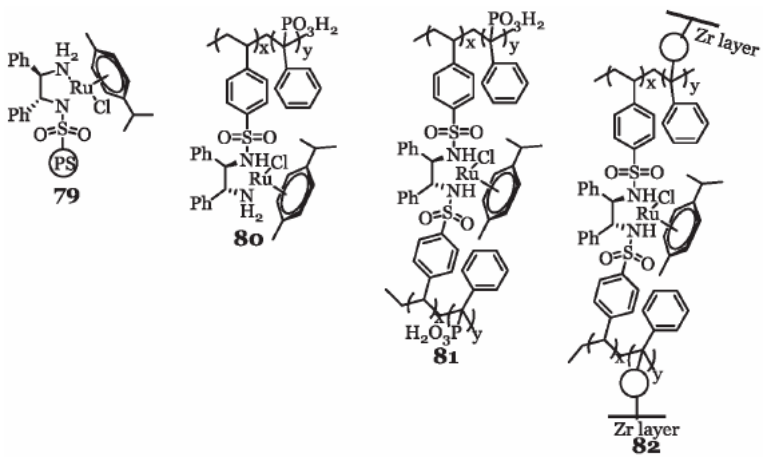

Figure 20.
*PS-supported Ru catalysts (**79–82**) for the ATH of carbonyl groups.*

proceeded smoothly to give the desired product 1-phenylethan-1-ol with *ca.* 97% ee and the conversion was found to be *ca.* 99%. A number of electron donating as well as withdrawing groups showed excellent reactivity with c*a*. 86–99% *ee* values with **79**. Ma and Peng's group independently documented the synthesis of the ruthenium complexes immobilized on various phosphonate-containing single- or double-stranded PS copolymer (**80**–**82**) [32–33]. The catalyst **80** can be efficiently employed for the aqueous ATH of carbonyls using NCOONa-Et3N to give *ca.* 94–98% yields of the desired alcohol with *ca.* 93.9–97.8% *ee,* and *ca.* 100% chemoselectivity [32]. Similarly, ATH of aryl ketone was also achieved with **82** with *ca.* 94% yield and *ca.* 95% *ee* [33]. Interestingly, catalysts **80** and **82** can be easily separated by means of centrifuge from the reaction mixture and were reused without the loss of catalytic efficiency for five consecutive cycles. A comparative reduction of acetophenone using catalyst **79**–**82** was demonstrated in **Table 1**.

Recently, Islam and co-workers have reported the synthesis of simple and efficient PS-supported ruthenium complex (**83**) for the TH of ketone. Both aliphatic and aromatic functionalized ketones showed great conversion to the corresponding alcohols with the yields *ca.* 84–99% using **83** in the presence of KOH and ^{i}PrOH (**Figure 21**) [34]. One of the major issues in a majority of heterogeneous catalyzed TH is the isolation of catalyst from the reaction mixture, which involves tedious filtration or centrifuge. Very recently, magnetic nanoparticles (MNPs) have shown powerful alternates because of the advantages like greater surface area, morphological control, straight forward preparation, and easy separation using magnetic forces. As a result, MNP-immobilized transition-metal catalysts are broadly investigated by the researchers and applied for TH reactions. Verma and co-workers have reported the assembly of the ruthenium incorporated magnetic nanoparticles (Ru@MNPs) having spherical shape and size ranges from 15–30 nm in one pot *via* aggregation of magnetic silica (Fe_3O_4@SiO_2) with binding of RuNPs [35]. The catalytic TH of acetophenone was carried out using Ru@MNPs. In the

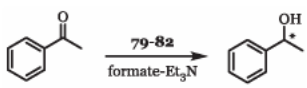

Sr. No.	Catalyst	Temp/Time	Conversion	Yield	ee
1	**79**	40 °C /24 h	99	97	97
2	**80**	50 °C /6 h	100	98	97
3	**82**	50 °C /16 h	>99	98	95

Table 1.
ATH of acetophenone.

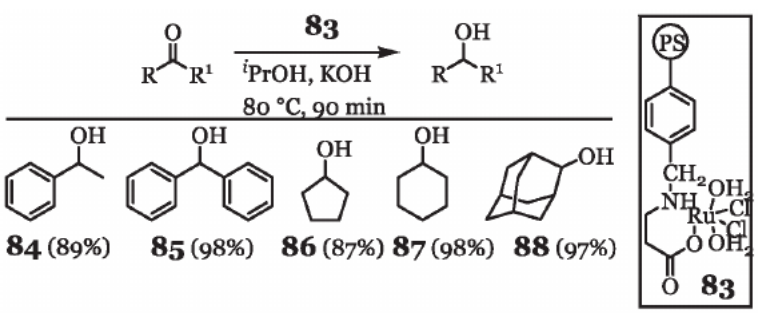

Figure 21.
Heterogeneous TH of ketone.

methodology, ^{i}PrOH was used as a hydrogen source along with KOH as base at a temperature of 100 °C under MW irradiation in 30 min to obtain the desired alcohol product with more than 99% yield. A wide range of substituted acetophenones showed great compatibility under optimal conditions to furnish the corresponding alcohols with good yield and selectivity (**Figure 22**). The catalyst can be easily recovered from the reaction mixture by using external magnet.

In 2015, Moores and co-workers used the iron/iron oxide core/shell NPs (FeCSNPs) as heterogeneous support for the synthesis of Ru-magnetic nanoparticles (Ru@FeCSNPs) [36]. The catalyst Ru@FeCSNPs was used as the catalyst of choice for the transfer hydrogenation of carbonyl compounds using KOH as base and ^{i}PrOH as hydrogen donor cum solvent at 100 °C (**Figure 23**). Aryl ketones bearing both electron-donation as well as electron withdrawing groups were converted to their corresponding alcohols very smoothly. The catalyst was found to be highly selective for the keto group over aldehyde or nitro functional group.

Although numerous catalysts and methods have been developed for the Ru-catalyzed heterogeneous TH, the exact mechanism is still unclear. However, several mechanistic studies lead to two possible pathways for the metal catalyzed TH reaction; (a) monohydride transfer mechanism and (b) dihydride transfer mechanism. It is believed that, both pathways are possible for Ru-catalyzed transfer hydrogenation [37]. The possible catalytic cycle for the catalytic TH of keto group shown in **Figure 24** uses ^{i}PrOH as the source of hydrogen. As shown in **Figure 24**, in the mono hydride mechanism, ^{i}PrOH in presence of base form the alkoxide ion which in turn react with the metal to form the active metal-alkoxide species **I**. The metal metal-alkoxide give the reactive metal hydride intermediate **II**, which react with the

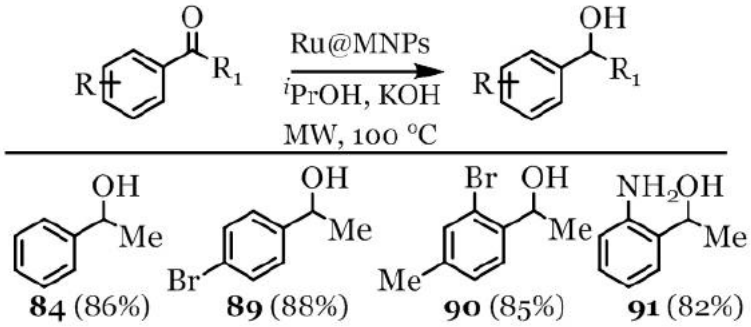

Figure 22.
Ru@MNPs-catalyzed transfer hydrogenation of ketones.

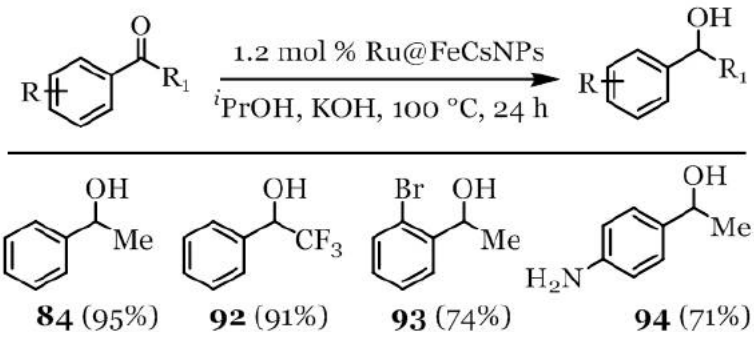

Figure 23.
Ru@FeCSNPs catalyzed TH of acetophenone.

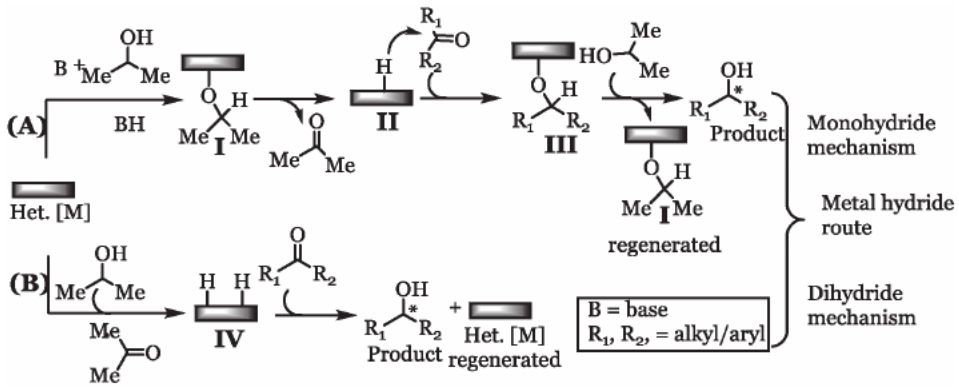

Figure 24.
Possible general mechanisms for the heterogeneous TH reactions: (A) monohydride CTH; (B) dihydride CTH.

keto group to transfer the hydride ion to the carbonyl carbon and result in the formation of substrate–metal alkoxide intermediate **III**. Finally, another molecule of ^{i}PrOH was reacted to form the product and regenerate the active catalytic species **I**. Similarly for the dihydride mechanism, both the protons of reducing agent got transfer to form the metal dihydride complex **IV**, which in turn react with the reactant carbonyl group to form the desired product along with regeneration of the metal catalyst.

3.2 Heterogeneous transfer hydrogenation of nitro group

The substituted aromatic amines act as important intermediates in the field of pharmaceuticals as well as agrochemicals. They also show great versatility in the production of dyes, polymers, herbicides and cosmetics. The aromatic nitro compounds can be easily converted to the corresponding aromatic amines *via* catalytic transfer hydrogenation. Lu and co-worker documented the use of ionic liquid (1-hexadecyl-3-methylimidazolium bromide) as a support in the synthesis of MCM-41-type mesoporous silica (OMS-IL) [37]. In their methodology, they used Ru nanoparticles immobilized on OMS-IL (Ru/OMS-IL) by transfusing OMS-IL with a $RuCl_3$ in water for reducing nitroarenes with good selectivity (**Figure 25**). Both mono and poly substituted nitroarenes were transformed into their respective

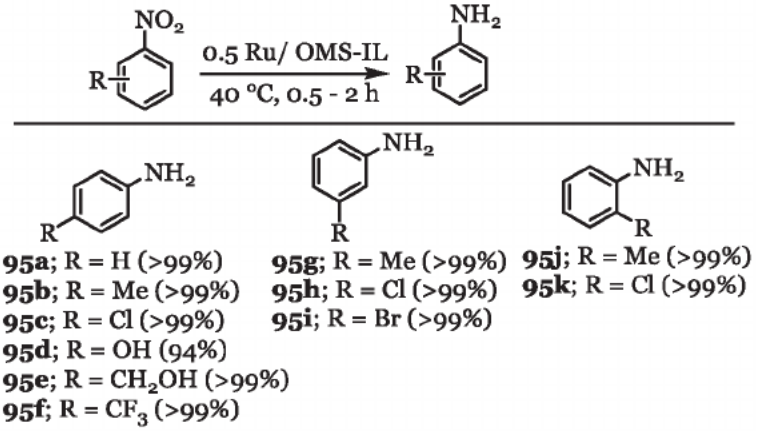

Figure 25.
Reduction of nitro arenes via ruthenium-catalyzed TH.

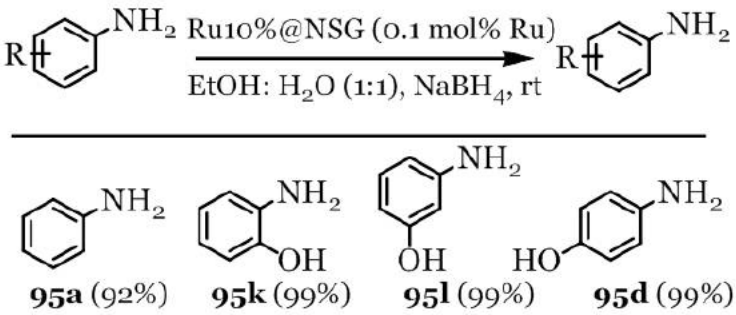

Figure 26.
Ru10%@NSG catalyzed reduction of nitroarenes.

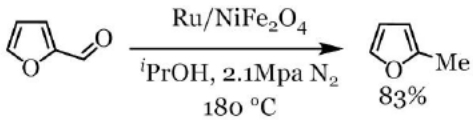

Figure 27.
Conversion of furfural to 2-methylfuran.

anilines in high yields (**95a-95j**). The most highlighted advantages of Ru/OMS-IL are: they show high catalytic activity as well as chemoselectivity. The catalysts are also highly stable and can be easily recovered from the reaction mixture. They showed great reactivity towards the reduction of the functionalized nitro compounds to the aromatic amines in the presence of ethanol as the solvent and hydrazine hydrate as a hydrogen donor and exhibited catalytic activity up to six cycles.

Dabiri and co-workers documented the use of graphene oxide and $RuCl_3$ as the starting precursors and thiourea as a reducing doping agent for the preparation of ruthenium nanoparticles supported on nitrogen and sulfur-doped 3-D graphene (Ru@NSG) nanohybrid through a one-pot hydrothermal method [38]. The catalytic efficiency of ruthenium-nanohybrid was compared with the reduction of nitroarenes to the analogous anilines using $NaBH_4$ as hydrogen doner in 1:1 ethanol/water solvent at room temperature (**Figure 26**). A broad range of functionalized nitro arenes were transformed to their corresponding aniline derivatives in decent yields.

3.3 Miscellaneous heterogeneous transfer hydrogenation

Furfural (FFA) derived from biomass is a promising energy source for the future biorefinery and is industrially produced *via* the dehydration of xylose and arabinose [39]. Over the last few decades, its synthesis received a great interest from the researchers. In this context, Liang and co-workers reported the synthesis of 2-methylfuran (MF) from furfural by using $Ru/NiFe_2O_4$ by catalytic TH using isopropanol as hydrogen donor under mild conditions. At 180 °C and 2.1 MPa nitrogen, the transformation of furfural was achieved up to c*a*. 97%, whereas MF was formed in *ca.* 83% yield (**Figure 27**) [40]. Additionally, the catalyst showed excellent activity up to five consecutive cycles.

4. Conclusion and future perspectives

The simple operational procedure, the mild reaction conditions with high catalytic activity and selectivity make the TH reactions an attractive alternative to direct

hydrogenation using H_2 gas. This research field is growing rapidly due to the high demand for the development of sustainable and green chemistry point of view. Recently, significant developments of Ru-catalyzed both TH and ATH of carbonyl, olefine, nitro and nitrile groups have been achieved. This improvement was perceived in several aspects, such as design of ligands or stabilizers to improve the reaction efficiency, exploration of "green" hydrogen source, generalization of reaction in water, enhancement in asymmetric synthesis, broadening of substrate diversity, and study of reaction mechanisms. Addition to these, TH has been explored in the syntheses of numerous compounds, in particular fine chemicals, bioactive molecules, agrochemicals, and products bearing multi-functional groups.

Although remarkable developments have been made in Ru-catalyzed TH reactions, many challenges and problems remain in most of the reported results. For example, majority of the reported reactions cannot be applicable for the practical and industrial applications. The catalytic results of ATH are not much promising compared to the direct asymmetric hydrogenations. The TH and ATH reactions of imines, olefins, and nitroarenes are very less efficient than that of ketones and are still not explored properly. The use of Ru-catalyzed heterogeneous TH and ATH is still under developed and mostly limited to the ketone group. However, at the present time, new findings are boosting the field by addressing these challenges which indicate TH has a bright future.

This chapter described the recently developed homogeneous and heterogeneous ruthenium catalysts for different substrates ketones, imines, olefins, nitriles, esters and nitroarenes. Attention was focused on mechanistic characteristics of TH/ATH with different ligands frame and their effects on ATH reaction rate.

Acknowledgements

We are grateful for the financial support from BITS, Pilani (DR); DST (SR/WOS-A/CS114/2017(G) (NT) and DST INSPIRE Faculty/CH-174/2015 (GB and PP).

Conflict of interest

The authors declare no conflict of interest.

DOI: http://dx.doi.org/10.5772/ITexLi.96464

References

[1] Evans D, Osborn JA, Jardine FH. Homogeneous hydrogenation and hydroformylation using ruthenium complexes. Nature. 1965;208:1203–1204. DOI: 10.1038/2081203b0

[2] Rylander PN. Hydrogenation methods. Best synthetic methods. London. San Diego. New York. Academic Press. 1985. 1–186 p.

[3] Fujii A, Hashiguchi S, Uematsu N. Ruthenium(II)-catalyzed asymmetric transfer hydrogenation of ketones using a formic acid—triethylamine mixture. Journal of the American Chemical Society. 1996;118:2521–2522. DOI. 10.1021/ja954126l

[4] Hayes AM, Morris DJ, Clarkson GJ. A class of ruthenium(II) catalyst for asymmetric transfer hydrogenations of ketones. Journal of the American Chemical Society. 2005;127:7318–7319. DOI: 10.1021/ja051486s

[5] Hannedouche J, Clarkson GJ, Wills M. A new class of "tethered" ruthenium(II) catalyst for asymmetric transfer hydrogenation reactions. Journal of the American Chemical Society. 2004;126: 986–987. DOI. 10.1021/ja0392768

[6] Nedden HG, Zanotti-Gerosa A, Wills M. The development of phosphine-free tethered ruthenium(II) catalysts for the asymmetric reduction of ketones and imines. The Chemical Record 2016; 16,2623–2643. DOI. 10.1002/tcr.201600084

[7] Mannu A, Grabulosa A, Baldino S. Transfer hydrogenation from 2-propanol to acetophenone catalyzed by $[RuCl_2(\eta^6\text{-arene})P]$ (P=monophosphine) and $[Rh(PP)_2]X$ (PP = diphosphine, X = Cl^-, BF_4^-) complexes. Catalysts. 2020;10: 162–181. DOI. 10.3390/catal10020162

[8] Nordin SJM, Roth P, Tarnai T. Chemistry-A European Journal. 2001;7: 1431–1436. DOI. 10.1002/1521-3765(20010401)7:7<1431::AID-CHEM1431>3.0.CO;2-L

[9] Viji M, Tyagi N, Ramaiah D. Design of air and moisture stable ruthenophane and ruthenium(II)-π complexes and study of their applications in catalysis. ChemistrySelect. 2017;2:11195–11199. DOI. 10.1002/slct.201702445

[10] Gürbüz N, Özcan EÖ, Özdemir I. Preparation of a series of Ru(ii) complexes with N-heterocyclic carbeneligands for the catalytic transfer hydrogenation of aromatic ketones. Dalton Transactions. 2012;41:2330–2339. DOI. 10.1039/C1DT11203A

[11] Viji M, Tyagi N, Naithani N. Aryl appended neutral and cationic half-sandwich ruthenium(ii)–NHC complexes: synthesis, characterisation and catalytic applications. New J Chem. 2017;41:12736–12745. DOI. 10.1039/C7NJ02822A

[12] Navarro M, Segarra C, Pfister T. Structural, electronic, and catalytic modulation of chelating pyridylideneamide ruthenium(II) complexes. Organometallics. 2020;39: 2383–2391. DOI. 10.1021/acs.organomet.0c00205

[13] Hey DA, Sauer MJ, Fischer PJ. Acetate acetylacetonate ampy ruthenium(II) complexes as efficient catalysts for ketone transfer hydrogenation. ChemCatChem. 2020;12:3537–3544. DOI. 10.1002/cctc.202000542

[14] Chen YC, Xue D, Deng JG. Efficient asymmetric transfer hydrogenation of activated olefins catalyzed by ruthenium amido complexes. Tetrahedron Letters. 2004;45:1555–1558. DOI. 10.1016/j.tetlet.2003.12.057

[15] Yamani K, Pierre H. Archambeau A. J. Asymmetric transfer hydrogenation of

gem-difluorocyclopropenyl esters: Access to enantioenriched gem-difluorocyclopropanes Angewandte Chemie International Edition. DOI. doi.org/10.1002/anie.202008572.

[16] Alshakova ID, Gabidullin B, Nikonov GI. Ru-catalyzed transfer hydrogenation of nitriles, aromatics, olefins, alkynes and esters. ChemCatChem. 2018;10:4860–4869. DOI. 10.1002/cctc.201801039

[17] Selva E, Sempere Y, Ruiz-Mart D. Synthesis of allylic amines by asymmetrictransfer hydrogenation of α,β-unsaturated N-(tert-butylsulfinyl) imines. The Journal of Organic Chemistry. 2017;82:13693–13699. DOI. 10.1021/acs.joc.7b02472

[18] Menndez-Pedregal E, Vaquero M, Lastra E. Highly enantioselective hydrogenation of N-aryl imines derived from acetophenones by using Ru–pybox complexes under hydrogenation or transfer hydrogenation conditions in isopropanol. Chemistry-A European Journal. 2015;21:549–553. DOI. 10.1002/chem.201405276

[19] Azua A, Finn M, Yi H. Transfer hydrogenation from glycerol: activity and recyclability of iridium and ruthenium sulfonate-hunctionalized N-heterocyclic carbene catalysts. ACS Sustainable Chemistry Engineering. 2017;5:3963–3972. DOI. 10.1021/acssuschemeng.6b03156

[20] Mizushima E, Yamaguchi M, Yamagishi T. Effective transfer hydrogenation of unsaturated compounds by ruthenium dihydride complex in propan-2-ol. Journal of Molecular Catalysis A: Chemical. 1999; 148:69–75. DOI. 10.1016/S1381-1169(99)00106-5

[21] Pablo O, Guijarro D, Yus M. Synthesis of nitrogenated heterocycles by asymmetric transfer hydrogenation of N-(tert-butylsulfinyl)haloimines. The Journal of Organic Chemistry. 2013;78: 9181–9189. DOI. 10.1021/jo4014386

[22] Barrios-Rivera J, Xu Y, Wills M. Asymmetric transfer hydrogenation of unhindered and non-electron-rich 1-aryl dihydroisoquinolines with high enantioselectivity. Organic Letters. 2020;22:6283–6287. DOI. 10.1021/acs.orglett.0c02034

[23] Werkmeister S, Bornschein C, Junge K. Selective ruthenium-catalyzed transfer hydrogenations of nitriles to amines with 2-butanol. Chemistry-A European Journal. 2013;19:4437–4440. DOI. 10.1002/chem.201204633

[24] Mai VH, Nikonov GI. Transfer hydrogenation of nitriles, olefins, and N-heterocycles catalyzed by an N-heterocyclic carbene-supported half-sandwich complex of ruthenium. Organometallics. 2016;35:943–949. DOI. 10.1021/acs.organomet.5b00967

[25] Paul B, Chakrabarti K, Kundu S. Optimum bifunctionality in a 2-(2-pyridyl-2-ol)-1,10-phenanthroline based ruthenium complex for transfer hydrogenation of ketones and nitriles: impact of the number of 2-hydroxypyridine fragments. Dalton Transactions. 2016;45:11162–11171. DOI. 10.1039/C6DT01961G

[26] Kim D, Kang B, Hong SH. Ruthenium-catalyzed selective imine synthesis from nitriles and secondary alcohols under hydrogen acceptor- and base-free conditions. Organic Chemistry Frontiers. 2016;3:475–479. DOI. 10.1039/C5QO00378D

[27] Lee SH, Nikonov GI. Transfer hydrogenation of ketones, nitriles, and esters catalyzed by a half-sandwich complex of ruthenium. ChemCatChem. 2015;7:107–113. DOI. 10.1002/cctc.201402780

[28] Robertson A, Matsumoto T, Ogo S. The development of aqueous transfer

hydrogenation catalysts. Dalton Transactions. 2011;40:10304–10310. DOI. 10.1039/C1DT10544B

[29] Wright WRH, Palkovits R. Development of heterogeneous catalysts for the conversion of levulinic acid to γ-valerolactone. ChemSusChem. 2012;5: 1657–1667. DOI. 10.1002/cssc.201200111

[30] Wang D, Astruc D. The golden age of transfer hydrogenation. Chemical Reviews. 2015;115:6621–6686. DOI. 10.1021/acs.chemrev.5b00203

[31] Marcos R, Jimeno C, Pericàs MA. Polystyrene-supported enantiopure 1,2-diamines: development of a most practical catalyst for the asymmetric transfer hydrogenation of ketones. Advanced Synthesis & Catalysis. 2011;353:1345–1352. DOI: 10.1002/adsc.201000948

[32] Xu X, Wang R, Wan J. Phosphonate-containing polystyrene copolymersupported Ru catalyst for asymmetric transfer hydrogenation in water. RSC Advances. 2013;3:6747–6751. DOI: 10.1039/c3ra22057e

[33] Wang R, Wan J, Ma X. Anchored $[RuCl_2(p\text{-cymene})]_2$ in hybrid zirconium phosphate-phosphonate coated and pillared with double-stranded hydrophobic Linear polystyrene as heterogeneous catalyst suitable for aqueous asymmetric transfer hydrogenation. Dalton Transactions. 2013;42:6513–6522. DOI: 10.1039/c3dt33015j

[34] Molla RA, Roy AS, Ghosh K. Polymer anchored ruthenium complex: a highly active and recyclable catalyst for one-pot azide-alkyne cycloaddition and transfer-hydrogenation of ketones under mild conditions. Journal of Organometallic Chemistry. 2015;776: 170–179. DOI: 10.1016/j.jorganchem.2014.11.007

[35] Baig RBN, Varma RS. Magnetic silica-supported ruthenium nanoparticles: an efficient catalyst for transfer hydrogenation of carbonyl compounds. ACS Sustainable Chemical Engineering. 2013;1:805–809. DOI: 10.1021/sc400032k

[36] Hudson R, Chazelle V, Bateman M. Sustainable synthesis of magnetic ruthenium-coated iron nanoparticles and application in the catalytic transfer hydrogenation of ketones. ACS Sustainable Chemical Engineering. 2015; 3:814–820. DOI: 10.1021/acssuschemeng.5b00206

[37] Wei N, Zou X, Huang H. Preparation of well-ordered mesoporous-silica-supported ruthenium nanoparticles for highly selective reduction of functionalized nitroarenes through transfer hydrogenation. European Journal of Organic Chemistry. 2018:209–214. DOI: 10.1002/ejoc.201701228

[38] Dabiri M, Miraghaee S, Nikbakht R. A one-step method for preparation of Ru nanoparticle decorated on three-dimensional graphene with high catalytic activity for reduction of nitroarenes. Journal of Cluster Science. DOI: 10.1007/s10876-020-01860-1

[39] Gilkey MJ, Xu B. Heterogeneous catalytic transfer hydrogenation as an effective pathway in biomass upgrading. ACS Catalysis. 2016;6:1420–1436. DOI: 10.1021/acscatal.5b02171

[40] Wang B, Li C, He B. Highly stable and selective $Ru/NiFe_2O_4$ catalysts for transfer hydrogenation of biomass-derived furfural to 2-methylfuran. Journal of Energy Chemistry. 2017;26: 799–807. DOI: 10.1016/j.jechem.2017.04.008

Hydrogenation and Hydrogenolysis with Ruthenium Catalysts and Application to Biomass Conversion

Thomas Ernst Müller

Abstract

With the rising emphasis on efficient and highly selective chemical transformations, the field of ruthenium-catalysed hydrogenation and hydrogenolysis reactions has grown tremendously over recent years. The advances are triggered by the detailed understanding of the catalytic pathways that have enabled researchers to improve known transformations and realise new transformations in biomass conversion. Starting with the properties of ruthenium, this chapter introduces the concept of the catalytic function as a basis for rational design of ruthenium catalysts. Emphasis is placed on discussing the principles of dissociative adsorption of hydrogen. The principles are then applied to the conversion of typical biomolecules such as cellulose, hemicellulose and lignin. Characteristic features make ruthenium catalysis one of the most outstanding tools for implementing sustainable chemical transformations.

Keywords: ruthenium, catalysis, reaction network, sequential reactions, hydrogen dissociation, hydrogenation, hydrogenolysis, biomass conversion

1. Introduction

Life on earth inherently depends on the element carbon creating the heart of a myriad of chemical compounds that, together with water and some inorganic compounds, build living matter. Over geologic periods, life has established a dynamic equilibrium of the flows of carbon through the different geo-habitats [1]. With the rise of mankind, this balance has been undermined through the exploitation of vast amounts of fossil resources for generating heat and materials. The carbon dioxide (CO_2) emissions from combustion of fossil resources have resulted in rising atmospheric CO_2 concentrations and an increasingly evident change in the climate worldwide. Replacing fossil resources that at present make up more than 90% of the energy demand and the feedstock for the chemical industry [2] is one of the most pressing challenges of mankind. All our primary energy demand of annually 12.5 TW a^{-1} could be covered by harnessing a fraction of the 8405 TW a^{-1} renewable energy available annually that comprises solar, wind, geothermal, tidal and wave energy [3]. Nevertheless, a sustainable energy supply will be needed for carbon-based compounds in order to close carbon recycle streams. Biomass is a globally

available resource that is considered a suitable alternative feedstock for producing basic chemical building blocks, so-called platform molecules [4], that could substitute the current fossil-based platform chemicals [5].

Biomass largely consists of complex molecules comprising mostly oxygen and other heteroatoms. Lignocellulose, the structural component of plants and the largest fraction of plant biomass, is essentially composed of cellulose, hemicellulose and lignin. Break down of the structure by depolymerisation of the corresponding molecular entities, followed by oxygen removal, yields fuels and platform chemicals for the value-chain of the chemical industry. Sustainable conversion depends on efficient conversion steps obtained ideally via catalytic processes. In this context, the catalytically highly active element ruthenium provides unique properties. Despite ruthenium being counted among the noble metals, it resembles a non-noble metal in many aspects. In metallic form, ruthenium atoms are highly polarisable. Unlike the higher homologue platinum, e.g., that has similar atomic radius, ruthenium has a much higher average electric dipole polarizability. Consequently, distinct catalytic functions can be realised with ruthenium catalysts.

To help readers understand why ruthenium catalysts are so frequently employed in biomass conversion, this chapter will first investigate the properties of ruthenium. Here, the catalytic properties of ruthenium are linked with its propensity to adsorb certain molecular entities. After exploring the interaction of adsorbed molecules with ruthenium surfaces, we will discuss the nature of selected adsorption states, the corresponding binding energies and structures of the adsorption complexes including ordering phenomena observed for molecules co-adsorbed on the ruthenium metal surface. This sets the scene for rational design of catalysts that are specific for the conversion of chemical entities in biomass. Last but not least, we will discuss selected examples for intriguing transformations of biomolecules.

To note here is that this chapter does not aim to comprehensively review the available data on catalysis with ruthenium. Nor does it attempt to summarise all data on the conversion of biomass with ruthenium catalysts. The extensive interest in this field is reflected presently by the more than 800 articles published each year on catalysis with ruthenium, more than 110 of which focus on biomass conversion. Instead, this chapter aims to summarise the catalytic principles governing hydrogenation and hydrogenolysis reactions with heterogeneous ruthenium catalysts with particular focus on applications in biomass conversion. Cited data and papers were selected to exemplify the field and illuminate the discussion.

2. Ruthenium

Ruthenium, from Latin *ruthenia* ("Russia"), is one of the late transition metals and is located in the periodic table in the 5th period and group 8 (**Figure 1**). With an abundance of 7.0 ± 0.9 ng·g^{-1} in the silicate shell [6], ruthenium is one of the rarest non-radioactive elements on earth. Its low abundance is due to segregation of the platinum group elements in the core of Earth that was partially compensated by addition of 0.3–0.8% of chondritic material after core formation had been complete [6]. Ruthenium is found mostly in deposits associated with the other platinum-group elements [7] and as the rare RuS_2 mineral called laurite [8]. Ruthenium is a silvery white, extraordinarily hard and brittle metal. With a density of 12.45 g·cm^{-3} [9], ruthenium is the second lightest platinum group metal after palladium. In the electronics industry, it is used in devices for perpendicular recording [10], a technology applied in hard disks that enables high-density data storage on magnetic media.

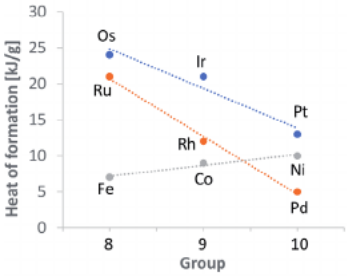

7	8	9	10	11	12
Mn	Fe	Co	Ni	**Cu**	Zn
Tc	**Ru**	**Rh**	**Pd**	**Ag**	Cd
Re	**Os**	**Ir**	**Pt**	**Au**	**Hg**

Figure 1.
Calculated heats of formation of the (unstable) binary hydrides M_nH_y ($n > y$) for group 8–10 transition metals [12] (left) and position of ruthenium (circle) in the periodic table (right) indicating the group of noble metals (bold, grey) and the platinum group metals (dark grey).

With regard to its chemical properties, ruthenium is stable in the absence of oxygen against non-oxidising acids. Consequently, it counts as a noble metal. Even so, ruthenium resembles a non-noble metal in many respects. Similar to the other metals of the 7th, 8th and 9th group of the periodic table, ruthenium does not form stable binary hydrides under ambient conditions; this region of the periodic table is called the "hydride gap" [11]. For these elements a positive value is obtained for the heats of formation calculated for the binary hydrides (**Figure 1**) [12]. Nonetheless, ruthenium monohydride (RuH) is formed by reaction of the elements at pressures above 14 GPa at room temperature. It transforms to Ru_3H_8 at pressures of more than 50 GPa and temperatures exceeding 1000 K, adopting a cubic structure, and RuH_4, when the pressure is increased above 85 GPa, crystallising in a structure comprising corner-sharing H_6 octahedra [13]. Interestingly, the hydride ligand exerts a strong *trans* influence in ruthenium complexes (*vide infra*), thereby weakening the binding of ligands located in *trans* position [14].

Due to its ability to dissociate hydrogen on the metal surface, ruthenium, in its metallic form, finds numerous applications as a catalyst in chemical processes such as ammonia synthesis, methanation, hydrogenation or hydrogenolysis (*vide infra*). Moreover, it can catalyse the oxidation of alcohols to aldehydes and carbonic acids. Ruthenium compounds are distinguished for their rich coordination chemistry, and compounds with ruthenium in oxidation states between −2 and + 8 are known. The most stable and most common oxidation states are +3 and + 4. With ruthenium at an intermediate oxidation state, +2, +3 or + 4, complexes have also been obtained that, similar to other late transition metal clusters (e.g., Ni, Pd, Pt [15]; Pt [16]; Co, Rh, Ir [17]; Au [18]), comprise ruthenium-ruthenium bonds. Ruthenium complexes, like Grubbs catalyst and Noyori catalyst (*vide infra*), play a significant role in chemical syntheses. Likewise, ruthenium compounds are employed in olefin metathesis polymerisation of cyclic alkenes [19–21]. The perovskite mixed oxide Ba_2LaRuO_6 is used in automotive exhaust gas catalysts [22]. Titanium electrodes covered with a layer of RuO_2 are applied in the chloralkaline electrolysis [23]. Moreover, ruthenium nanoparticles are interesting Deacon catalysts for the gas-phase oxidation of hydrogen chloride to chlorine [24].

3. Concept of catalytic function

At first sight, most catalytic systems appear to be unnecessarily complex. A look at biologic systems, however, reveals that many biological systems are built on chains of different catalysts. There, substrate molecules are passed from one enzyme to another. Thus, in the conversion of molecular oxygen, about ten

different catalysts are involved before the oxidising equivalents are reacted with carbon compounds [25].

Thinking in terms of sequences of consequential reaction steps is a useful strategy to rationally design heterogeneous catalysts. A good starting point is considering the catalytic functions [26] necessary for realising the desired transformations. The dissociative adsorption of molecular hydrogen is one of the key steps for hydrogenation and hydrogenolysis reactions, the focus of this chapter. In the case of transfer hydrogenation, the concepts equally apply to suitable hydrogen surrogates. As such, dissociative adsorption of hydrogen, as one of the important steps of catalysis, will be elucidated below. With the Langmuir-Hinshelwood mechanism most prominent in catalysis with late transition metals, co-adsorption of the substrate and transfer of hydrogen atoms to an unsaturated substrate need to be considered next. Other catalytic functions important for biomass conversion are the ability of a catalyst to either cleave or form C-C, C-O or C-N bonds. This results in a list of complementary catalytic functions that are required for realising the desired transformation. Thereby it is useful to consider orthogonal catalytic functions that do not interfere with each other. Rather molecules ought to be passed from one catalytic function to the next, like in a molecular assembly line. Noteworthy, such assembly lines may involve a single material comprising different functions. Frequently the support plays an important role even when the actual transformation occurs on supported metal nanoparticles. One aspect to be considered regarding hydrogenation and hydrogenolysis reactions is spill-over of hydrogen to surface sites on the support. Another concept for realising such assembly lines involve mechanical mixtures of two or more materials that comprise different catalytic functions. An example is given below. Whereas heterogeneous ruthenium catalysts can accommodate many of these catalytic functions, homogeneous ruthenium catalysts enable unique, highly distinct catalytic transformations. Once the necessary catalytic functions have been identified, it is useful to derive the link to the desired active state and the structure of the pre-catalysts that is to be used. This provides a straightforward path for rationally designing a particular catalyst for the desired transformation.

4. Sequential reactions

Rational and straight-forward catalyst design is the foundation of systematic conceptualisation of highly active catalysts that provide extraordinary specificity for a given transformation. Such specificity is essential upon designing catalysts for biomass transformations, because the chemist typically encounters many different molecules or molecular entities rather than single types of molecules that are to be converted. If chosen in the appropriate way, the catalyst will adsorb and convert only one type of molecule or chemical entity while leaving all other molecules and chemical entities untouched. This concept is also valuable for devising catalysts for sequentially connected, mutually exclusive catalytic reactions.
To develop such catalysts, the chemist needs to fundamentally understand the nature and catalytic role of active sites to guide the design of new and improved catalysts. Two examples are described here. The general principle is exemplified for a radical reaction with a MOF catalyst; the potential is then demonstrated for the hydrogenation of a multifunctional substrate over a Ru/CNT-Pt/CNT catalyst mixture.

Metal organic framework (MOF) compounds are porous materials commonly obtained by hydrothermal reaction of metal ions and bridging organic

ligands [27]. MOFs combine the high porosity of a heterogeneous catalyst with the tunability of molecular functional groups. This combination of features has been exploited for the sequential oxidation of alcohols to carboxylic acids with molecular oxygen in the presence of TEMPO modified MOF UiO-68 [28]. The conversion involves two sequential oxidation steps, i.e., the aerobic oxidation of alcohols to aldehydes, and the consequential autoxidation of the aldehydes to carboxylic acids. Whereas the first step is a radical reaction, the second step is inhibited by radicals. Thus, the two reactions are mutually exclusive. Complete removal of the MOF catalyst after the first radical-catalysed aerobic oxidation step by filtration provides the radical scavenger-free conditions that are necessary for the second radical-inhibited autoxidation step. This is a beautiful example of the use of a functional heterogeneous catalyst for a sequential organic transformation.

The concept of connecting consecutive one-pot reactions with a "molecular assembly line" has been explored for the hydrogenation of bifunctional substrates A-B to products A^H-B^H [29]. Two catalysts were chosen in such a way that one catalyst (M^1) preferentially adsorbs one of the substrate moieties, and the other catalyst (M^2) preferentially adsorbs the second substrate moiety (**Figure 2**). In this case both catalysts function optimally, thereby yielding improved rates and selectivities compared to single or conventional bimetallic catalysts [29]. Moreover, substrate inhibition can be avoided. By adjusting the relative quantity of the two catalysts, the relative rates of the two sequential transformations can be adjusted to be equal, because this results in the highest overall rate at the lowest catalyst concentration.

This concept has been applied successfully to the full hydrogenation of nitroaromatics to cycloaliphatic amines over a mechanical mixture of carbon nanotube (CNT)-supported Ru/CNT - Pt/CNT catalysts [29]. Noteworthy is that the aromatic ring, considered to be "soft" due to the aromatic π-system delocalised over six carbon atoms, preferentially adsorbs on ruthenium that is readily polarizable. The nitro group, considered to be "hard" due to the negative charge which is delocalised over only two oxygen atoms, preferentially adsorbs on platinum with highly shielded d-electrons. Notably, metallic Ru and Pt have similar atomic radii of 133 and 137 pm, while differing in the static average electric dipole polarizability of 9.6 and 6.4 10^{-24} cm^3, respectively. A 95:5 mixture of the Ru/CNT (M^1) and Pt/CNT (M^2) catalysts provides the required equal rates for hydrogenation of the two respective moieties and optimum selectivity to the target product cyclohexylamine (**Figure 3**).

		Affinity	
		M^1	**M^2**
Substrate	A-B	High	Low
Intermediate	A^H-B	Low	High
Product	A^H-B^H	Low	Low

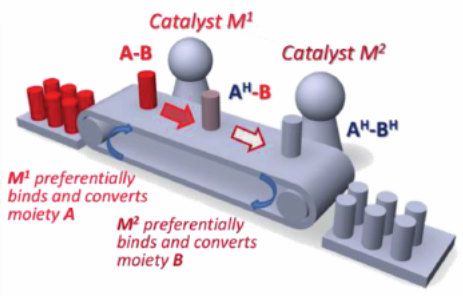

Figure 2.
Concept of a molecular assembly line for catalysing the consecutive one-pot reaction of a bifunctional subtract A-B to product a^H-B^H with a mixture of orthogonal catalysts M^1 and M^2 (right) and requirements concerning the affinity for binding of the respective moieties to the metal centres M^1 and M^2 (table, left).

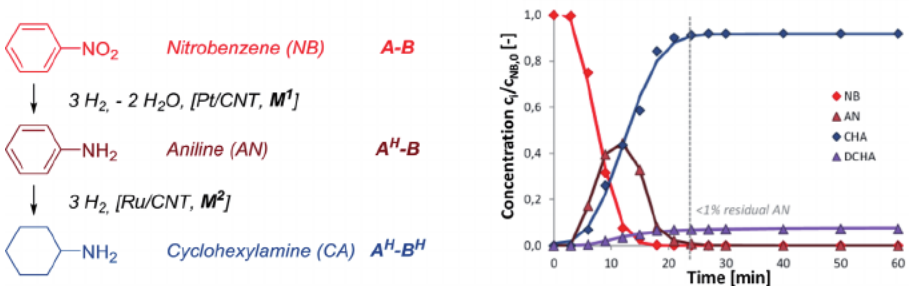

Figure 3.
Concept of a molecular assembly line applied to the hydrogenation of nitrobenzene (NB, A-B, blue) to cyclohexylamine (CA, d^H-B^H, brown) over a mixture of orthogonal catalysts Pt/CNT (M^1) and Ru/CNT (M^2) and time-concentration profile showing also the intermediate aniline (AN, A^H-B, green) and the side product dicyclohexylamine (DA, purple) (right).

5. Catalytic transformations with ruthenium catalysts

Based on the unique catalytic functions given by heterogeneous and homogeneous ruthenium catalysts, a large number of important transformations have been realised. Many of these transformations are applied on an industrial scale. For hydrogenation and hydrogenolysis reactions, in particular, heterogeneous ruthenium catalysts are among the most frequently applied catalysts, because they provide outstanding activities and excellent selectivities.

5.1 Ammonia synthesis and methanation with ruthenium catalysts

Analogous to iron and osmium, ruthenium catalyses the formation of ammonia from nitrogen and hydrogen (Eq. 1). Ruthenium has superior catalytic activity compared to iron [30] and results in enhanced NH_3 yields at lower pressures. A ruthenium catalyst, which is supported on a carbon matrix and improved by barium and caesium as promoters, has been in industrial use in two production sites in Trinidad since 1998 [31]. As the slow methanation of the carbon support [32] interferes with the process, alternative supports are preferred for ruthenium catalysts applied in ammonia synthesis. Efficiencies as close as possible to the theoretical limit are highly relevant for decentralised, islanded ammonia production plants [33, 34], where round-trip efficiencies of up to 61% can be reached [35]. An example for a highly active and stable low-temperature ammonia catalyst are ruthenium nanoparticles on a Ba-Ca$(NH_2)_2$ support [36]. At a weight hourly space velocity (WHSV) of 36 L g^{-1} h^{-1}, a rate of 23.3 $mmol_{NH3}$ g^{-1} h^{-1} is obtained at 300 °C and 9 bar. Such catalytic activity is about 6 times higher than that of industrial iron-based benchmark catalysts (at 340 °C) and 100 times higher than that of industrial ruthenium-based benchmark catalysts (Cs-doped Ru/MgO, at 260 °C) [36]. In addition, for the reverse reaction of ammonia cleavage, high activities are likewise important [37, 38] and imply the use of ruthenium catalysts for the upcoming production of CO_x-free hydrogen by ammonia cleavage in energy applications.

$$N_2 + 3H_2 \rightleftarrows 2NH_3 \quad \rightarrow \quad \Delta H_r^\circ = -91.8\,kJ\,mol^{-1} \qquad (1)$$

Analogous to nickel, ruthenium catalyses methanation, the production of methane from hydrogen and carbon dioxide (Eq. 2) or carbon monoxide (Eq. 3), the so-called Sabatier reaction. Water is obtained as by-product. Carbon dioxide

methanation could be seen as the combination of the reverse water gas shift reaction that converts a mixture of carbon dioxide and hydrogen to carbon monoxide and water (Eq. 4), and methanation. Over ruthenium catalysts, such as Ru/Al_2O_3, the coproduction of CO is negligible [39]. This suggests a different reaction pathway not involving the intermediate formation of CO. Both reactants, H_2 and CO_2, are strongly adsorbed on the surface [39] giving rise to a Langmuir-Hinshelwood mechanism. Ruthenium catalysts are highly selective to methane and provide a very low fraction of side products, such as higher hydrocarbons, alcohols, or formic acid. Due to the exothermicity and volume reduction, the reaction is thermodynamically favoured at low temperatures and high pressures. Typical operation conditions are 200–500 °C and pressures of 10–30 bar [40]. Since ruthenium catalysts have a higher activity than nickel catalysts, they enable higher conversions at low temperature. Methanation has long been used for removing CO_x from the hydrogen-nitrogen syngas mixture used in ammonia production [41]. Carbon dioxide methanation is an option for biogas upgrading that constitutes an alternative to the removal of carbon dioxide [42]. Carbon dioxide methanation has also been discussed in the context of storing intermittent energy generated as a result of electricity production from renewable resources. Methane can be transported and stored in the existing natural gas grid. Therefore, methanation of carbon dioxide is being discussed as one of the promising Power-to-X technologies [43].

$$CO_2 + 4\ H_2 \rightleftarrows CH_4 + 2\ H_2O \quad \rightarrow \quad \Delta H_r^\circ = -165.12\ \text{kJ mol}^{-1} \qquad (2)$$

$$CO + 3\ H_2 \rightleftarrows CH_4 + H_2O \quad \rightarrow \quad \Delta H_r^\circ = -206.28\ \text{kJ mol}^{-1} \qquad (3)$$

$$CO_2 + H_2 \rightleftarrows CO + H_2O \quad \rightarrow \quad \Delta H_r^\circ = +41.16\ \text{kJ mol}^{-1} \qquad (4)$$

5.2 Hydrogenation with ruthenium catalysts

Ruthenium is an efficient catalyst for hydrogenating aromatics, acids, ketones and unsaturated nitrogen compounds. The selective hydrogenation of aromatic amines to cycloaliphatic primary amines is an industrially relevant transformation, but is impaired by formation of secondary amines and other side products. Modification of carbon nanotube (CNT)-supported ruthenium catalysts Ru/CNT catalysts with a base (LiOH) significantly improves selectivity in toluidine hydrogenation [44, 45] without decreasing the activity of the catalysts. LiOH-modified Ru/CNT catalysts can efficiently convert also other challenging substrates, such as methylnitrobenzenes [46]. The effect of LiOH is understood as (i) LiOH reducing acidic sites on the catalyst support, (ii) enhancing hydrogen dissociation and reducing hydrogen spillover from ruthenium to the support (*vide infra*) and (iii) shifting the adsorption mode of the substrate on the ruthenium metal nanoparticles from binding of the amine group to the aromatic ring. In a similar manner, nitro compounds are able to change the binding mode of aromatic amines to the ruthenium surface [47, 48].

5.3 Hydrogenolysis with ruthenium catalysts

The hydrogenolysis of alkanes is an important unit operation in refineries for reducing the chain length of acyclic alkanes. It also serves as a model for the hydrogenolysis of C-O and C-N bonds in various applications relevant for oil refining

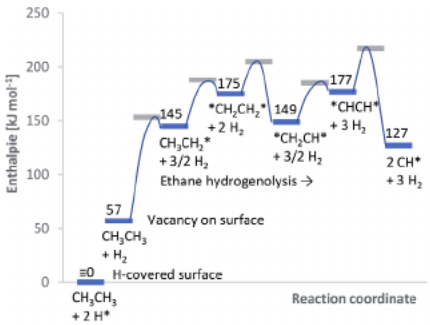

		10	11
		Ni CH_2CH * +39	**Cu** CH_3CH_2 * -72
8	**9**		
Ru $*CH_2CH$ * +51	**Rh** $*C_HC*$ +69	**Pd** CH_3CH * +12	**Ag** CH_3CH_2 * -221
Os $*CH_2CH$ * +67	**Ir** $*CH_2CH$ * +88	**Pt** CH_3C* +34	**Au** CH_3CH_2 * -133

Figure 4.
*Calculated reaction enthalpies for the elementary steps in the hydrogenolysis of ethane on a Ru(001) surface (593 K, left) and intermediates with the lowest activation free-energy barrier relative to *CH-CH* bond activation (right) [49]. Energies are relative to a surface covered with chemisorbed hydrogen (H*); * denotes coordination to the ruthenium surface.*

and biofuel generation. Cleavage of the C-C bond is preceded by a series of quasi-equilibrated dehydrogenation steps (see **Figure 4** for ethane hydrogenolysis [49]). Desorption of two chemisorbed hydrogen atoms generates the necessary adsorption sites on the surface. Physisorbed ethane dissociates stepwise via CH_3CH_2*, $*CH_2CH_2$*, $*CH_2CH$* to form *CHCH*. Activation of the C-C bond in *CH-CH* has a lower intrinsic barrier in further dehydrogenation. Cleavage of the C-C bond in the *CH-CH* surface intermediate is thought to be the rate limiting step. During the entire process, the surface is covered to a large extent with chemisorbed hydrogen (H*). The high hydrogen coverage also enhances the re-hydrogenation of the unsaturated fragments to produce methane that is desorbed from the surface.

Similar to Ru, C-C bond cleavage in more deeply dehydrogenation intermediates is preferred for Os, Rh, Ir, and Pt relative to cleavage of the C-C bond in more saturated intermediates (**Figure 4**, right). Cleavage of the C-C bond in more saturated intermediates starts to compete as one moves more to the right of the periodic table. For the group 10 metals (Ni, Pd, Pt), the most favourable mechanism is C-C activation in *CHCH*, while other intermediates have activation energies of about 40 kJ mol^{-1} suggesting that multiple routes may coexist. For the coinage metals (Cu, Ag, Au), there is a preference for cleavage of the C-C bond in the most saturated intermediate CH_3CH_2*. The overall free-energy barrier for C-C bond activation is lowest for Ru providing the highest turnover rate for *CHCH* bond cleavage. Thus, the less noble metal Ru is more active than the more noble metals. This is also consistent with experimental data that show a decrease in the turnover rate in the sequence Ru > Rh > Ir > Pt [49].

5.4 Catalysis with molecular ruthenium catalysts

Some very active molecular ruthenium (pre)catalysts were developed for catalytic hydrogenation and transfer hydrogenation. Selected examples are shown in **Figure 5**. Ruthenium hydride complexes [50] with phosphine or diamine ligands are active for the hydrogenation of many substrates. Transfer hydrogenation with ruthenium catalysts is frequently used for the reduction of ketones to alcohols [51] and amides, imines and nitriles to amines [52, 53]. Isopropanol is commonly employed as hydrogen donor [54]. The hydrogenation and transfer hydrogenation can be stereoselective if the starting material is prochiral and a chiral complex is employed [52, 55]. However, chiral BINAP catalysts can reduce only functionalised ketones in a stereoselective manner. Whereas Noyori precatalysts of the type [$RuCl_2$(diphosphane)(diamine)] enable the asymmetric hydrogenation of ß-keto esters as well as the

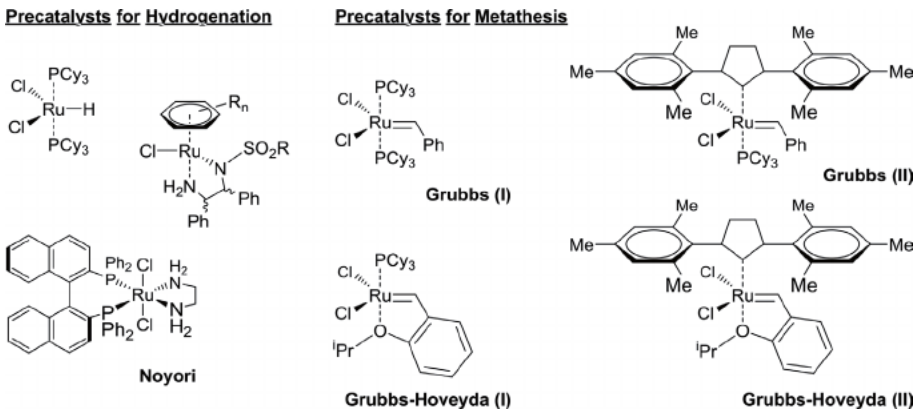

Figure 5.
Examples of molecular ruthenium complexes that are used in homogeneously catalysed hydrogenation and metathesis reactions.

reduction of prochiral ketones and aldehydes, olefins are usually not converted. The stereoselectivity is enhanced, when the substituents on the ligands differ in size. The concept of bifunctional asymmetric catalysis with ruthenium complexes has later been transferred to a variety of C-C, C-O and C-N forming reactions [56].

Ruthenium is also the central metal in the Grubbs catalysts [57], which are among the most important precatalysts for olefin metathesis. There are two generations of Grubbs catalysts (**Figure 5**). The first generation is often employed for ring-opening polymerisation (ROMP [21]) and for the synthesis of large rings by metathesis. The second generation [58] has a much higher activity. In Grubbs-Hoveyda catalysts, one of the tricyclohexylphosphine (PCy_3) ligands of the Grubbs catalysts is replaced by an aromatic ether that links to the carbon substituent. There is a wide field for ruthenium-catalysed cyclisation reactions [59]. Ruthenium *N*-heterocyclic carbene (NHC) complexes based on the second-generation Grubbs catalysts have also been applied in a variety of related transformations, such as hydrogenation [60], hydrosilylation, and isomerization [61]. Metathesis can also be combined with a second chemical transformation to tandem reaction sequences [61]. Likewise, living free radical polymerizations are feasible with ruthenium complexes [62]. An example is the polymerisation of methyl methacrylate with $[RuCl_2(PPh_3)_3]$ as a catalyst [63, 64].

6. Hydrogen adsorption on metallic ruthenium

As for the other platinum group elements, metallic ruthenium is characterised by excellent catalytic results for a variety of transformations. The interaction of molecular hydrogen with the surface of ruthenium is particularly interesting as far as catalytic hydrogenation or hydrogenolysis reactions are concerned; it will be analysed in further detail here. Accordingly, the fundamental concepts discussed here likewise are valid for transfer hydrogenation reactions.

Dissociative chemisorption of hydrogen on the surface is a pivotal step of the transformation and is often rate-limiting. The adsorption of hydrogen may be considered as competing molecular and dissociative adsorption of hydrogen (**Figure 6**) [65]. Molecular adsorption is governed by the van der Waals interactions between molecular dihydrogen and the ruthenium surface [66]. On a Ru(0001) surface with point group symmetry C_{3v} [67], the four high-symmetry adsorption sites involve binding of the hydrogen molecule to a single ruthenium atom (*on top*), a position bridging two ruthenium atoms (*brg*) or three-fold coordination at *fcc* or *hcp* sites (**Figure 6**) [67, 68].

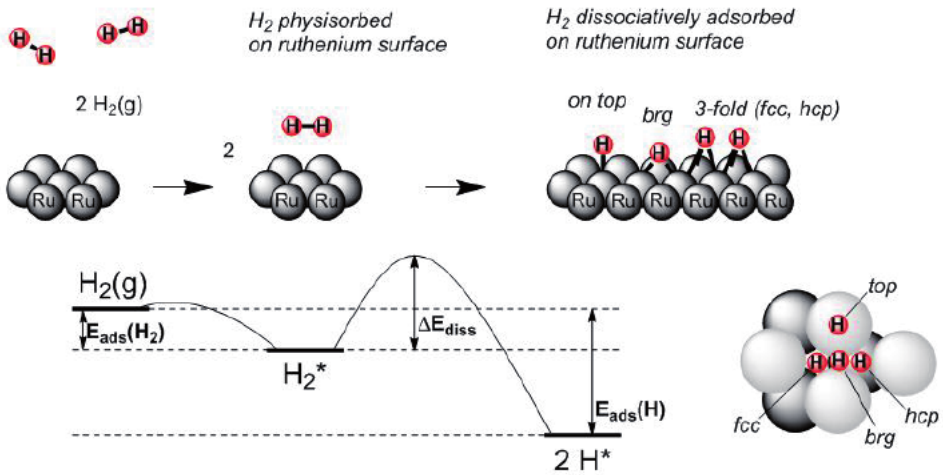

Adsorption site	$\Delta H_{ads}(H_2)$ [kJ·mol^{-1}]	ΔE_{diss} [kJ·mol^{-1}]	$\Delta H_{ads}(H)$ [kJ·mol^{-1}]
on top	-20.3	16.4	-207.9
brg	-4.8	28.9	-242.7
fcc	-4.8	41.5	-258.6
hcp	-4.8	48.2	-258.2

Figure 6.
Physisorption and chemisorption of molecular hydrogen on extended ruthenium surfaces and the C_{3v} high-symmetry adsorption sites on the Ru(0001) surface on top (u_{CM} = 0; v_{CM} = 0), brg (1/2;1/2), fcc (2/3;1/3) and hcp (1/3,2/3) (top) [67] and changes in adsorption energy for physisorption of hydrogen $E_{ads}(H_2)$, dissociation barrier ΔE_{diss} and chemisorption of hydrogen $E_{ads}(H)$ (physisorption vdW-DF2 + PBE level, [66], chemisorption GGA with periodic plane-wave basis set, 1 monolayer coverage, no correction for zero point energy [78].

Physisorption attracts a charge of −0.04 electrons to the hydrogen molecule [66]. This is consistent with promotion of dissociative adsorption of hydrogen in the presence of alkaline metal cations [69]. Electron transfer to the anti-binding orbitals of hydrogen and upward shift of the transition metal d-band centre towards the Fermi level are likely explanations.

For coordination of hydrogen in the molecular state [70], the *on top* site provides the highest adsorption energy of −20.3 kJmol^{-1} and the lowest dissociation barrier of 16.4 kJ mol^{-1} [66]. Consequently, an entrance channel barrier is missing, and this dissociation channel appears to be active even for dissociation of H_2 molecules with negligible incident energy. Nevertheless, a suitable approach of the H_2 molecules to the ruthenium surface is essential for such a low dissociation barrier. Dissociation of molecular hydrogen on ruthenium is a rather slow process [69], and equilibrium is obtained only after several hours [71]. Point-like defect structures, like Ru vacancies or Ru adatoms on the surface do not seem to provide comparably low dissociation barriers. Other defects that are present at finite temperatures on the surface include steps, kinks and adatom islands [72, 73]. Low coordinated defect sites may be the preferential sites for a direct dissociative adsorption pathway on ruthenium nanoparticles [74]. Due to the low barrier, the *on top* site is likely the most reactive site for hydrogen dissociation on extended ruthenium surfaces [67]. For supported ruthenium catalysts, a rapid H_2/D_2 isotopic equilibration reaction has been reported [69]. Even so, the isotope exchange is slowed down considerably in the presence of alkaline metal cations that prevent spillover [70, 75] of hydrogen atoms to the support.

Dissociative adsorption occurs when the bonds formed between the two hydrogen atoms and the ruthenium surface are stronger than the strength of the hydrogen–hydrogen bond (460 kJ mol^{-1}). This is the case when the hydrogen atoms adsorb at either

the *fcc* or the *hcp* hollow site (−258.6 and − 258.2 kJmol^{-1}, respectively). Noteworthy is the relatively small difference in energy between the *fcc* and *hcp* hollow sites. As for extended surfaces of other late transition metals, hydrogen, thus, has a pronounced preference for binding to multi-fold coordination sites [76, 77]. As far as metal clusters and nanoparticles are concerned, the number of adsorption sites can differ, whereby specific 2-, 3-, and 4-fold coordination to surface atoms has been reported [76]. The barrier for surface diffusion [70] of hydrogen is rather small and was estimated to 13–21 kJ mol^{-1}. There is a small decrease of −12.1 kJ·mol^{-1} in adsorption energy with coverage θ increasing from partial (1/3) to monolayer coverage.

At low temperature, the catalytically active ruthenium surface is normally covered to a large extent with hydrogen. The surface coverage remains incomplete under reaction conditions even at elevated pressures. Thus, at 100 bar, a coverage θ of ca. 85% was calculated at room temperature, whereby it decreased to ca. 70% at increasing temperature (500 °C) [78]. Temperature-programmed desorption of hydrogen from ruthenium catalysts shows two distinct desorption peaks as a characteristic feature [71, 74]. The peaks represent strongly and weakly chemisorbed hydrogen, consistent with distinct NMR signals at −60 and − 30 ppm [79]. The corresponding heats of adsorption were determined to be 40–70 kJ·mol^{-1} (α_H) and 10 kJ mol^{-1} (β_H), respectively, by microcalorimetry [69]. This suggests that part of the hydrogen is not dissociated over real samples. Consequently, a chemisorption stoichiometry x_M exceeding unity is frequently considered (x_M = 1.4 [74]; 2 [71, 80]; 5 [79]). Although surface processes dominate, subsurface hydrogen cannot be ruled out [70, 81]. Furthermore, the support can act as a reservoir for hydrogen [69].

Under catalytic conditions, surfaces are saturated by hydrogen or one or more adsorbed intermediates. This leads to strong co-adsorbate interactions. These interactions are not accounted for in kinetic models built on Langmuir isotherms. In real catalysts, however, mostly supported metal nanoparticles are employed, where these co-adsorbate interactions are lessened. The curvature of the nanoparticles allows for adlayer relaxation [82]. Thus, CO hydrogenation rates on Ru clusters are much higher at high CO coverage than predicted based on a Langmuir approach [83]. Activation of adsorbed CO by reaction with surface hydrogen results in transition states that occupy less space than [82] the pair of surface moieties that they replace. This causes the overall activation energy to decrease with increasing CO* coverage.

Interestingly, species co-adsorbed on a ruthenium surface may show a strong tendency to segregate. Thus, with carbon monoxide and hydrogen co-adsorbed on a Ru(0001) surface, the carbon monoxide molecules form islands that are surrounded by hydrogen atoms [84]. At cryogenic temperatures, the carbon monoxide molecules form triangular islands of up to 21 molecules located on the *on top* sites. Through this type of island formation, long-range lateral CO-H repulsive interactions are minimised. With an increase in temperature, the carbon monoxide molecules shift to the *hcp* sites and the island size decreases to 3–6 molecules [84]. Through this decrease in domain size, repulsive CO–CO interactions that become more prominent upon increasing the temperature are reduced. The proximity of the carbonyl and hydride adsorbate species to one another (3.0–3.7 Å distance) [84] explains the propensity of ruthenium surfaces for Fischer-Tropsch reactions. The ensuing CO bond cleavage is facilitated by the formation of partially hydrogenated CHO and COH intermediates.

7. Supports for heterogeneous ruthenium catalysts

For applicable heterogeneous catalysts, metallic ruthenium is supported in form of ruthenium nanoparticles on a suitable support. This ensures a high dispersion and a large surface area of ruthenium. Carbon supports, in particular active carbons

and carbon nanotubes, and oxidic supports are frequently employed. To ensure that the ruthenium nanoparticles are immobile on the support surface under the catalytic conditions, there has to be a sufficiently strong interaction between metal nanoparticles and the support. Otherwise, there would be pronounced sintering of the ruthenium nanoparticles that would lead to gradual loss of the catalytic activity. The support also influences the electron density in the ruthenium nanoparticles, thereby lowering or increasing the Fermi level. For oxidic supports, the interaction between nanoparticles and the support cannot be too strongly pronounced, because ruthenium cations tend to diffuse into the bulk of the support material.

For carbonaceous materials anchoring sites have to be generated on the surface to anchor the ruthenium nanoparticles. Providing high surface area, active carbons and carbon nanotubes thus usually undergo an oxidative pre-treatment. As a result, oxygenated moieties are generated to which the ruthenium nanoparticles strongly bind. In this aspect, the property of ruthenium being at the borderline between noble and non-noble metals is exploited. Under more driving reductive conditions of a hydrogen atmosphere, however, the susceptibility of carbon carriers to methanation is challenging for carbon-supported ruthenium catalysts, because it leads to degradation of the carrier and sintering of the ruthenium clusters. Compared to active carbons, carbon nanotubes lend a more defined support and higher stability.

Carbon nanotubes combine physicochemical properties that make them interesting as support for ruthenium, such as high surface area, good mechanical strength, chemical and thermal stability, high heat and electric conductivity. So far, the high costs incurred by elaborate synthesis procedures [85–89] hinder their more widespread use as well-defined catalyst supports [90]. For immobilisation of metal nanoparticles, anchoring sites need to be generated on the surface of the carbon support. A method of preparing a Ru/CNT catalyst with supported ruthenium nanoparticles involves treatment of the CNT in refluxing nitric acid [91]. Deposition-precipitation of the ruthenium precursor $Ru(NO)(NO_3)_x(OH)_y$ followed by reduction of the precursor to the metal with molecular hydrogen provides well-dispersed surface-anchored Ru nanoparticles (**Figure 7**) [29]. Such catalysts are excellent hydrogenation and hydrogenolysis catalysts (see below).

Oxidic supports that are frequently employed comprise silica, alumina (mostly γ-Al_2O_3), zirconia, ceria and the corresponding mixed oxides. Even though amorphous materials provide the necessary high surface area, they often are associated with certain distribution of surface functions. Yet as surface groups, they may be harmful in catalysis. The presence of different surface sites often leads to alternative

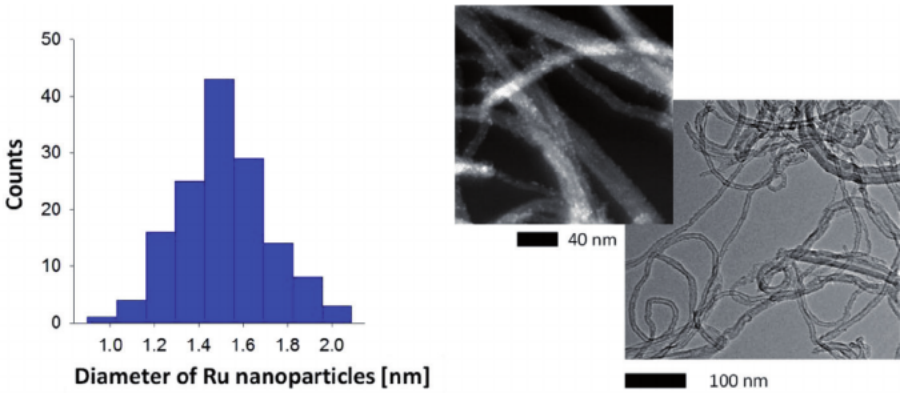

Figure 7.
Particle size distribution of the ruthenium nanoparticles for a typical Ru/CNT catalyst and representative transmission electron microscopy images [29]. The carbon nanotubes are Baytubes C 150 P.

Activated carbons		*Oxidic supports*		
Adsorbent	**Hydrophobicity index (HI)**	**Adsorbent**	**Pore size [Å]**	**Hydrophobicity index (HI)**
Darco-KBB	26.3	Y	7.35	0
SX1G	26.2	Beta	5.95	1.4
F300	160	ZSM-5, Silicalite-1	4.46	8, 15.2
Duksan	296	MCM-41	16–42	9

Table 1.
Comparison of the hydrophobicity of carbon supports (left) and oxidic supports (right) [27]; the pore size of zeolites (Beta, Y, ZSM-5, Silicalite-1 [92]) and mesoporous materials (MCM-41 [93]) is the maximum diameter of a sphere that can diffuse through the channels.

catalytic pathways that result in reduced selectivity of the transformation. Instead, more defined support materials are nanoporous zeolites, such as zeolite Y, Beta, and ZSM-5, or mesoporous materials, such as MCM-41. The internal pore system (**Table 1**) provides a uniform environment for the catalytic transformation. Nevertheless, many biomolecules are too large to enter the pore system and need to be cut to molecular entities first. Catalysis at the pore mouth or using molecular catalysts is an option for the depolymerisation step.

The hydrophobicity index (HI) is a good measure for assessing the internal hydrophobicity of porous materials. HI can be determined by the competitive adsorption of a toluene-water mixture. The hydrophobicity index is defined by the ratio of the adsorption capacity for toluene ($Q_{Toluene}$) to that of water (Q_{Water}). For comparison, the reported HIs of some activated carbons, microporous zeolites, and mesoporous materials are listed in **Table 1** [27]. The hydrophobicity index (HI) of typical zeolites, such as beta, Y and ZSM-5 is low (HI = 1.4, 0, 8, respectively), which is consistent with the hydrophilic nature of the pore walls. This is attributed to a certain polarity of the zeolite walls that results from the aluminium atoms substituting a certain part of the silicon atoms. All-silica zeolites, such as Silicalite-1, are clearly more hydrophobic (HI = 15.2) and more resemble activated carbons which are commonly regarded as hydrophobic adsorbents.

Unsupported metal nanoparticles can be employed as quasi-homogeneous catalysts but need to be stabilised by ligation or generation of an electric double layer to prevent agglomeration of the nanoparticles [94]. Upon decreasing the size of the metal nanoparticles, the boundary of the metallic state is obtained for two-shell clusters of about 1.5 nm in diameter [95]. Ruthenium nanoparticles stabilised with a thin layer of ionic liquid tartaric acid tetraoctylammonium $[TA^{2-}][N^{+}_{8888}]_2$ or glycine tetraoctylammonium $[Gly^{-}][N^{+}_{8888}]$ have shown excellent catalytic properties for the hydrogenation of challenging substrates. One example is the conversion of nitrobenzene to cyclohexylamine. Catalytic activity and selectivity of the quasi-homogeneous nanoparticle catalyst resemble that of a corresponding supported Ru/C catalyst. Upon switching to the less polar ionic liquid dimethylglycine tetraoctylammonium $[Me_2Gly^{-}][N^{+}_{8888}]$, the selectivity changes to the reaction intermediate aniline. This is attributed to the relative binding strength of ionic liquid and intermediates to the ruthenium surface. Thus, the use of ionic liquids as stabiliser lends a ready method to tailor the properties of the catalyst. Interestingly, ionic liquid-stabilised nanoparticles are readily supported on a mesoporous support [96, 97] thus turning the quasi-homogeneous catalyst into a true heterogeneous catalyst. Noteworthy, the catalytically active site remains in the flexible environment of the ionic liquid [98] which imparts beneficial properties to the catalyst [99]. During the chemical transformation,

the active species can easily adapt to the geometry changes that occur during the path from reactant to transition and product state. Moreover, the equivalence of all catalytically active sites is readily maintained which can render enhanced selectivity. The ionic liquid then again provides a polar medium for tailoring the adsorption of the substrate molecules and desorption of the product molecules [100] that precede and succeed the catalytic reaction, respectively. Interestingly, in supported films of ionic liquid. Rates as well as chiral induction can be enhanced, as was demonstrated for the hydrogenation of the prochiral substrate acetophenone over [Ru((R)-BINAP)$(PPh_3)_nCl_{3-n}$], n = 0, 1 [101]. A useful feature of such supported catalysts is that fixed-bed reactor technology common in continuous chemical processes can be employed [97].

8. Biomass conversion with ruthenium catalysts

About 1% of the incoming solar radiation on earth is captured for generating biomass [102]. This energy is utilised in photosynthesis [103] to build a myriad of complex molecules [104] such as carbohydrates, lignin, proteins, fats and oils, and terpenes. In this way about 170 x 10^9 t/a of complex substances are produced annually [105]. In plants, the radiation use efficiency is controlled by the net-photosynthetic capacity and the canopy structure [106, 107]. Cultivars with a heavy canopy and long growth period are able to harness more solar radiation [108]. A large fraction of the produced biomass is characterised by a high oxygen content (**Table 2**). Cellulose, a polymeric carbohydrate, and lignin a randomly linked phenolic polymer constitute a major fraction of plant biomass (around 95% [109]). Their oxygen content is much higher than that of fossil resources such as crude oil, natural gas and coal (**Table 2**). About 56% of the oil extracted from the resources is utilised to make liquid fuels (70.6%) for transport purposes [2]. About 14% of the oil and 8% of the gas extracted from these resources is utilised to make petrochemicals. Both fuels and many petrochemical products are characterised by a low oxygen-to-carbon ratio. Some examples are given in **Table 2**. Consequently, in order to exploit biomass, a controlled de-functionalisation is necessary. In particular, efficient strategies are needed to decrease the oxygen-to-carbon ratio.

At present, biorefinery routes [118, 119] have been improved to more efficiently exploit biomass feedstock. In the production of bioethanol from lignocellulosic biomass, e.g., by hydrolysis of wood with dilute acids, hexoses are obtained that are good feedstock for fermentation [4]. The target product then needs to be separated from the aqueous fermentation broth. By producing ethanol in this way, about 8.7% of the mass and 11% of the energy contained originally in the wood are found in the product [109]. The remainder are 37% by-products and 40% waste products, mostly carbon dioxide (36%) that need to be utilised or disposed. Green chemistry metrics [120], notably the E-factor and atom economy, clearly need to be improved further. One option is the direct chemical conversion of lignocellulosic biomass in a single reaction step over a multifunctional catalyst as outlined below. Such transformation follows the principles of a molecular assembly line. Thus, efficient and frequently multistep catalysis is one of the keys for realising fast and highly selective conversion of biomass [109]. Before the particular aspects of ruthenium catalysts in biomass conversion are considered, the general architecture and the availability of biomass is analysed briefly. Lignocellulose makes up the structural components of plants and a large fraction of the plant biomass available for producing platform chemicals. Wood, e.g., is essentially composed of cellulose (39–45%), hemicelluloses (27–32%) and lignin (22–31%) [121].

	Category	Compound		O/C
Natural compound	Sugar-based	Cellulose $(C_6H_{10}O_5)_n$		0.83
		Carbohydrates $C_6H_{10}O_5$ [*7]		0.83
		Glucose $C_6H_{10}O_6$		1
	Lignin-based	Lignocellulose [*6]		0.8–0.9
		Lignin [*1]		0.3–0.4
	Other	Proteins $C_{147}H_{228}O_{46}N_{40}S$ [*7]		0.31
		Lipids $C_{53}H_{89}O_6$ [*7]		0.11
Derived product	Fuels	Ethanol		0.5
		Biodiesel [*4]		0.15
Fossil feedstock	Coal	Peat [*5,8]	Increasing degree of coalification [*2]	0.37–0.66
		Lignite [*5]		0.23
		Black [*3]		0.03–0.15
		Bituminous [*3]		0.03–0.10
		Anthracite [*3]		0.02–0.05
	Crude oil [*9]	Heavy (Venezuela) [*10]		0.02
	Natural gas	Methane		0
Derived product [*11]	Fuels	Petroleum [*3]		<0.2
		Diesel [*4]		0
	Petrochemicals	BTX		0
		Propene		0
		Ethene		0
		Polyethylene		0

*[*1] [110]; [*2] increasing degree of coalification relates with decreasing O/C ratio; [*3] originating from Pennsylvania [4]; [*4] [111]; [*5] [112]; [*6] [113]; [*7] [114]; [*8] [115]; [*9] [116]; [*10] [117]; [*11] for global mass flows refer to [5];*

Table 2.
Oxygen content of typical components of biomass in comparison to fossil resources and selected derived products.

9. Sustainable feedstock from biomass

Cellulose is an important structural component of the cell wall of green plants, many forms of algae and the oomycetes. Many bacteria secrete it to form biofilms [122]. Plants build about 10^{11}–10^{12} t/a of cellulose annually mostly in combination with hemicelluloses and lignin [123]. This makes cellulose the most abundant organic polymer on Earth [124]. Cellulose is a polysaccharide, a linear chain with the formula $(C_6H_{10}O_5)_n$ consisting of 7,000–15,000 of $\beta(1 \rightarrow 4)$ linked D-glucose units [125].

Even though hemicellulose is a polysaccharide often associated with cellulose, cellulose and hemicellulose have distinct compositions and structures. Hemicellulose is a branched polymer but cellulose is unbranched. Whereas hemicellulose is built from diverse sugars, cellulose is derived exclusively from glucose. For instance [126], besides glucose, sugar monomers in hemicelluloses can include hexose sugars, such as mannose and galactose, and pentose sugars, such as xylose and arabinose. Unlike cellulose, the side chains in hemicelluloses are often modified with acetyl and glycosyl groups.

Lignin is a randomly linked polymer (**Figure 8**) comprising phenolic *p*-hydroxyphenyl (**H**), guaiacyl (**G**) and syringyl (**S**) moieties (see also **Figure 9**) that are linked *via* ether linkages (*ß-O-4'*, *α-O-4'*, *4-O-5'*), biphenyl (*5–5'*), resinol *(ß-ß')*, and other condensed linkages (*ß-5'*, *ß-1'*) as well as dibenzodioxocin, and phenylcoumaran linkages [109, 127]. The complex structure of lignin is the result of the biosynthetic pathway that involves oxidation of phenolic precursors to radicals followed by radical coupling that leads to stepwise build-up of the lignin structure [128].

The components of plant biomass are normally fractionated using biochemical [129, 130], thermochemical [131] and/or catalytic methods [132]. Lignin is particular is that respect that it is highly resistant to depolymerisation. Consequently, at present the lignin fraction is often used to a large extent as fuel for heat generation. Methods have been developed to utilise the phenolic structure for producing polymers, resins, additives, fuels and chemicals. Common methods for depolymerisation of lignin into monomeric phenolic compounds involve pyrolysis [133–136], enzyme [137, 138], acid or base [139, 140] catalysed hydrolysis, and hydrogenolysis [141–143]. Catalysts based on metallic ruthenium are frequently employed in hydrolysis and hydrogenolysis of the ether linkages or hydrodeoxygenation [110, 144] of the phenol products (*vide supra*).

In subsequent downstream processing, the biomass fractions are converted to platform chemicals. Based on the generally accessible biomass, platform molecules (**Figure 9** [4]) include organic acids, such as propionic acid, 3-hydroxypropionic acid, succinic acid, fumaric acid, itaconic acid, and levulinic acid [145], fat and oil-derived polyols, in particular glycerol, as well as sugar-derived polyols such as sorbitol and xylitol. Additional platform chemicals are alcohols such as methanol, ethanol, and propanol, cyclic ethers, such as furfural and 5-hydroxymethylfurfural, and terpenes, such as isoprene. Such platform molecules can be exploited as fuels

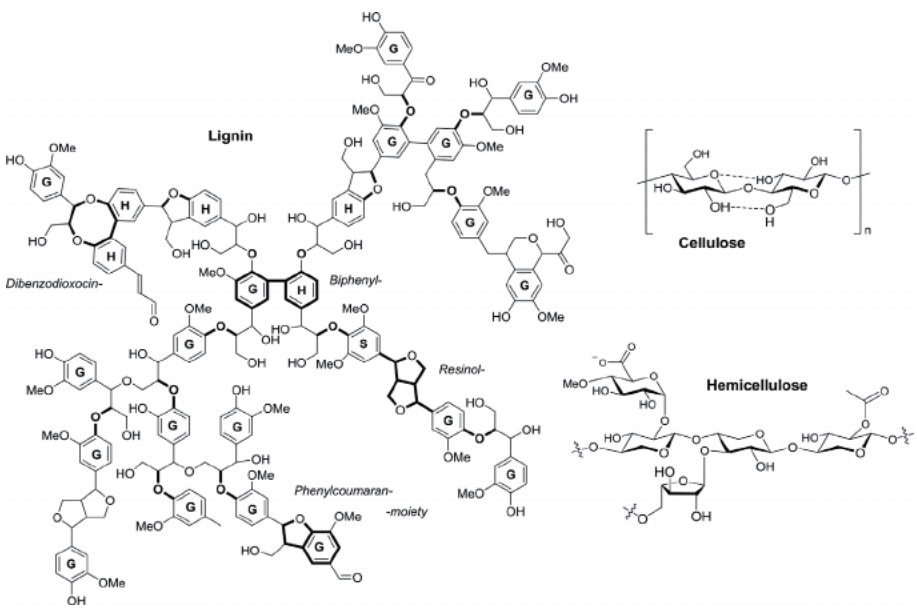

Figure 8.
*Chemical structure of important biomass fractions, lignin (left), cellulose with 1,4-glycosidic linkages and selected hydrogen bonds (right, top) and the common molecular motif of hemicellulose (right, bottom). For the structure of lignin, the characteristic aromatic p-hydroxyphenyl (***H***), guaiacyl (***G***) and syringyl (***S***) moieties as well as aromatic ether linkages (-**O**-), dibenzodioxocin, biphenyl, resinol, and phenylcoumaran linkages [109, 127] were marked.*

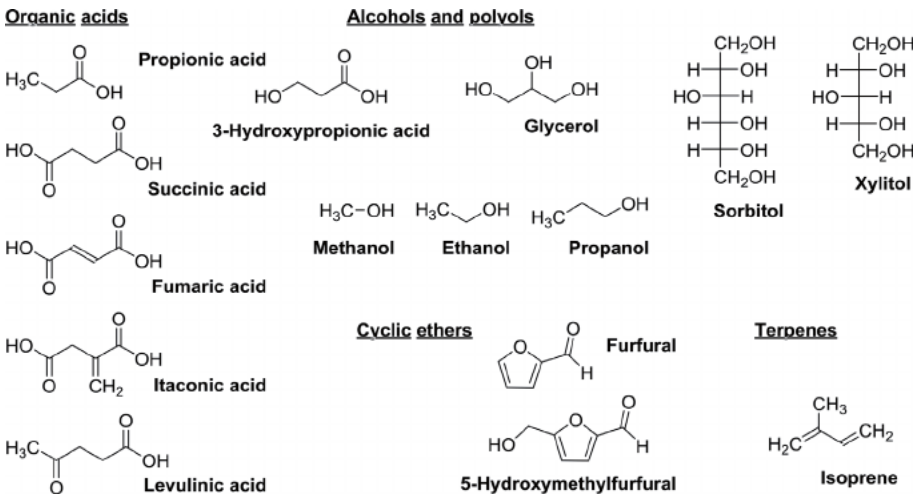

Figure 9.
Biomass derived platform chemicals.

and industrially relevant chemicals or are readily transformed into such fuels and chemicals. Ruthenium-based catalysts are frequently employed in key transformations such as hydrogenation, hydrogenolysis, and oxydehydrogenation [146]. Compared to nickel-based catalysts, ruthenium-based catalysts provide higher activity and better stability that result in lower catalyst loadings, longer lifetimes and less pronounced deactivation. Although ruthenium-based catalysts are more expensive, these costs are offset by their higher activity and their lower tendency to leach.

10. Ruthenium catalysts in cellulose conversion

While first-generation bioethanol is produced on the million t/a scale, production of second-generation bioethanol from cellulosic biomass is still in its infancy [4]. The challenge is the enzyme- or acid-catalysed hydrolysis of lignocellulosic materials to simple sugars that can be fed into fermentation, from which ethanol is separated by distillation [147]. A one-step catalytic conversion of cellulosic biomass (bagasse and corn stalk) to bioethanol has been realised with a ruthenium-based catalyst [148]. The catalyst comprises well-dispersed Ru and WO_x nanoparticles on a H-ZSM-5 solid acid support. Under catalytic conditions, also highly dispersed Ru_3W_{17} alloy nanoparticles are formed. In a cascade reaction cellulose undergoes hydrolysis on moderately acidic sites of the H-ZSM-5 support, followed by glucose retro-aldol condensation to glycolaldehyde over WO_x and hydrogenation over Ru to yield ethylene glycol that is dehydrated and finally hydrogenated to ethanol on the Ru_3W_{17} alloy sites.

Interestingly, subcritical water is an efficient reaction medium for cellulose conversion [149, 150]. Thus, cellulose is converted to polyols over ruthenium supported on crosslinked polystyrene [149, 151]. Swelling of the polymer [152] thereby facilitates access of the substrate to the catalytic sites.

A carbon-supported ruthenium hybrid catalyst with a specific surface area of 1200 $m^2 g^{-1}$ was employed for the direct hydrogenolytic cleavage of cellulose to sorbitol [153]. High microporosity and low acidity of the carbon support favour high dispersion of the metallic ruthenium. Interestingly, ball-milling of cellulose with carbon supported ruthenium provides enhanced conversions and selectivities to sorbitol [154, 155].

Selective conversion of cellulose to sorbitol is achieved *i.a.* by use of bi-functional ruthenium catalysts supported on sulphated zirconia and sulphated silica-zirconia [156]. Tetragonal zirconia, associated with generation of superacidity, is the active phase for cellulose depolymerisation that accompanies the hydrogenation function of ruthenium. Also, zeolite- [146, 157] and silica- [158] supported ruthenium nanoparticles are suitable for the hydrogenation of glucose to the sugar alcohol sorbitol.

Hydrogenolysis of sorbitol to ethylene glycol and 1,2-propanediol is obtained over bifunctional Ru-WO_x/CNT catalysts [159]. Furthermore, addition of $Ca(OH)_2$ proved beneficial for the hydrogenolysis activity.

11. Ruthenium catalysts in lignin conversion

Hydrogenolysis of lignin involves reductive bond cleavage of C-O bonds linking the phenolic moieties, thereby generating hydrogenated and therefore less reactive monomeric species. For the reduction step, ruthenium catalysts are frequently employed. A variety of reducing agents have been suggested [141, 160, 161], such as hydrogen [142], carbon monoxide, formic acid ($HCOOH/NEt_3$ [53]), methanol, ethanol, isopropyl alcohol [54], acetonitrile, acetone. The energy needed for producing the reductant and the associated CO_2-footprint ought to be taken into account when the lignin-derived products are utilised as biofuels [162]. Supercritical fluids as solvent have been claimed to produce fewer solid residues and provide higher biomass conversions [163, 164]. Catalytic transfer hydrogenolysis of corn stover lignin in supercritical ethanol with a Ru/C catalyst yields bio-oil with a high fraction of monomeric moieties [163]. The key transformation is the reductive cleavage of ether linkages. Sequential extraction with a series of solvents differing in polarity results in monomer fractions that are enriched in alkylated phenols, guaiacols, syringols and hydrogenated hydroxycinnamic acid derivatives (**Figure 10**).

For using bio-oils as fuel, hydrotreating is necessary for lowering the oxygen content. Hydrotreating increases stability and energy density while decreasing the viscosity of the bio-oils. Ruthenium catalysts are often used in this hydrogenolytic upgrading of bio-oils. Even though zeolites are a good support material, substituted phenols cannot enter the micropores of typical zeolites. One concept for overcoming this challenge are catalysts comprising hierarchical pore systems. Thus, Ru supported on mesoporous ZSM-5 with a characteristic pore size of 4.5–4.7 Å of the MFI lattice channels (**Figure 11**) [92] and the mesopore system aligned to the *b*-axis was found to be effective for the hydrodeoxygenation of phenolic biomolecules [144]. For comparison, the Van-der-Waals radius of the syringol molecule is estimated to

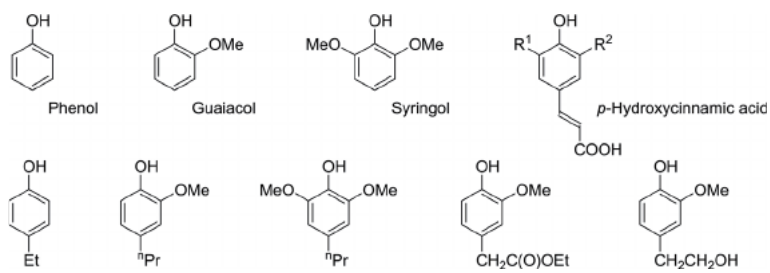

Figure 10.
Phenol-, guaiacol-, syringol- and hydroxycinnamic acid (top row)-derived monomers typically found in lignin hydrogenolysates (bottom row).

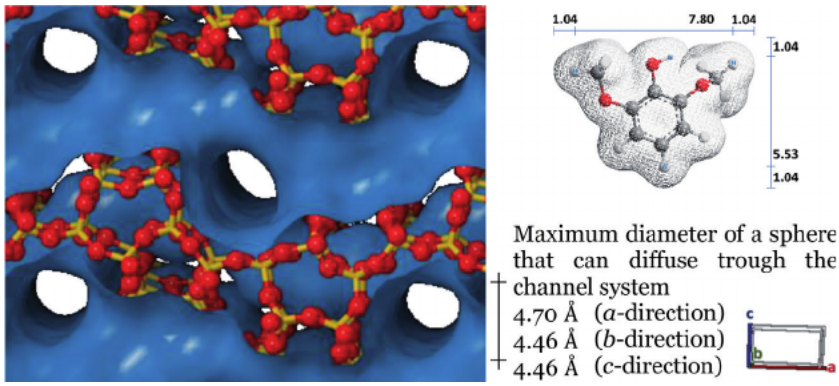

Figure 11.
Comparison of the characteristic dimensions of syringol (top right) and the three-dimensional MFI pore system of zeolite ZSM-5, here viewed down the b-direction (left; not to scale; red, oxygen atoms; orange, silicon atoms), and maximum diameter of a sphere that can diffuse through the channel system (bottom right).

be 9.88 × 7.61 Å (**Figure 11**) based on the distance of the outermost hydrogen atoms [165] and a Van-der-Waals radius for hydrogen of 1.04 Å [166]. Only at the channel entries do the open mesopores expose acid sites to the approach of bulky molecules necessary for catalysing the cleavage of the phenolic C-O bonds. This type of catalyst was found to effectively catalyse the hydrodeoxygenation of phenol and 2,6-dimethoxyphenol at 4.0 MPa H_2-pressure and a temperature of 150 °C [144]. Conversions were > 99.5 and 97.5% after a 4 h reaction time, respectively; product selectivities to cyclohexane were accordingly 95.0 and 70.0%.

12. Conclusions on biomass transformation with ruthenium catalysts

Ruthenium, a late transition element, provides catalytic pathways that make it highly promising for catalysts applied for biomass conversion. Biomass, a globally available resource, is a sustainable feedstock for producing platform chemicals, that could substitute the current fossil-based platform chemicals in the chemical industry. However, in order to implement further processes in small and large-scale biorefineries, more efficient transformations will be required. Here, the distinct catalytic functions provided by ruthenium and ruthenium complexes could open new pathways. Biomass largely consists of complex molecules that comprise oxygen and other heteroatoms. Catalytic transformations need to accommodate for these heteroatoms, because molecules with heteroatoms tend to adsorb strongly to catalytic sites possibly causing substrate- or product inhibition. However, the preferential adsorption of chemical moieties associated with heteroatoms on the catalytically active site can be exploited for directing catalytic transformations. The principle has been explored for the consecutive hydrogenation of unsaturated moieties on a molecular assemble line. In this context, it is useful considering the concept of orthogonal catalytic functions, where a catalyst preferentially binds and transforms a selected chemical entity without hindering other catalysts that may be added for realising preceding or subsequent catalytic transformations.

In this context, the catalytically highly active element ruthenium embodies unique features. Ruthenium does not form binary hydrides that are stable under usual catalytic conditions. Nevertheless, metallic ruthenium can dissociate molecular hydrogen. Under an atmosphere of hydrogen, the surface of metallic ruthenium is covered with hydrogen atoms. Adsorption states and chemical reactivity of this hydrogen is well understood. Desorption of a fraction of the

hydrogen provides the empty coordination sites necessary for co-adsorption of reactant molecules. Typically following a Langmuir-Hinshelwood-type mechanism, hydrogen atoms can be transferred to unsaturated moieties. Remarkably, ruthenium can also form and cleave C-C, C-O and C-N bonds. Combined with its strong propensity for hydrogenation, this ability gives rise to hydrogenation, hydrogenolysis and hydrodeoxygenation transformations that make ruthenium catalysts so interesting for biomass conversion. Noteworthy are the distinct catalytic transformations that can be realised with ruthenium catalysts. Selected examples for intriguing transformations of biomolecules and bio-derived molecules have been discussed above.

Understanding the interaction of adsorbed molecules with ruthenium surfaces, the nature of adsorption states, binding energies and structures of the adsorption complexes lies at the heart of rational design of catalysts that are specific for the conversion of the chosen chemical entity in biomass. It is anticipated that new transformations will be realised based on the unique catalytic functions provided by heterogeneous and homogeneous ruthenium catalysts. Serving as important tools for the synthetic chemist, these transformations will bolster the use of biomass as sustainable feedstock for the chemical industry.

Acknowledgements

With financial support from the state government of North Rhine-Westphalia and the Indo-German Science & Technology Centre (IGSTC). TEM acknowledges the support of Fraunhofer-Institut für Umwelt-, Sicherheits- und Energietechnik UMSICHT. P. Tomkins and E. Gebauer-Henke are gratefully acknowledged for the characterisation of the Ru/CNT catalyst, C. Herwartz (GFE) for TEM measurements, M. Hermesmann for the literature searches on environmental impact, as well as D. Panke for drawing the chemical structure of biomass fractions.

Conflict of interest

There are no conflicts of interest to declare.

Notes

For compiling **Figure 2**, image 1961095 was obtained with the standard licence from Shutterstock.

Abbreviations and nomenclature

*	Surface adsorbed species
Θ	Coverage
x_M	Chemisorption stoichiometry
ads	Adsorption
AN	Aniline
CA	Cyclohexylamine
CNT	Carbon nanotube
diss	Dissociation
GFE	Gemeinschaftszentrum für Elektronenmikroskopie

DOI: http://dx.doi.org/10.5772/ITexLi.97034

HI	Hydrophobicity index
M	Metal
NB	Nitrobenzene
NMR	Nuclear magnetic resonance
ROMP	Ring opening metathesis polymerisation
Beta	Zeolite Beta with BEA structure
H-ZSM-5	Zeolite ZSM-5 with MFI structure in the proton form
MCM-41	Mesoporous material
Y	Zeolite Y with FAU structure
brg	bridging adsorption site
fcc	three-fold coordination
hcp	three-fold coordination
on top	terminal adsorption site
a	annum
kJ	kilojoule
t	metric ton
TW	Terawatts

References

[1] Tomkins P, Müller TE. Evaluating the carbon inventory, carbon fluxes and carbon cycles for a long-term sustainable world. Green Chemistry. 2019;21(15):3994-4013.

[2] The Future of Petrochemicals. IEA International Energy Agency; 2018.

[3] Jacobson MZ, Delucchi MA. Providing all global energy with wind, water, and solar power, Part I: Technologies, energy resources, quantities and areas of infrastructure, and materials. Energy Policy. 2011;39(3):1154-69.

[4] Mika LT, Cséfalvay E, Németh Á. Catalytic Conversion of Carbohydrates to Initial Platform Chemicals: Chemistry and Sustainability. Chemical Reviews. 2018;118(2):505-613.

[5] Levi PG, Cullen JM. Mapping Global Flows of Chemicals: From Fossil Fuel Feedstocks to Chemical Products. Environmental Science & Technology. 2018;52(4):1725-34.

[6] Puchtel IS. Platinum Group Elements. In: White WM, editor. Encyclopedia of Geochemistry. Switzerland: Springer International Publishing; 2016.

[7] Zientek ML, Loferski PJ. Platinum-Group Elements—So Many Excellent Properties. Reston, VA; 2014. Contract No.: 2014-3064.

[8] Crundwell FK, Moats MS, Ramachandran V, Robinson TG, Davenport WG. Platinum-Group Element. Extractive Metallurgy of Nickel, Cobalt and Platinum Group Metals. Surface Coating and Modification of Metallic Biomaterials. 2011. p. 1-18.

[9] Ruthenium [Internet]. Thieme Gruppe. 2006 [cited 2006/12/17]. Available from: https://roempp.thieme.de/lexicon/RD-18-02130.

[10] Yuan H, Laughlin DE, Zhu X, Lu B. Ru+oxide interlayer for perpendicular magnetic recording media. Journal of Applied Physics. 2008;103(7):07F513.

[11] Wulfsberg G. Hydrides, Alkyls, and Aryls of the Elements. Inorganic Chemistry. Sausalito, CA, US: University Science Books; 2000. p. 978.

[12] Bouten PCP, Miedema AR. On the heats of formation of the binary hydrides of transition metals. Journal of the Less Common Metals. 1980;71(1):147-60.

[13] Binns J, He Y, Donnelly M-E, Peña-Alvarez M, Wang M, Kim DY, et al. Complex Hydrogen Substructure in Semimetallic RuH4. The Journal of Physical Chemistry Letters. 2020;11(9):3390-5.

[14] Morris RH. Estimating the Wavenumber of Terminal Metal-Hydride Stretching Vibrations of Octahedral d6 Transition Metal Complexes. Inorganic Chemistry. 2018;57(21):13809-21.

[15] Soini TM, Genest A, Nikodem A, Rösch N. Hybrid Density Functionals for Clusters of Late Transition Metals: Assessing Energetic and Structural Properties. Journal of Chemical Theory and Computation. 2014;10(10):4408-16.

[16] Müller TE, Ingold F, Menzer S, Mingos DMP, Williams DJ. Platinum (I) dimers and platinum (0) triangles with polyaromatic phosphine ligands. Journal of organometallic chemistry. 1997;528(1-2):163-78.

[17] Meng X, Wang F, Jin G-X. Construction of M–M bonds in late transition metal complexes. Coordination Chemistry Reviews. 2010;254(11):1260-72.

[18] Mingos DMP. High nuclearity clusters of the transition metals and a re-evaluation of the cluster surface analogy. Journal of Cluster Science. 1992;3(4):397-409.

[19] Luh T-Y, Lin W-Y, Lai G. Determination of the Orientation of Pendants on Rigid-Rod Polymers. Chemistry – An Asian Journal. 2020;15(12):1808-18.

[20] Dragutan I, Dragutan V. Ruthenium allenylidene complexes. A promising alternative in metathesis catalysis. Platinum Metals Review. 2006;50(2):81-94.

[21] Muhlebach A, Van Der Schaaf PA, Hafner A, Kolly R, Rime F, Kimer HJ. Ruthenium catalysts for ring-opening metathesis polymerization (ROMP) and related chemistry. NATO Science Series II: Mathematics, Physics and Chemistry. 2002;56(Ring Opening Metathesis Polymerisation and Related Chemistry):23-44.

[22] Donohue PC, McCann EL, III. Novel perovskites M2IILnIIIRuVO6 as emission control catalysts. Materials Research Bulletin. 1977;12(5):519-24.

[23] Cairns JF, Hodgson DR, inventors; Imperial Chemical Industries PLC, UK . assignee. Electrode patent EP479423A1. 1992.

[24] Schmidt T, Gürtler C, Kintrup J, Müller TE, Loddenkemper T, Gerhartz F, et al., inventors; Bayer MaterialScience AG, Germany . assignee. Method for production of chlorine by gas phase oxidation on nano-structured ruthenium carrier catalysts patent WO2011012226A2. 2011.

[25] Williams RJP. Possible functions of chains of catalysts. Journal of Theoretical Biology. 1961;1(1):1-17.

[26] Heidary N, Ly KH, Kornienko N. Probing CO2 Conversion Chemistry on Nanostructured Surfaces with Operando Vibrational Spectroscopy. Nano Letters. 2019;19(8):4817-26.

[27] Xie L-H, Xu M-M, Liu X-M, Zhao M-J, Li J-R. Hydrophobic Metal–Organic Frameworks: Assessment, Construction, and Diverse Applications. Advanced Science. 2020;7(4):1901758.

[28] Kim S, Lee H-E, Suh J-M, Lim MH, Kim M. Sequential Connection of Mutually Exclusive Catalytic Reactions by a Method Controlling the Presence of an MOF Catalyst: One-Pot Oxidation of Alcohols to Carboxylic Acids. Inorganic Chemistry. 2020;59(23):17573-82.

[29] Tomkins P, Gebauer-Henke E, Müller TE. Molecular Assembly Line: Stepwise Hydrogenation of Multifunctional Substrates over Catalyst Mixtures. ChemCatChem. 2016;8(3):546-50.

[30] Saadatjou N, Jafari A, Sahebdelfar S. Ruthenium Nanocatalysts for Ammonia Synthesis: A Review. Chemical Engineering Communications. 2015;202(4):420-48.

[31] Anon. KBR's KAAP Ammonia Plant Design, Proven in Trinidad, Available for 2000 MTPD. IP.com Journal. 2012;12(5B):68.

[32] Iost KN, Borisov VA, Temerev VL, Surovikin YV, Pavluchenko PE, Trenikhin MV, et al. Study on the metal-support interaction in the Ru/C catalysts under reductive conditions. Surfaces and Interfaces. 2018;12:95-101.

[33] Morgan E, Manwell J, McGowan J. Wind-powered ammonia fuel production for remote islands: A case study. Renewable Energy. 2014;72:51-61.

[34] Valera-Medina A, Xiao H, Owen-Jones M, David WIF, Bowen PJ. Ammonia for power. Progress

in Energy and Combustion Science. 2018;69:63-102.

[35] Rouwenhorst KHR, Van der Ham AGJ, Mul G, Kersten SRA. Islanded ammonia power systems: Technology review & conceptual process design. Renewable and Sustainable Energy Reviews. 2019;114:109339.

[36] Kitano M, Inoue Y, Sasase M, Kishida K, Kobayashi Y, Nishiyama K, et al. Self-organized Ruthenium–Barium Core–Shell Nanoparticles on a Mesoporous Calcium Amide Matrix for Efficient Low-Temperature Ammonia Synthesis. Angewandte Chemie International Edition. 2018;57(10):2648-52.

[37] Ju X, Liu L, Yu P, Guo J, Zhang X, He T, et al. Mesoporous Ru/MgO prepared by a deposition-precipitation method as highly active catalyst for producing COx-free hydrogen from ammonia decomposition. Applied Catalysis B: Environmental. 2017;211:167-75.

[38] Yao L, Shi T, Li Y, Zhao J, Ji W, Au C-T. Core–shell structured nickel and ruthenium nanoparticles: Very active and stable catalysts for the generation of COx-free hydrogen via ammonia decomposition. Catalysis Today. 2011;164(1):112-8.

[39] Garbarino G, Bellotti D, Riani P, Magistri L, Busca G. Methanation of carbon dioxide on Ru/Al2O3 and Ni/Al2O3 catalysts at atmospheric pressure: Catalysts activation, behaviour and stability. International Journal of Hydrogen Energy. 2015;40(30):9171-82.

[40] Stangeland K, Kalai D, Li H, Yu Z. CO2 Methanation: The Effect of Catalysts and Reaction Conditions. Energy Procedia. 2017;105:2022-7.

[41] Wender I. Reactions of synthesis gas. Fuel Processing Technology. 1996;48(3):189-297.

[42] Jürgensen L, Ehimen EA, Born J, Holm-Nielsen JB. Dynamic biogas upgrading based on the Sabatier process: Thermodynamic and dynamic process simulation. Bioresource Technology. 2015;178:323-9.

[43] Hermesmann M, Grübel K, Scherotzki L, Müller TE. Promising pathways: The geographic and energetic potential of power-to-x technologies based on regeneratively obtained hydrogen. Renewable and Sustainable Energy Reviews. 2021;138:110644.

[44] Gebauer-Henke E, Blumenthal L, Prokofieva A, Vogt H, Voss G, Müller TE. Diastereomer control in the hydrogenation of o- and p-toluidine over ruthenium catalysts. Al'ternativnaya Energetika i Ekologiya. 2010(4):29-36.

[45] Tomkins P, Müller TE. Enhanced Selectivity in the Hydrogenation of Anilines to Cyclo-aliphatic Primary Amines over Lithium-Modified Ru/CNT Catalysts. ChemCatChem. 2018;10(6):1438-45.

[46] Kraynov A, Gebauer-Henke E, Leitner W, Müller TE. Unexpectedly high catalytic activity of ruthenium catalysts in the hydrogenation of nitrobenzene. Al'ternativnaya Energetika i Ekologiya. 2010;4:37-44.

[47] Gebauer-Henke E, Tomkins P, Leitner W, Müller TE. Nitro Promoters for Selectivity Control in the Core Hydrogenation of Toluidines: Controlling Adsorption on Catalyst Surfaces. ChemCatChem. 2014;6(10):2910-7.

[48] Tomkins P, Gebauer-Henke E, Leitner W, Müller TE. Concurrent Hydrogenation of Aromatic and Nitro Groups over Carbon-Supported Ruthenium Catalysts. ACS Catalysis. 2015;5(1):203-9.

[49] Almithn A, Hibbitts D. Comparing Rate and Mechanism of Ethane

Hydrogenolysis on Transition-Metal Catalysts. The Journal of Physical Chemistry C. 2019;123(9):5421-32.

[50] Morris RH. Physical insights into mechanistic processes in organometallic chemistry: an introduction. Faraday Discussions. 2019;220(0):10-27.

[51] Morris RH. Moving Hydrogen Using Iron Catalysts. Preprints of Papers-American Chemical Society, Division of Energy & Fuels. 2013;58(1):694-5.

[52] Václavík J, Kačer P, Kuzma M, Červený L. Opportunities Offered by Chiral η6-Arene/N-Arylsulfonyl-diamine-RuII Catalysts in the Asymmetric Transfer Hydrogenation of Ketones and Imines. Molecules. 2011;16(7):5460-95.

[53] Pan Y, Luo Z, Xu X, Zhao H, Han J, Xu L, et al. Ru-Catalyzed Deoxygenative Transfer Hydrogenation of Amides to Amines with Formic Acid/Triethylamine. Advanced Synthesis & Catalysis. 2019;361(16):3800-6.

[54] Labes R, González-Calderón D, Battilocchio C, Mateos C, Cumming GR, de Frutos O, et al. Rapid Continuous Ruthenium-Catalysed Transfer Hydrogenation of Aromatic Nitriles to Primary Amines. Synlett. 2017;28(20):2855-8.

[55] Cotman AE. Escaping from Flatland: Stereoconvergent Synthesis of Three-Dimensional Scaffolds via Ruthenium(II)-Catalyzed Noyori–Ikariya Transfer Hydrogenation. Chemistry – A European Journal. 2021;27(1):39-53.

[56] Ikariya T, Murata K, Noyori R. Bifunctional transition metal-based molecular catalysts for asymmetric syntheses. Organic & Biomolecular Chemistry. 2006;4(3):393-406.

[57] Grubbs RH, Trnka TM. Ruthenium-Catalyzed Olefin Metathesis. Ruthenium in Organic Synthesis. 2004:153-77.

[58] Beligny S, Blechert S. N-Heterocyclic Carbene–Ruthenium Complexes in Olefin Metathesis. In: Nolan SP, editor. N-Heterocyclic Carbenes in Synthesis. Weinheim: Wiley-VCH; 2006. p. 1-25.

[59] Schmidt B. Ruthenium-Catalyzed Cyclizations: More than Just Olefin Metathesis! Angewandte Chemie International Edition. 2003;42(41):4996-9.

[60] Hey DA, Reich RM, Baratta W, Kühn FE. Current advances on ruthenium(II) N-heterocyclic carbenes in hydrogenation reactions. Coordination Chemistry Reviews. 2018;374:114-32.

[61] Burling S, Paine BM, Whittlesey MK. Ruthenium N-Heterocyclic Carbene Complexes in Organic Transformations (Excluding Metathesis). In: Nolan SP, editor. N-Heterocyclic Carbenes in Synthesis. Weinheim: Wiley-VCH; 2006. p. 27-53.

[62] Nishikawa T, Kamigaito M, Sawamoto M. Living Radical Polymerization in Water and Alcohols: Suspension Polymerization of Methyl Methacrylate with RuCl2(PPh3)3 Complex. Macromolecules. 1999;32(7):2204-9.

[63] Ando T, Sawauchi C, Ouchi M, Kamigaito M, Sawamoto M. Amino alcohol additives for the fast living radical polymerization of methyl methacrylate with RuCl2(PPh3)3. Journal of Polymer Science Part A: Polymer Chemistry. 2003;41(22):3597-605.

[64] Hamasaki S, Kamigaito M, Sawamoto M. Amine Additives for Fast Living Radical Polymerization of Methyl Methacrylate with RuCl2(PPh3)3. Macromolecules. 2002;35(8):2934-40.

[65] Nieuwenhuys BE. Adsorption and Reactions of CO, NO, H2 and O2 on Group VIII Metal Surfaces. In: Joyner RW, van Santen RA, editors. Elementary Reaction Steps in Heterogeneous Catalysis. Dordrecht: Springer Netherlands; 1993. p. 155-77.

[66] Puisto M, Nenonen H, Puisto A, Alatalo M. Effect of van der Waals interactions on H2 dissociation on clean and defected Ru(0001) surface. The European Physical Journal B. 2013;86(9):396.

[67] Luppi M, Olsen RA, Baerends EJ. Six-dimensional potential energy surface for H2 at Ru(0001). Physical Chemistry Chemical Physics. 2006;8(6):688-96.

[68] Gutmann T, del Rosal I, Chaudret B, Poteau R, Limbach H-H, Buntkowsky G. From Molecular Complexes to Complex Metallic Nanostructures—2H Solid-State NMR Studies of Ruthenium-Containing Hydrogenation Catalysts. ChemPhysChem. 2013;14(13):3026-33.

[69] García-García FR, Bion N, Duprez D, Rodríguez-Ramos I, Guerrero-Ruiz A. H2/D2 isotopic exchange: A tool to characterize complex hydrogen interaction with carbon-supported ruthenium catalysts. Catalysis Today. 2016;259:9-18.

[70] Walaszek B, Yeping X, Adamczyk A, Breitzke H, Pelzer K, Limbach H-H, et al. 2H-solid-state-NMR study of hydrogen adsorbed on catalytically active ruthenium coated mesoporous silica materials. Solid State Nuclear Magnetic Resonance. 2009;35(3):164-71.

[71] Scholten JJF, Pijpers AP, Hustings AML. Surface Characterization of Supported and Nonsupported Hydrogenation Catalysts. Catalysis Reviews. 1985;27(1):151-206.

[72] Groß A. Theoretical Surface Science. 2 ed. Berlin Heidelberg: Springer-Verlag; 2009. XIII, 342 p.

[73] Vattuone L, Savio L, Rocca M. Bridging the structure gap: Chemistry of nanostructured surfaces at well-defined defects. Surface Science Reports. 2008;63(3):101-68.

[74] Zupanc C, Hornung A, Hinrichsen O, Muhler M. The Interaction of Hydrogen with Ru/MgO Catalysts. Journal of Catalysis. 2002;209(2):501-14.

[75] Vayssilov GN, Petrova GP, Shor EAI, Nasluzov VA, Shor AM, Petkov PS, et al. Reverse hydrogen spillover on and hydrogenation of supported metal clusters: insights from computational model studies. Physical Chemistry Chemical Physics. 2012;14(17):5879-90.

[76] Swart I, de Groot FMF, Weckhuysen BM, Gruene P, Meijer G, Fielicke A. H2 Adsorption on 3d Transition Metal Clusters: A Combined Infrared Spectroscopy and Density Functional Study. The Journal of Physical Chemistry A. 2008;112(6):1139-49.

[77] Nordlander P, Holloway S, Nørskov JK. Hydrogen adsorption on metal surfaces. Surface Science. 1984;136(1):59-81.

[78] Faglioni F, Goddard WA. Energetics of hydrogen coverage on group VIII transition metal surfaces and a kinetic model for adsorption/desorption. The Journal of Chemical Physics. 2004;122(1):014704.

[79] Bhatia S, Engelke F, Pruski M, Gerstein BC, King TS. Interaction of Hydrogen with Supported Ru Catalysts: High Pressure in Situ NMR Studies. Journal of Catalysis. 1994;147(2):455-64.

[80] Berthoud R, Délichère P, Gajan D, Lukens W, Pelzer K, Basset J-M, et al. Hydrogen and oxygen adsorption stoichiometries on silica supported ruthenium nanoparticles. Journal of Catalysis. 2008;260(2):387-91.

[81] Peden CHF, Goodman DW, Houston JE, Yates JT. Subsurface hydrogen on Ru(0001): Quantification by Cu titration. Surface Science. 1988;194(1):92-100.

[82] Almithn A, Hibbitts D. Effects of Catalyst Model and High Adsorbate Coverages in ab Initio Studies of Alkane Hydrogenolysis. ACS Catalysis. 2018;8(7):6375-87.

[83] Liu J, Hibbitts D, Iglesia E. Dense CO Adlayers as Enablers of CO Hydrogenation Turnovers on Ru Surfaces. Journal of the American Chemical Society. 2017;139(34):11789-802.

[84] Lechner BAJ, Feng X, Feibelman PJ, Cerdá JI, Salmeron M. Scanning Tunneling Microscopy Study of the Structure and Interaction between Carbon Monoxide and Hydrogen on the Ru(0001) Surface. The Journal of Physical Chemistry B. 2018;122(2):649-56.

[85] Makgabutlane B, Nthunya LN, Maubane-Nkadimeng MS, Mhlanga SD. Green synthesis of carbon nanotubes to address the water-energy-food nexus: A critical review. Journal of Environmental Chemical Engineering. 2020;9(1):104736.

[86] Omoriyekomwan JE, Tahmasebi A, Dou J, Wang R, Yu J. A review on the recent advances in the production of carbon nanotubes and carbon nanofibers via microwave-assisted pyrolysis of biomass. Fuel Processing Technology. 2020;214:106686.

[87] Müller TE, Reid DG, Hsu WK, Hare JP, Kroto HW, Walton DRM. Synthesis of nanotubes via catalytic pyrolysis of acetylene: A SEM study. Carbon. 1997;35(7):951-66.

[88] Reddy CK, Priya L, Saikumari G. Carbon nano tubes. Eur J Biomed Pharm Sci. 2019;6(13):201-4.

[89] Soni SK, Thomas B, Kar VR. A Comprehensive Review on CNTs and CNT-Reinforced Composites: Syntheses, Characteristics and Applications. Materials Today Communications. 2020;25:101546.

[90] Esteves LM, Oliveira HA, Passos FB. Carbon nanotubes as catalyst support in chemical vapor deposition reaction: A review. Journal of Industrial and Engineering Chemistry. 2018;65:1-12.

[91] Datsyuk V, Kalyva M, Papagelis K, Parthenios J, Tasis D, Siokou A, et al. Chemical oxidation of multiwalled carbon nanotubes. Carbon. 2008;46(6):833-40.

[92] Database of Zeolite Structures [Internet]. [cited 30.12.2020]. Available from: http://www.iza-structure.org/databases/.

[93] Jana SK, Mochizuki A, Namba S. Progress in Pore-Size Control of Mesoporous MCM-41 Molecular Sieve Using Surfactant Having Different Alkyl Chain Lengths and Various Organic Auxiliary Chemicals. Catalysis Surveys from Asia. 2004;8(1):1-13.

[94] Kraynov A, Müller TE. Concepts for the Stabilization of Metal Nanoparticles in Ionic Liquids. In: Scott, editor. Applications of Ionic Liquids in Science and Technology. 9. Tennessee: InTech; 2011. p. 235-60.

[95] Schmid G, editor. At the boundary of the metallic state. 1996: Vieweg.

[96] Gu Y, Li G. Ionic Liquids-Based Catalysis with Solids: State of the Art. Advanced Synthesis & Catalysis. 2009;351(6):817-47.

[97] Meijboom R, Haumann M, Müller TE, Szesni N. Synthetic methodologies for supported ionic liquid materials. In: Fehrmann R, Riisager A, Haumann M, editors. Supported Ionic

Liquids. Weinheim: Wiley-VCH Verlag GmbH & Co. KGaA; 2014. p. 75-93.

[98] Sievers C, Jimenez O, Müller TE, Steuernagel S, Lercher JA. Formation of Solvent Cages around Organometallic Complexes in Thin Films of Supported Ionic Liquid. Journal of the American Chemical Society. 2006;128(43):13990-1.

[99] Müller TE. Supported Ionic Liquids as Part of a Building-Block System for Tailored Catalysts. Supported Ionic Liquids. Wiley Online Books. Weinheim: Wiley-VCH Verlag GmbH & Co. KGaA; 2014. p. 209-32.

[100] Jimenez O, Müller TE, Lercher JA. Tailoring Adsorption—Desorption Properties of Hydroamination Catalysts with Ionic Liquids. Ionic Liquids in Organic Synthesis. ACS Symposium Series. 950: American Chemical Society; 2007. p. 267-80.

[101] Fow KL, Jaenicke S, Müller TE, Sievers C. Enhanced enantioselectivity of chiral hydrogenation catalysts after immobilisation in thin films of ionic liquid. Journal of Molecular Catalysis A: Chemical. 2008;279(2):239-47.

[102] Goldstein IS. Chemicals from cellulose. In Goldstein IS, editor. Organic chemicals from biomass. Boca Raton: CRC Press; 1981. p. 101-24.

[103] Okada K, Fujiwara S, Tsuzuki M. Energy conservation in photosynthetic microorganisms. The Journal of General and Applied Microbiology. 2020;66(2):59-65.

[104] Ragauskas AJ, Williams CK, Davison BH, Britovsek G, Cairney J, Eckert CA, et al. The Path Forward for Biofuels and Biomaterials. Science. 2006;311(5760):484.

[105] Kamm B, Gruber PR, Kamm M. Biorefineries-industrial processes and products. Weinheim: Wiley-VCH; 2016.

[106] Louarn G, Lecoeur J, Lebon E. A Three-dimensional Statistical Reconstruction Model of Grapevine (*Vitis vinifera*) Simulating Canopy Structure Variability within and between Cultivar/Training System Pairs. Annals of Botany. 2008;101(8):1167-84.

[107] Vargas LA, Andersen MN, Jensen CR, Jørgensen U. Estimation of leaf area index, light interception and biomass accumulation of *Miscanthus sinensis* 'Goliath' from radiation measurements. Biomass and Bioenergy. 2002;22(1):1-14.

[108] Bai Z, Mao S, Han Y, Feng L, Wang G, Yang B, et al. Study on Light Interception and Biomass Production of Different Cotton Cultivars. PLOS ONE. 2016;11(5):e0156335.

[109] Rinaldi R, Schüth F. Design of solid catalysts for the conversion of biomass. Energy & Environmental Science. 2009;2(6):610-26.

[110] Laskar DD, Yang B, Wang H, Lee J. Pathways for biomass-derived lignin to hydrocarbon fuels. Biofuels, Bioproducts and Biorefining. 2013;7(5):602-26.

[111] Hoekman SK, Broch A, Robbins C, Ceniceros E, Natarajan M. Review of biodiesel composition, properties, and specifications. Renewable and Sustainable Energy Reviews. 2012;16(1):143-69.

[112] Dorrestijn E, Laarhoven LJJ, Arends IWCE, Mulder P. The occurrence and reactivity of phenoxyl linkages in lignin and low rank coal. Journal of Analytical and Applied Pyrolysis. 2000;54(1):153-92.

[113] BabeŁ K, Janasiak D, Waliszewska B, PrĄDzyŃSki W. Chemical composition of lignocellulose materials and porous structure of activated carbons. Annals of Warsaw University of Life Sciences-SGGW,

Forestry and Wood Technology. 2012;77:33-40.

[114] Figueiras FG, Fraga F, Pérez FF, Ríos AF. Theoretical limits of oxygen:carbon and oxygen:nitrogen ratios during photosynthesis and mineralisation of organic matter in the sea. Scientia Marina. 1998;62(1-2):161-8.

[115] Moore TR, Large D, Talbot J, Wang M, Riley JL. The Stoichiometry of Carbon, Hydrogen, and Oxygen in Peat. Journal of Geophysical Research: Biogeosciences. 2018;123(10):3101-10.

[116] Strel'nikova EB, Goncharov IV, Serebrennikova OV. Concentration and distribution of oxygen-containing compounds in crude oils from the southeastern part of Western Siberia. Petroleum Chemistry. 2012;52(4):278-83.

[117] Guo K, Zhang Y, Shi Q, Yu Z. The Effect of Carbon-Supported Nickel Nanoparticles in the Reduction of Carboxylic Acids for in Situ Upgrading of Heavy Crude Oil. Energy & Fuels. 2017;31(6):6045-55.

[118] Wagemann, K. et al. Roadmap Bioraffinerien. Berlin: Bundesministerium für Ernährung, Landwirtschaft und Verbraucherschutz (BMELV), Bundesministerium für Bildung und Forschung (BMBF), Bundesministerium für Umwelt, Naturschutz und Reaktorsicherheit (BMU), Bundesministerium für Wirtschaft undEnergie (BMWi); 2014.

[119] Chaturvedi T, Torres AI, Stephanopoulos G, Thomsen MH, Schmidt JE. Developing Process Designs for Biorefineries—Definitions, Categories, and Unit Operations. Energies. 2020;13(6):1493.

[120] Sheldon RA. Biocatalysis and Green Chemistry. In: Patel, RN, editor. Green Biocatalysis. Hoboken: Wiley & Sons Ltd; 2016:1-15.

[121] Sjostrom E. Wood chemistry: fundamentals and applications. London: Academic Press; 2013. 293 p.

[122] Sun L, Vella P, Schnell R, Polyakova A, Bourenkov G, Li F, et al. Structural and Functional Characterization of the BcsG Subunit of the Cellulose Synthase in Salmonella typhimurium. Journal of Molecular Biology. 2018;430(18, Part B):3170-89.

[123] Yang P, Kobayashi H, Fukuoka A. Recent Developments in the Catalytic Conversion of Cellulose into Valuable Chemicals. Chinese Journal of Catalysis. 2011;32(5):716-22.

[124] Pontes MH, Lee E-J, Choi J, Groisman EA. Salmonella promotes virulence by repressing cellulose production. Proceedings of the National Academy of Sciences. 2015;112(16):5183.

[125] Li S, Bashline L, Lei L, Gu Y. Cellulose synthesis and its regulation. Arabidopsis Book. 2014;12:e0169-e.

[126] Berglund J, Angles d'Ortoli T, Vilaplana F, Widmalm G, Bergenstråhle-Wohlert M, Lawoko M, et al. A molecular dynamics study of the effect of glycosidic linkage type in the hemicellulose backbone on the molecular chain flexibility. The Plant Journal. 2016;88(1):56-70.

[127] Schulze M, Bergs M, Monakhova Y, Diehl B, Konow C, Völkering G, et al. Lignins Isolated via Catalyst-free Organosolv Pulping from Miscanthus x giganteus, *M. sinensis*, *M. robustus* and M. nagara: A Comparative Study. Preprints 2021:2021010181.

[128] Crestini C, Melone F, Sette M, Saladino R. Milled Wood Lignin: A Linear Oligomer. Biomacromolecules. 2011;12(11):3928-35.

[129] Song B, Lin R, Lam CH, Wu H, Tsui T-H, Yu Y. Recent advances and challenges of inter-disciplinary

biomass valorization by integrating hydrothermal and biological techniques. Renewable and Sustainable Energy Reviews. 2021;135:110370.

[130] Hiras J, Wu Y-W, Deng K, Nicora CD, Aldrich JT, Frey D, et al. Comparative Community Proteomics Demonstrates the Unexpected Importance of Actinobacterial Glycoside Hydrolase Family 12 Protein for Crystalline Cellulose Hydrolysis. mBio. 2016;7(4):e01106-16.

[131] Solarte-Toro JC, González-Aguirre JA, Poveda Giraldo JA, Cardona Alzate CA. Thermochemical processing of woody biomass: A review focused on energy-driven applications and catalytic upgrading. Renewable and Sustainable Energy Reviews. 2021;136:110376.

[132] Morales G, Iglesias J, Melero JA. Sustainable catalytic conversion of biomass for the production of biofuels and bioproducts. Catalysts. 2020;10(5):581.

[133] Li W, Wanninayake N, Gao X, Li M, Pu Y, Kim D-Y, et al. Mechanistic Insight into Lignin Slow Pyrolysis by Linking Pyrolysis Chemistry and Carbon Material Properties. ACS Sustainable Chemistry & Engineering. 2020;8(42):15843-54.

[134] Ghysels S, Dubuisson B, Pala M, Rohrbach L, Van den Bulcke J, Heeres HJ, et al. Improving fast pyrolysis of lignin using three additives with different modes of action. Green Chemistry. 2020;22(19):6471-88.

[135] Terrell E, Dellon LD, Dufour A, Bartolomei E, Broadbelt LJ, Garcia-Perez M. A Review on Lignin Liquefaction: Advanced Characterization of Structure and Microkinetic Modeling. Industrial & Engineering Chemistry Research. 2020;59(2):526-55.

[136] Kawamoto H, Horigoshi S, Saka S. Pyrolysis reactions of various lignin model dimers. Journal of Wood Science. 2007;53(2):168-74.

[137] Dionisi D, Anderson JA, Aulenta F, McCue A, Paton G. The potential of microbial processes for lignocellulosic biomass conversion to ethanol: a review. Journal of Chemical Technology & Biotechnology. 2015;90(3):366-83.

[138] Zeng Y, Zhao S, Yang S, Ding S-Y. Lignin plays a negative role in the biochemical process for producing lignocellulosic biofuels. Current Opinion in Biotechnology. 2014;27:38-45.

[139] Beauchet R, Monteil-Rivera F, Lavoie JM. Conversion of lignin to aromatic-based chemicals (L-chems) and biofuels (L-fuels). Bioresource Technology. 2012;121:328-34.

[140] Evstigneyev EI, Shevchenko SM. Lignin valorization and cleavage of arylether bonds in chemical processing of wood: a mini-review. Wood Science and Technology. 2020;54(4):787-820.

[141] Margellou A, Triantafyllidis KS. Catalytic Transfer Hydrogenolysis Reactions for Lignin Valorization to Fuels and Chemicals. Catalysts. 2019;9(1):43.

[142] Jing Y, Dong L, Guo Y, Liu X, Wang Y. Chemicals from Lignin: A Review of Catalytic Conversion Involving Hydrogen. ChemSusChem. 2020;13(17):4181-98.

[143] Chen X, Guan W, Tsang C-W, Hu H, Liang C. Lignin Valorizations with Ni Catalysts for Renewable Chemicals and Fuels Productions. Catalysts. 2019;9(6):488.

[144] Wang L, Zhang J, Yi X, Zheng A, Deng F, Chen C, et al. Mesoporous ZSM-5 Zeolite-Supported Ru Nanoparticles as Highly Efficient

Catalysts for Upgrading Phenolic Biomolecules. ACS Catalysis. 2015;5(5):2727-34.

[145] Fiorani G, Crestini C, Selva M, Perosa A. Advancements and Complexities in the Conversion of Lignocellulose Into Chemicals and Materials. Frontiers in Chemistry. 2020;8:797.

[146] Mishra DK, Dabbawala AA, Park JJ, Jhung SH, Hwang J-S. Selective hydrogenation of d-glucose to d-sorbitol over HY zeolite supported ruthenium nanoparticles catalysts. Catalysis Today. 2014;232:99-107.

[147] Ziolkowska JR. Chapter 1 - Biofuels technologies: An overview of feedstocks, processes, and technologies. In: Ren J, Scipioni A, Manzardo A, Liang H, editors. Biofuels for a More Sustainable Future. Amsterdam: Elsevier; 2020. p. 1-19.

[148] Li C, Xu G, Wang C, Ma L, Qiao Y, Zhang Y, et al. One-pot chemocatalytic transformation of cellulose to ethanol over Ru-WOx/HZSM-5. Green Chem. 2019;21(9):2234-9.

[149] Manaenkov OV, Kislitza OV, Filatova AE, Doluda VY, Sulman EM, Sidorov AI, et al. Cellulose conversion to polyols in subcritical water. Russian Journal of Physical Chemistry B. 2016;10(7):1116-22.

[150] Matveeva VG, Sulman EM, Manaenkov OV, Filatova AE, Kislitza OV, Sidorov AI, et al. Hydrolytic hydrogenation of cellulose in subcritical water with the use of the Ru-containing polymeric catalysts. Catalysis Today. 2017;280:45-50.

[151] Dabbawala AA, Mishra DK, Hwang J-S. Selective hydrogenation of D-glucose using amine functionalized nanoporous polymer supported Ru nanoparticles based catalyst. Catalysis Today. 2016;265:163-73.

[152] Martinuzzi S, Cozzula D, Centomo P, Zecca M, Müller TE. The distinct role of the flexible polymer matrix in catalytic conversions over immobilised nanoparticles. RSC Advances. 2015;5(69):56181-8.

[153] Rey-Raap N, Ribeiro LS, Orfao JJdM, Figueiredo JL, Pereira MFR. Catalytic conversion of cellulose to sorbitol over Ru supported on biomass-derived carbon-based materials. Applied Catalysis B: Environmental. 2019;256:117826.

[154] S. Ribeiro L, Órfão JJM, R. Pereira MF. Enhanced direct production of sorbitol by cellulose ball-milling. Green Chemistry. 2015;17(5):2973-80.

[155] Ribeiro LS, Delgado JJ, de Melo Órfão JJ, Pereira MFR. Direct conversion of cellulose to sorbitol over ruthenium catalysts: Influence of the support. Catalysis Today. 2017;279:244-51.

[156] Song Z, Wang H, Niu Y, Liu X, Han J. Selective conversion of cellulose to hexitols over bi-functional Ru-supported sulfated zirconia and silica-zirconia catalysts. Frontiers of Chemical Science and Engineering. 2015;9(4):461-6.

[157] Guo X, Wang X, Guan J, Chen X, Qin Z, Mu X, et al. Selective hydrogenation of D-glucose to D-sorbitol over Ru/ZSM-5 catalysts. Chinese Journal of Catalysis. 2014;35(5):733-40.

[158] Wang S, Wei W, Zhao Y, Li H, Li H. Ru–B amorphous alloy deposited on mesoporous silica nanospheres: An efficient catalyst for D-glucose hydrogenation to D-sorbitol. Catalysis Today. 2015;258:327-36.

[159] Guo X, Guan J, Li B, Wang X, Mu X, Liu H. Conversion of biomass-derived sorbitol to glycols over carbon-materials supported Ru-based catalysts. Scientific Reports. 2015;5:16451pp.

[160] Bouxin FP, Strub H, Dutta T, Aguilhon J, Morgan TJ, Mingardon F, et al. Elucidating transfer hydrogenation mechanisms in non-catalytic lignin depolymerization. Green Chemistry. 2018;20(15):3566-80.

[161] Wu H, Song J, Xie C, Wu C, Chen C, Han B. Efficient and Mild Transfer Hydrogenolytic Cleavage of Aromatic Ether Bonds in Lignin-Derived Compounds over Ru/C. ACS Sustainable Chemistry & Engineering. 2018;6(3):2872-7.

[162] Petrus L, Noordermeer MA. Biomass to biofuels, a chemical perspective. Green Chemistry. 2006;8(10):861-7.

[163] Kalinoski RM, Li W, Mobley JK, Asare SO, Dorrani M, Lynn BC, et al. Antimicrobial Properties of Corn Stover Lignin Fractions Derived from Catalytic Transfer Hydrogenolysis in Supercritical Ethanol with a Ru/C Catalyst. ACS Sustainable Chemistry & Engineering. 2020;8(50):18455-67.

[164] Shirai M, Osada M, Yamaguchi A, Hiyoshi N, Sato O. Chapter 15 - Utilization of Supercritical Fluid for Catalytic Thermochemical Conversions of Woody-Biomass Related Compounds. In: Pandey A, Bhaskar T, Stöcker M, Sukumaran RK, editors. Recent Advances in Thermo-Chemical Conversion of Biomass. Boston: Elsevier; 2015. p. 437-53.

[165] Müller TE, Mingos DMP. Determination of the Tolman cone angle from crystallographic parameters and a statistical analysis using the crystallographic data base. Transition Metal Chemistry. 1995;20(6):533-9.

[166] Batsanov SS. Van der Waals Radii of Hydrogen in Gas-Phase and Condensed Molecules. Structural Chemistry. 1999;10(6):395-400.

Access to *N*-Heterocyclic Molecules *via* Ru(II)-Catalyzed Oxidative Alkyne Annulation Reactions

Bhisma K. Patel and Amitava Rakshit

Abstract

In last few decades, the transition metal-catalyzed C-H bond activation and alkyne annulation reactions have turned out to be effective methods for the construction of highly important heterocycles. In particular, the Ru(II) catalysts have been used for the oxidative coupling between an internal alkynes and readily available nitrogen directed compounds in a rapid and sustainable manner. The Ru (II) catalysts are very much beneficial due to their stability in both air and water, ease of preparation, inexpensive than those of Rh(III) and designer Co(III) catalysts usually used for alkyne annulation reactions, requirement of mild reaction conditions, and compatible with various oxidants. Owing to these advantages of Ru(II) catalysts herein, we attempt to highlight the recent development in C-H activation and annulation reactions, which lead to the formation of several important *N*-heterocycles.

Keywords: Ru(II)-catalysts, C-H activation, alkyne annulation, *N*-heterocycles

1. Introduction

The development of highly efficient methods for the synthesis of *N*-heterocyclic skeletons is one of the important targets in organic synthesis. This is because, the nitrogen-containing heterocycles represents a significant class of organic substances, which are particularly found in various biologically active compounds, natural products, drugs, and other medicinally related compounds [1–10]. The *N*-heterocycles especially, pyrroles [2], pyridines/pyridinos [3, 4], indoles [5], isoquinolines [6], quinozalines/quinolizines [7, 8] are useful building blocks of many biologically as well as pharmaceutically active molecules, constitute the core motif of many natural products, and also found wide application in the field of materials science. Due to photo and electrochemical properties highly substituted π-conjugated fused polycyclic *N*-heterocyclic compounds are extensively used as organic semiconductors or luminescent materials [9]. Furthermore, some of these polycyclic *N*-heteroarenes derivatives are versatile building blocks for various natural products [10]. Consequently, in the light of their importance, a large number of efficient methods have been developed, among which the transition metal [Rh(III), Co(III), Ru(II), Pd(II), Ni(II)/Ni(0)]-catalyzed C-H bond activation and oxidative

alkyne annulation reactions are serving as most attractive methodologies, for the construction of *N*-heterocycles [11–16]. The *ortho*-C-H bond activation *via* the use of coordinative functional group followed by cyclization with internal alkynes, commonly known as annulation reaction is extremely motivating as it allows the formation of highly important heterocycles in an atom economical fashion. In this context, the Ru(II) catalysts have been used extensively for the catalytic activation of unreactive C-H bonds and oxidative annulation reactions, particularly with internal alkynes. This is due to several advantages of Ru(II) catalyst such as both air and water stability, easy to prepare, mild reaction conditions, compatible with various oxidants, relatively cheaper and provides excellent chemo- and regio-selective functionalizations than those of Rh(III) and Co(III) catalysts. In this chapter, we attempt to highlight the progresses in the field of C-H bond activation catalyzed by Ru(II) complexes leading to the construction of various *N*-heterocycles via oxidative alkyne annulation reactions.

2. The ruthenium(II) catalyst

For C-H bond activation and oxidative alkyne annulation reactions, the commonly used ruthenium(II) catalyst is dichloro(*p*-cymene)ruthenium(II) dimer, $[Ru(p\text{-cymene})Cl_2]_2$. This dimeric Ru(II) catalyst in combination with acetate/carbonate bases or acetate containing oxidants $Cu(OAC)_2{\bullet}H_2O$ generates the active species *via* ligand exchange which is responsible for the deprotonative C-H or C-H/N-H activation. In the presence of other oxidants such as $AgSbF_6$ or KPF_6, the dimeric Ru(II) complex forms an active cationic species either in the absence or presence of $Cu(OAC)_2{\bullet}H_2O$. Again, the oxidants are necessary to reoxidize the Ru (0) to Ru(II) after the reductive elimination to regenerate the active catalyst. The various combination of reagents with Ru(II) dimeric complex for the *in situ* generation of active Ru(II) catalyst in the C-H bond activation and oxidative alkyne annulation processes are shown in **Figure 1**.

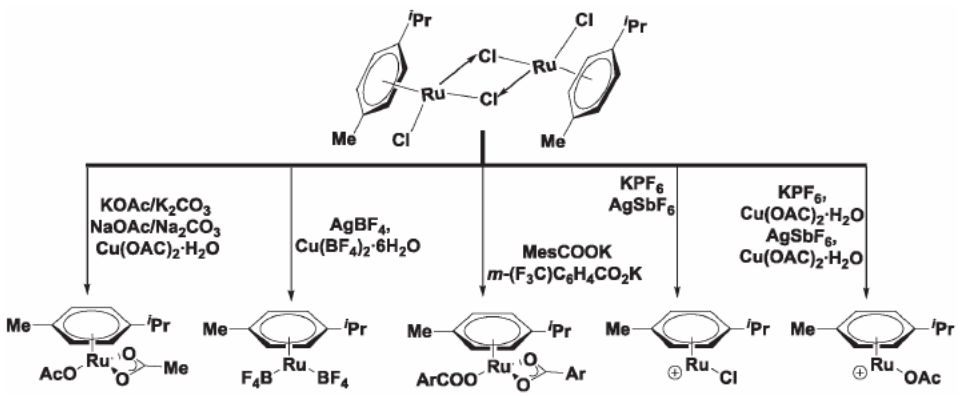

Figure 1.
In Situ *generated active Ru(II) complex.*

3. Ruthenium(II)-catalyzed C-H bond activation

In the past few decades, Ru(II)-catalyzed C-H bond activation has become much popular for the C-C cross coupling reactions. In particular, the directing group assisted (chelation-assisted) C–H bond activation using coordinative functional

DOI: http://dx.doi.org/10.5772/ITexLi.95987

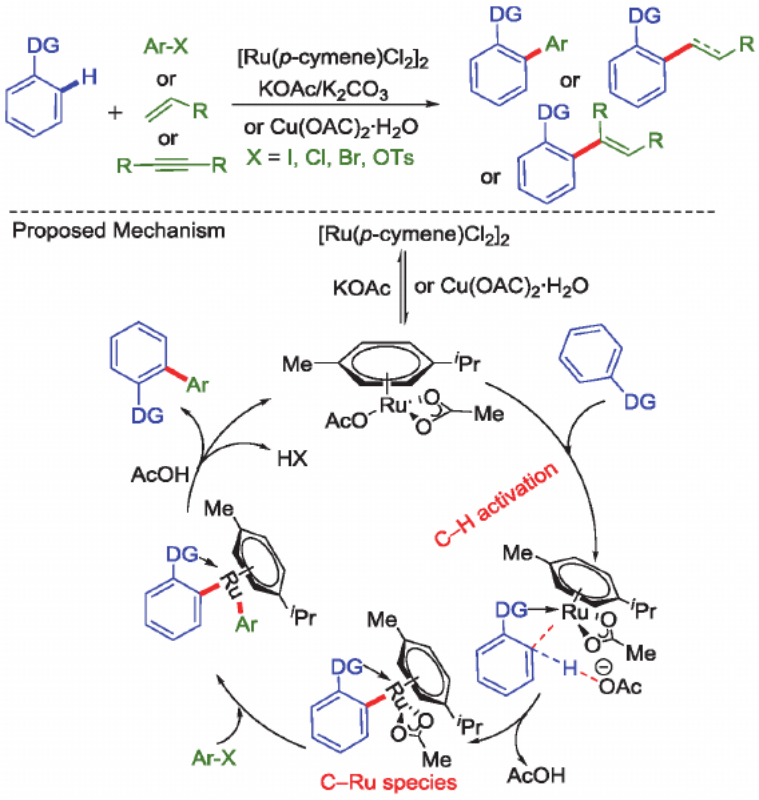

Figure 2.
Ru(II)-catalyzed C-H bond activation for the construction of C-C bond.

group has offered several advantages [17]. Actually this activation strategy uses the proximate effect by coordination of a functional group in a given substrate to the ruthenium centre of the catalyst that brings about regioselective C-H bond activation and functionalization. In the processes of C-H bond activation reactions, the active Ru(II) catalysts facilitates the deprotonation of C-H bonds, before any oxidative addition and the process occur via the assistance of Ru(II) site and *in situ* coordinated carbonate [18] or carboxylate [19]. Alternatively, an intermolecular deprotonation of C-H bonds by carboxylate activates the Ru(II) [20] thereby forming a C − Ru species, which is the key intermediate in the coupling reactions (**Figure 2**).

4. Ru(II)-catalyzed oxidative alkyne annulation reactions

The chelating group assisted ruthenium(II)-catalyzed insertion of an internal alkynes into the *ortho*-C_{Sp2}-H bond, followed by an intramolecular cyclization with the directing heteroatom (particularly O and N atom) or insertion of the alkynes into the C_{Sp2}-H/heteroatom-H bonds is commonly known as oxidative alkyne annulation reaction. These oxidative alkyne annulation reactions provide an environmentally friendly approach and are popular for the synthesis of a verity of useful heterocyclic compounds via the formation of C-C and C-heteroatom bonds in a step economical fashion (**Figure 3**) [21]. The ruthenium(II)-catalyzed alkyne annulation reaction proceeds mainly via insertion of the *in situ generated* active ruthenium(II) complex into the *ortho*-C_{Sp2}-H bond thereby forming a ruthenacycle complex,

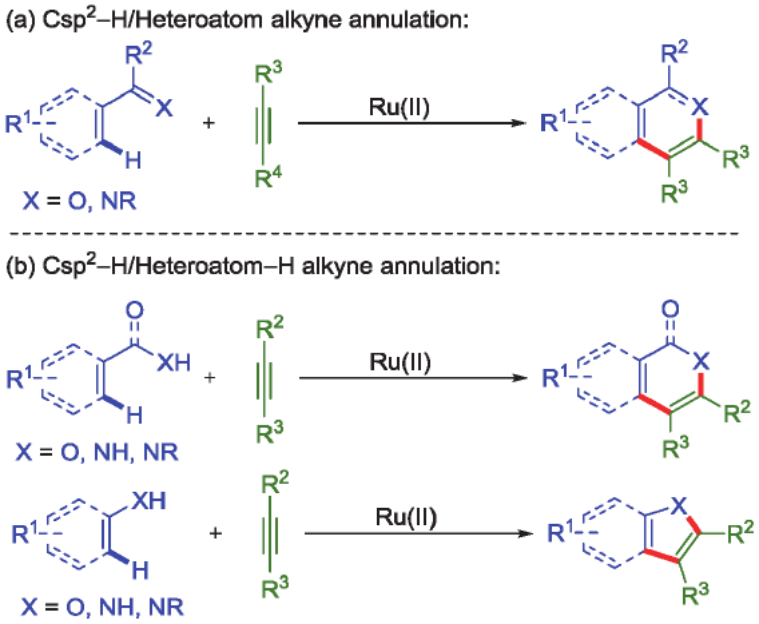

Figure 3.
Ru(II)-catalyzed oxidative alkyne annulation reactions.

insertion of an internal alkyne partner and finally reductive elimination of the active ruthenium complex. Herein, the applications of the ruthenium(II)-catalyzed C_{Sp2}-H/N and C_{Sp2}-H/N-H oxidative alkyne annulation reactions leading to the construction of various *N*-heterocyclic molecules is highlighted.

5. Mechanisetic aspect of Ru(II)-catalyzed C-H/N & C-H/N-H alkyne annulation reactions

5.1 Nature of the C-H bond activation

Ruthenium(II)-catalyzed alkyne annulation reaction started via the activation of the C-H bond *ortho* to the nitrogen atom of the directing group thereby forming a C-Ru species. In this C-H bond activation, whether the C-H ruthenation step is reversible or irreversible can be confirmed by a deuterium-scrambling experiment (**Figure 4**) [22]. If the deuterium exchange on a specific substrate in the absence or presence of alkyne under the standard reaction condition in a deuterated solvent (ionisable) did not afford any H/D exchange or undergoes a minor exchange at the *ortho*-C-H position, suggest an irreversible C-Ru bond formation. On the other hand, if the H atom of the *ortho*-C-H undergoes a significant H/D exchange then the ruthenation step might be reversible.

5.2 Kinetic Isotop effect (KIE) study

In Ru(II)-catalyzed oxidative alkyne annulation reactions the rate-determining step can be explained on the basis of kinetic isotop effect [23]. This can be done by an intermolecular competitive experiment between a non-deuterated and corresponding deuterated substrates with an internal alkyne under the standard reaction condition (**Figure 5a**) or from two parallel reaction involving non-deuterated and corresponding deuterated substrates individually (**Figure 5b**).

DOI: http://dx.doi.org/10.5772/ITexLi.95987

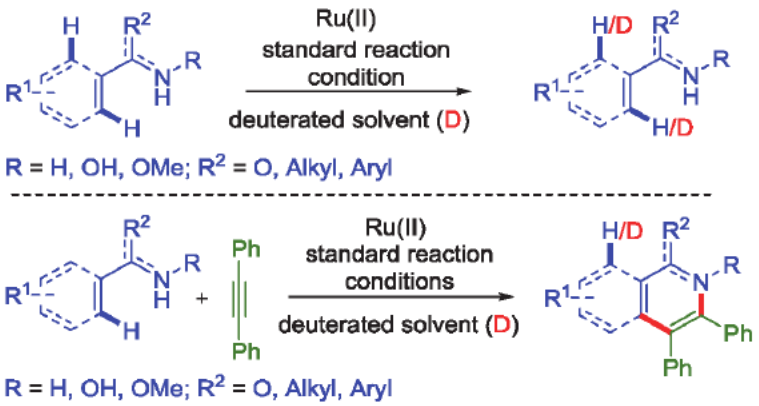

Figure 4.
Deuterium-scrambling experiment.

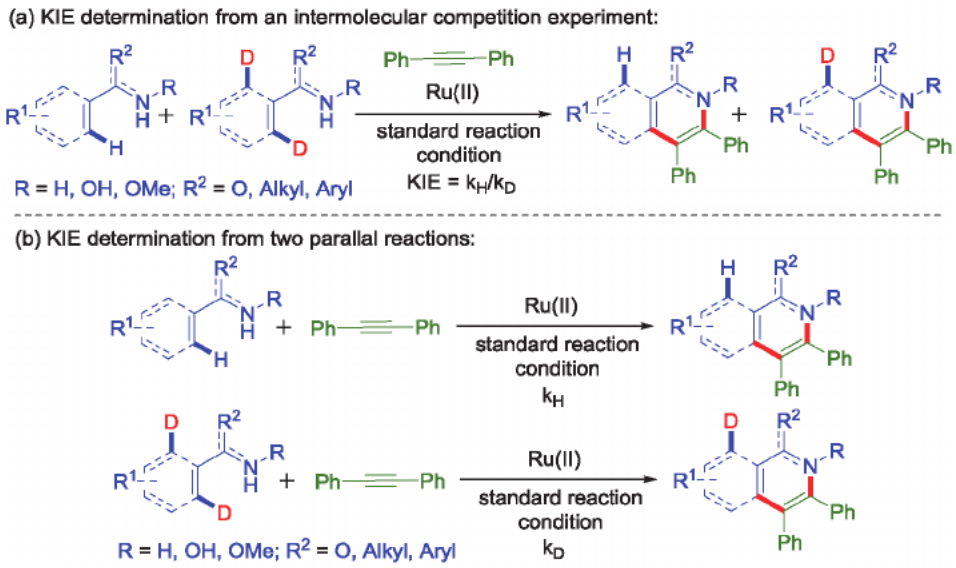

Figure 5.
KIE determination experiment.

If these experiments provide a $k_H/k_D > 1.0$ than it is suggests that the initial C-H bond cleavage, *i.e.*, the C-Ru (reversible or irreversible) bond formation is the rate determining step. The KIE is determined from the ratio between the kinetic constants for the non-deuterated (k_H) and deuterated (k_D) substrates. Nevertheless, it is also estimated indirectly by the measurement of the ratio of individual yield of the corresponding undeuterated product and deuterared analogues or from their ^{1}HNMR spectra in the case of a mixture of products on the basis of their integration ratio.

5.3 Regioselectivity of the alkyne annulation

The regioselectivity of these Ru(II)-catalyzed oxidative alkyne annulation can be determined by the reaction of an unsymmetrical internal alkyne having an alkyl and an aryl substituent such as 1-phenyl-1-propyne. It has been found that the internal

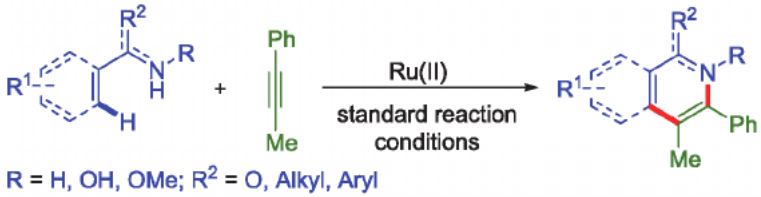

Figure 6.
Regioselectivity of the internal alkyne.

alkyne inserts into the C-H bonds through the carbon atom towards the alkyl part while the aryl substituted carbon center of the internal alkyne is connected to the nitrogen atom (**Figure 6**). This preferential reactivity of the nitrogen atom at the benzylic carbon of an unsymmetrical internal alkynes leading to regioselective annulation is quite similar to that of C-H/O-H C-H/S-H annulation reactions [24, 25].

6. Ru(II)-catalyzed C-H activation and oxidative alkyne annulation reactions for the synthesis of *N*-heterocycles

In the chelation-assisted Ru(II)-catalyzed C-H bond activation the nitrogen-containing directing groups have been consistently used for the reaction with internal alkynes to access *N*-heterocycles through the formation of C-C and C-N bonds respectively [26–34]. In this annulation processes the lone pair of nitrogen atom directs the active ruthenium complex to get inserted into the *ortho*-C-H bond, thereby forming a cyclic ruthenium complex. This cyclic ruthenium complex on subsequent alkyne insertion and finally reductive elimination of the active Ru(II) catalyst left the nitrogen atom becomes part of the final cyclic product.

i. In 2012, Ackermann *et al.* reported a cationic ruthenium(II)-catalyzed efficient redox-neutral annulations of alkynes with readily available oximes for the synthesis of isoquinolines (**Figure 7**) [26]. Herein, C-H/N-O functionalizations occurs by carboxylate-free cationic ruthenium(II) catalyst in the absence of external oxidants through a reversible Ru-C cycloruthenation.

ii. In 2012, Jeganmohan and co-workers reported the synthesis of substituted isoquinolines *via* ruthenium(II)-catalyzed C-H bond activation using ketoximes with internal alkynes (**Figure 8**) [27].

iii. Cheng and co-workers developed a one pot three-component reaction for the synthesis of isoquinolinium salts from benzaldehydes, amines, and alkynes using Ru(II)-catalyst via C-H bond activation and annulation (**Figure 9**) [28]. In this reaction, the active Ru(II) complex first coordinates with the nitrogen atom of the in situ generated imine followed by *ortho*-C-H activation forming a five membered ruthenacycle, this is followed by an alkyne insertion, reductive elimination of the ruthenium to afford the isoquinolinium salts and finally reoxidation to the active Ru(II) by Cu $(BF_4)_2$ allows its further participation in the catalytic cycle.

iv. In 2013, Cheng *et al.* used the in-situ generated Ru(II) catalyst for vinylic C-H bond activation and alkyne annulation to synthesize quinazoline salts

DOI: http://dx.doi.org/10.5772/ITexLi.95987

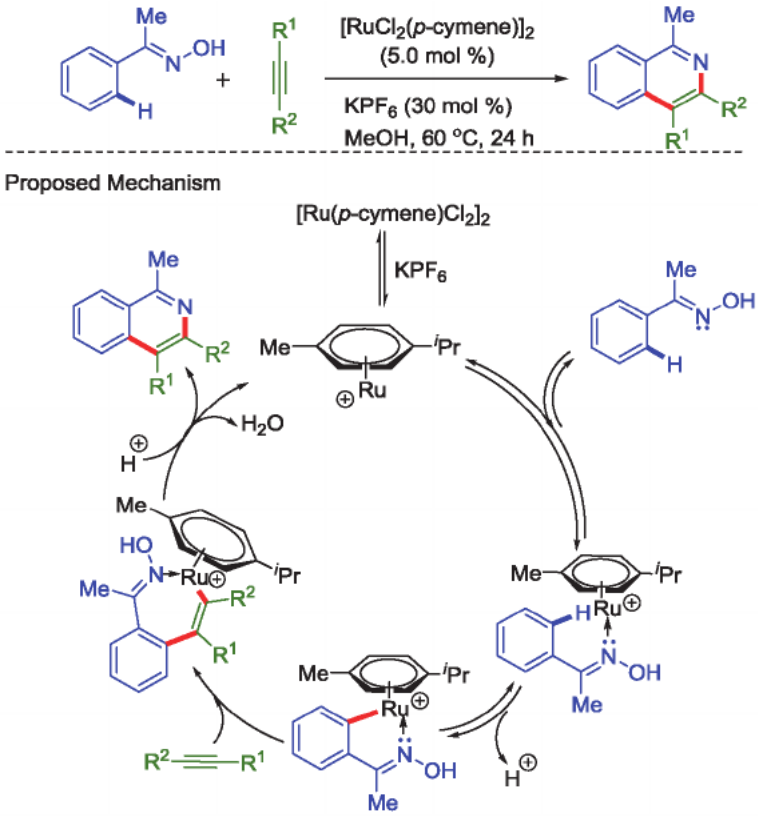

Figure 7.
Carboxylate-free Cataionic ruthenium(II)-catalyzed synthesis of Isoquinolines.

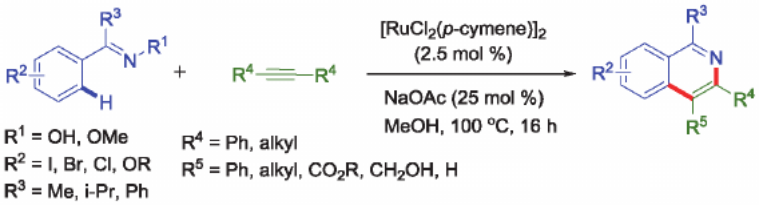

Figure 8.
Ruthenium(II)-catalyzed synthesis of substituted Isoquinolines.

(**Figure 10**) [29]. A possible mechanism involving pyridine assisted vinylic *ortho*-C-H activation of 2-vinylpyridines, followed by an alkyne insertion and reductive elimination is proposed.

v. In 2014, Ackermann *et al.* effectively used carboxylate-assisted cationic Ru (II) complex for the synthesis of exo-methylene-1,2-dihydroisoquinolines via imine-assisted C-H bond activation and oxidative alkyne annulation reaction of ketimines with alkynes (**Figure 11**) [30]. This C-H bond functionalization proceeded with excellent chemo-, site-, and regio-selectivity under an ambient atmosphere of air. The mechanistic studies were indicative of a reversible C-H bond ruthenation step followed by tautomeraization and migratory insertion of the alkyne.

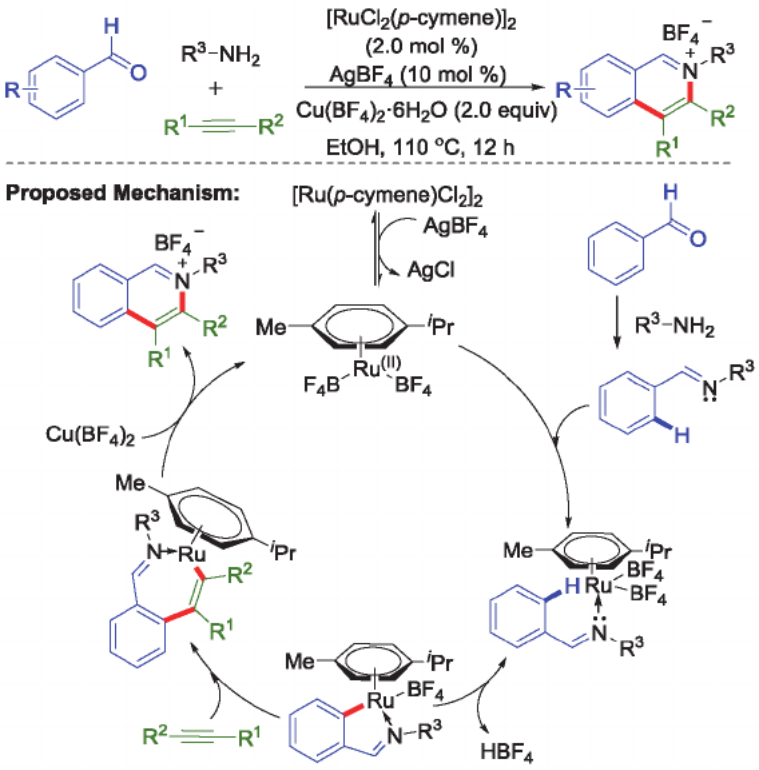

Figure 9.
Ruthenium(II)-catalyzed synthesis of Isoquinolinium salt.

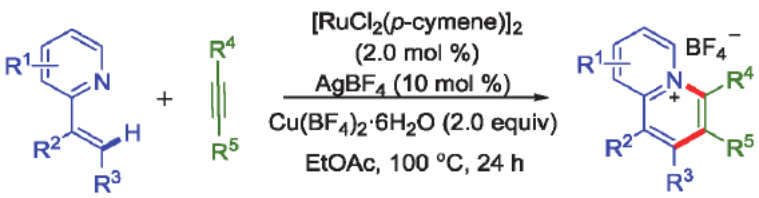

Figure 10.
Ruthenium(II)-catalyzed synthesis of Quinazoline salt.

vi. In 2014, Kundu and co-workers developed an in situ generated iminophosphoranes directed efficient synthesis of isoquinoline-2(1*H*)-ones *via* the Ru(II)-catalyzed ortho C-H bond activation (**Figure 12**) [31]. The reaction involves the coordination of the active Ru(II) catalyst with the *N*-atom of the iminophosphorane intermediate, *ortho* C-H cycloruthenation, insertion of an alkyne into the Ru-C bond, and protonative reductive elimination.

vii. In 2014, Ackermann *et al.* reported a Ru(II)-catalyzed annulation reaction of redox-active challenging ferrocenylalkynes with oximes via C-H/N-O bond functionalization to afford isoquinolines bearing a ferrocene moiety (**Figure 13a**) [32]. They extended the annulations reaction of ferrocenylalkynes with *N*-methoxybenzamides via a ruthenium(II)-catalyzed carboxylate-assisted C-H/N-H bond activation for an efficient

DOI: http://dx.doi.org/10.5772/ITexLi.95987

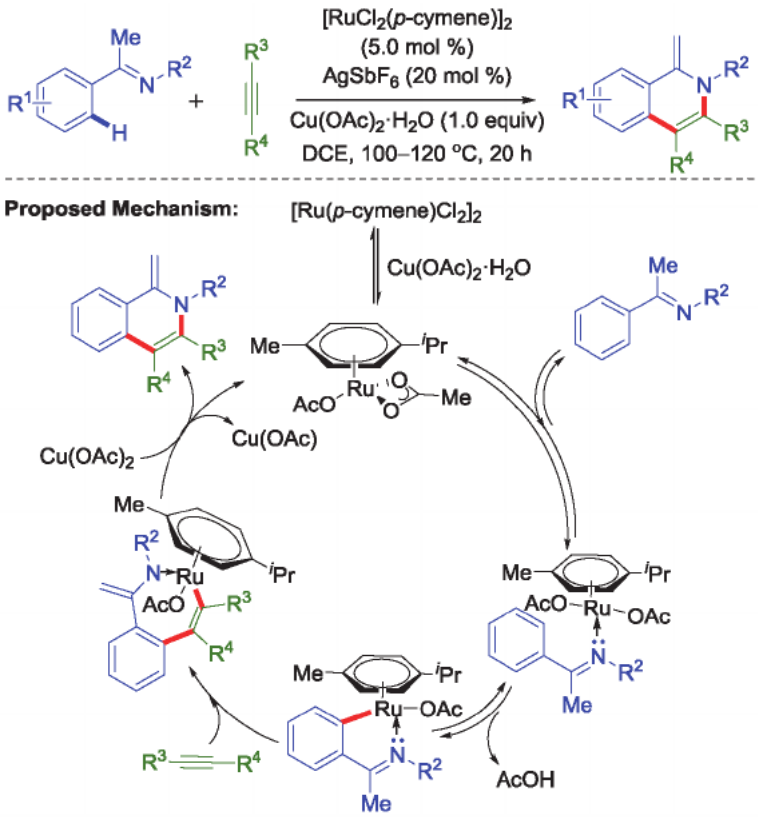

Figure 11.
Ruthenium(II)-catalyzed synthesis of Exo-methylene-1,2-dihydroisoquinolines.

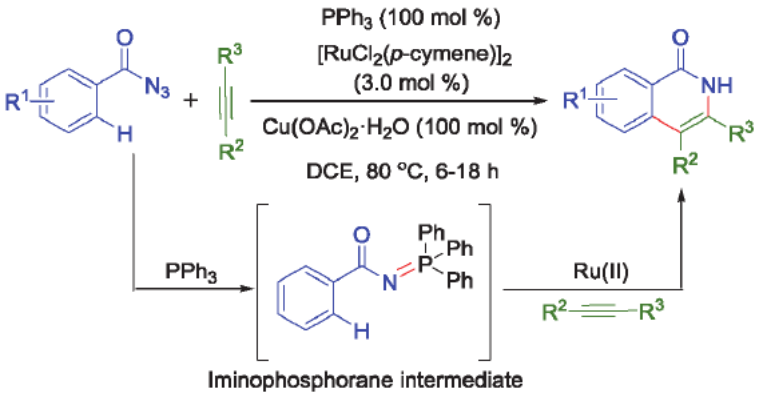

Figure 12.
*Ruthenium(II)-catalyzed synthesis of Isoquinoline-2(1*H*)-ones.*

syntheses of ferrocenated isoquinolones in water as a sustainable reaction medium (**Figure 13b**).

viii. In 2015 wang *et al.* Reported a ruthenium(II)-catalyzed dehydrative [4 + 2] cycloaddition between enamides and alkynes for the construction of a highly substituted pyridines (**Figure 14**) [33]. Herein, instead of the N atom, the carbonyl group of the enamide coordinated to the Ru center to

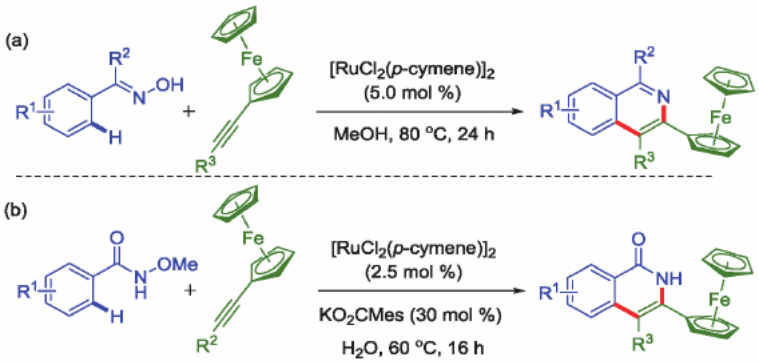

Figure 13.
Ruthenium(II)-catalyzed synthesis Isoquinolines/Isoquinolones.

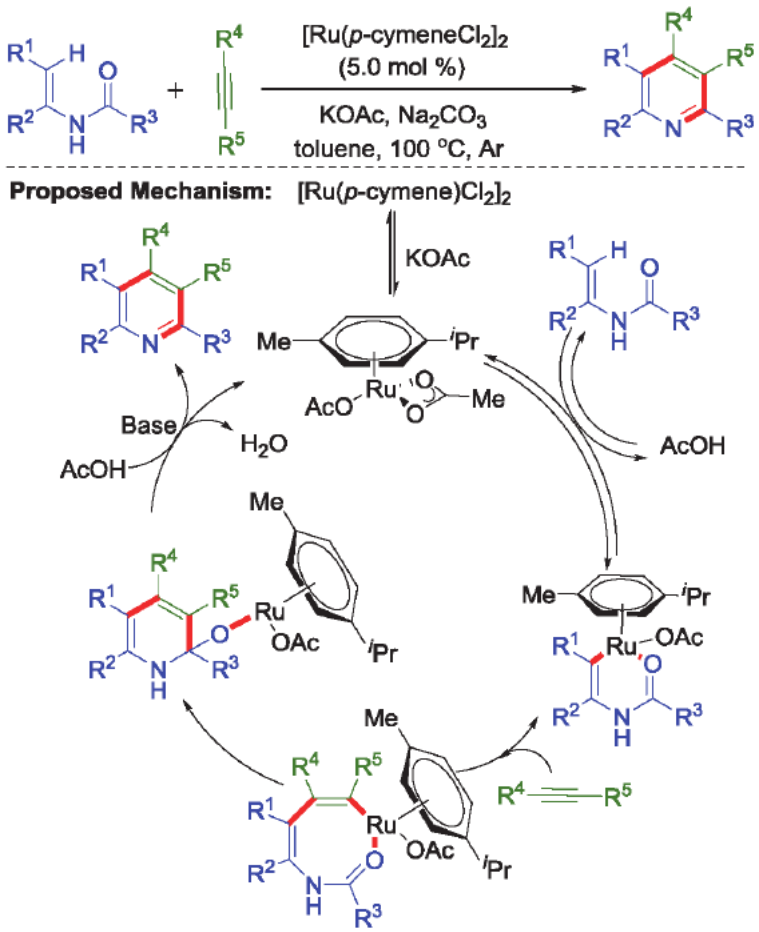

Figure 14.
Ruthenium(II)-catalyzed substituted pyridine synthesis.

direct the C-H activation to generates a six-membered ruthenacycle intermediate. Then the alkyne is inserted into the Ru-C bond giving rise to an eight-membered ruthenacycle intermediate and finally afforded the pyridine analogue through a dehydration path with excellent regioselectivities.

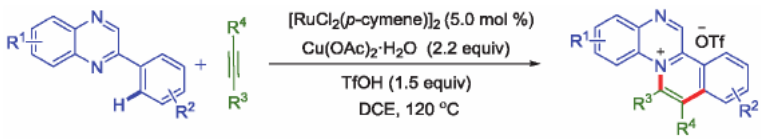

Figure 15.
Ruthenium(II)-catalyzed synthesis of Quinoxalinium salts.

ix. In 2019 our group reported a Ru(II)-catalyzed synthesis of highly luminescent quinoxalinium salt *via* quinoxaline *N*-directed oxidative annulation of 2-arylquinoxalines with an internal alkyne in the presence of a $Cu(OAc)_2{\cdot}H_2O$ via the formation of C-C and C-N bonds (**Figure 15**) [34].

7. Synthesis of *N*-heterocycles *via* Ru(II)-catalyzed C-H/N-H dual activation and alkyne annulation reactions

Simultaneously activation of C-H and N-H bonds occurs when the nitrogen atom of the directing group possesses an acidic hydrogen atom. The active Ru(II) catalyst first forms a cyclic Ru complex via a concerted deprotonative metalation generally through acetate/carboxylate assisted N-H/C-H activation. A subsequent alkyne insertion and reductive elimination of the ruthenium affords various *N*-hetreocyclic molecules particularly pyrroles, 2-pyridones, indoles, isoquinolines/isoquinolones derivatives, and various others π-conjugated polycyclic *N*-heteroaromatic molecules in a step-economical fashion *via* C-C and C-N bond formation [35–58].

7.1 Synthesis of *pyrroles via* C-H/N-H alkyne annulation

i. In 2013, Ackermann group reported a versatile synthesis of pyrrole through a ruthenium(II)-catalyzed C-H/N-H bond functionalization and oxidative annulation reaction of electron-rich enamines with various alkynes utilizing air as the ideal oxidant (**Figure 16**) [35].

ii. Baiquan Wang and co-workers reported an efficient and regioselective Ru (II)-catalyzed *N*-acetyl-substituted pyrroles synthesis *via* the cleavage of C (sp^2)-H/N-H bonds and oxidative annulation reaction of enamides with alkynes (**Figure 17**) [36]. The reaction afforded *N*-acylated pyrroles by addition of $AgSbF_6$ as an additive in MeOH solvent.

iii. In 2013, Liu *et al.* developed an efficient cationic Ru(II)-catalyzed oxidative annulation of enamides with alkynes for the synthesis of N-acetylpyrrole derivatives in dimethoxyethane solvent (**Figure 18**) [37]. Further, the reaction can be carried out in an aqueous medium providing 95% yield when diphenylacetylene was used. The yield decreased significantly in aqueous medium when substituted diphenylacetylenes were employed as the coupling partner.

7.2 Synthesis of 2-pyridones *via* C-H/N-H alkyne annulation

In 2011, Ackermann and co-workers used a ruthenium catalyst to execute the C-H/N-H activation and oxidative alkyne annulation reaction to synthesize substituted 2-pyridones via C-C and C-N bond formation (**Figure 19**) [38]. They

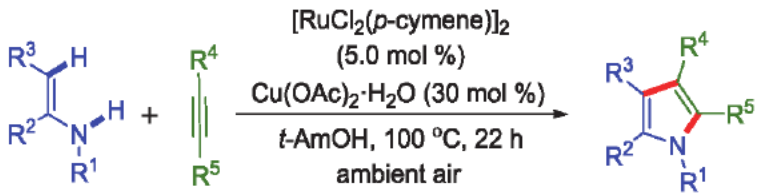

Figure 16.
Ruthenium(II)-catalyzed pyrrole synthesis via *C-H/N-H alkyne annulation.*

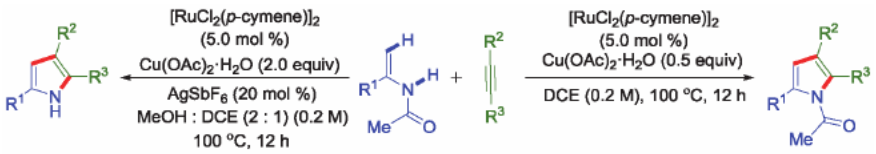

Figure 17.
Ruthenium-catalyzed pyrrole synthesis.

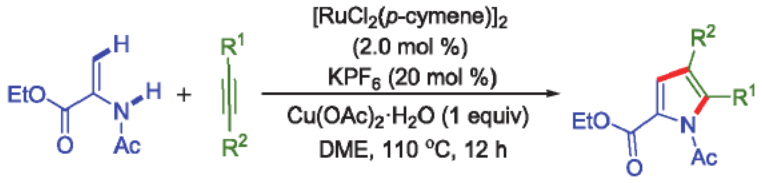

Figure 18.
Cationic Ru(II)-catalyzed synthesis of N*-acetylpyrroles.*

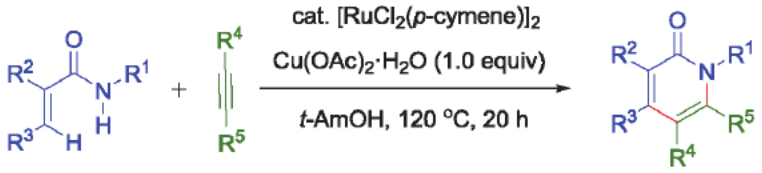

Figure 19.
Ruthenium(II)-catalyzed synthesis of 2-Pyridones.

used various electron-rich and electron-deficient *N*-substituted acrylamides as well as diaryl- and dialkyl-substituted internal alkynes which shows a broad and improved range of substrate scope.

7.3 Synthesis of indoles *via* C-H/N-H alkyne annulation

i. In 2012, Ackermann and co-workers demonstrated an cationic Ru(II) catalyzed (generated *in situ*) oxidative C–H/N–H bond functionalizations of anilines using a removable directing group to synthesize various bioactive substituted indole derivatives (**Figure 20**) [39]. Herein, the oxidative alkyne annulation occurs through the construction of C-C and C-N bonds using water as the solvent. Mechanistic studies indicate that the reaction proceeds through the reversible formation of a six-membered ruthenacycles as the key intermediates.

DOI: http://dx.doi.org/10.5772/ITexLi.95987

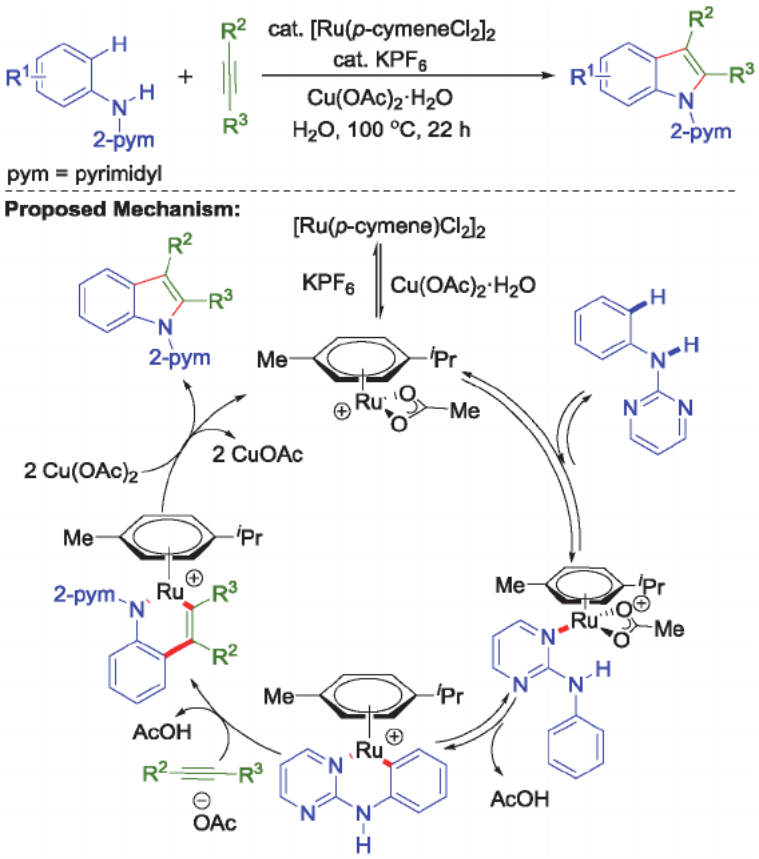

Figure 20.
Cationic ruthenium(II)-catalyzed synthesis of indoles.

ii. In 2014, Huang *et al.* for the first time developed a Ru(II)-catalyzed redox-neutral C-H activation reaction via N-N bond cleavage for the regioselective synthesis of *N*-substituted indoles (**Figure 21**) [40]. The N-N bond of pyrazolidin-3-one acts as the directing group that enables C-H activation and annulation reactions with a broad scope of alkynes. The reaction proceeds via Ru(II)-catalyzed N-H/C-H bond activation, alkyne insertion, internal oxidation of Ru(II) to Ru(IV) and reductive elimination pathways.

iii. In 2018 Xu *et al*. established a ruthenium(II)-catalyzed electrochemical dehydrogenative C-H/N-H bond activation and annulation reaction for the efficient synthesis of indoles using N-2-pyrimidyl-substituted anilines and internal alkynes (**Figure 22**) [41]. Here, the electrolysis reaction proceeds in a simple undivided cell in an aqueous solution and instead of any external oxidant the electric current is used to regenerate the active ruthenium catalyst.

7.4 Synthesis of Isoquinolines/Isoquinolones *via* C-H/N-H alkyne annulation

i. In 2011, Ackermann *et al.* reported an unparalleled ruthenium(II)-catalyzed annulations of alkynes using *N*-benzyl-substituted benzamides as the substrates and internal alkynes as the annulating partner. Here,

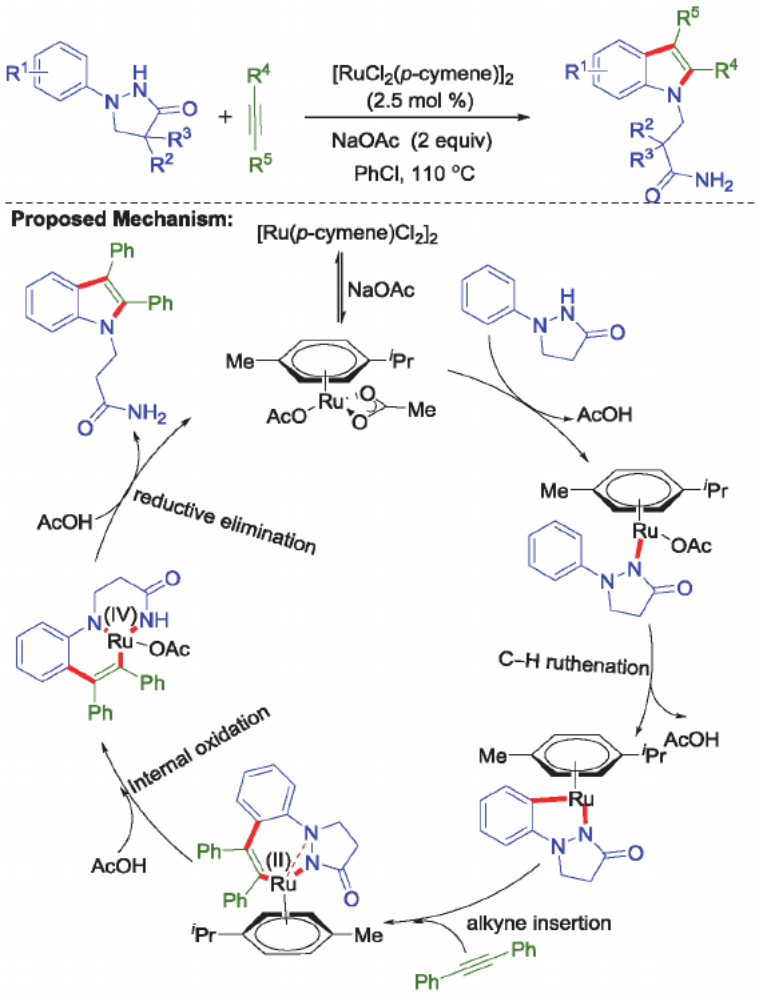

Figure 21.
Ruthenium(II)-catalyzed synthesis of indoles via *N-N cleavage.*

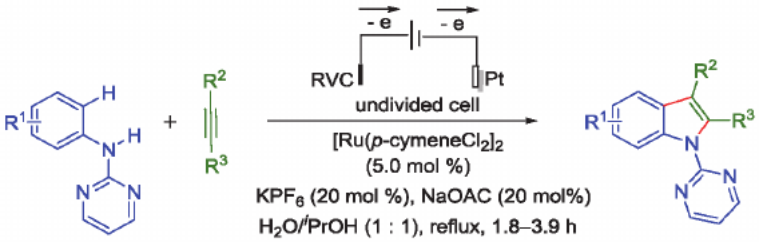

Figure 22.
Ruthenium(II)-catalyzed electrochemical synthesis of indoles.

chemo- and site-selective functionalization of both C-H and N-H bonds occurs during the synthesis of isoquinolone derivatives (**Figure 23**) [42]. Mechanistic studies in deuterated ^{t}AmOH suggests an irreversible C-H bond ruthenation. Further, the kinetic isotope effect (KIE) study provided strong evidence for a rate-limiting C-H bond ruthenation through carboxylate assistance.

DOI: http://dx.doi.org/10.5772/ITexLi.95987

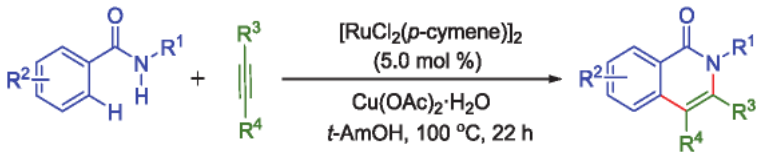

Figure 23.
Ruthenium(II)-catalyzed synthesis of Isoquinolones.

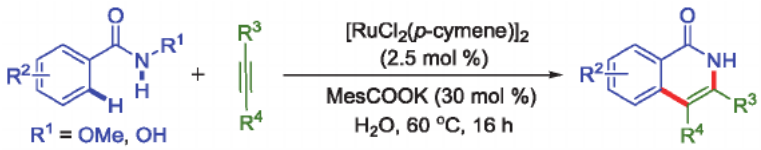

Figure 24.
Ruthenium(II)-catalyzed external oxidant free synthesis of Isoquinolones.

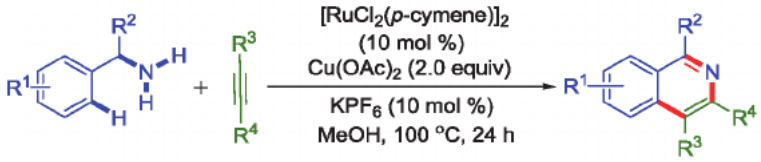

Figure 25.
Ruthenium catalyzed synthesis of Isoquinoline derivatives.

ii. Ackermann group established an external oxidant-free annulation reaction for the synthesis of isoquinolones which proceeds via N-H/C-H activation. The reaction is accomplished through a carboxylate assisted ruthenium(II) catalyst with ample substrate scope in an aqueous medium. In this annulation reaction, the N-O bond of N-methoxybenzamides served as the internal oxidant and free hydroxamic acids were also found to be good substrates for this alkyne annulation due to chemoselectivity of the ruthenium(II) carboxylate catalyst (**Figure 24**) [43].

iii. In 2013, Urriolabeitia and co-workers have developed an unprotected primary amine (benzylamines) directed Ru(II)-catalyzed oxidative coupling with internal alkynes for the synthesis of isoquinolines (**Figure 25**) [44].

iv. In 2014, another external oxidant-free alkyne annulation reaction was reported by Ackermann *via* an *in situ* generated ruthenium(II) biscarboxylate catalyst. This dehydrative alkyne annulations proceeds via a C − H/N − H activation followed by N-OH cleavage of NH-free hydroxamic acids in water producing water as the sole by product (**Figure 26**) [45]. The ruthenium(II) catalyst derived from the electron-deficient carboxylic acid *m*-$(F_3C)C_6H_4CO_2H$ displayed highly regio- and site-selective C − H functionalizations with a broad substrate scope. Further, detailed mechanistic studies suggest a kinetically relevant C − H metalation by carboxylate assistance along with subsequent migratory alkyne insertion, reductive elimination, and intramolecular oxidative addition.

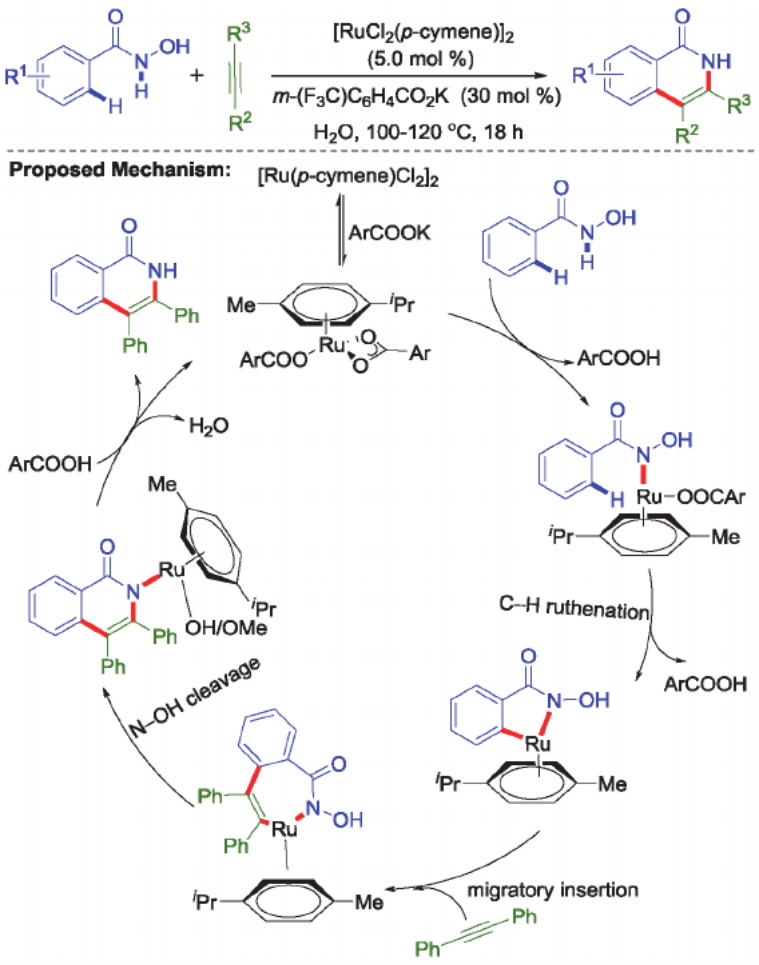

Figure 26.
Ruthenium(II)-catalyzed external oxidant free synthesis of Isoquinolones.

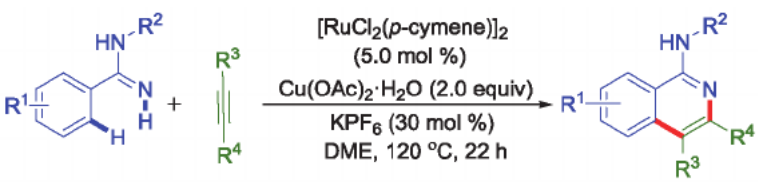

Figure 27.
Ru(II)-CatalyZed synthesis of 1-Aminoisoquinolines derivatives.

v. In the same year, Ackermann group developed an efficient C-H functionalizations and oxidative annulation reaction on aryl and heteroaryl amidines with internal alkynes to access 1-aminoisoquinolines (**Figure 27**) [46]. Herein, the in situ generated cationic Ru(II) complexes derived from KPF_6 or AgOAc displayed a reversible C-H bond activation and C-H/N-H alkyne annulation with high site-, regio- and, chemoselectivity.

vi. In the year 2014, Swamy and co-workers use 8-aminoquinoline moiety as an auxiliary bidentate directing group for ruthenium(II)-catalyzed oxidative annulation of *N*-quinolin-8-yl-benzamides with alkynes to

DOI: http://dx.doi.org/10.5772/ITexLi.95987

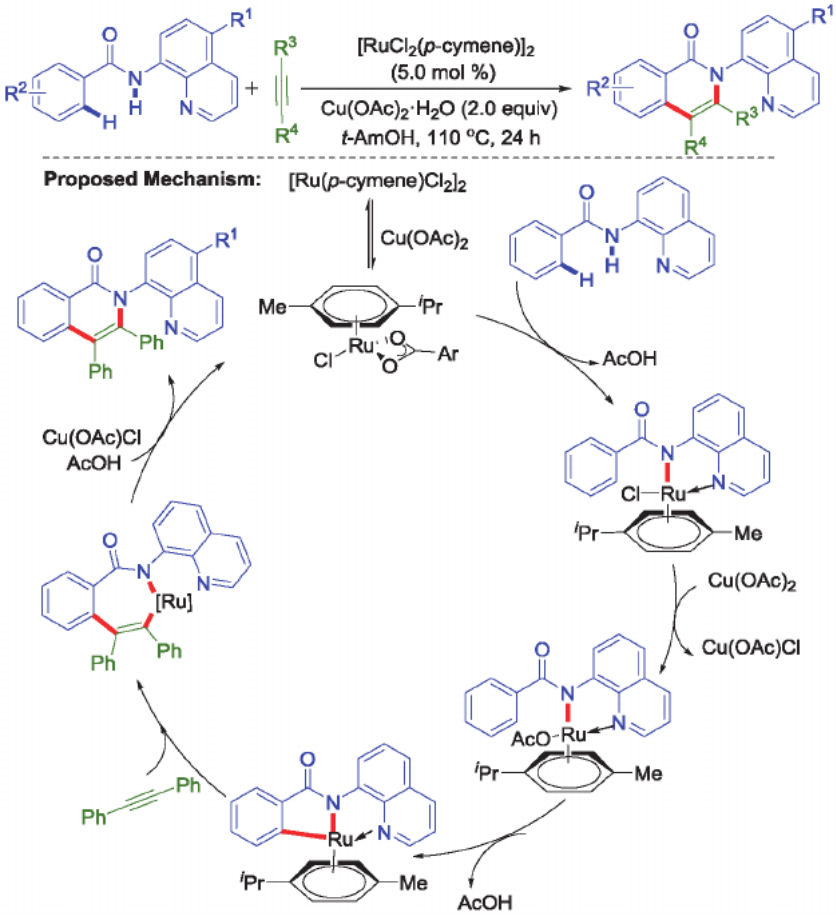

Figure 28.
Ruthenium(II)-catalyzed synthesis of Isoquinolone derivatives.

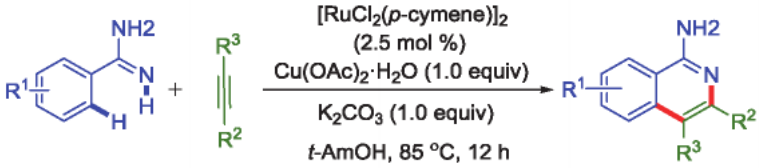

Figure 29.
Ru(II)-catalyzed synthesis of Isoquinoline derivatives.

achieve isoquinolones with high regioselectivity, broad substrate scope and broad functional group tolerance (**Figure 28**) [47]. The reaction occurs in the presence of $[RuCl_2(p\text{-cymene})]_2$ as the catalyst and $Cu(OAc)_2{\cdot}H_2O$ as an oxidant with the involvement of a monoacetate complex [RuCl(OAc)(*p*-cymene)] instead of the bis-acetate complex $[Ru(OAc)_2(p\text{-cymene})]$. The mechanistic studies reveals involvement of a ruthenium N-quinolin-8-yl- benzamide complex (i.e. N,N-bidentate chelate complex).

vii. In 2017, Gogoi *et al.* reported a Ru(II)-catalyzed C-H/N-H activation and oxidative annulation of benzamidines and internal alkynes for the facile synthesis of 1-aminoisoquinolines with excellent regioselectivity (**Figure 29**) [48].

viii. In 2017, Urriolabeitia *et al.* described a carboxylate assisted Ru(II)-catalyzed synthesis of isoquinoline-1-carboxylate derivatives through C-H/N-H oxidative annulation reaction between *N*-unprotected methyl esters of phenylglycine and internal alkynes (**Figure 30**) [49]. The *N*-fluoro-2,4,6-trimethylpyridinium triflate works as the terminal oxidant and the process shows a remarkable tolerance to the presence of diverse electron-releasing and electron-donating functional groups at the phenyl ring of the amino acid.

7.5 Synthesis of π-conjugated polycyclic *N*-Heteroaromatic molecules *via* C-H/N-H oxidative alkyne annulation

i. In 2012, Ackermann *et al.* reported a ruthenium(II)-catalyzed aerobic oxidative coupling of alkynes with 2-arylindoles in the presence of a catalytic amount of $Cu(OAc)_2 \cdot H_2O$ and air as the oxidants for the facile synthesis of fused polycyclic indolo[2,1-*a*]isoquinolines (**Figure 31a**) [50]. Further, they extended the scope of this C-H/N-H oxidative annulations reaction between 2-arylpyrroles and alkynes which afforded good yields of pyrrolo[2,1-*a*]isoquinolines (**Figure 31b**) [50].

ii. In the same year, Ackermann group developed a cationic ruthenium(II)-catalyzed effective oxidative annulations of aryl- and alkyl-substituted alkynes with 5-aryl-1H-pyrazoles with excellent chemo- and regioselectivities. This C-H/N-H bond functionalization strategy provided conjugated pyrazolo[5,1-*a*]isoquinolines derivatives with ample substrate scope. Detailed mechanistic investigation agreed for a reversible C-H bond ruthenation with the cationic ruthenium(II) catalyst (**Figure 32**) [51].

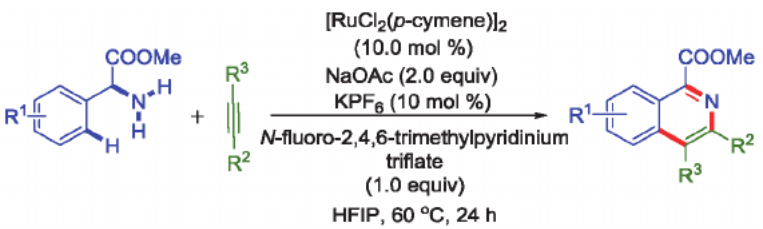

Figure 30.
Ru(II)-catalyzed synthesis of Isoquinoline derivatives.

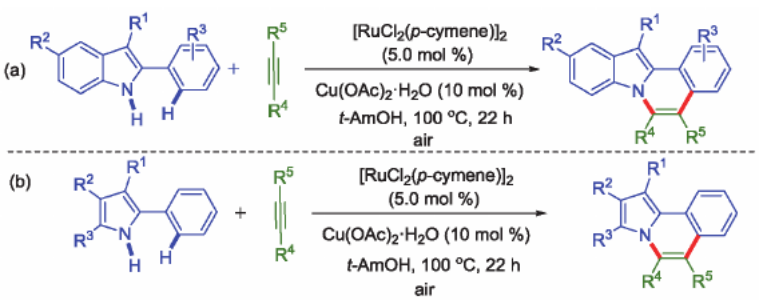

Figure 31.
Ruthenium(II)-catalyzed synthesis of Indolo[2,1-a]isoquinolines and Pyrrolo[2,1-a]isoquinolines.

DOI: http://dx.doi.org/10.5772/ITexLi.95987

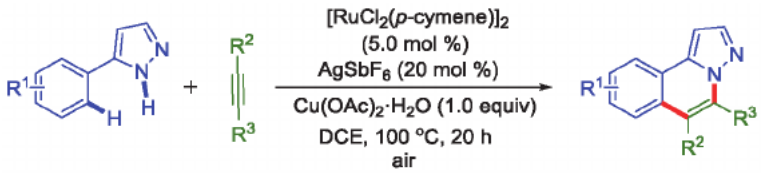

Figure 32.
Cationic ruthenium(II)-catalyzed synthesis of Pyrazolo[5,1-a]isoquinolines.

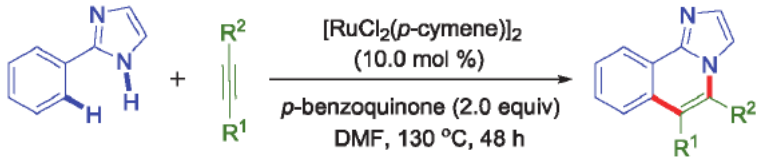

Figure 33.
Ruthenium(II)-catalyzed synthesis of Imidazo[2,1-a]isoquinolines.

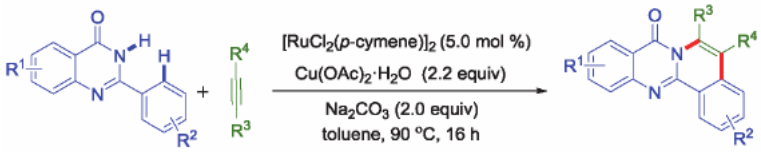

Figure 34.
Ruthenium(II)-catalyzed synthesis of tetracyclic Heteroarenes.

iii. In 2014, Wang and co-workers reported an efficient access to various imidazo[2,1-*a*]isoquinolines via a ruthenium(II)-catalyzed oxidative alkyne annulation reaction of 2-phenylimidazole in the presence of para-benzoquinone as the oxidant (**Figure 33**) [52]. In this cascade C-H/N-H bond functionalization reaction a wide range of electron deficient alkynes are converted into the fused isoquinolines with high chemo- and regioselectivity.

iv. In the same year, Peng group published C-H/N-H bond activation of quinazolones with internal alkynes for the facile construction of fused tetracyclic heteroarenes in the presence of $[RuCl_2(p\text{-cymene})]_2$ and $Cu(OAc)_2{\cdot}H_2O$ under mild reaction conditions (**Figure 34**) [53].

v. In 2015 a one-pot synthesis of fused polycyclic nitrogen-heteroarenes was reported via the Ru(II)-catalyzed oxidative dehydrogenation followed by C-H/N-H activation and annulation reaction of heteroaryl dihydroquinazolinones and internal alkynes. This one-pot method does not require any copper salt as the external oxidant, rather the oxidation occurs by the molecular oxygen (**Figure 35**) [54].

vi. In 2017, Swamy and co-workers achieved an amide group-directed, Ru(II)-catalyzed highly regioselective C-H/N-H activation and oxidative annulation reaction between 2*H*-chromene-3-carboxamides with internal alkynes for the synthesis of benzopyran-fused 2-pyridones (**Figure 36**) [55]. In addition, a double C-H activation reaction was also developed in the same one-pot using an excess of the alkyne. Herein, the first C-H

functionalization involves Ru-N covalent bond while the second C-H functionalization most likely involves Ru-O coordinate bond.

vii. In 2018 Gogoi et al. reported an unprecedented Ru(II)-catalyzed N-H/C-H activation and annulation reaction of of *N*-arylpyrazol-5-ones and diaryl/arylalkyl-substituted alkynes in the presence of bidented ligand 1,3-bis(diphenylphosphino)propane for the synthesis of quinazolines

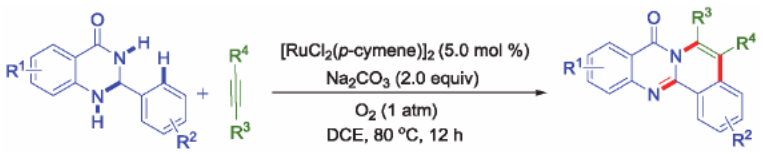

Figure 35.
Ruthenium(II)-catalyzed external oxidant FreeSynthesis of tetracyclic Heteroarenes.

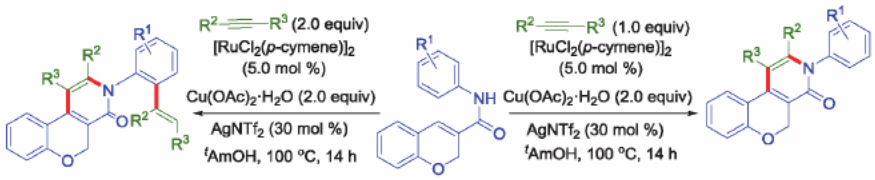

Figure 36.
Ruthenium catalyzed synthesis of Benzopyran-fused 2-pyridones.

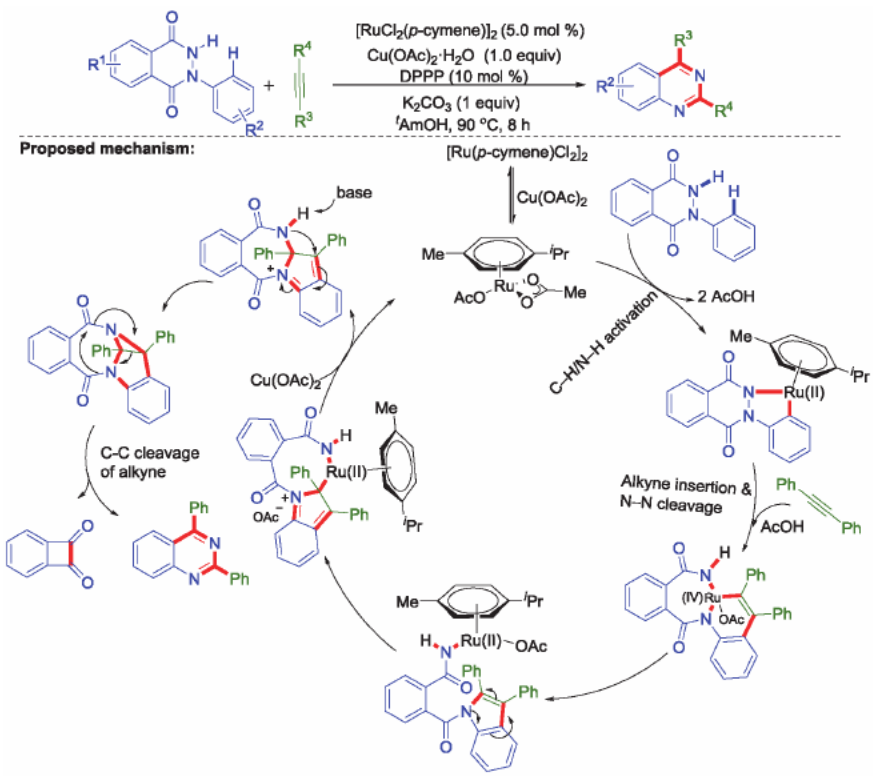

Figure 37.
Ruthenium(II)-catalyzed synthesis of Quinozaline.

DOI: http://dx.doi.org/10.5772/ITexLi.95987

(**Figure 37**) [56]. This annulation reaction proceeds mainly via oxidation of Ru(II) to Ru(IV) by cleavage of the N-N bond and cleavage of the triple bond of the alkyne.

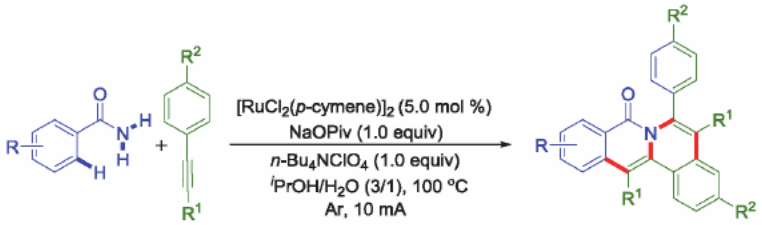

Figure 38.
Ruthenium(II)-catalyzed synthesis of polycyclic Isoquinolinones.

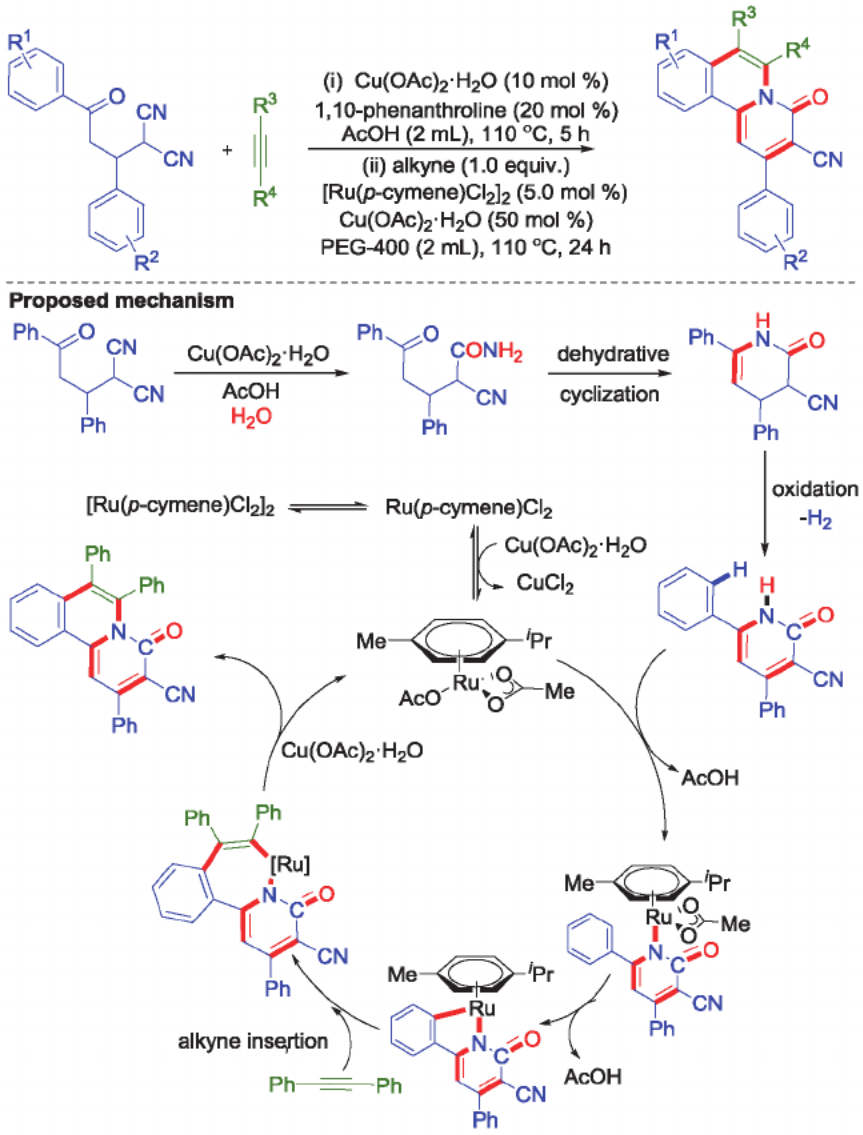

Figure 39.
Ruthenium(II)-catalyzed synthesis of conjugated fused Isoquinolines.

viii. In 2019, Tang and co-workers reported a Ru-catalyzed electrochemically enabled dehydrogenative annulation reaction of amides and alkynes for the synthesis of antitumor polycyclic isoquinolinones through a double C − H bond activation route (**Figure 38**) [57].

ix. In 2019 Patel *et al.* developed a one-pot sequential synthesis of highly conjugated fused isoquinolines via Cu(II)-catalyzed intramolecular cyclization followed by Ru(II)-catalyzed C-H/N-H oxidative alkyne annulation reactions (**Figure 39**) [58]. This one pot synthesis consisting of selective hydrolysis of a cyano group to an amide, dehydrative cyclization of the amide to a cyclic amide, aromatization of the cyclic amide (2-oxo-1,2,3,4-tetrahydropyridine moiety) to a 2-oxo-1,2-dihydropyridine and finally, the C-H/N-H annulation with an internal alkyne.

8. Conclusion

In summary, the ruthenium(II)-catalyzed activation of C-H bonds for the construction of C-C bond in organic synthetic methodologies have caused a revolution.[The development of methodologies introducing multiple C-H/N-H activation is an[emerging area of research and the oxidative alkyne annulation reactions allowing[for the formation of C-C and C-N bonds in a single step. These approaches have[already been competently used in the synthesis of several essential *N*-heterocycles[from readily available reactants. The presence of nitrogen directing groups appears[to be highly useful as starting materials for the direct access of various N-heterocycles in the field of ruthenium (II)-catalyzed C-H activation and oxidative[alkyne annulations. Further, these reactions were also extended to other hetero-atoms such as oxygen and sulfur directed groups for the straight forward synthesis[of diverse oxygen and sulfur containing heterocyclic molecules. Therefor this[methodology can definitely play a very useful part as an application in the field of[natural products, biologically important molecules and heterocycles with potential[application in the field of material science. Further developments in this area may[open up broad opportunities for straightforward, efficient, and atom economical[synthesis of various complex *N*-heterocyclic compounds from simple starting[materials.

References

[1] Alvarez-Builla J, Vaque-ro JJ, Barluenga J. Modern Heterocyclic Chemistry. Wiley-VCH. Weinheim; 2011.

[2] Bhardwaj V, Gumber D, Abbot V, Dhiman S, Sharma P. Pyrrole: a resourceful small molecule in key medicinal hetero-aromatics RSC Advanced. 2015;**5**:15233–15266. DOI: 10.1039/c4ra15710a

[3] Jessen HJ, Gademann K. 4-Hydroxy-2-pyridone alkaloids: Structures and synthetic approaches. Natural Product Representatives. 2010;**27**:1168–1185. DOI: 10.1039/B911516C

[4] Su S-J, Sasabe H, Takeda T, Kido J. Pyridine-Containing Bipolar Host Materials for Highly Efficient Blue Phosphorescent OLEDs. Chemistry of Materials. 2008;**20**:1691–1693. DOI: 10.1021/cm703682q

[5] Garg V, Maurya RK, Thanikachalam PV, Bansal G, Monga V. An insight into the medicinal perspective of synthetic analogs of indole: A review. European Journal of Medicinal Chemistry. 2019;**180**:562–612. DOI:10.1016/j.ejmech.2019.07.019

[6] Giri P, Kumar GS. Isoquinoline Alkaloids and their Binding with Polyadenylic Acid: Potential Basis of Therapeutic Action. Mini-Review. Medicinal Chemistry. 2010;**10**:568–577. DOI: 10.2174/138955710791384009

[7] Tariq S, Somakala K, Amir M. Quinoxaline: An insight into the recent pharmacological advances. European Journal of Medicinal Chemistry. 2018; **143**:542–557. DOI:10.1016/j.ejmech.2017.11.064

[8] Barbafina A, Amelia M, Latterini L, Aloisi GG, Elisei F. Photophysical Properties of Quinolizinium Salts and Their Interactions with DNA in Aqueous Solution. Journal of Physical Chemistry A. 2009;**113**:14514–14520. DOI: 10.1021/jp9040315

[9] Mitschke U, Bauerle P. The electroluminescence of organic materials. Journal of Material Chemistry. 2000;**10**:1471–1507. DOI: 10.1039/A908713C

[10] Bailly C. Contemporary Challenges in the Design of Topoisomerase II Inhibitors for Cancer Chemotherapy. Chemical Reviews. 2012;**112**:3611–3640. DOI: 10.1021/cr200325f

[11] Yang Y, Li K, Cheng Y, Wan D, Li M, You J. Rhodium-catalyzed annulation of arenes with alkynes through weak chelation-assisted C–H activation. Chemical Communications. 2016;**52**:2872–2884. DOI: 10.1039/C5CC09180B

[12] Ladea DM, Pawar AB. Cp*Co(III)-catalyzed vinylic C–H bond activation under mild conditions: expedient pyrrole synthesis via (3 + 2) annulation of enamides and alkynes. Organic Chemistry Frontiers. 2016;**3**:836–840. DOI: 10.1039/C6QO00108D

[13] Duarah G, Kaishap PP, Begum T, Gogoi S. Recent Advances in Ruthenium (II)-Catalyzed C−H Bond Activation and Alkyne Annulation Reactions. Advanced Syntheis and Catalysis. 2019; **361**:654–672. DOI: 10.1002/adsc.201800755

[14] Xu Y-H, He T, Zhang Q-C, Loh T-P. Synthesis of multi-substituted pyrroles using enamides and alkynes catalyzed by $Pd(OAc)_2$ with molecular oxygen as an oxidant. Chemical Communications. 2014;**50**:2784–2786. DOI: 10.1039/C3CC49683J

[15] Song W, Ackermann L. Nickel-catalyzed alkyne annulation by anilines:

versatile indole synthesis by C–H/N–H functionalization. Chemical Communications. 2013;**49**:6638–6640. DOI: 10.1039/C3CC43915A

[16] Obata A, Sasagawa A, Yamazaki K, Ano Y, Chatani N. Nickel-catalyzed oxidative C–H/N–H annulation of N-heteroaromatic compounds with alkynes. Chem. Sci. 2019;10:3242–3248. DOI: 10.1039/C8SC05063E

[17] Shan C, Zhu L, Qu LB, Bai R, Lan Y. Mechanistic view of Ru-catalyzed C–H bond activation and functionalization: computational advances. Chemical Society Reviews. 2018;**47**:7552–7576. DOI: 10.1039/C8CS00036K

[18] Ozdemir I, Demir S, Cetinkaya B, Gourlaouen C, Maseras F, Bruneau C, Dixneuf PH. Direct Arylation of Arene C−H Bonds by Cooperative Action of NHCarbene−Ruthenium(II) Catalyst and Carbonate via Proton Abstraction Mechanism. Journal of the American Chemical Society. 2008;**130**:1156–1157. DOI: 10.1021/ja710276x

[19] Ackermann L, Vicente R, Potukuchi HK, Pirovano V. Mechanistic Insight into Direct Arylations with Ruthenium(II) Carboxylate Catalysts. Organic Letters. 2010;**12**:5032–5035. DOI: 10.1021/ol102187e

[20] Ferrer-Flegeau E, Bruneau C, Dixneuf PH, Jutand A. Autocatalysis for C–H Bond Activation by Ruthenium(II) Complexes in Catalytic Arylation of Functional Arenes. Journal of the American Chemical Society. 2011;**133**: 10161–10170. DOI: 10.1021/ja201462n

[21] Ackermann L. Carboxylate-Assisted Ruthenium-Catalyzed Alkyne Annulations by C–H/Het–H Bond Functionalizations. Account of Chemical Research. 2014;**47**:281–295. DOI: 10.1021/ar3002798

[22] Prechtl MHG, Holscher M, Ben-David Y, Theyssen N, Loschen R, Milstein D, Leitner W. H/D Exchange at Aromatic and Heteroaromatic Hydrocarbons Using D_2O as the Deuterium Source and Ruthenium Dihydrogen Complexes as the Catalyst. Angewandte Chemie. 2007;**119**:2319–2322. DOI: 10.1002/ange.200603677

[23] Simmons EM, Hartwig JF. On the Interpretation of Deuterium Kinetic Isotope Effects in C-H Bond Functionalizations by Transition-Metal Complexes. Angewandte Chemie, International Edition. 2012;**51**:3066–3072. DOI: 10.1002/anie.201107334

[24] Banerjee A, Santra SK, Mohanta PR, Patel BK. Ruthenium(II) Catalyzed Regiospecific C–H/O–H Annulations of Directing Arenes via Weak Coordination. Organic Letters. 2015;**17**: 5678–5681. DOI: 10.1021/acs.orglett.5b02967

[25] Modi A, Sau P, Chakraborty N, Patel BK. A "Thiocarbonyl-Directed" Regiospecific C−H/S−H Annulation of Quinoline-4(1H)-thiones with Alkynes. Advanced Syntheis and Catalysis. 2019; **361**:1368–1375. DOI: 10.1002/adsc.201801537

[26] Kornhaaß C, Li J, Ackermann L. Cationic Ruthenium Catalysts for Alkyne Annulations with Oximes by C–H/N–O Functionalizations. The Journal of Organic Chemistry. 2012;**77**:9190–9198. DOI: 10.1021/jo301768b

[27] Chinnagolla RK, Pimparkar S, Jeganmohan M. Ruthenium-Catalyzed Highly Regioselective Cyclization of Ketoximes with Alkynes by C–H Bond Activation: A Practical Route to Synthesize Substituted Isoquinolines. Organic Letters. 2012;**14**:3032–3035. DOI: 10.1021/ol301091z

[28] Parthasarathy K, Senthilkumar N, Jayakumar J, Cheng C-H. Ru(II)-Catalyzed C–H Bond Activation for the Synthesis of Substituted Isoquinolinium Salts from Benzaldehydes, Amines, and

Alkynes. Organic Letters. 2012;**14**:3478–3481. DOI: 10.1021/ol301445r

[29] Luo C-Z, Gandeepan P, Cheng C-H. A convenient synthesis of quinolizinium salts through Rh(III) or Ru(II)-catalyzed C–H bond activation of 2-alkenylpyridines. Chemical Communications. 2013;**49**:8528–8530. DOI: 10.1039/C3CC45004J

[30] Li J, Ackermann L. Ruthenium-catalyzed oxidative alkyne annulation by C–H activation on ketimines. Tetrahedron. 2014;**70**:3342–3348. DOI: 10.1016/j.tet.2013.10.003

[31] Arigela RK, Kumar R, Joshi T, Mahar R, Kundu B. Ruthenium(ii)-catalyzed C–H activation/C–N bond formation via in situ generated iminophosphorane as the directing group: construction of annulated pyridin-2(1H)-ones. RSC Advances. 2014;**4**:57749–57753. DOI: 10.1039/C4RA10105G

[32] Kornhaaß C, Kuper C, Ackermanna L. Ferrocenylalkynes for Ruthenium-Catalyzed Isohypsic C-H/N-O Bond Functionalizations. Advanced Syntheis and Catalysis. 2014;**356**: 1619–1624. DOI: 10.1002/adsc.201301156

[33] Wu J, Xu W, Yu Z-X, Wang J. Ruthenium-Catalyzed Formal Dehydrative [4 + 2] Cycloaddition of Enamides and Alkynes for the Synthesis of Highly Substituted Pyridines: Reaction Development and Mechanistic Study. Journal of the American Chemical Society. 2015;**137**:9489–9496. 10.1021/jacs.5b06400

[34] Ghosh S, Pal S, Rajamanickam S, Shome R, Mohanta PR, Ghosh SS, Patel BK. Access to Multifunctional AEEgens via Ru(II)-Catalyzed Quinoxaline-Directed Oxidative Annulation. ACS Omega. 2019;**4**: 5565–5577. DOI: 10.1021/acsomega.9b00274

[35] Wang L, Ackermann L. Versatile Pyrrole Synthesis through Ruthenium (II)-Catalyzed Alkene C–H Bond Functionalization on Enamines. Organic Letters. 2013;**15**:176–179. DOI: 10.1021/ol303224e

[36] Li B, Wang N, Liang Y, Xu S, Wang B. Ruthenium-Catalyzed Pyrrole Synthesis via Oxidative Annulation of Enamides and Alkynes. Organic Letters. 2013;**15**:136–139. DOI: 10.1021/ol303159h

[37] Murugan K, Liu S-T. Preparation of substituted pyrroles via Ru(II)-catalyzed coupling of alkynes with enamides. Tetrahedron Letters. 2013;**54**: 2608–2611. DOI: 10.1016/j.tetlet.2013.03.013

[38] Ackermann L, Lygin AV, Hofmann N. Ruthenium-Catalyzed Oxidative Synthesis of 2-Pyridones through C–H/N–H Bond Functionalizations. Organic Letters. 2011;**13**:3278–3281. DOI: 10.1021/ol201244s

[39] Ackermann L, Lygin AV. Cationic Ruthenium(II) Catalysts for Oxidative C–H/N–H Bond Functionalizations of Anilines with Removable Directing Group: Synthesis of Indoles in Water. Organic Letters. 2012;**14**:764–767. DOI: 10.1021/ol203309y

[40] Zhang Z, Jiang H, Huang Y. Ruthenium-Catalyzed Redox-Neutral C–H Activation via N–N Cleavage: Synthesis of N-Substituted Indoles. Organic Letters. 2014;**16**:5976–5979. DOI: 10.1021/ol502998n

[41] Xu F, Li Y-J, Huang C, Xu H-C. Ruthenium-Catalyzed Electrochemical Dehydrogenative Alkyne Annulation. ACS Catalysis. 2018;**8**:3820–3824. DOI: 10.1021/acscatal.8b00373

[42] Ackermann L, Lygin AV, Hofmann N. Ruthenium-Catalyzed Oxidative Annulation by Cleavage of C-

H/N-H Bonds. Angewandte Chemie. 2011;**123**:6503–6506. DOI: 10.1002/ange.201101943

[43] Ackermann L, Fenner S. Ruthenium-Catalyzed C–H/N–O Bond Functionalization: Green Isoquinolone Syntheses in Water. Organic Letters. 2011;**13**:6548–6551. DOI: 10.1021/ol202861k

[44] Villuendas P, Urriolabeitia EP. Primary Amines as Directing Groups in the Ru-Catalyzed Synthesis of Isoquinolines, Benzoisoquinolines, and Thienopyridines. The Journal of Organic Chemistry. 2013;**78**:5254–5263. DOI: 10.1021/jo400344m

[45] Yang F, Ackermann L. Dehydrative C–H/N–OH Functionalizations in H_2O by Ruthenium(II) Catalysis: Subtle Effect of Carboxylate Ligands and Mechanistic Insight. The Journal of Organic Chemistry. 2014;**79**:12070–12082. DOI: 10.1021/jo501884v

[46] Li J, John M, Ackermann L. Amidines for Versatile Ruthenium(II)-Catalyzed Oxidative C-H Activations with Internal Alkynes and Acrylates. Chemistry A European Journal. 2014;**20**:5403–5408. DOI: 10.1002/chem.201304944

[47] Allu S, Swamy KCK. Ruthenium-Catalyzed Synthesis of Isoquinolones with 8-Aminoquinoline as a Bidentate Directing Group in C–H Functionalization. The Journal of Organic Chemistry. 2014;**79:**3963–3972. DOI: 10.1021/jo500424p

[48] Kaishap PP, Duarah G, Chetiab D, Gogoi S. Ru(II)-Catalyzed annulation of benzamidines and alkynes by C–H/N–H activation: a facile synthesis of 1-aminoisoquinolines. Organic and Biomolecular Chemistry. 2017;**15**:3491–3498. DOI: 10.1039/C7OB00389G

[49] Ruiz S, Sayago FJ, Cativiela C, Urriolabeitia EP. Ru-catalyzed C-H functionalization of phenylglycine derivatives: Synthesis of isoquinoline-1-carboxylates and isoindoline-1-carboxylates. Journal of Molecular Catalysis A: Chemical. 2017;**426**:407–418. DOI: 10.1016/j.molcata.2016.06.026

[50] Ackermann L, Wang L, Lygin AV. Ruthenium-catalyzed aerobic oxidative coupling of alkynes with 2-aryl-substituted pyrroles. Chemical Science. 2012;**3**:177–180. DOI: 10.1039/C1SC00619C

[51] Ma W, Graczyk K, Ackermann L. Ruthenium-Catalyzed Alkyne Annulations with Substituted 1H-Pyrazoles by C–H/N–H Bond Functionalizations. Organic Letters. 2012;**14**:6318–6321. DOI: 10.1021/ol303083n

[52] Wang R, Falck JR. Ruthenium catalyzed oxidative annulation with alkynes via cascade C–H/N–H bond functionalizations. Journal of Organometallic Chemistry. 2014;**759**:33–36. DOI: 10.1016/j.jorganchem.2014.02.014

[53] Lu H, Yang Q, Zhou Y, Guo Y, Deng Z, Ding Q, Peng Y. Cross-coupling/annulations of quinazolones with alkynes for access to fused polycyclic heteroarenes under mild conditions. Organic and Biomolecular Chemistry. 2014;**12**:758–764. DOI: 10.1039/C3OB41955J

[54] Lingayya R, Vellakkaran M, Nagaiah K, Nanubolu JB. Ruthenium as a Single Catalyst for Two Steps: One-Pot Ruthenium(II)-Catalyzed Aerobic Oxidative Dehydrogenation of Dihydroquinazolinones and Cross-Coupling/Annulation to give N-Fused Polycyclic Heteroarenes. Asian Journal of Organic Chemistry. 2015;**4**:462–469. DOI: 10.1002/ajoc.201500025

[55] Tulichala RNP, Shankar M, Swamy KCK. Ruthenium-Catalyzed

Oxidative Annulation and Hydroarylation of Chromene-3-carboxamides with Alkynes via Double C–H Functionalization. The Journal of Organic Chemistry. 2017;**82**:5068–5079. DOI: 10.1021/acs.joc.7b00008

[56] Prakash R, Bora BR, Boruah RC, Gogoi S. Ru(II)-Catalyzed C–H Activation and Annulation Reaction via Carbon–Carbon Triple Bond Cleavage. Organic Letters. 2018;**20**:2297–2300. DOI: 10.1021/acs.orglett.8b00643

[57] Wang Z-Q, Hou C, Zhong Y-F, Lu Y-X, Mo Z-Y, Pan Y-M, Tang H-T. Electrochemically Enabled Double C–H Activation of Amides: Chemoselective Synthesis of Polycyclic Isoquinolinones. Organic Letters. 2019;**21**:9841–9845. DOI: 10.1021/acs.orglett.9b03682

[58] Rakshit A, Sau P, Ghosh S, Patel BK. One-Pot Sequential Synthesis of Fused Isoquinolines via Intramolecular Cyclization/Annulation and their Photophysical Investigation. Advanced Syntheis and Catalysis. 2019;**361**:3824–3836. DOI: 10.1002/adsc.201900543

Chapter 8

Ruthenium Catalyst for Epoxidation Reaction

Raiedhah A. Alsaiari

Abstract

The role of ruthenium as a heterogeneous catalyst for epoxidation reaction has not been investigated extensively. Therefore, the purpose of this chapter is to provide overview of the epoxidation of alkene using ruthenium catalysts. The chapter is divided into two main sections. The first section is about epoxidation of alkene using supported ruthenium catalysts, while the second using ruthenium complexes (homogenous catalysts).

Keywords: ruthenium catalysts, epoxidation, alkene, homogeneous and heterogenous catalysis

1. Introduction

Synthetic organic chemistry relies on organic substrate oxidation not only in applications of large scale, but also in fine chemical production. Affording greater control over chemical process activity and selectivity whilst concomitantly ensuring sustainability is currently the pursued goal for catalyst design. Among the existing techniques of C=C bond functionalization, a major one is epoxidation [1].

Both laboratory syntheses and chemical production draw on epoxides as useful intermediate. Epoxide is one of the key intermediates in the manufacture of functionalized fine chemicals, pharmaceutics, agrochemical, and perfume industry as well as in natural product synthesis [2–4].

The most eloquent instance is Sharpless asymmetric epoxidation based on titanium tartrate complexes [5]. A significant aspect related to epoxidation catalysts; ruthenium complexes have enjoyed considerable advancement in recent times.

Another domain that has been developed substantially is heterogeneous epoxidation with ruthenium catalysis. In this context, catalysts have been devised through several effective processes, such as derivatization and immobilization, involving known homogeneous catalysts.

The role of ruthenium as a heterogeneous catalyst for epoxidation has not been investigated extensively. Herein, it will be provided an updated overview of developments in the epoxidation of alkene using ruthenium catalysts (**Figure 1**).

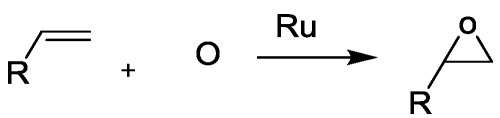

Figure 1.
Epoxidation of alkene using ruthenium catalysts.

This chapter is divided into two major sections. The first section focuses exclusively on using supported ruthenium catalysts to catalyze alkene epoxidation, while the second covers using ruthenium complexes for this reaction.

2. Supported ruthenium catalysts for epoxidation of alkenes

In 1998 [6], Mesoporous MCM-41 molecular sieves are used for the immobilization of a ruthenium complex of meso-tetrakis (2,6-dichlorophenyl)porphyrin (**Figure 2**), [Ru^{II}(TDCPP)(CO)(EtOH)]. The supported Ru catalyst can affect highly selective heterogeneous alkene epoxidations with the terminal oxidant of choice being 2,6-dichloropyridine N-oxide in the presence of CH_2Cl_2. Conversion of aromatic and aliphatic alkenes to their epoxides can be successfully undertaken, with satisfactory amounts and selectivity, while the epoxidation of cis-alkenes (e.g. cis-stilbene) can be undertaken in a stereospecific manner as shown in **Table 1**. The leaching and/or deactivation of the catalyst may be the reason why activity is lost.

Another study in 2002 observed that poly(ethylene glycol) (PEG) binds to ruthenium porphyrin through a covalent etheric bond. What characterizes these catalysts is that they are highly reactive and selective for epoxidation of alkenes with 2,6-dichloropyridine N-oxide as terminal oxidant [7].

Ethene was subjected to electrochemical epoxidation with 0.3 M chloride ion concentration by employing nanocrystalline RuO_2 and Co-doped RuO_2 deposited electrodes in aqueous acidic media [8]. The by-products of this reaction were oxirane and 2-chloroethanol. Epoxide formation was achieved based on a three-membered transition state involving the binding of ethylene to an oxygen on the surface of RuO_2. Furthermore, a single-step sol gel process (SSSG) facilitated the synthesis of RuO_2-loaded meso-porous assembled TiO_2 nanocrystals with high selectivity and recyclability for the purpose of liquid-phase cyclohexene epoxidation employing H_2O_2 [9]. In this context, it was observed that the temperature of calcination influenced both the catalytic activity and the catalyst selectivity. In the case of SSSG, the optimal calcination temperature was established to be 450 °C, which yielded maximal epoxide selectivity of up to 80%. The epoxide selectivity and conversion related to the calcined SSSG did not alter even on the third sequential run.

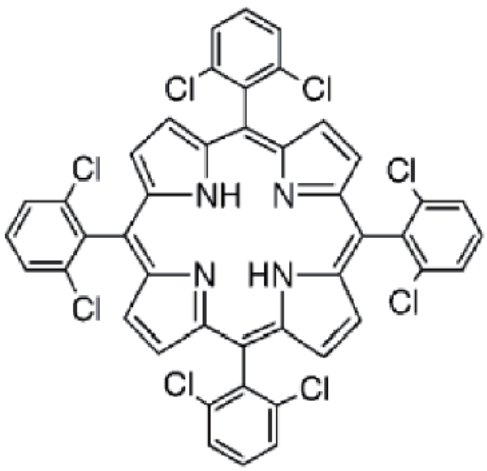

Figure 2.
Meso-Tetrakis(2,6-dichlorophenyl)porphyrin (TDCPP).

Entry	Alkene	Reaction time (h)	Conversion (%)	Epoxide yield (%)[a]	TOF/h^{-1}
1		24	98	91[b]	4550 (209)
2		30	76	98	3819
3	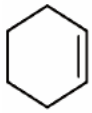	18	84	61[c]	2628 (142)
4	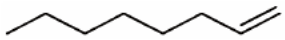	24	80	92	3774 (158)
5	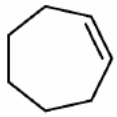	20	89	91	3762 (161)

Reaction conditions: alkene (1 mmol), Cl_2pyNO (1.1 mmol), 0.4 wt % Ru/M-41(m) (0.195 μmol of Ru), HCl (~0.3 mmol), CH_2Cl_2 (5 mL), 40 °C under an Ar atmosphere.
[a]Yields are based on the number of substrates consumed; products were identified and quantified by either GLC or 1H NMR.
[b]Trace amounts of benzaldehyde and phenylacetaldehyde were also detected.
[c]2-Cyclohexen-1-ol (14%) and 2-cyclohexen-1-one (11%) were formed. TOF were determined by monitoring the reactions using GC within the first 2 h of the reactions.

Table 1.
Epoxidations of different alkenes using a MCM-41-supported ruthenium porphyrin complexes [6].

In one synthetic approach that has been proposed, an amino acid L-valine was affixed to styrene-divinylbenzene co-polymer beads with 8% and 6% cross-linking. The formation of the metal complex on the support was achieved by applying a ruthenium (III) chloride solution to polymeric ligands that included bidentate N,O donor sites. The supported catalysts were employed to investigate the catalytic epoxidation of styrene, Norbornylene, cyclooctene and cyclohexene, with *tert*-butyl hydroperoxide as the terminal oxidant. In the case of Norbornylene and cis-cyclooctene, it was noted that epoxides formed selectively and with increase the reaction temperature from 28 °C to 45 °C there is an increase in the epoxide yield at similar levels of catalyst concentration. Meanwhile, the equivalent epoxide, benzaldehyde and acetophenone were derived for styrene. Although the catalyst could be reused, repeated recycling caused the metal to leach gradually from the support, with negative implications for its use [10].

One study investigated alkene epoxidation with ruthenium(III) salophen chloride [Ru(salophen)Cl] based on support of functionalized chloromethylated polystyrene (PS). 1,4-diaminobenzene, 4-aminophenol and 4-aminothiophenol were used for PS modification, while axial ligation facilitated the binding of [Ru(salophen)Cl] to the supports. Alkene epoxidation with sodium periodate ($NaIO_4$) as a best oxidant at ambient temperature was successfully performed with the employed catalysts, satisfactory activity being noted. It was possible to use the heterogeneous catalysts again in the reactions, and they were recycled repeatedly. They also observed that the benefits provided by these catalysts include the fact that they are uncomplicated to prepare and handle, the support is available on the market, and the supported catalysts can be readily recovered and reused [11].

Another study showed preparation of ruthenium-doped H-Montmorillonite (H-Mont) and Ti-pillared clay (PILC) was undertaken to investigate cyclohexene

oxidation, with the chosen source of oxygen being *tert*-butyl hydroperoxide (TBHP). Ru/Ti-PILC showed better effective catalytic activity than Ru/H-Mont. The use of 5% Ru/Ti-PILC as catalyst resulted in conversion of cyclohexene in proportion of 59%, selectivity of 87% and 13% respectively for 2-cyclohexene-1-one and 2-cyclohexene-1-ol at a temperature of 700 °C for six hours, without formation of epoxide. It was observed that the oxidation of cyclohexene was heterogeneous, and no leaching of ruthenium was observed [12, 13].

In our previous work, supported ruthenium catalysts (1%Ru/TiO_2) have been utilized for the epoxidation of 1-decene under solvent-free conditions. The reaction was continued for 24 h at 90 °C in atmospheric air with very small amount of *tetra*-butyl hydroperoxide (TBHP). 1% Ru/TiO_2 catalyst was prepared using two different preparation methods called sol-immobilization and wet-impregnation. For preparation of sol-immobilization, in brief, an appropriate quantity of $RuCl_3$. xH_2O was added to deionized water (800 mL) with continuous stirring. To protect and stabilize the Ru nanoparticles, a freshly prepared 1 wt.% solution of poly (vinyl alcohol) (m.w. = 10 000, 80% hydrolyzed) was added (PVA/Ru (by wt) = 0.65). After a further 15 min of stirring, a dark brown sol was generated by the addition of a freshly prepared solution of sodium borohydride (0.2 M, molar ratio $NaBH_4$/Ru = 5). The sol was stirred for a further 30 min with dropwise addition of H_2SO_4 to adjust the acidity to pH = 2. The TiO_2 support (~1.98 g) was then added and the mixture stirred for 2 h prior to wash thoroughly with deionized water (2 L) and dried at 110 °C for 16 h. In the wet-impregnation method, catalyst (1 g) was prepared by dissolving an appropriate quantity of $RuCl_3 \cdot xH_2O$ in deionized water and added an appropriate amount of TiO_2 support and allowed water to evaporate with continuous stirring at 80 °C. The obtained paste was dried for 16 h at 110 °C and grounded prior to calcination for 3 h in static air at 300 °C (heating rate = 20 °C/min).

For the preparation of 1 g of catalyst via the wet impregnation technique, a suitable amount of $RuCl_3 \cdot xH_2O$ was dissolved in deionized water, after which a suitable quantity of TiO_2 support was added, and water evaporation was permitted with constant stirring at 80 °C. This process yielded a paste that was left to dry for 16 hours at 110 °C and was ground before being calcined for 180 minutes in static air at 300 °C, with a heating rate of 20 °C min^{-1}. The standard reaction of epoxidation involved addition of 0.1 g catalyst to 1-decene (53 mmol, 10 mL) in a glass flask with a round bottom and 50 cm_3 volume affixed with a reflux condenser. Following the addition of 0.01 mL *ter*-butyl hydroperoxide (TBHP) as the radical initiator, the reaction mixture was placed on a hotplate to heat to 90 °C with magnetic stirring. When the established reaction time ended, the mixture was allowed to reach ambient temperature and was subjected to filtration before being analyzed via gas chromatography (GC) [14].

1-Decene epoxidation under solvent free conditions was investigated based on 1%Ru/TiO_2. The reaction was performed for 24 hours at 90 °C in air with a catalytic quantity of TBHP. The initial step involved assessing the blank reaction with solely TBHP present, which revealed poor epoxidation reaction activity, with 2% conversion, and 10% selectivity to 1,2-epoxydecane (**Figure 3**). Subsequent assessment of TiO_2 displayed poor 1-decene conversion (4%) and epoxide selectivity (16%) as well. However, when 1% Ru/TiO_2 synthesized via sol-immobilization was used, the epoxide yield improved substantially. This was reflected in the increase in 1-decen conversion from 4 to 16% and in the increase in epoxide selectivity from 16 to 37% (**Figure 3**) [14].

High epoxide selectivity continues to pose difficulties in the context of the epoxidation reaction. This has led to the identification and quantification of several additional by-products, which have been comprehensively detailed in earlier studies

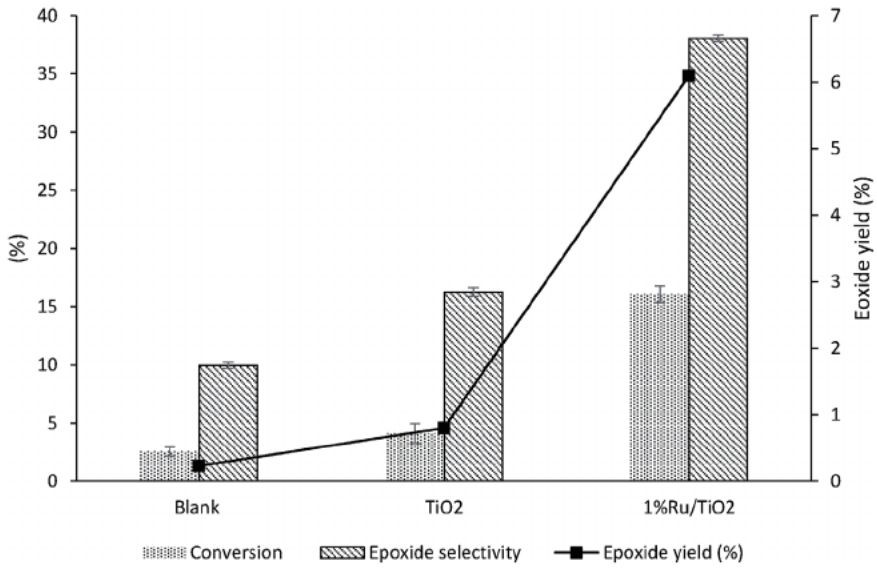

Figure 3.
Effect of TiO_2 and 1% Ru/TiO_2 on 1-decene epoxidation. Reaction conditions: Catalyst (0.1 g), 1-decene (53 mmol, 10 mL), TBHP (0.064 mmol, 0.01 mL), 90 °C, atmospheric pressure air, reaction time 24 h, rate of stirring 900 rpm. Error bars indicate range of data based on three repeat experiments.

[15, 16]. When the reaction runs for 24 hours, it results in the formation of substantial amounts of allylic products. Therefore, since the formation of certain products may accompany the oxidation of other products, it is useful to examine the product profile as the reaction unfolds. Time online studies were undertaken for 96 hours to gain insight into the reaction profile of 1-decene epoxidation with 1% Ru/TiO_2 catalyst. The increase in the reaction time from 4 to 96 hours determined an equivalent increase in 1-decene conversion from 1 to 35%, without an interval of induction (**Figure 4**). This means that the lengthier the reaction run, the higher the 1-decene conversion is likely to be. Furthermore, at the start of the reaction, epoxide selectivity was poor, with the main products being allylic compounds. However, as the reaction time increased up to 48 hours, so did the epoxide selectivity. On the other hand, epoxide selectivity gradually declined to 18% at 96 hours when the reaction time exceeded 48 hours, which is usually explained in terms of the ring opening reaction that occurs between epoxide and water as a by-product of condensation reactions or the breakdown of hydroperoxyl intermediate to the allylic ketone and water [16]. After formation of water, epoxide is immediately hydrolyzed to diol. Earlier studies also found that increase in reaction time improved alkene conversion and epoxide selectivity in the case of the terminal alkenes 1-decene, 1-hexene, and 1-octene. Additionally, it was observed that cracking of heptanoic, octanoic, and nonanoic acids was accompanied by enhanced selectivity as well [16].

The technique of synthesis is a major determinant of catalytic activity [17]. By contrast to the wet-impregnation technique, preparation of 1% Ru/TiO_2 catalyst via sol-immobilization displays greater activity for 1-decene epoxidation (**Figure 5**). More specifically, 1% Ru/TiO_2 is associated with 15% conversion and 37% epoxide selectivity when prepared via sol-immobilization and 10% conversion and 29% epoxide selectivity when prepared via wet impregnation.

The 1% Ru/TiO_2 catalyst synthesized via sol-immobilization was employed in excess amount to conduct the above reaction and thus evaluate reusability [14]. The procedures that followed reaction termination included catalyst filtration, washing with acetone, and 16-hour oven drying at 110 °C. Subsequently, the amount

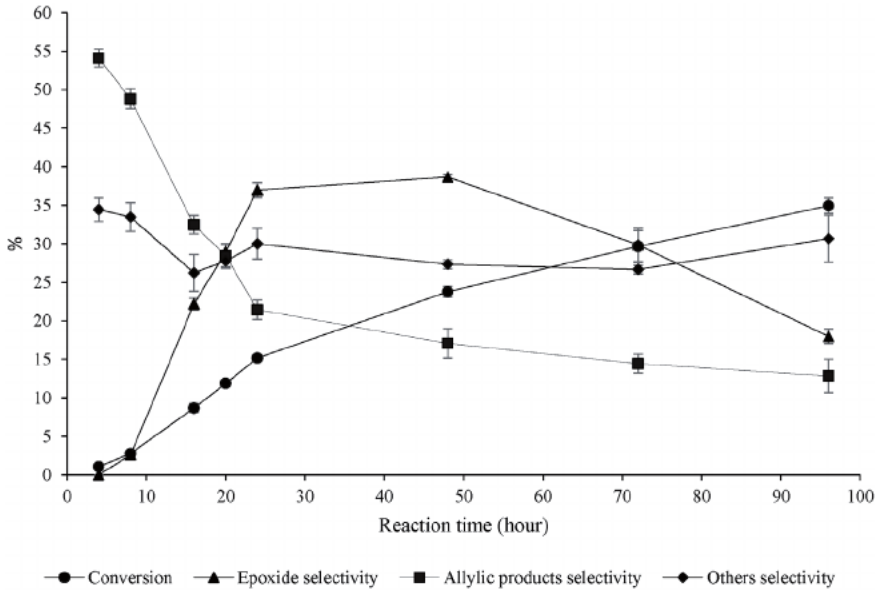

Figure 4.
Effect of reaction time on conversion and selectivity. Reaction conditions: 1% Ru/TiO_2 (0.1 g), 1-decene (53 mmol, 10 mL), TBHP (0.064 mmol, 0.01 mL), 90 °C, atmospheric pressure air, rate of stirring 900 rpm. Allylic products = ∑ (1-decen-3-one, 1-decen-3-ol, 2-decenal, 2-decen-1-ol). Others = ∑ (C_7 + C_8 + C_9 acids, C_8 + C_9 aldehyde, C_7 + C_8 alcohols, 3-nonen-1-ol, 3-nonanone, cyclododecane, 2-decenoic acid). Error bars indicate range of data based on three repeat experiments.

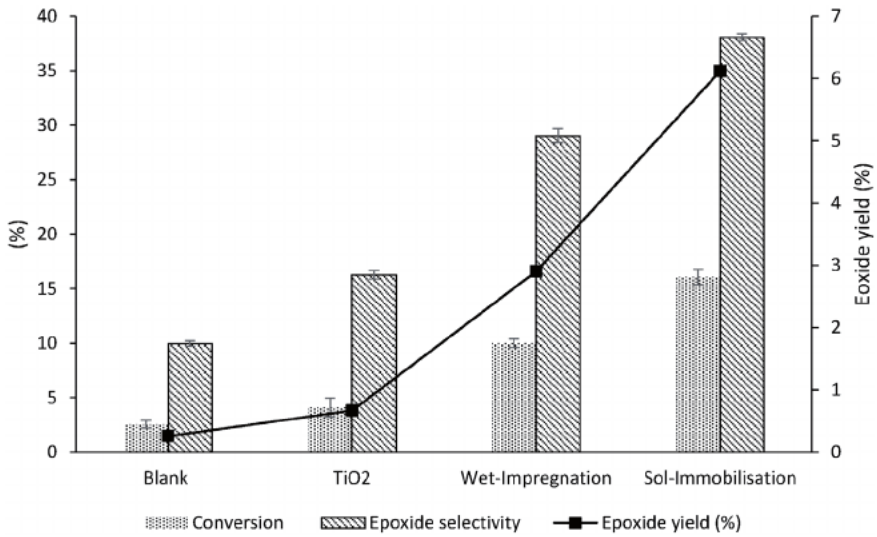

Figure 5.
Effect of the catalyst preparation method on 1-decene oxidation [14]. Reaction conditions: 1% Ru/TiO_2 (0.1 g), 1-decene (53 mmol, 10 mL), TBHP (0.064 mmol, 0.01 mL), 90 °C, atmospheric pressure air, rate of stirring 900 rpm. Error bars indicate range of data based on three repeat experiments.

of catalyst necessary for regular reaction was extracted to be used again. **Table 2** provides the activity data related to both the fresh and reused catalysts. Thus, by contrast to the fresh catalyst, which allowed 15% conversion of 1-decene and 37% epoxide selectivity, the reused catalyst subjected to drying with no previous washing showed suboptimal activity, so reuse was unsuccessful. One reason for this could be the fact that the adsorbed reaction products that were present caused the catalyst

Washing conditions	Conversion (%)	Epoxide selectivity (%)
Fresh catalyst	15	37
Reused without washing, dried static air at 110 °C for 16 h	7	17
Reused and washed with acetone (200 mL), dried static air at 110 °C for 16 h	10	24

Reaction conditions: 1% Ru/TiO_2 (0.1 g), 1-decene (53 mmol, 10 mL), TBHP (0.064 mmol, 0.01 mL), 90 °C, atmospheric pressure air, reaction time 24 h, rate of stirring 900 rpm.

Table 2.
Catalyst reusability study for epoxidation of 1-decene: 1% Ru/TiO_2.

to deactivate. On the other hand, better conversion (10%) and epoxide selectivity (24%) were exhibited by the catalyst washed with acetone before being reused, but even so, the activity was still poorer compared to that of fresh catalyst, most likely owing to the fact that carbon inhibited active sites. Active component leaching into the solution is major problem of heterogeneous catalysts, particularly in the liquid phase. However, ICP analysis suggested that ruthenium did not leach.

3. Ruthenium complexes for epoxidation of alkene

Being a transition metal, ruthenium displays several oxidation states that can be readily interchanged. Consequently, ruthenium facilitates the exchange or replacement of ligands in the complexed state, thus mediating access for metal-oxo species. The latter represent the main olefin epoxidation intermediate and are highly useful catalysts because they act as oxygen donor to alkenes. A variety of ruthenium-catalyzed epoxidation catalysts are supplied by homogeneous ruthenium complexes with ligands like porphyrin [18], polypyridyl [19], Schiff base [20], oxazoline [21], and pyrazolyl [22].

In 1984, Balavoine and colleagues suggested that $RuCl_3$, 2,2′-bipyridyl and sodium periodate could be employed in a two-phase reaction medium for alkene epoxidation [23]. Although the mechanism remained unclear, it was possible that a Ru(IV)-0x0 complex, potentially [Ru″‘(bipy)&l(O)]’, represented the active species. In 1985, Eskanazi and colleagues demonstrated that it was possible to control the rate and stereoselectivity of alkene oxidation by substituting the 2,2′-bipyridyl with different ligands [24].

Fackler and colleagues applied the method of Sonogashira coupling with a bromo-substituted porphyrin and terminal alkyne to create a ruthenium porphyrin epoxidation catalyst of high enantioselectivity and regioselectivity. This catalyst achieved enantioface-selective oxo transfer to alkene functionalized quinolones, pyridones, and amides via non-covalent hydrogen bond interactions [25–26].

In 1998 [27], ruthenium complexes that included pyridine and picoline ligands were used to subject cyclohexene and styrene to catalytic oxidation. Alteration of the oxidant character led to marked variability. Cyclohexene oxidation yielded 2-cyclohexen-l-ol and 2-cyclohexenone when the oxidizing agent was cumene-hydroperoxide (CHP), and 2-cyclohexenone when the oxidizing agent was N-methylmorpholine-N-oxide (NMO). Contrary to expectations, it was not epoxide but benzaldehyde that resulted from the oxidation of styrene. Hydrogen bond interactions could facilitate the engagement of the diaxial-dioxoruthenium species displaying catalytic activity with vinyl or alkenyl fragments (**Figure 6**). In this way, oxygen can be supplied to a specific alkene prochiral face [28].

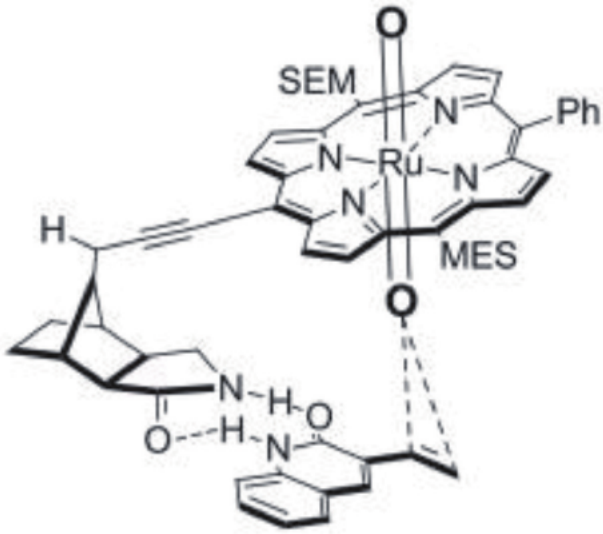

Figure 6.
Dioxo ruthenium-substrate interaction visualized based on semi empirical calculation [28].

Stoichiometric quantities of Cl_2pyNO were used as oxidant to perform the epoxidations in benzene. Epoxidation of n-hydro-3-vinylquinolones was achieved with high enantioselectivity, which was reduced for N-methylated quinolones as one of the two hydrogen bond interactions was lost. Meanwhile, 3,7-divinylquinolone exhibited high regioselectivity, with epoxidation of the vinyl group since it was readily accessible to ruthenium oxocentre. Trans-epoxides with enantioselectivity higher than 90% were obtained by subjecting the 3-alkenyl quinolones to stereospecific and enantioselective epoxidation.

Another study by Man and his group [29] was found that olefin asymmetric epoxidation with ruthenium as catalyst was significantly improved when $PhI(OAc)_2$ was present. The increase in the reaction rate when water was added was two orders of magnitude. It was possible to achieve reactions of aliphatic as well as aromatic olefins, with enantioselectivities being as high as 71% ee.

A novel pentadentatepolypyridine (L_5pyr) ruthenium complex $[Ru(L_5pyr)(CH_3CN)]_2P$ was proposed by Hamelin and colleagues. When iodosyl benzene was employed as oxidant, this complex was observed to generate satisfactory amounts of epoxide for cyclooctene and trans-b-methyl styrene. The preparation of the complex involved use of $RuCl_2$ $(dmso)_2$ to reflux L_5pyr and subsequent replacement with acetonitrile. Enhanced catalytic activity of $[Ru(L_5pyr)(CH_3CN)]_2þ$ depends greatly on the pentadentate ligand with electron abundance. This is reflected by the fact that epoxidation with lower dentate pyridine analogues $[Ru(bpy)_2(CH_3CN)_2]_2þ$ produce suboptimal yields and turnover frequencies [30].

Two $Ru(^{II})$-aqua complex catalysts underpinned by oxazoline ligands viz. $[Ru^{II}(iPr\text{-}box\text{-}C)(tpm)OH_2](PF_6)_2$ and $[Ru^{II}(iPr\text{-}box\text{-}O)(tpm)OH_2](PF_6)$ were developed in recent times. The preparation of the complexes involved derivation from $[Ru^{III}Cl_3(tpm)]$ by base catalyzed oxazoline ligand exchange, with the generated chloro complex being subsequently hydrolyze with silver acting as catalyst. $Phl(OAc)_2$ was employed as oxidant to analyze the potential of the two complexes as epoxidation catalysts for trans-stilbene. Results showed that catalyst 1 was associated with 85% epoxide selectivity and catalyst 2 was associated with 81% epoxide selectivity, while the conversion was nearly identical in both cases. Furthermore, catalyst 1 was regioselective for the terminal alkene segment of 4-vinylcyclohexene [31] (**Figure 7**).

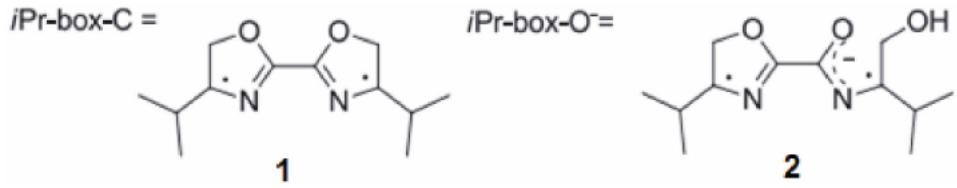

Figure 7.
Oxazoline ligands [31].

In another study, a range of olefins were subjected to asymmetric epoxidation with ruthenium as catalyst and TBHP as oxidant. Under catalysis by ruthenium(pyridinebisoxazoline)-(pyridinedicarboxylate) complexes, aromatic and aliphatic olefins produced the equivalent epoxides at ambient temperature in moderate-to-high yields and enantioselectivity as high as 65% ee. The reaction yield and chemoselectivity were markedly enhanced by adding the stoichiometric oxidant in a gradual way [32].

In a similar study [33], olefins were subjected to asymmetric epoxidation with general ruthenium as catalyst and hydrogen peroxide as oxidant. Various aromatic olefins exhibited enantioselectivity as high as 84%. The reaction was successful especially because pyboxazines, a novel group of ligands, were added. It was anticipated that the catalytic behavior of common pybox derivatives harmonized well with such ligands. Furthermore, differences in catalyst structure were diminished by employing two distinct ligands, facilitating refinement of catalytic attributes.

One study undertook the synthesis of bis-facial dinuclear ruthenium complex that included a hexadentate pyrazolate-bridging ligand (Hbimp) and bpy as auxiliary ligands [34]. Additionally, the ability of water and alkene oxidation of this complex was assessed. Various alkenes were successfully subjected to epoxidation under catalysis by the *in situ*-produced bis-aqua complex, $\{[Ru^{II}(bpy)(H_2O)]2(\mu\text{-bimp})\}^{3+}$.

The difficulty of ruthenium complex heterogenization stems from the fact that it is necessary to preserve the ligand properties (e.g. lability, enantiopurity, relative orientation) that greatly influence epoxidation reactivity, enantioselectivity, regioselectivity, and chemoselectivity. One possible approach is to anchor the catalyst to a polymer, for which one of the ligands must include a reactive functional group or polymerizable moiety. An additional viable option is to immobilize catalysts in channels of materials of high porosity (e.g. zeolites, molecular sieves), with shape selectivity being afforded by characteristic pore sizes.

To conclude, It was shown that the chemical nature of the solvent, oxidant, type of catalysts and type of the ligand have a significant effect on the catalytic properties and stability of the active species.

Acknowledgements

Raiedhah Alsaiari would like to express her gratitude to the ministry of education and the deanship of scientific research – Najran University – Kingdom of Saudi Arabia for their support under code number (NU/ESCI/17/061).

Conflict of interest

The author declares no conflict of interest.

References

[1] Ansmann A., Kawa R. and Neuss M., US Patent 7,083,780 B2, Aug. 1, 2006.

[2] Everett, J. L.; Roberts, J. J.; Ross, W. C. J. J. Chem. Soc. 1953, 2386.

[3] Levene, P. A.; Walti, A. J. Biol. Chem. 1931, 94 (1931) 367.

[4] Beracierta, A. P.; Whiting, D. A. J. Chem. Soc., Perkin Trans. 1(1978) 1257.

[5] Katsuki, T.; Sharpless, K. B. J. Am. Chem. Soc. 1980, 102 (1980) 5974.

[6] Chun-Jing L., Wing-Yiu Y., Shou-Gui L. and Chi-Ming C., J. Org. Chem. 63 (1998) 7364.

[7] Jun-Long Z. and Chi-Ming C., Org. LETTERS 4 (2002) 1911.

[8] Jirkovsky, J. S.; Busch, M.; Ahlberg, E.; Panas, I.; Krtil, P. J. Am. Chem. Soc. 2011,133 (2011) 5882.

[9] Woragamon, K.; Jongpatiwut, S.; Sreethawong, T. Catal. Lett. 2010, 136 (2010) 249.

[10] Vaibhav B. V., Gopal L. T., Marayil R. and Rama H.S., REACT. FUNCT. POLYM. 56 (2003) 1.

[11] Moghadama M., Mirkhania V., Tangestaninejada S., Mohammadpoor-Baltorka I., Kargarb H., Sheikhshoaeic I. and Hatefid M., J. Iran.Chem. Soc. 8 (2011) 1019.

[12] Dali A., Rekkab-Hammoumraoui I., Choukchou-Braham A. and Bachir R., RSC Advances 5 (2015) 29167.

[13] Ahmed D., Rekkab-Hammoumraoui I., Sanaa E. K., Souheyla B. and Abderrahim C. B., Bull. Chem. React. Eng. Catal. 14 (2019) 614.

[14] Alsaiari R., Asian J. Chem. 32 (2020) 771.

[15] Engel R.V., Alsaiari R., Nowicka E., Pattisson S., Miedziak P.J., Kondrat S.A., Morgan D.J. and Hutchings G.J., Top. Catal., 61 (2018) 509.

[16] Gupta U.N., Dummer N.F., Pattisson S., Jenkins R. L., Knight D.W., D. Bethell and G.J. Hutchings, Catal. Lett., 145 (2015) 689.

[17] Miedziak P., Sankar M., Dimitratos N., Lopez-Sanchez J.A., Carley A. F., Knight D.W., Taylor S.H., Kiely C.J. and Hutchings G.J., Catal. Today, 164 (2011) 315.

[18] Lai, T. S.; Zhang, R.; Cheung, K. K.; Kwong, H. L.; Che, C. M. Chem. Commun. 1998,1583.

[19] Gallagher, L. A.; Meyer, T. J. J. Am. Chem. Soc., 123 (2001) 5308.

[20] Nakata, K.; Takeda, T.; Mihara, J.; Hamada, T.; Irie, R.; Katsuki, T. Chem.d Eur. J., 7 (2001) 3776.

[21] Nishiyama, H.; Shimada, T.; Itoh, H.; Sugiyama, H.; Motoyama, Y. Chem. Commun. 1997, 1863.

[22] Zhang, R.; Yu, W. Y.; Lai, T. S.; Che, C. M. Chem. Commun. 1999, 409.

[23] Eskerazi C., Meunier F. and Riviere H., Tetrahedron L&t. 25 (1984) 3187.

[24] Eskanazi C., Balavoine G., Meunier F. and Riviere H., Chem. Commun. 1985, 1111.

[25] Fackler, P.; Berthold, C.; Voss, F.; Bach, T. J. Am. Chem. Soc., 13, (2010) 15911.

[26] Fackler, P.; Huber, S. M.; Bach, T. J. Am. Chem. Soc.,134 (2012) 12869.

[27] Kanmani A. S. and Vancheesan S., Stud Surf Sci Catal. 113 (1998) 285.

[28] J. Am. Chem. Soc. 132 (2010) 15911.

[29] Man Kin T., Santosh B., Markus K., Christian D. and Matthias B., Tetrahedron L&t. 44 (2003) 7479.

[30] Hamelin, O.; Menage, S.; Charnay, F.; Chavarot, M.; Pierre, J. L.; Pecau, J.; Fontecave, M. Inorg. Chem. 47 (2008) 6413.

[31] Serrano, I.; Lopez, M. I.; Ferrer, I.; Poater, A.; Parella, T.; Fontrodona, X.; Sola, M.;Llobet, A.; Rodriguez, M.; Romero, I. Inorg. Chem., 50 (2011) 6044.

[32] Bhor S., Tse M. K., Klawonn M., Döbler C., Mägerlei W. and Beller M., ADV. SYNTH. CATAL. 346 (2004) 263.

[33] Tse M. K., Döbler C., Bhor S., Klawonn M., Mägerlein W., Hugl H. and Beller M., Angew. Chem. Int. Ed. 43 (2004) 5255.

[34] Aguiló J., Francàs L., Bofill R., Gil-Sepulcre M., García-Antón J., Poater A. and Sala X., J. Inorg. Chem. 54 (2015) 6782.

Computational Study of A15 Ru-Based Alloys for High-Temperature Structural Applications

Bhila Oliver Mnisi, Evans Moseti Benecha and Meriam Malebo Tibane

Abstract

The structural, magnetic, electronic and elastic properties of A15 X_3Ru (X = Sc, Ti, V, Cr, Mn, Fe, Co, Ni, Cu and Zn) binary alloys are investigated using first-principles density functional theory (DFT) methods. Ru-based alloys have attracted remarkable research interest due to their unique properties, which make them suitable for high-temperature structural applications. In this chapter, the properties of several A15 Ru-based alloys are investigated in order to select the best suitable alloy/s for aerospace application. Heats of formation are calculated to determine the thermodynamic stability of the materials. Knowledge of the values of elastic constants is essential for understanding the mechanical properties of the materials. From our calculated elastic constants, the bulk modulus, shear modulus, Young's modulus, Poisson's ratio, melting temperature, anisotropic factor and the ratio B/G are determined. The electronic density of states are calculated and discussed. Lastly, the magnetic properties of A15 X_3Ru alloys are studied. Thermodynamically stable Mn_3Ru possesses high-magnetic moment compared to other X_3Ru alloys, these results could pave way to experimental realization (synthesis) of Mn_3Ru material.

Keywords: structural stability, heats of formation, DFT calculations, mechanical properties, 3d transition metal alloys

1. Introduction

High-temperature structural materials have attracted considerable interest in the world of materials research for many years. There is a huge demand for materials that can resist extreme mechanical, thermal and chemical environments. Ni-based super-alloys (NBSA) are currently used for high-temperature application due to their phenomenal properties such as high creep strength, good ductility at elevated and room temperature environments, low density and high melting points. Despite the accomplishment of NBSA, 90% of Ni's melting point have already been exploited [1]. Many metal alloys are currently being studied [2] as potential alternatives to NBSAs.

Currently, ruthenium (Ru) based alloys have been under intense study [3, 4] due to their attractive combination of physical and mechanical properties, including

high melting point and good oxidation and corrosion resistance. Furthermore, Ru has the capability to increase the microstructural stability of other material systems [3]. In particular, Ru (2334 °C) has a superior melting point compared to Ni (1543 °C), making Ru-based alloys suitable for high temperature structural applications. Previously in Ru–Cr phase diagram, many structures such as Cr_3Ru, $C_{r2}Ru$ and Cr_4Ru phases were found to exist experimentally in different temperature formations [4–6], while the narrow homogeneity range of 31.5 atm% Ru and 32–36 atm% Ru for A15 Cr_3Ru and Cr_2Ru (σ phase) have been identified by Venkatraman and Neumann [7] respectively. Recent studies in this class of alloys have projected phase stability in a several X-Ru (X = Mo, Ti, V, Hf, Ir, Os, Pt, Ta, Tc, Mn and Zn) binaries at low temperatures [8, 9]. Ruthenium alloys with platinum and palladium make extremely durable electrical contacts and resistors. Ruthenium thin films are used in hard disk drives and plasma display panels [8]. The addition of ruthenium improves the mechanical properties and corrosion resistance of titanium, platinum, palladium, gold, and nickel-based superalloys used in jet engine turbine blades [10]. Also, the addition of ruthenium in modern nickel superalloys inhibits the formation of topographical closed packing (TCP) phases, thereby extending their creep capability to higher temperatures [11–13].

In this chapter, the structural, magnetic, electronic and elastic properties of the A15 Ru-based alloys in the X_3Ru (X = Sc, Ti, V, Cr, Mn, Fe, Co, Ni, Cu and Zn) crystal phase are investigated using first principles density functional theory calculations. All the structures proposed here in A15 phase are new except A15 Cr_3Ru that exist experimentally [7] as stated above. Therefore more experimental research is needed specifically for these novel alloys studied herein. We determine the heats of formation, density and magnetic moments, these properties are very important in aerospace and spintronic applications. Stability study based on heats of formation can be used to identify suitable X_3Ru material for high temperature structural application. The electronic properties such as band structures and density of states are useful to provide valuable information about a material's conducting characteristics at the Fermi energy level. Knowledge of the values of elastic constants (C_{ij}) is crucial in describing the mechanical resistance in a crystal when external stresses are applied. From the C_{ij}'s, we can determine the bulk, shear and Young's modulus that provides information about the strength of the material. To gain deeper understanding of X_3Ru alloys, we compute more properties such as anisotropic factor and Poisson's ratio. The computed properties are compared with the available theoretical and experimental results. The results found herein will pave way to recommend new metals in elevated temperature applications.

2. Theoretical calculations by density functional theory (DFT)

2.1 Crystal structure of transition metal-Ru alloys

Ru-based intermetallic alloys exist in different crystal structure phases such as A15, DOc, DO_c' tP16, $L1_2$, and B2. However, in this chapter we will focus on A15 Ru-based alloys as illustrated in **Figure 1**. The X_3Ru (X = Sc, Ti, V, Cr, Mn, Fe, Co, Ni, Cu and Zn) crystallizes in a cubic A15 type with a space group Pm-3 N (number 223) and a theoretical lattice constant of 4.63 Å [14]. Moreover, this cubic phase possess a prototype of Cr_3Si. The A15 phases are described as a series of intermetallic compounds with a formula A_3B; where A is a transitional metal and B can be any element. In the case of X_3Ru, Ru and X represent the A and B respectively. The proposed study seeks to model the properties of 3d transition metal-Ru

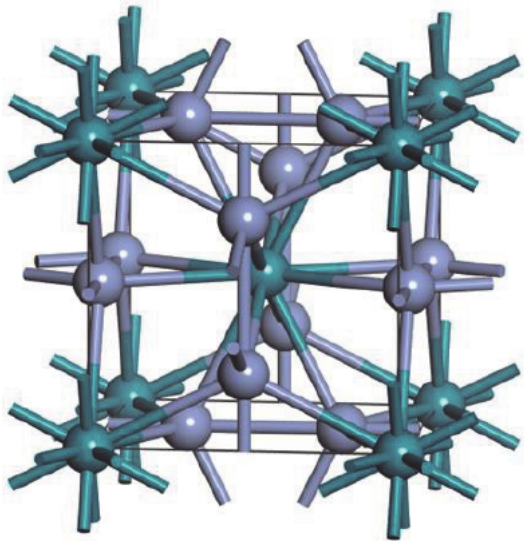

Figure 1.
Ball and stick illustration of A15 crystal structure phase of X_3Ru alloys. Gray balls represent X = Sc, Ti, V, Cr, Mn, Fe, Co, Ni, Cu and Zn- atoms; green balls represent Ru- atoms.

intermetallic systems for A15 phase, using density functional theory techniques. The density functional theory enables determination of many ground state properties of material systems with sufficient accuracy, and is widely used in characterizing the properties of new materials.

2.2 Quantum mechanical techniques

In material science, the energy of a system is needed in order to evaluate the properties of a material. Numerically, this is obtained by solving the Schrödinger wave equation [15].

$$H\psi = E\psi \tag{1}$$

where H is the Hamiltonian operator, E is the energy of the particle and ψ is the wavefunction is the particle's wavefunction. Hamiltonian H in Eq. (1) for a system of many interacting particles (electrons and nucleus) can be expressed as

$$H_{ele-nuc} = T_{ele} + T_{nuc} + V_{ele-nuc} + V_{ele-ele} + V_{nuc-nuc} \tag{2}$$

where T_{ele} and T_{nuc} are the kinetic energy operators of the electrons and nuclei respectively, $V_{nuc\text{-}nuc}$, $V_{ele\text{-}ele}$ and $V_{ele\text{-}nuc}$ are potential energy operators of the ele-nuc, ele-ele and nuc-nuc, respectively, due to Coulomb interactions. Eq. (2) can be solved analytically for few atoms, however, for very large number of atoms ($N \sim 10^{23}$) it is intractable to solve; hence, a number of approximations are needed to find its exact solution. The first approximation in solving the Schrödinger equation for a many-body interacting system is called the Born and Oppenheimer approximation [15]. This approximation decouples the electron motion from that of heavier ions, setting the kinetic energy operator of the nuclei to zero, while the potential energy operator becomes a constant. The Born and Oppenheimer approximation reduces the complexity of Eq. (2) to

$$H_{ele-nuc} = T_{ele} + V_{ele-nuc} + V_{ele-ele} \tag{3}$$

To solve the Eq. (3), the last two terms: $V_{ele\text{-}ele}$ and $V_{ele\text{-}nuc}$ must be known. Quantum mechanical techniques, such as the density functional theory and the Hatree-Fock approximation aim to obtain accurate ground state energy of a material system comprising of electrons and nucleus. Thereafter, other properties related to the total energy of the system can be easily determined. In order to achieve this aim, the exact forms of the terms on the right hand side (RHS) of Eq. (3) must be known. All the terms are known except the exchange correlation energy of interacting electrons that remains unknown. The density functional theory accounts for the electron exchange correlation (E_{xc}) effect for many interacting particle system. However, the Hatree-Fock has difficulties in predicting the properties of metallic and magnetic systems accurately.

2.3 Density functional theory

The density functional theory minimizes the difficulty in strong electron-nuclei and electron–electron interactions in many body systems (Eq.(2)) by mapping it onto the single particle moving in an effective potential [16]. This effective potential is not explicitly known, but can be approximated to accurately predict the solid-state properties. The basic idea of the DFT is that any property of a system of many interacting particles can be expressed as a functional of the ground state electron density ρ(r).

$$E = E[\rho(r)] \tag{4}$$

DFT is established from the Hohenberg-Kohn theory [16], which expresses a one-to-one correspondence between the electron density ρ(r) of a many electron–electron interacting system and the external potential V_{ext} imposed by the nucleus. Thus, the accurate ground state wave function is obtained from the external potential expression due to a correct ground state electron density. Therefore, the minimum energy can be expressed as:

$$E[\rho(r)] = T_{ele}[\rho(r)] + F_{HK}[\rho(r)] + V_{ext}[\rho(r)] \tag{5}$$

where, $F_{HK}[\rho(r)]$ is the universal functional of the electron density due to kinetic energy $T_{ele}[\rho(r)]$ and potential interactions $V_{ele\ -ele}$. The universal functional is called the Hohenberg-Kohn density functional and can be expressed in terms of the interaction from the electron-exchange and correlation and Hatree potential V_H due to classical electrostatic interactions [17] as:

$$F_{HK}[\rho(r)] = T_{ele}[\rho(r)] + \int \frac{\rho(r')}{|r - r'|} dr' + V_{xc}[\rho(r)] \tag{6}$$

where, the first term is the kinetic energy of the non-interacting electron system, second term is the Hatree potential V_H and the third term is the exchange-correlation potential due to electron-nuclei interactions.

Now the total energy can be written as:

$$E[\rho(r)] = T_{ele}[\rho(r)] + \int \frac{\rho(r')}{|r - r'|} dr' + V_{xc}[\rho(r)] + V_{ext}[\rho(r)] \tag{7}$$

where, the last two terms are external potentials that are split into two categories namely: classical and non-classical energies due to the nuclei $V_{ext}(r)$ and exchange-correlation effects V_{xc} (r).

Eq. (7) can be written as:

$$H_{KS}\psi_i = \left(-\frac{\hbar^2}{2m_e}\nabla^2 + \int \frac{\rho(r')}{|r-r'|}dr' + V_{ext}(r) + V_{xc}(r)\right)\psi_i(r) = \varepsilon_i\psi_i(r) \tag{8}$$

Eq. (8) is called the Kohn-Sham energy equation for non-interacting particles. The Kohn-Sham equation substitutes the many body interacting particle into a single independent particle equation as a functional of the ground state charge density, where ψ_i is the single particle Kohn-Sham wave function. The ground state density can be then be described as:

$$\rho(r) = \sum_{i=1}^{N} |\psi_i|^2 \tag{9}$$

whilst the exchange-correlation potential, V_{xc} (r) is given by the functional derivative of the ground state total energy with respect to the ground state charge density:

$$V_{xc}(r) = \frac{\delta E_{xc}[\rho(r)]}{\delta\rho(r)} \tag{10}$$

2.4 Approximations to exchange-correlation functional

While the DFT is in principle an accurate theory describing ground state interactions in a many-particle system, in practice, approximations are needed to describe the electronic exchange correlation term in the Kohn-Sham Eq. (8). Therefore, the application of DFT depends on the accuracy and reliability of the approximations to the exchange correlation potential, V_{xc}. Consequently, a large number of exchange-correlation functionals, including the LDA, GGA, and other hybrid functional have been developed in order to obtain a numerical solution to the Kohn-Sham equations, as illustrated in **Figure 2**.

2.4.1 Local density approximation

The simplest approximation to the exchange-correlation term in the Kohn-Sham equations is the Local Density Approximation (LDA) [15]. LDA assumes the density

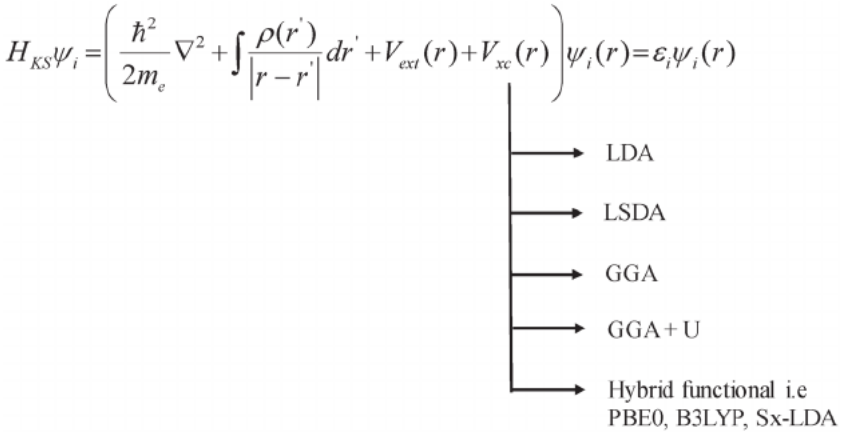

Figure 2.
Kohn-sham-DFT equation and its methods of implementation.

of homogeneous electron gas with a slowly varying electron density gradient, for the exchange correlation functional, expressed as [16].

$$E_{xc}^{LDA}[\rho] = \int \rho(r)\varepsilon_{xc}(\rho(r))dr \tag{11}$$

where ε_{xc} is the exchange-correlation energy per electron in a homogenous electron gas. One of the limitations of the LDA approximation is that it does not account for in homogeneities in electron density resulting in overestimation of bonding energies in both molecular and solid systems. Then Local spin density approximation (LSDA) [15, 17, 18] improves Eq. (11) by including the effect of spin density, where the charge density is the total summation of spin up α and down β densities.

$$E_{XC}^{LSDA}[\rho] = \int \rho(r)\varepsilon_{xc}\left(\rho_{\alpha}(r), \rho_{\beta}(r)\right)dr \tag{12}$$

2.4.2 Generalized gradient approximation

The generalized gradient approximation (GGA) functional is an improvement over the LDA, which takes into account the gradient of the electron density$|\nabla\rho|$ as well as their magnitude at each point r.

Therefore, the total energy can be expressed as a functional of the gradient of the density as

$$E_{XC}^{GGA}[\rho] = \int \rho(r)\varepsilon_{xc}(\rho(r), |\nabla\rho(r)|)dr \tag{13}$$

Inclusion of the information on the electron density spatial variation in GGA results in greater flexibility in describing real materials. However, GGA is inadequate in describing the properties of strongly correlated material systems, such as transition metals and magnetic systems. In order to improve the accuracy of GGA, an additional term called the "Hubbard U parameter" is used to treat the delocalised and localized orbitals with strong on-site coulomb interactions. The Hubbard U parameter is usually obtained semi empirically, but can also be extracted from ab initio calculations, although both methods do not permit transferability of U across compounds. The GGA + U functional will be used in this study owing to its accuracy and relatively minimal computational cost compared to non-local hybrid functionals such as B3LYP, HSE03 and Sx-LDA.

2.5 Numerical solution of Kohn-sham equation

To solve the Kohn-Sham single particle equation, the electron wave function ψ_i for the orbitals must be known. The Kohn-Sham equations are solved iteratively within a self-consistent field, where an initial density $\rho_1(r)$ is "guessed" to obtain the starting wavefunctions. These variables are then used to build Kohn-Sham Hamiltonian of which an improved density $\rho_2(r)$ is obtained. The wavefunctions continues to obtain better approximations to the electron density $\rho_{3\ldots\ldots N}(r)$, until self-consistency is reached, as illustrated in **Figure 3** [19].

2.6 Mechanical properties

Mechanical stability is a measure of material's strength, and is used to characterize the structural stability and deformation of a system under external load [18].

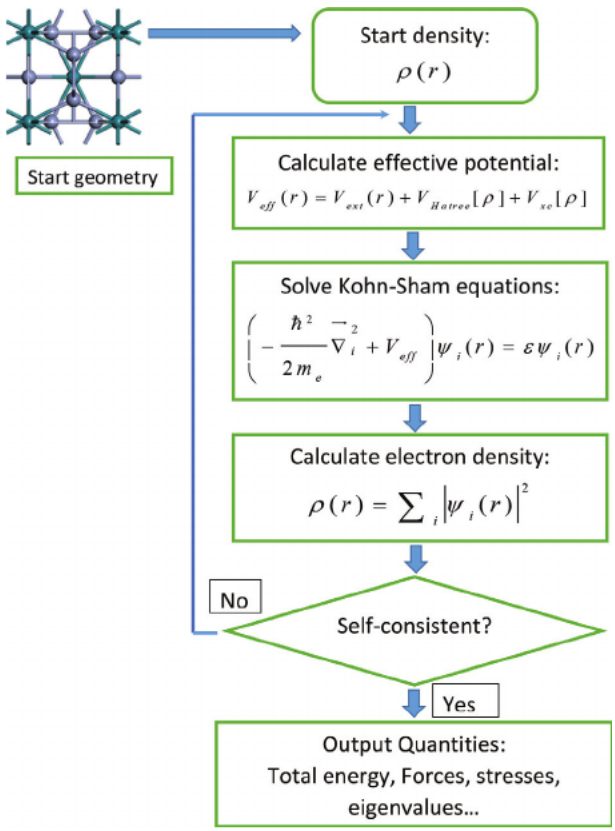

Figure 3.
Schematic representation of the SCF method used in DFT.

Material's mechanical stability is defined in terms of elastic constants C_{ij}, Bulk Modulus (B), Shear Modulus (G), Young's modulus (E) and elastic anisotropy (A), from which other properties such as hardness and ductility can be determined. In this study, the calculated elastic constants will be used to initially outline the general mechanical stability of each A15 X_3Ru structures based on the Born mechanical stability criteria [19]. In addition, the elastic constants can be used to measure the tensile, shear strength of materials, and provide important information on the bonding characteristics between the adjacent crystal atoms and the long-ranged elastic interaction between various dislocations [20].

2.6.1 Bulk modulus

Bulk Modulus (B) is a measure of the material's resistance to uniform compression. A high value of bulk modulus B indicates that a material resists compression, while a low bulk modulus imply that a material may be easily compressed. For cubic crystal structures, B is defined as

$$B = B_H = \left(\frac{B_V + B_R}{2}\right) \tag{14}$$

where

$$B = B_R = B_V = \frac{C_{11} + 2C_{12}}{3} \tag{15}$$

with B_R, B_V and $B = B_H$ being the Bulk modulus for Reuss, Voigt and Hill approximations [21].

2.6.2 Shear modulus

The shear modulus (G) of a material describes its response to shear stress, and is a measure of a material's stiffness. For cubic structures, G can be expressed as:

$$G = G_H = \left(\frac{G_V + G_R}{2}\right) \tag{16}$$

where the G_R and G_V are the Reuss and Voigt bounds [22], with

$$G_V = \left(\frac{C_{11} - C_{12} + 3C_{44}}{5}\right) \tag{17}$$

and

$$G_R = \left(\frac{(5(C_{11} - C_{12})C_{44})}{(4C_{44} + 3(C_{11} - C_{12}))}\right) \tag{18}$$

2.6.3 Young's modulus

Young's modulus (E) describes the material's strain response to uniaxial stress in the direction of this stress, and it can be written as:

$$E = \left(\frac{9B_H G_H}{3B_H + G_H}\right) \tag{19}$$

2.6.4 Elastic anisotropy

Anisotropic behavior is very important in engineering science as well as crystal physics due to its high relation with micro-cracks in materials. In calculating elastic anisotropy, more information about a material will result such as micro-cracks, phase transformation, precipitation and dislocation dynamics [23]. The elastic anisotropy (A) assist to distinguish the micro-cracks in different materials [24–26] and can be understood by calculating the anisotropic factor (A) for cubic structures as follows:

$$A = \left(\frac{2C_{44} + C_{12}}{C_{11}}\right) \tag{20}$$

2.6.5 Ductility

Ductility is the ability of a material to undergo plastic deformation before rapture. It is an important property for material engineering design. An empirical relation linking materials ductility and its elastic moduli (B/G) was proposed by Pugh [27], in which the critical value separating ductile and brittle materials is around 1.75; if B/G > 1.75, the material is ductile, otherwise it is brittle. Another classification rule was given by Frantsevich et al. [28] to distinguish brittleness and ductility by Poisson's ratio:

$$\upsilon = \left(\frac{3B_H - 2G_H}{(2(3B_H + G_H))}\right) \tag{21}$$

The critical value for Poisson's ratio is 1/3. For brittle materials, the Poisson's ratio is less than 1/3.

2.7 Density

Density is a vital tool used to characterize light/heavy weight materials. The weight of a material plays an essential role especially in rotating components. Therefore, it will be of interest to evaluate the density of the proposed X_3Ru alloys for lightweight (high temperature) structural applications. Density will be calculated from the Eq. (22) below:

$$\rho^{cal} = \left[\frac{M_W * N}{Vol * A_0}\right] \tag{22}$$

where *Vol* is the volume of the unit cell, M_W is the average molecular weight of the elements in the unit cell, N is the total number of atoms and A_0 is the Avogadro's number ($6.022\ X10^{23}$).

2.8 Melting point temperature

The melting point is the temperature at which a material changes from the solid to the liquid state. In other words, the vapor pressure of the solid and the liquid are equal at its melting point temperature. The melting temperature (Tm) of a material depends on its mechanical properties, and it follows a linear relationship with its elastic constants [29–32]. For cubic systems, the melting point temperature is given by:

$$T_m = 553K + \left(\frac{591K}{Mbar}\right) * C_{11}(Mbar) \pm 300K \tag{23}$$

2.9 Computational details

The Cambridge Serial Total Energy Package (CASTEP) code [33] based on DFT was employed to examine the behavior of cubic A15 X_3Ru (X = Sc, Ti, V, Cr, Mn, Fe, Co, Cu, Ni and Zn) compounds. The calculations were carried out with plane wave pseudo-potentials [34] built within the generalized gradient approximation (GGA) to represent the valence core interactions. In the present calculations, the GGA + Hubbard U [35, 36] model for A15 compounds are used for electron–electron interaction. The wave functions are expanded in the plane waves up to a kinetic energy cutoff of 800 eV, while well converged 15×15×15 k-point sampling by Monkhorst-Pack [37] was used for integration over the Brillouin zone for all the A15 structures. This plane-wave energy cut-off value is convenient for electronic band structures and density of states. The equilibrium lattice parameters have been computed by minimizing the geometry of the crystal using the well-converged k-points allowing the total energy and forces to converge to less than 1 meV/atom and 0.03 eV/Å. For the elastic constants, the stress–strain method was applied on all A15 with cubic symmetry of C_{11}, C_{12} and C_{44} elastic constants. The Voigt, Reuss and Hill average has been applied for bulk (B), shear (G) and Young (E)'s modulus [38].

3. Results and discussion

3.1 Structural parameters and heats of formation

Ruthenium based transition metal alloys belong to the family of A15 X_3Z structures which consist of X atoms that occupy six equivalent positions in c-site (0.25, 0, 0.5) and Z atoms that occupy bcc positions (0, 0, 0), as illustrated by **Figure 1** in section 2.1.

Table 1 indicates the calculated lattice constants, heats of formation and magnetic moments of A15 X_3Ru alloys (X = Sc, Ti, V, Cr, Mn, Fe, Co, Cu, Ni, Zn). It can be seen in X_3Ru alloys that consist of transition metal atoms in the middle of the 3d series have lower lattice constants compared to those early or late in the series, in consistent with the trends of atomic radii of transition metal atoms across the 3d series. The computed lattice constants for Cr_3Ru (5.59 Å) and Ni_3Ru (4.84 Å) structures are comparable with those obtained from other theoretical investigations Cr_3Ru (4.61 Å, 4.623 Å and 4.62 Å) [14, 39, 40] and Ni_3Ru (4.57 Å) [39], confirming the accuracy of our results. The slight deviations between our calculated lattice constants and previous theoretical data can be attributed to the use of different plane wave cutoff energies and k-points grid. In this paper we have applied deeper energy cutoff (800 eV) and k-points grid of 15 x 15 x 15 compared to previous calculations. The heat of formation ΔH_f was calculated using Eq. (24) for all the structures as:

$$\Delta H_f = \left[\frac{E(X_3Ru) - aE_{Ru}^g - bE_X^g}{a+b}\right] \tag{24}$$

Where $E(X_3Ru)$ is the total energy of the system, E_{Ru}^g and E_X^g are the energies of each individual metal species in their ground states, a and b are the number of atoms for individual metals and X = Sc, Ti, V, Cr, Mn, Fe, Co, Cu, Ni and Zn. A negative value ΔH_f indicates stability while the positive value of ΔH_f shows instability. It was found that Mn_3Ru have negative heats of formation, indicating that the alloy is thermodynamic stable. This result indicates a possibility of synthesizing Mn_3Ru experimentally due to the existence of the A15 Cr_3Ru phase [41]. Other

System	Lattice constant (Å)	Heat of formation (eV/atom)	Magnetic Moment (μ_B/atom)	Density $\rho = g/cm^3$	X-Ru bond length (Å)
Sc_3Ru	5.51	1.09	0.01	4.48	3.081
Ti_3Ru	5.15	0.88	0.27	5.94	2.88
V_3Ru	5.15	0.79	0.03	6.16	2.881
Cr_3Ru	5.59	0.89	0.22	4.88	3.126
Mn_3Ru	5.37	−-0.64	2.59	5.72	2.999
Fe_3Ru	4.9	1.34	1.58	7.57	2.741
Co_3Ru	4.9	1.41	1.7	7.85	2.738
Ni_3Ru	4.84	2.11	1	8.13	2.704
Cu_3Ru	4.97	1.12	0.4	7.89	2.779
Zn_3Ru	5.24	1.02	0.01	6.86	2.929

Table 1.
Calculated lattice constants of X_3Ru (X = Cr, Sc, Ti, V, Mn, Fe, Cu, Ni, Co and Zn) unit cell as well as the heats of formation, magnetic moment, density and the X-Ru bond-length of A15 structures.

structures such as Sc_3Ru, Ti_3Ru, V_3Ru, Cr_3Ru, Fe_3Ru, Co_3Ru, Ni_3Ru, Cu_3Ru and Zn_3Ru have positive heats of formation indicating that they are thermodynamically unstable, hence synthesis may be difficult. However, it has been suggested previously [14, 42, 43] that doping lowers the heats of formation in some materials, which may make it possible to synthesize some of these structures. Importantly, we find a strong direct correlation between the heats of formation of the X_3Ru alloys and their magnetic moments, with higher magnetic moments corresponding to more stable alloys, as illustrated in **Figure 4**. This can be attributed to strong metallic bonding in transition metals arising from the delocalized electrons.

Similarly the larger atomic radii difference between the Ru atom and transition metal atoms results in crystal strain which has a positive impact on the overall magnetic moment, as summarized in **Table 2.** The density of an alloy plays an important role in determining its use in lightweight applications, such as the aerospace industry. We have therefore, evaluated the density of the proposed X_3Ru alloys for lightweight (high temperature) structural applications. From **Table 1**, we note that X_3Ru alloys with small lattice constants have higher densities and the results are consistent with Eq. (22). However, the density of the most stable alloy Mn_3Ru ($5.72\,g/cm^3$), is slightly lower than that of $L1_2\,Ni_3Al$ ($6.14\,g/cm^3$) [44], which is commonly used in the aerospace industry. Therefore, the application of these alloys with high densities may be limited. Whereas, Mn_3Ru may be a possible candidate for aerospace application due to lower density.

3.2 Electronic and magnetic properties

The calculated magnetic moments and the stability of intermetallic alloys can be rationalized from their electronic properties [45]. **Figure 5** presents the projected spin-polarized density of states (PDOS) of X_3Ru (X = Sc, Ti, V, Cr, Mn, Fe, Co, Ni, Cu and Zn) alloys. It can be seen that the spin up and spin down bands are symmetric in Sc, Ti, V, Cr, Cu and Zn systems, with no net spin polarization. This symmetric balance of the spin up and spin down bands leads to a cancelation of the magnetic moment associated with electronic spin, thus explaining the zero (or negligible) calculated magnetic moments (**Table 1**). On the other hand, the density of states in Mn, Fe, Co and Ni are spin-polarized, which explains the origin of the non-zero calculated magnetic moments in these systems. The predicted magnetic

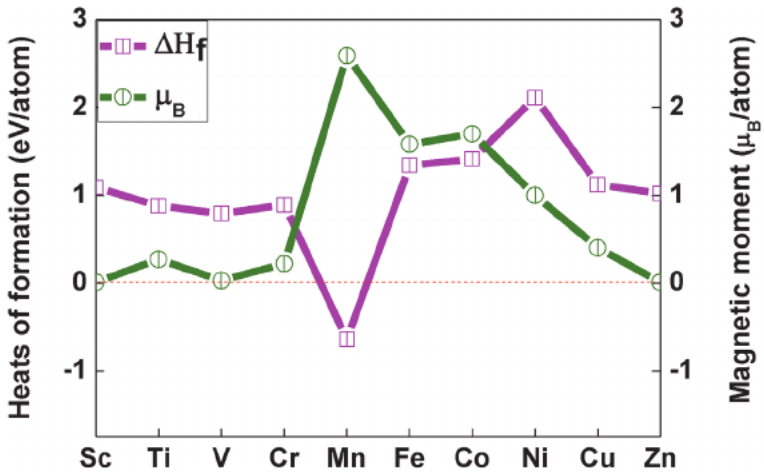

Figure 4.
A comparison of the calculated heats of formation (eV/atom) and magnetic moment (μ_B/atom) of X_3 Ru (X = Sc, Ti, V, Cr, Mn, Fe, Ni, Co, Cu and Zn) alloys.

Element	Atomic radii (pm)	Relative Ru-X atomic radii (pm)	Magnetic moments/ atom	Relative Ru-X magnetic moment (Ru = 0.00μ_B/ atom)	Electronic configuration	No: of unpaired spin
Sc	162	16	0.95	0.95	[Ar] $3d^1 4s^2$	2
Ti	147	31	2.09	2.09	[Ar] $3d^2 4s^2$	1
V	134	44	0.79	0.79	[Ar] $3d^3 4s^2$	0
Cr	128	50	4.93	4.93	[Ar] $3d^5 4s^1$	2
Mn	161	17	5	5	[Ar] $3d^5 4s^2$	2
Fe	156	22	2.64	2.64	[Ar] $3d^6 4s^2$	3
Co	152	26	1.68	1.68	[Ar] $3d^7 4s^2$	4
Ni	159	29	1.28	1.28	[Ar] $3d^8 4s^2$	5
Cu	145	33	0	0	[Ar] $3d^{10} 4s^1$	3
Zn	142	36	0	0	[Ar] $3d^{10} 4s^2$	3

Table 2.
The atomic radii, atomic radii difference, magnetic moments, electronic configuration and number of paired electrons of 3d transition metal from Sc-Zn bonded with central Ru atom.

moments in these compounds could lead to novel applications such as spintronics and spin injections.

The total density of states (DOS) can be used to investigate the atomic bonding character of Ru-based alloys [45]. It is clear that the bonding character mainly arises from the hybridization of X-*d* and Ru-*d* below the Fermi energy (−4 to -1 eV). Around the Fermi energy, from the spin up and down channels, the most visible feature is the presence of a valley known as the pseudo-gap, which indicates covalent bonding [46, 47] in these compounds. The pseudo-gap exist due to strong hybridization in X-*d* and Ru-*d* states and separates the bonding states from the anti-bonding states. The phase stability of intermetallic compounds is dependent on the location and magnitude of the DOS at the Fermi energy $N(E_f)$ [48–50], with lower $N(E_f)$ corresponding to a more stable phase [51]. The electronic properties can be related with the heats of formation, Mn_3Ru structure have less density of states at the Fermi and therefore, it is most stable. This result explains the calculated heats of formation results of Mn_3Ru discussed in section 3.1 above, where Mn_3Ru is thermodynamically stable and this attributes to its lowest heats of formation.

3.3 Elastic properties

Elastic constants are parameters that express the mechanical behavior of the materials within the stress range that the materials exhibit elastic behavior. In science and technology, they are essential physical quantities to determine the mechanical properties. The elastic constants C_{ijs} of A15 X_3Ru (X = Sc, Ti, V, Cr, Mn, Fe, Co, Ni, Cu and Zn) compounds are shown in **Table 3**. For the cubic X_3Ru compounds, the condition of Born mechanical stability [52] follows the equations:

$$C_{44} > 0, C_{12} > 0, C_{11} - C_{12} > 0 \quad (25)$$

The elastic constants of Cr_3Ru satisfies the above formulae, whilst other structures do not and this attributes to $C_{44} < 0$ and $C_{12} > 0$. For these elastic constants, the bigger the elastic constant C_{11} is, the stronger the linear compression resistance

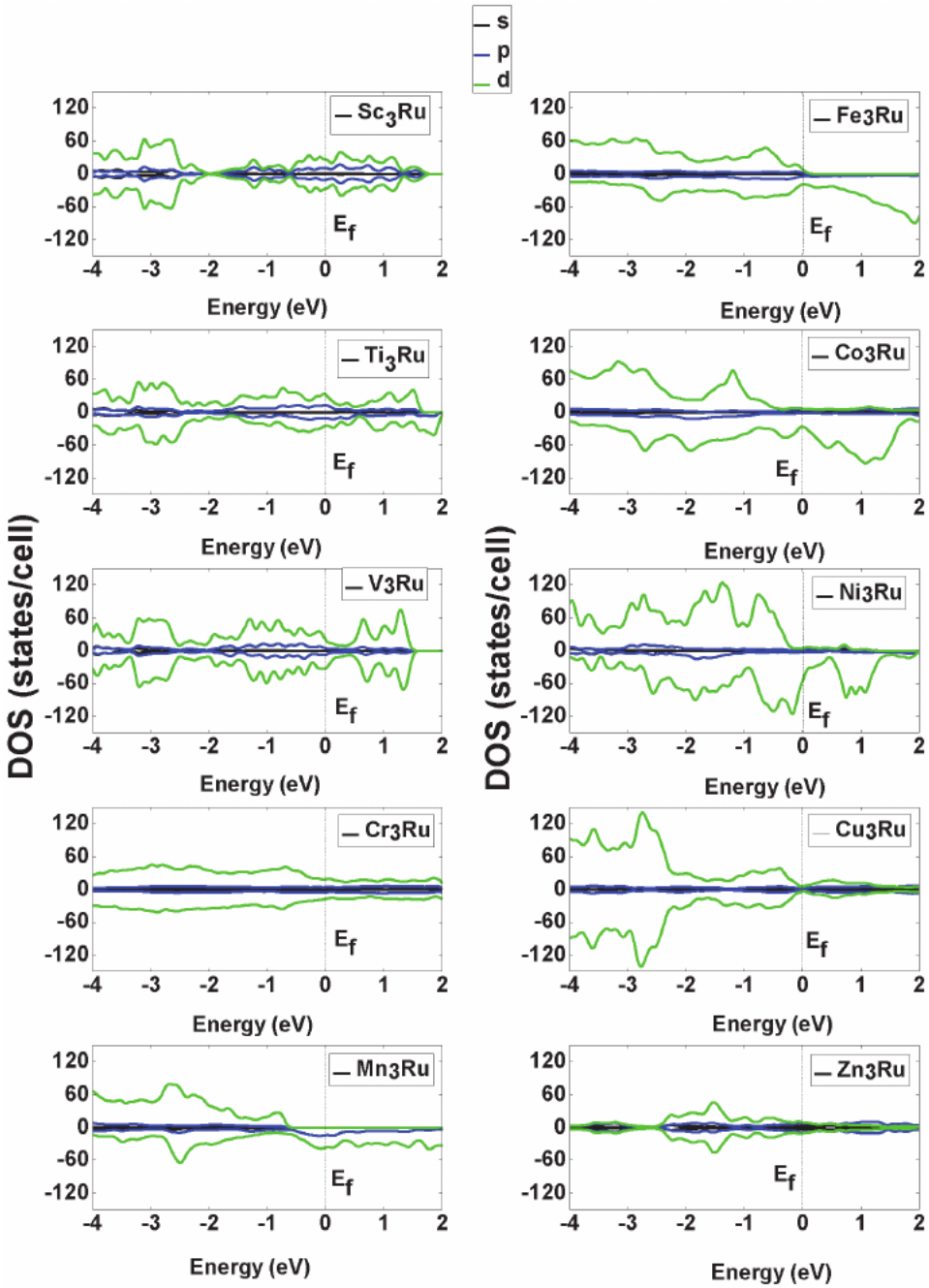

Figure 5.
Partial density of states of binary X_3Ru (X = Sc, Ti, V, Cr, Mn, Fe, Co, Ni, Cu and Zn). The Fermi energy is taken as zero energy, indicated with the vertical dotted line.

along the X-axis direction [53]. Ti_3Ru has the strongest resistance to the compressibility among all the structures, due to the largest C_{11} (1061 GPa) value [54]. The elastic constant C_{44} reflects the degree of shear resistance in the (100) plane and affects the hardness of solid materials indirectly [55]. Fe_3Ru has a larger C_{44} (137 GPa) suggesting a stronger ability to resist shear distortion in (100) plane. The elastic modulus such as (bulk modulus B, shear modulus G and Young's modulus E), Poisson's ratio υ, melting temperature Tm and anisotropic factor are used to

determine the mechanical properties. The elastic moduli of A15 X_3Ru (X = Sc, Ti, V, Cr, Mn, Fe, Co, Ni, Cu and Zn) structures are shown in **Table 3**. Bulk modulus reflects the incompressibility of solid materials. The stronger incompressibility in solid material correspond to larger bulk modulus. Under constant volume conditions, the shear modulus denotes the deformation resistance of solid materials, whilst the Young's modulus offers a measure of the stiffness of a solid.

The Fe_3Ru structure indicates larger bulk (1060 GPa), shear (209 GPa) and Young's modulus (672 GPa) as shown in **Table 3** and therefore shows stronger resistance to compressibility, shear deformation and stiffness. It is noted that the X_3Ru (X = Sc, V, Co, Ni, Cu and Zn) structure have negative shear modulus and Young's modulus. Furthermore, Co indicates the smallest negative shear modulus (−991.0 GPa) and Young's modulus ($-2.2*10^5$ GPa) indicating instability associated with phase change. This instability is also observed in ferro-elastic phase transformation [56]. The negative elastic modulus is due to Landau theory [57] when two local minima form in a strain energy function. Besides, solids with negative elastic modulus can be stabilized with sufficient constraint. The ratio of B/G is larger than 1.75 and predicts ductile behavior in a solid material [27]. Otherwise, it will exhibit the brittle behavior. Similar trend is expected in Poisson's ratio [28], which refers to ductile compounds normally with a large ($\upsilon > 0.3$) and lastly, positive Cauchy pressure (C_{12}-C_{44}) [58, 59] shows that the given material is expected to be ductile whilst negative Cauchy pressure indicates brittleness as shown in **Table 3**.

The X_3Ru (X = Ti, Mn, Cr and Fe) structures are ductile due to B/G values greater than 1.75 whilst, Sc_3Ru, Co_3Ru, Ni_3Ru, Cu_3Ru and Zn_3Ru are brittle. It is noted that Cr_3Ru (19.6) is more ductile indicated in **Table 3** and possess high fracture toughness. This is in agreement with the Poisson's ratio and Cauchy pressure results discussed. A positive Cauchy pressure in Mn_3Ru (52 GPa) and Cr_3Ru (241 GPa) is observed with B/G ratio of 16 and 19.6 and Poisson's ratio of (0.5 and 0.5) indicating ductile characteristics. Similar trend of results are shown in A15 XNb_3 (X = Al, Ge, Si, Sn, Pt and Ir) studies, and ductility can be attributed by positive Cauchy pressure [60, 61].

System	C_{11}	C_{12}	C_{44}	B	G	E	B/G	C_{12}-C_{44}	υ	T_m (K)	A
	GPa	GPa	GPa	GPa	GPa	GPa		GPa	GPa		
Sc_3Ru	78	104	33	95	−33	−113	−2.9	71	0.7	1014	2.2
Ti_3Ru	1061	74	−34	403	58	167	7	108	0.4	6824	0.01
V_3Ru	242	95	−621	144	−60	−209	−2.4	716	0.7	1983	−4.70
Cr_3Ru	336	245	4	275	14	40	19.6	241	0.5	2539	0.8
Mn_3Ru	145	48	−4	80	5	14	16	52	0.5	1410	0.3
Fe_3Ru	−1328	−922	137	1060	209	672	5.1	−1059	0.6	−7295	0.5
Co_3Ru	765	120	−340	335	−991	$-2.2x10^5$	−0.3	460	110	5074	−0.70
Ni_3Ru	91	102	−163	98	−57	−210	−1.7	265	0.9	1091	−2.50
Cu_3Ru	156	54	−43	88	−85	−374	−1.0	97	1.2	1475	−0.20
Zn_3Ru	79	40	−19	53	−47	−198	−1.1	59	1.1	1020	0.03

Table 3.
Calculated elastic constants (C_{ij}), Moduli (average B, G, E_{VRH}), Poisson's ratio (υ), Shear moduli (C), the ratio of Bulk to Shear (B/G), Cauchy pressure (C_{12}-C_{44}), Melting temperature (T_m) and elastic anisotropy (A). All elastic constants and Moduli are in GPa.

3.4 Melting temperatures (T_m) of A15 Ru-based alloys

To assess the potential of high-temperature application of X_3Ru structures, we have calculated their melting temperatures based on the elastic constants C_{ij}, [30, 32] as presented in **Table 3**. It is evident that Ti_3Ru (6824 K) structure possesses high melting point whereas Fe_3Ru (−7295 K) has a low melting point. This attributes to the elastic constant C11 factor in these structures that leads to variation in melting temperatures. The calculated melting temperatures (T_m) of several studied X_3Ru are in the same range as Nb_3Al (2333 K) [1] and Ni_3Al (1668 K) [44] which are obtained experimentally and theoretically. The calculated T_m of V_3Ru (1983 K), Cr_3Ru (2539 K), Co_3Ru (5074 K) and Ti_3Ru (6824) are greater than the T_m of Ni_3Al (1668 K).

3.5 Elastic anisotropy

If the anisotropic index A is close to 1 (unity) respectively, the solid materials are predicted to be isotropic. Otherwise, it will be anisotropic. The anisotropic factors (A) of X_3Ru (X = Sc, Ti, V, Cr, Mn, Fe, Co, Ni, Cu and Zn) ranges from −4.7 to 2.2 respectively. It is clear that all the X_3Ru (X = Sc, Ti, V, Cr, Mn, Fe, Co, Ni, Cu and Zn) values have deviated away from unity; thus, the structures are anisotropic.

4. Conclusion

Using first principles density functional theory calculations, we have investigated the structural, electronic, magnetic and elastic properties of X_3Ru (X = Sc, Ti, V, Cr, Fe, Co, Cu and Zn) binary alloys in search of potential materials for high temperature structural application. The negative heat of formation in Mn_3Ru has been observed, indicating that the system is thermodynamically stable compared to other studied X_3Ru alloys that exhibited positive heats of formation. The total partial density of states show a strong overlap between the valence and conduction bands in Sc_3Ru, Ti_3Ru, V_3Ru, Cr_3Ru Fe_3Ru, Cu_3Ru and Zn_3Ru indicating that these systems are metallic, whilst X_3Ru (X = Mn, Co and Ni) are found to be half-metallic. Furthermore, Cr_3Ru is known to exist experimentally, on the other hand, no experimental data has been reported on all the remaining X_3Ru systems. The elastic constants and related mechanical parameters such as bulk modulus, shear modulus, Young's modulus, B/G ratio and Poisson's ratio, melting temperatures and anisotropy factor are calculated. According to the elastic stability criteria, all X_3Ru structures are mechanically unstable except Cr_3Ru with highest B/G ratio of 19.6. The calculated anisotropic factor indicates that all the X_3Ru (X = Sc, Ti, V, Cr, Mn, Fe, Co, Ni, Cu and Zn) are anisotropic. Co_3Ru, Fe_3Ru, Ni_3Ru and Mn_3Ru possess magnetic moments of 1.70, 1.58, 0.97 and 2.59 u_B, respectively, while Sc_3Ru, Ti_3Ru, V_3Ru, Cu_3Ru, Cr_3Ru and Zn_3Ru are non-magnetic. The results for stable Mn_3Ru with high magnetic moment could pave way for experimental realization (synthesis) of this material. Finally, the thermodynamic stable alloy Mn_3Ru is predicted to be a good candidate for high temperature and spintronic applications.

Acknowledgements

This work was supported by the National Research Foundation (grant number: 121479) and UNISA Masters and Doctoral Bursary. The computational work was

performed using High-Performance Computing (HPC) facilities at the University of South Africa. Special thanks to Mr. Brian Nyandoro (PhD student) for fruitful discussions related to this work.

References

[1] C.T. Sims, N.S. Stoloff, W.C. Hagel, superalloys II, Wiley New York, 1987.

[2] Y. Yamabe-Mitarai, Y. Gu, C. Huang, R. Völkl, H. Harada, Platinum-group-metal-based intermetallics as high-temperature structural materials, JOM. 56 (2004) 34–39.

[3] P. Caron, High y'solvus new generation nickel-based superalloys for single crystal turbine blade applications, Superalloys. 2000 (2000) 737–746.

[4] P.K. Liao, K.E. Spear, T.B. Massalski, Binary alloy phase diagrams, ASM Int. Mater. Park. Ohio. 1 (1990) 557–559.

[5] R. Süss, L.A. Cornish, U. Glatzel, Comparison of experimentally determined and CALPHAD-determined results of the Pt-Cr-Ru System, CALPHAD XXXIII Progr. Abstr. 34 (2004).

[6] W. Wopersnow, C.J. Raub, The Alloys of Ruthenium with Palladium and Chromium as well as with Some Other Transition Metals, Metall. 33 (1979) 1261–1265.

[7] B.M. Venkatraman, J.P. Neumann, The Cr-Ru (Chromium-Ruthenium) System 51.996 101.07, Bull. Alloy Phase Diagrams. 8 (1987) 109–112.

[8] M. Jahnátek, O. Levy, G.L.W. Hart, L.J. Nelson, R. V Chepulskii, J. Xue, S. Curtarolo, Ordered phases in ruthenium binary alloys from high-throughput first-principles calculations, Phys. Rev. B. 84 (2011) 214110.

[9] A.R. Miedema, A.K. Niessen, F.R. De Boer, R. Boom, W.C.M. Matten, Cohesion in metals: transition metal alloys, Report, Philips Res. Lab. Eindhoven, Netherlands. FR Boer, R. Boom, WCM Mattens, AR Miedema, AK Niessen Cohes. Met. Transit. Met. Alloy. North-Holl. Publ. Co., Amsterdam. (1989).

[10] D.R. Lide, CRC handbook of chemistry and physics, CRC Boca Raton, 2012.

[11] R.A. Hobbs, L. Zhang, C.M.F. Rae, S. Tin, Mechanisms of topologically close-packed phase suppression in an experimental ruthenium-bearing single-crystal nickel-base superalloy at 1100 C, Metall. Mater. Trans. A. 39 (2008) 1014–1025.

[12] A. Sato, H. Harada, T. Yokokawa, T. Murakumo, Y. Koizumi, T. Kobayashi, H. Imai, The effects of ruthenium on the phase stability of fourth generation Ni-base single crystal superalloys, Scr. Mater. 54 (2006) 1679–1684.

[13] A.C. Yeh, S. Tin, Effects of Ru and Re additions on the high temperature flow stresses of Ni-base single crystal superalloys, Scr. Mater. 52 (2005) 519–524.

[14] M.M. Tibane, Phase stability study of Pt-Cr and Ru-Cr binary alloys, (2011).

[15] M. Born, R. Oppenheimer, Zur quantentheorie der molekeln, Ann. Phys. 389 (1927) 457–484.

[16] P. Hohenberg, W. Kohn, Inhomogeneous electron gas, Phys. Rev. 136 (1964) B864.

[17] S. Tosoni, C. Tuma, J. Sauer, B. Civalleri, P. Ugliengo, A comparison between plane wave and Gaussian-type orbital basis sets for hydrogen bonded systems: Formic acid as a test case, J. Chem. Phys. 127 (2007) 154102.

[18] X. Li, H. Zhang, S. Lu, W. Li, J. Zhao, B. Johansson, L. Vitos, Elastic properties of vanadium-based alloys from first-principles theory, Phys. Rev. B. 86 (2012) 14105.

[19] M. Born, On the stability of crystal lattices. I, in: Math. Proc. Cambridge

Philos. Soc., Cambridge University Press, 1940: pp. 160–172.

[20] C.L. Fu, M.H. Yoo, Electronic structure and mechanical behavior of transition-metal aluminides: A first-principles total-energy investigation, Mater. Chem. Phys. 32 (1992) 25–36.

[21] R. Hill, The elastic behaviour of a crystalline aggregate, Proc. Phys. Soc. Sect. A. 65 (1952) 349.

[22] A. Reuss, Calculation of the flow limits of mixed crystals on the basis of the plasticity of monocrystals, Z. Angew. Math. Mech. 9 (1929) 49–58.

[23] X. Liu, Q. Feng, B. Tang, J. Zheng, Z. Zheng, W. Zhou, J. Tian, J. Wang, First-principles calculations of mechanical and thermodynamic properties of tetragonal Be 12 Ti, RSC Adv. 9 (2019) 5302–5312.

[24] Z.Q. Lv, Z.F. Zhang, Q. Zhang, Z.H. Wang, S.H. Sun, W.T. Fu, Structural, electronic and elastic properties of the Laves phases WFe2, MoFe2, WCr2 and MoCr2 from first-principles, Solid State Sci. 56 (2016) 16–22.

[25] V. Tvergaard, J.W. Hutchinson, Microcracking in ceramics induced by thermal expansion or elastic anisotropy, J. Am. Ceram. Soc. 71 (1988) 157–166.

[26] H. Fu, D. Li, F. Peng, T. Gao, X. Cheng, Ab initio calculations of elastic constants and thermodynamic properties of NiAl under high pressures, Comput. Mater. Sci. 44 (2008) 774–778.

[27] S.F. Pugh, XCII. Relations between the elastic moduli and the plastic properties of polycrystalline pure metals, London, Edinburgh, Dublin Philos. Mag. J. Sci. 45 (1954) 823–843.

[28] I.N. Frantsevich, F.F. Voronov, S.A. Bokuta, Elastic Constants and Elastic Moduli of Metals and Insulators Handbook, edited by IN Frantsevich (Naukova Dumka, Kiev, 1983), Google Sch. (1983) 60–180.

[29] A.I. Popoola, Computational study of noble metal alloys, (2014).

[30] D.J. Skinner, M. Zedalis, Elastic modulus versus melting temperature in aluminum based intermetallics, Scr. Metall. 22 (1988) 1783–1785.

[31] M. Blackman, On the calculation of characteristic temperatures from the Elastic constants, London, Edinburgh, Dublin Philos. Mag. J. Sci. 42 (1951) 1441–1442.

[32] M.E. Fine, L.D. Brown, H.L. Marcus, Elastic constants versus melting temperature in metals, Scr. Metall. 18 (1984) 951–956.

[33] S.J. Clark, M.D. Segall, C.J. Pickard, P.J. Hasnip, M.I.J. Probert, K. Refson, Mike C Payne, First principles methods using CASTEP, Zeitschrift Fur Krist. 220 (2005) 567–570. https://doi.org/10.1524/zkri.220.5.567.65075.

[34] D. Vanderbilt, Soft self-consistent pseudopotentials in a generalized eigenvalue formalism, Phys. Rev. B. 41 (1990) 7892.

[35] J. Perdew, K. Burke, M. Ernzerhof, PBE and PBE0, Phys. Rev. Lett. 77 (1996) 3865–3868. https://doi.org/10.1103/PhysRevLett.77.3865.

[36] A.I. Liechtenstein, V.I. Anisimov, J. Zaanen, Density-functional theory and strong interactions: Orbital ordering in Mott-Hubbard insulators, Phys. Rev. B. 52 (1995) R5467.

[37] H.J. Monkhorst, J.D. Pack, Special points for Brillouin-zone integrations, Phys. Rev. B. 13 (1976) 5188.

[38] V. Petrman, J. Houska, Trends in formation energies and elastic moduli of ternary and quaternary transition metal

nitrides, J. Mater. Sci. 48 (2013) 7642–7651.

[39] N.I. Medvedeva, A.L. Ivanovskii, Ab-initio study of Re and Ru effect on stability of TCP nanoparticles in Ni-based superalloys, Наносистемы: Физика, Химия, Математика. 5 (2014).

[40] B.O. Mnisi, E.M. Benecha, H.R. Chauke, P.E. Ngoepe, M.M. Tibane, Effect of transition metal doping on Cr–Ru alloys using first principles approach, Bull. Mater. Sci. 43 (2020) 1–9.

[41] Y.F. Gu, H. Harada, Y. Ro, T. Kobayashi, Microstructural Evolution and Mechanical Properties of Cr-Ru Alloys, 36 (2005) 577–582.

[42] A. Continenza, G. Profeta, S. Picozzi, Transition metal doping and clustering in ge, Appl. Phys. Lett. 89 (2006) 202510.

[43] F. Kong, R.C. Longo, M.-S. Park, J. Yoon, D.-H. Yeon, J.-H. Park, W.-H. Wang, K.C. Santosh, S.-G. Doo, K. Cho, Ab initio study of doping effects on LiMnO 2 and Li 2 MnO 3 cathode materials for Li-ion batteries, J. Mater. Chem. A. 3 (2015) 8489–8500.

[44] A.I. Popoola, J.E. Lowther, Computational Study of Platinum Group Superalloys, Int. J. Mod. Phys. B. 28 (2014) 1450066.

[45] J. Bai, J.M. Raulot, Y.D. Zhang, C. Esling, X. Zhao, L. Zuo, Crystallographic, magnetic, and electronic structures of ferromagnetic shape memory alloys Ni 2 XGa (X= Mn, Fe, Co) from first-principles calculations, J. Appl. Phys. 109 (2011) 14908.

[46] J. Xu, A.J. Freeman, Bandfilling and structural stability of trialuminides: YAl 3, ZrAl 3, and NbAl 3, J. Mater. Res. 6 (1991) 1188–1199.

[47] M. Krajci, J. Hafner, Covalent bonding and bandgap formation in intermetallic compounds: a case study for Al3V, J. Phys. Condens. Matter. 14 (2002) 1865.

[48] B.H. Cheong, K.-J. Chang, First-principles study of the structural properties of Sn under pressure, Phys. Rev. B. 44 (1991) 4103.

[49] Y. Song, Z.X. Guo, R. Yang, D. Li, First principles study of site substitution of ternary elements in NiAl, Acta Mater. 49 (2001) 1647–1654.

[50] T. Hong, T.J. Watson-Yang, X.-Q. Guo, A.J. Freeman, T. Oguchi, J. Xu, Crystal structure, phase stability, and electronic structure of Ti-Al intermetallics: Ti 3 Al, Phys. Rev. B. 43 (1991) 1940.

[51] C. Yu, J. Liu, H. Lu, P. Li, J. Chen, First-principles investigation of the structural and electronic properties of Cu6− xNixSn5 (x= 0, 1, 2) intermetallic compounds, Intermetallics. 15 (2007) 1471–1478.

[52] D.C. Wallace, Thermodynamics of crystals, Courier Corporation, 1998.

[53] X. Gao, Y. Jiang, R. Zhou, J. Feng, Stability and elastic properties of Y–C binary compounds investigated by first principles calculations, J. Alloys Compd. 587 (2014) 819–826.

[54] X. Li, D. Chen, Y. Wu, M. Wang, N. Ma, H. Wang, Assessment on the structural, elastic and electronic properties of Nb3Ir and Nb3Pt: A first-principles study, AIP Adv. 7 (2017) 65012.

[55] G. Grimvall, Thermophysical properties of materials, Elsevier, 1999.

[56] E. Salje, Phase transitions in ferroelastic and co-elastic crystals, Ferroelectrics. 104 (1990) 111–120.

[57] F. Falk, Model free energy, mechanics, and thermodynamics of

shape memory alloys, Acta Metall. 28 (1980) 1773–1780.

[58] S. Ganeshan, S.L. Shang, H. Zhang, Y. Wang, M. Mantina, Z.K. Liu, Elastic constants of binary Mg compounds from first-principles calculations, Intermetallics. 17 (2009) 313–318.

[59] D.G. Pettifor, Theoretical predictions of structure and related properties of intermetallics, Mater. Sci. Technol. 8 (1992) 345–349.

[60] X. Li, D. Chen, Y. Wu, M. Wang, N. Ma, H. Wang, Assessment on the structural, elastic and electronic properties of Nb_3Ir and Nb_3Pt: A first-principles study, AIP Adv. 7 (2017) 065012. https://doi.org/10.1063/1.4986906.

[61] I. Papadimitriou, C. Utton, P. Tsakiropoulos, Ab initio investigation of the Nb–Al system, Comput. Mater. Sci. 107 (2015) 116–121.